UNIVERSITY OF CALIFORNIA, SAN DIEGO

Computational Investigations of Large Strain Consolidation and Consolidation-Induced Contaminant Transport

A Dissertation submitted in partial satisfaction of the requirements for the degree Doctor of Philosophy

in

Structural Engineering

by

Hefu Pu

Committee in charge:

Professor Patrick J. Fox, Chair
Professor Tara C. Hutchinson
Professor Peter M. Shearer
Professor P. Benson Shing
Professor Daniel M. Tartakovsky

2014

The Dissertation of Hefu Pu is approved, and it is acceptable in quality and form for publication on microfilm and electronically:

_____

_____

_____

_____

_____

_____

Chair

University of California, San Diego

2014

DEDICATION

To my parents whose love and support never failed.

EPIGRAPH

When we are not sure,

we are alive.

– Graham Greene

TABLE OF CONTENTS

LIST OF SYMBOLS

a_v coefficient of compressibility

c fluid (i.e., dissolved) concentration

c_b fluid concentration at bottom boundary

c_e effluent fluid concentration

c_f final fluid concentration

c_o initial fluid concentration

c_t fluid concentration at top boundary

c_v coefficient of consolidation

C total solute mass

C_c compression index

C_f dissolved solute mass

C_{fo} initial dissolved solute mass

C_r recompression index

C_s sorbed solute mass

D^* effective diffusion coefficient

D_{GML} diffusion coefficient for geomembrane liner

D_L longitudinal hydrodynamic dispersion coefficient

D_{Ls} equivalent series longitudinal hydrodynamic dispersion coefficient

D_o free solution diffusion coefficient

e void ratio

e_{avg} average void ratio of soil specimen

e_f final void ratio

e_o initial void ratio

e_p preconsolidation void ratio

f_o initial seepage force per unit volume

f_{oc} organic carbon fraction

F Freundlich isotherm parameter (Chapter 5)

F contaminant mass flux at the base of liner per unit area (Chapter 7)

F_{ss} steady-state contaminant mass flux at the base of liner per unit area

G_s specific gravity of solids

h total head

h_b total head at bottom boundary

h_t total head at top boundary

H height of soil layer or soil specimen

H_{dr} longest drainage path

H_o initial height of soil layer or soil specimen

i hydraulic gradient

i_{cz} vertical fluid concentration gradient

j element coordinate

J_z dispersion mass flux

k vertical hydraulic conductivity

k_o initial vertical hydraulic conductivity

k_s equivalent series vertical hydraulic conductivity

K_d distribution coefficient for linear sorption isotherm

K_{GML} partition coefficient for geomembrane liner

K_{oc} organic carbon partition coefficient

K_p Freundlich isotherm parameter

L height of element

L_f height of fluid element

L_{fo} initial height of fluid element

L_o initial height of element

L_s height of solid element

L_{so} initial height of solid element

LL liquid limit

M effective diffusion coefficient exponent

M_e cumulative solute mass outflow from specimen

M_{ef} cumulative final solute mass outflow from specimen

M_o total initial solute mass inside specimen

m fluid element coordinate

m_b fluid element adjacent to bottom boundary

m_t fluid element adjacent to top boundary

N_L value used to calculate D_{Ls}

n porosity

P Peclet number

PI plasticity index

PL plastic limit

q_f final vertical effective stress at top boundary

q_o initial vertical effective stress at top boundary

r average rate of strain

R_F ratio of C simulation result over NC-F simulation results (Chapter 7)

R_I ratio of C simulation result over NC-I simulation results (Chapter 7)

R_j number of solid elements

R_{mo} initial number of fluid elements

R_M solute mass outflow ratio

R_{Mf} final solute mass outflow ratio

R_s number of data points for compressibility relationship

R_t number of data points for hydraulic conductivity relationship

s sorbed concentration

s_f final sorbed concentration

s_o initial sorbed concentration

S settlement of soil layer or soil specimen

$\tilde{S}$ required settlement of soil specimen

S_{ult} ultimate settlement of soil layer

t time

t_q landfill loading time

T time factor

u pore pressure

u_{ex} excess pore pressure

$u_{ex,b}$ excess pore pressure at base of specimen

U_{avg} average degree of consolidation

v boundary water outflow rate

v_{rf} relative discharge velocity

v_o steady discharge velocity

v_s seepage velocity

V_f volume of fluid in fluid element

V_{fo} initial volume of fluid in fluid element

z vertical coordinate

z_f elevation of fluid element node

z_{fb} elevation of bottom boundary of fluid element

z_{fo} initial elevation of fluid element node

z_{ft} elevation of top boundary of fluid element

z_s elevation of solid element node

z_{so} initial elevation of solid element node

z_o initial elevation of element node

Z normalized elevation

α constant

α_L longitudinal dispersivity

β normalized strain rate

Δq change in vertical effective stress at top boundary

$\Delta q_{\max}$ maximum vertical effective stress at top boundary

Δt time increment

Δs change in sorbed concentration

ε vertical strain

ε_{avg} average vertical strain of soil specimen

$\varepsilon_{avg,f}$ final average vertical strain of soil specimen

γ moist unit weight of soil

γ_{sat} saturated unit weight of soil

γ_w unit weight of water

γ'_o initial buoyant unit weight of soil

λ sorption rate constant

λ_c decay constant

ρ_d dry density of soil

ρ_w density of water

σ vertical total stress

σ' vertical effective stress

σ'_{avg} average vertical effective stress within soil specimen

σ'_o initial vertical effective stress

σ'_p preconsolidation stress

SUPERSCRIPTS

t time

^ data points for compressibility relationship

– data points for hydraulic conductivity relationship

~ data points for loading schedule

SUBSCRIPTS

b summation index

j j^{th} solid element

m m^{th} fluid element

R_j top element

s s^{th} data point for compressibility relationship

t t^{th} data point for hydraulic conductivity relationship

LIST OF FIGURES

LIST OF TABLES

ACKNOWLEDGEMENTS

I would like to thank my advisor, Professor Patrick J. Fox, for his tireless dedication to supporting my Ph.D. research at the University of California, San Diego. His persistence and encouragement have challenged me to grow beyond what I thought possible. I express my most sincere gratitude and deepest appreciation for his guidance and support.

I would also like to thank my committee members, Professor Tara C. Hutchinson, Professor Peter M. Shearer, Professor P. Benson Shing, and Professor Daniel M. Tartakovsky, for the contribution of their time and help in my research efforts. I thank Dr. Charles D. Shackelford, Professor of Civil Engineering at Colorado State University, for several insightful discussions regarding contaminant transport through compacted clay liner systems. I thank Dr. R. Kerry Rowe, Professor of the Department of Civil Engineering at Queen's University, for providing additional information about the Gloucester test fill.

I would like to thank my friend Dr. Yong Li for his valuable help, discussions, and friendship during my PhD studies. My gratitude extends to my friends Yewei Zheng, Ning Wang, Yujia Liu, Weiyi Lu, Zhu Mao, Xiaowei Deng, Xiang Wang, Weian Liu, and Jinhui Yan for their help and friendship. I would like to express my gratitude to my lab-mates Alexander Stern, Stuart Thielmann, Andrew Sander, and Michael Sanders for their help and friendship.

Chapter 3 of this dissertation is based on material published by the International Journal of Geomechanics titled "Enhanced CS2 Model for Large Strain Consolidation"

with authors, Patrick J. Fox and Hefu Pu (2012). The dissertation author is the second author of this paper.

Chapter 4 of this dissertation is based on material published by the International Journal for Numerical and Analytical Methods in Geomechanics titled "Model for Large Strain Consolidation under Constant Rate of Strain" with authors, Hefu Pu, Patrick J. Fox, and Yong Liu (2013). The dissertation author is the first author of this paper.

Chapter 5 of this dissertation is based on material published by the Journal of Geotechnical and Geoenvironmental Engineering titled "Consolidation-Induced Solute Transport for Constant Rate of Strain. I: Model Development and Simulation Results" with authors, Hefu Pu, and Patrick J. Fox (2014). The dissertation author is the first author of this paper.

Chapter 6 of this dissertation is based on material published by the Journal of Geotechnical and Geoenvironmental Engineering titled "Consolidation-Induced Solute Transport for Constant Rate of Strain. II: Comparison with Incremental Loading" with authors, Patrick J. Fox and Hefu Pu (2014). The dissertation author is the second author of this paper.

Chapter 7 of this dissertation is based on material from a manuscript under preparation for publication, tentatively titled "Assessment of Consolidation-Induced Contaminant Transport for Geoenvironmental Applications: Compacted Clay Liner Systems," with a preliminary author list of Hefu Pu, Patrick J. Fox, and Charles D. Shackelford (2014). The dissertation author is the first author of this paper.

Appendix A of this dissertation is based on material published by the Journal of Geotechnical and Geoenvironmental Engineering titled "CS3: Large Strain Consolidation

Model for Layered Soils" with authors, Patrick J. Fox, Hefu Pu, and James D. Berles (2014). The dissertation author is the second author of this paper.

Financial support for this research was provided by Grant No. CMMI-1001023 from the Geotechnical Engineering Program of the U.S. National Science Foundation. This support is gratefully acknowledged.

VITA AND PUBLICATIONS

2003-2007 Bachelor of Engineering in Civil Engineering,

Huazhong University of Science and Technology, China

2007-2010 Master of Science in Geotechnical Engineering,

Huazhong University of Science and Technology, China

2010-2014 Doctor of Philosophy in Structural Engineering,

University of California, San Diego, USA

Journal Publications

1. Fox, P.J., and Pu, H.-F. (2012). "Enhanced CS2 model for large strain consolidation," *International Journal of Geomechanics, ASCE*, 12(5), 574-583.
2. Pu, H.-F., Fox, P.J., and Liu, Y. (2013). "Model for large strain consolidation under constant rate of strain," *International Journal for Numerical and Analytical Methods in Geomechanics*, 37(11), 1574-1590.
3. Fox, P.J., Pu, H.-F., and Berles, J.D. (2014). "CS3: Large strain consolidation model for layered soils," *Journal of Geotechnical and Geoenvironmental Engineering, ASCE*, 140(8), 04014041.
4. Fox, P.J., Pu, H.-F., and Christian, J.T. (2014). "Evaluation of data analysis methods for the CRS consolidation test," *Journal of Geotechnical and Geoenvironmental Engineering, ASCE*, 140(6), 04014020.
5. Pu, H.-F., and Fox, P.J. (2014). "Consolidation-induced solute transport for constant rate of strain. I: Model development and simulation results," *Journal of Geotechnical and Geoenvironmental Engineering, ASCE*, in press.
6. Fox, P.J., and Pu, H.-F. (2014). "Consolidation-induced solute transport for constant rate of strain. II: Comparison with incremental loading," *Journal of Geotechnical and Geoenvironmental Engineering*, *ASCE*, in press.
7. Pu, H.-F., Fox, P.J., and Shackelford, C.D. (2014). "Assessment of consolidation-induced contaminant transport for geoenvironmental applications: Compacted clay liner systems," *Journal of Geotechnical and Geoenvironmental Engineering*, ASCE, in preparation.

8. Pu, H.-F., Fox, P.J., and Shackelford, C.D. (2014). "Assessment of consolidation-induced contaminant transport for geoenvironmental applications: Confined disposal and subaqueous capping," *Journal of Geotechnical and Geoenvironmental Engineering*, *ASCE*, in preparation.

Conference Publications

1. Pu, H.-F., and Fox, P.J. (2012). "Updated CS2 model for large strain consolidation of clay," *Proceedings, Geo-Congress 2012*: *State of the Art and Practice in Geotechnical Engineering*, ASCE Geotechnical Special Publication 225, R.D. Hryciw, A. Athanasopoulos-Zekkos, and N. Yesiller, eds., Oakland, CA, pp. 115-124.

2. Pu, H.-F., and Fox, P.J. (2014). "Model for coupled large strain consolidation and solute transport under constant rate of strain," *Proceedings, Geo-Congress 2014*: *Geo-Characterization and Modeling for Sustainability*, ASCE Geotechnical Special Publication 234, M. Abu-Farsakh, X. Yu, and L.R. Hoyos, eds., Atlanta, GA, pp. 2725-2734.

3. Pu, H.-F., and Fox, P.J. (2014). "Model for coupled CRS consolidation and contaminant transport," *Proceedings, GeoShanghai International Conference 2014: Geoenvironmental Engineering*, ASCE Geotechnical Special Publication 241, R.R. Krishna, and S. Shen, eds., Shanghai, China, pp. 40-49.

ABSTRACT OF THE DISSERTATION

Computational Investigations of Large Strain Consolidation and Consolidation-Induced Contaminant Transport

by

Hefu Pu

Doctor of Philosophy in Structural Engineering

University of California, San Diego, 2014

Professor Patrick J. Fox, Chair

The phenomenon of coupled consolidation and contaminant transport occurs for a variety of practical applications in the area of geotechnical and geoenvironmental engineering. These applications, among others, include mechanical dewatering of contaminated soil or slurry, and contaminant transport through a landfill compacted clay liner during waste placement operations. In these applications, soil consolidation and contaminant transport occur simultaneously and the coupled effects must be accounted for in order to accurately simulate the transport process.

First, an enhanced version of the CS2 model (Fox and Berles 1997) is presented for one-dimensional large strain soil consolidation. A variety of numeric examples indicate that the new capabilities describe important considerations for consolidation analysis.

Based on the enhanced CS2 model, a numerical model, called CCRS1, is developed for one-dimensional large strain consolidation under constant rate of strain (CRS) loading conditions. Results indicate that analytical solutions obtained using small strain theory can be in significant error for large strain conditions with changing coefficient of consolidation.

Based on an existing CST2 model (Fox and Lee 2008) and the newly developed CCRS1 model, a numerical model, called CSTCRS1, is developed for coupled one-dimensional large strain consolidation and solute transport under CRS loading conditions. Numerical investigations are presented to illustrate the effects of initial concentration distribution, transport conditions, applied strain rate, initial specimen height, and drainage and concentration boundary conditions on consolidation-induced solute transport for CRS loading conditions. Using the CST2 model and CSTCRS1 model, numerical investigation is conducted to compare the solute transport for increment loading (IL) and CRS consolidation conditions.

Using the CST2 model, the results of a numerical investigation are presented to assess the significance of compacted clay liner (CCL) consolidation on contaminant transport through single CCL and composite geomembrane/CCL landfill bottom liner systems. Simulation results indicate that consolidation can have an important effect on contaminant transport through CCL, not only during the course of the consolidation

process but also long after consolidation has ended. Analysis based on traditional advective-diffusive transport fails to consider the transient advection and properties changes of CCL caused by consolidation and thus can lead to significant errors.

Chapter 1

Introduction

1.1 Background and Objectives

Consolidation-induced contaminant transport is a coupled process where saturated soil media undergo consolidation while at the same time contaminants move within the soil. The phenomenon of consolidation-induced contaminant transport occurs for many practical applications in the area of geotechnical and geoenvironmental engineering. These applications include confined disposal of contaminated soil or slurry in disposal impoundments, mechanical dewatering of contaminated soil or slurry, remediation of source zones contaminated with chlorinated solvents, contaminant transport through a compacted clay liner during landfill placement operations, capping of subaqueous contaminated sediments, and consolidation of a contaminated aquitard due to groundwater pumping (Fox and Shackelford 2010). In each of these cases, soil consolidation and the transport of contaminants within the soil occur simultaneously and

the coupled effects must be accounted for in order to accurately characterize the transport process.

One example of consolidation-induced contaminant transport is the disposal of contaminated sediments (Fox 2007a). The International Joint Commission (IJC), organization launched by Canada and the United States for protecting the Great Lakes water, has designated 43 Areas of Concern (AOCs) in the Great Lakes region where the environment has been severely polluted. Contaminated sediments have been identified as a problem in 42 of these 43 AOCs. The most critical pollutants are polychlorinated biphenyls (PCBs) and other chlorinated compounds, polyaromatic hydrocarbons (PAHs), and metals (such as mercury, cadmium, and lead). The current state of practice to remediate the polluted sediments is either removal of the sediments for ex-situ disposal or treatment, or in-situ isolation using clean soil and/or geosynthetic materials (e.g., geosynthetic clay liner, reactive core mat) (USEPA 2005). When the sediments are severely contaminated, they are usually dredged and then placed in a confined disposal facility such as shown in Figure 1.1 for dewatering. Confined disposal facility is usually very large, with lateral dimensions approaching a kilometer or even more and heights approaching 50 m (Fox and Shackelford 2010). Millions cubic meter of sediments can be placed in such a confined disposal facility and large strain consolidation will occur, causing the transport of contaminants within. When the sediments are lightly contaminated, an alternative remedial approach is to cap the contaminated sediments underwater, such as shown in Figure 1.2, with clean sediments (e.g., clean sand) to reduce the spread of contamination (USEPA 1998). When the underlying sediments are highly compressible, the cap will result in sediment consolidation which causes

contaminant transport into the cap and eventually into the surrounding aquatic environment. Several key questions arise when any of such applications is contemplated (Fox 2007a): (1) What will be the amount and rate of pore water effluent? (2) What will be the concentration of contaminants in the effluent? (3) What will be the concentration and distribution of remaining contaminants in the consolidated soil media? Rigid-media transport models are not capable of answering such questions because they cannot handle contaminant transport driven by transient advective flows associated with the consolidation process. Large strains and nonlinear constitutive behavior are also typically encountered due to high material compressibility, which further complicates the problem.

Figure 1.1 Aerial photo of confined disposal facility at Grand Calumet River in Gary after grading (Lee 2007).

Several numerical models have been developed to simulate consolidation-induced contaminant transport within deforming porous media. Fox and Berles (1997) developed a piecewise-linear numerical model, called CS2 (Consolidation Settlement 2), for one-dimensional large strain consolidation of a single saturated soil layer. Using the CS2 framework, Fox (2007a) developed a model, called CST1 (Consolidation and Solute Transport 1), for modeling coupled large strain consolidation and contaminant transport. Fox and Lee (2008) upgraded CST1 to CST2 with the addition of some important features. The research of this dissertation represents continued work on the basis of CS2 model and CST2 model, with the enhancement to some existing models and development of some new models for large strain consolidation and coupled consolidation and contaminant transport.

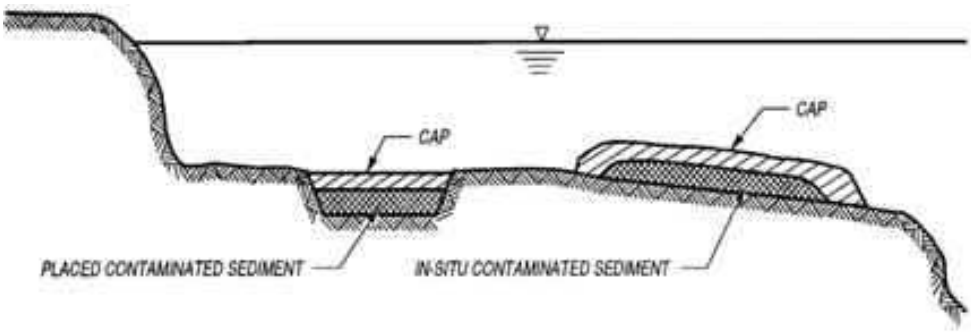

Figure 1.2 Schematic illustration of subaqueous capping of contaminated sediments (after Palermo et al. 1998).

The coupling of large strain consolidation and contaminant transport is a complicated problem, and it cannot be accurately simulated without a state-of-the-art consolidation model as its foundation. Any inappropriate assumptions made in the

consolidation algorithm will give rise to erroneous consolidation results such as porosity and seepage velocity, which subsequently yields erroneous contaminant transport results. The first objective of this research is to incorporate some important enhancements to the existing CS2 (Fox and Berles 1997) consolidation model. The addition of some new capabilities of the enhanced CS2 model enables the simulation of more realistic consolidation problems and serves as a basis for improved simulation of coupled consolidation and contaminant transport.

Constant rate of strain (CRS) consolidation test is a common laboratory test used for the measurement of soil properties of fine-grained soils. CRS consolidation has received considerable research in the past decades using analytical, experimental, and numerical methods. Despite the considerable development of CRS consolidation, no model has been developed to predict consolidation-induced contaminant transport for CRS loading conditions. Such a model would be useful for the analysis of mechanical dewatering of contaminated soils. The second objective of this research is to develop a numerical model that is able to simulate the coupled CRS consolidation and contaminant transport.

Bottom liner systems are required for modern landfills to isolate leachate and waste materials from the surrounding environment. During waste filling operations, consolidation of compacted clay liner (CCL) will occur and the induced transient advective flows and changes in CCL transport properties will affect the transport of contaminants through the liner systems. Although most aspects of transport analysis for the landfill liner systems can be handled with the existing contaminant transport theory, the effect of CCL consolidation on contaminant transport has received relatively little

attention (Rowe 2005). Although there have been several studies on this subject, different opinions exist with regard to the importance of consolidation on contaminant transport through landfill liner systems. The third objective of this research is to conduct a rigorous and comprehensive numerical analysis to clarify how consolidation influences the contaminant transport through a landfill liner system.

1.2 Dissertation Organization

This dissertation is organized as follows:

This Chapter presents the background and objective of the research topic followed by dissertation organization. Chapter 2 presents a literature review of past work related to the research topic.

Chapter 3 presents the development of the enhanced CS2 numerical model including model verification with existing analytical and numerical solutions, and a parametric study on the significance of time-dependent loading, external hydraulic conductivity, unload/reload effect, and stress path.

Chapter 4 presents the development of the CCRS1 numerical model including model verification with existing analytical and numerical solutions, and a parametric study on the effects of soil constitutive relationships on CRS consolidation response.

Chapter 5 presents the development of the CSTCRS1 numerical model including verification and a series of parametric studies on the effects of initial concentration distribution, transport conditions, applied strain rate, initial specimen height, and drainage

and concentration boundary conditions on consolidation-induced solute transport for CRS loading conditions.

Chapter 6 presents a comparative study of consolidation-induced solute transport for incremental loading and constant rate of strain loading conditions, and a series of parametric studies to illustrate the effects of transport conditions, concentration boundary conditions, initial concentration distribution, initial layer height, multiple loading increments, and applied strain rate on consolidation-induced solute transport.

Chapter 7 presents a numerical investigation of the significance of compacted clay liner (CCL) consolidation on contaminant transport through single CCL and composite geomembrane (GML)/CCL landfill bottom liner systems, and a series of parametric studies on the effects of initial CCL thickness, final vertical stress level, loading time, organic carbon fraction in CCL, and effective diffusion coefficient exponent.

Finally, Chapter 8 presents conclusions and recommendations for future research.

Appendix A presents a paper published by the Journal of Geotechnical and Geoenvironmental Engineering titled “CS3: Large Strain Consolidation Model for Layered Soils” with authors, Patrick J. Fox, Hefu Pu, and James D. Berles (2014). This is part of the dissertation author’s research work during PhD studies and is a significant extension for Chapter 3.

Chapter 2

Literature Review

This chapter reviews published research that is relevant to the research topic of this dissertation, with the first half focusing on large strain soil consolidation and the second half focusing on consolidation-induced contaminant transport for large strain conditions.

2.1 Consolidation Theory

This section reviews the work of some of the important researchers who have made important contributions to these areas.

2.1.1 Consolidation under general loading condition

Consolidation is a process during which the pore water within soil flows out under excess pore pressure and, as a result, excess pore pressure dissipates and soil volume decreases. Many advances have been made in the area of consolidation over the past several decades. Most of this work has been conducted within the context of small

(i.e., infinitesimal) strain theory. Terzaghi (1925) proposed the first classical theory of one-dimensional consolidation theory based on the following assumptions: (1) the soil is fully saturated by pore water, (2) the soil is laterally confined, thus water flow and soil deformation only occur in one direction, (3) Darcy's law is valid, (4) hydraulic conductivity is constant throughout consolidation, (5) the soil particles and water are incompressible, (6) deformation of the soil layer is infinitesimal, (7) the coefficient of compressibility of soil is constant, and (8) secondary compression does not occur. Terzaghi's consolidation theory uses properties that can be easily measured in laboratory test, and involves only simple hand-calculations, thus it has gained wide application in geotechnical engineering practice. However, due to the limiting assumptions of Terzaghi's theory, the observed time rate of settlement may differ significantly from the calculated value (Duncan 1993). Maintaining small strain assumption, Schiffman (1958) extended the theory of consolidation by including changing hydraulic conductivity and time-dependent loading during the process of consolidation. Schiffman (1958) concluded that the change in hydraulic conductivity has an important effect on the correct estimate of time rate of consolidation and using an average hydraulic conductivity to calculate the rate of consolidation may result in significant error.

Later, more interesting work has been conducted within the context of large strain consolidation theory. Gibson et al. (1967) derived a general one-dimensional consolidation theory that accounts for finite strain, changing compressibility and hydraulic conductivity relationships with strain. The results suggest that Terzaghi's solution gives erroneous prediction when large strain occurs. Using an Eulerian coordinate system and moving boundary approach, Lee and Sills (1979) solved the

consolidation problem involving finite strain and nonlinear material properties including compressibility and hydraulic conductivity relationships. Their results compare favorably with the results of Gibson et al. (1967).

Yong et al. (1983) introduced piecewise-linear method to solving the large strain consolidation problem. Fox and Berles (1997) developed a piecewise-linear numerical model, called CS2 (Consolidation Settlement 2), for one-dimensional large strain consolidation of a single homogeneous saturated soil layer. CS2 accounts for vertical strain, general constitutive relationships, soil self-weight, relative velocity of fluid and solid phases, and changing material properties during consolidation. Piecewise-linear consolidation models are generally considered to have greater versatility with regard to initial conditions, boundary conditions, and material heterogeneity than models based on material coordinates (Townsend and McVay 1990). In the piecewise-linear method, all variables pertaining to geometry, material properties, fluid flow, and effective stress are updated at each time step with respect to a fixed coordinate system (Yong et al. 1983; Fox and Berles 1997). Mass conservation can be strictly enforced and, as such, the CS2 method is actually a Lagrangian approach that follows the motion of the solid phase throughout the consolidation process. Soil constitutive relationships are specified using discrete data points and do not require mathematical approximations or derivative functions. These features give CS2 high accuracy and considerable versatility to accommodate additional effects with excellent results. Using the CS2 method, subsequent large strain consolidation models have been developed to investigate accreting layers (Fox 2000), vertical and radial flows (Fox et al. 2003), compressible pore fluid (Fox and Qiu 2004), high-gravity conditions in a geotechnical centrifuge (Fox et al.

2005; Lee and Fox 2005), coupled solute transport (Fox 2007a, 2007b; Fox and Lee 2008; Lee and Fox 2009; Pu and Fox 2014), wave propagation (Qiu and Fox 2008), and consolidation under constant rate of strain (Pu et al. 2013; Fox et al. 2014). These studies have extensively verified the accuracy of the CS2 method using analytical solutions, numerical solutions, and experimental data, including solutions obtained using material coordinates (Gibson et al. 1967) and the moving boundary approach of Lee and Sills (1979). CS2 and related models have also been widely used by other researchers for new applications and to validate numerical analyses (Aydilek et al. 2000; Berilgen et al. 2000; Kokusho and Kojima 2002; Berilgen 2004; Bicer 2005; Berilgen et al. 2006; Kwon et al. 2007; Lewis 2009; Meric et al. 2010; Bharat and Sharma 2011; Lee and Park 2013). Most recently, the CS2 method has been adapted to model electro-osmotic consolidation (Zhou et al. 2013), and coupled contaminant transport (Meric et al. 2013) with impressive results.

2.1.2 Consolidation under constant rate of strain condition

The constant rate of strain (CRS) consolidation test is a common test used in laboratory for the measurement of consolidation properties of fine grained soils. It is perhaps the most significant advancement in the last 50 years with regard to consolidation testing. The CRS test is a displacement-controlled, one-dimensional compression test in which the soil specimen is subjected to a constant rate of vertical deformation with single drainage at the top boundary. The two primary measurements are total applied stress at the top boundary and pore pressure at the base of the specimen. Although the average vertical strain is known at any time during a test, local strains vary

from this average depending on the distribution of pore pressure, and hence vertical effective stress, within the specimen. For this reason, some have preferred the term "constant rate of deformation", or CRD, test (Lee 1981; Znidarcic et al. 1986); however, the more established term of CRS is maintained in this dissertation.

The CRS test has some clear advantages as compared to the standard incremental loading consolidation test, including generation of continuous data, better suitability for automated data acquisition, and shorter total test duration. In particular, the generation of continuous data allows for improved definition of the preconsolidation stress, which was a primary motivation for original development of the test (Hamilton and Crawford 1959). Disadvantages of the CRS test include the need for more sophisticated experimental apparatus, inability to measure secondary compression, and common dependence of the measured response, including the preconsolidation stress, on the applied strain rate (Vaid et al. 1979; Leroueil et al. 1985). This rate effect has not been observed for some reconstituted clays (Smith and Wahls 1969; Sheahan and Watters 1997). Provided that the strain rate is sufficiently slow, measured values of preconsolidation stress are generally comparable or proportional to those obtained using incremental loading consolidation tests (Leroueil et al. 1983a; Larsson and Sälfors 1986). Standard procedures for the CRS test (e.g., ASTM D 4186) therefore impose limits on the applied strain rate.

Assuming small strain, linear soil compressibility, and steady state conditions, Smith and Wahls (1969) developed the first theory for CRS consolidation. Also assuming small strain and a constant coefficient of consolidation, Wissa et al. (1971) developed the first full solutions for linear and nonlinear soil compressibility that

included both transient and steady state responses. The theory of Wissa et al. (1971) has also been adapted by American Society for Testing and Materials (ASTM D4186) to guide CRS consolidation test. The small strain assumption is limiting for CRS analysis due to the continuous nature of the test, with total strain magnitudes of 20% or more often reported in the literature (Smith and Wahls 1969; Leroueil et al. 1983b; Silvestri et al. 1986). Assuming a constant coefficient of consolidation, Lee (1981) developed the first large strain CRS theory using a moving boundary approach and showed that small and large strain solutions diverge as vertical strain increases. Znidarcic et al. (1986) presented a large strain theory based on material coordinates. In this case, the governing equations were linearized by assuming the function $g(e)$, which is related to both soil compressibility and hydraulic conductivity, is constant. The above simplifying assumptions with regard to soil constitutive relationships yield mathematical advantage but generally fall short of real soil behavior, especially when large strains are considered. For example, the above theories cannot accommodate a preconsolidation stress and the associated change in soil stiffness that separates overconsolidated and normally consolidated conditions. A large strain CRS consolidation model that can account for more general constitutive relationships as well as changing compressibility and hydraulic conductivity during consolidation would thus represent a significant advance in the area of CRS consolidation.

2.2 Consolidation-Induced Contaminant Transport

2.2.1 Contaminant transport under general consolidation

Classical solutions for contaminant transport through porous media are derived for rigid media in which no volumetric strain occurs during the transport process and advection is steady (Ogata 1970; Bear 1972; Freeze and Cherry 1979). These assumptions are valid for the cases where applied loads are small or the compressibility of media is low. In engineering applications, however, there are many cases in which applied loads are large and/or the compressibility of media is high. As a result, consolidation of the porous media occurs and the associated transient advective flow may play an important, sometimes even dominant, role in the contaminant transport process. Such engineering applications include confined disposal of contaminated soil or slurry, mechanical dewatering of contaminated soil or slurry, remediation of source zones contaminated with chlorinated solvents, contaminant transport through a landfill compacted clay liner during waste filling operations, consolidation of contaminated sediments due to subaqueous capping, and consolidation of a contaminated aquitard due to groundwater pumping (Fox and Shackelford 2010). Transport models based on rigid media are not capable of simulating these problems because they cannot consider the contaminant transport driven by transient advective flows associated with the consolidation process. Large strains and nonlinear constitutive behavior are also typically encountered due to high material compressibility, which further complicates the analysis.

Several research groups have turned their attention to the modeling of coupled consolidation and contaminant transport. Most of this work has been conducted within the context of infinitesimal (i.e., small) strain consolidation theory (Potter et al. 1994; Loroy et al. 1996; Smith 1997; Peters and Smith 1998; Van Impe et al. 2002; Alshawabkeh et al. 2005). Gibson et al. (1995) were the first to discuss coupled contaminant transport within the context of large strain consolidation theory. Their theoretical development is presented without solution and addresses various coordinate references frames, boundary conditions, and dependent variables for the transport of a single tracer (i.e., non-sorbing) solute. Smith (2000) expanded the small strain model of Smith (1997) to include nonlinear large strain theory and presented analytical solutions for quasi-steady-state small strain transport. Peters and Smith (2002) further extended the theory of Smith (2000) to consider time-dependent contaminant transport through deforming porous media in both spatial (Eulerian) and material (Lagrangian) coordinates.

The piecewise-linear numerical approach for modeling large strain consolidation is generally considered to have greater versatility than models based on material coordinates. CS2 (Fox and Berles 1997) is currently the leading piecewise-linear model. The framework of CS2 is particularly suitable for incorporating additional capabilities and has proven to be both reliable and robust in subsequent studies. Using the CS2 framework as a point of departure, a new approach for modeling coupled large strain consolidation and contaminant transport is developed and is coded in the numerical model CST1 (Fox 2007a) and CST2 (Fox and Lee 2008). A complete review of the formulation and capabilities of CST2 is provided by Fox and Lee (2008), and only a brief summary is provided herein. The consolidation algorithm, the same as CS2, is one-

dimensional and accounts for vertical strain, soil self-weight, general constitutive relationships, relative velocity of fluid and solid phases, changing compressibility and hydraulic conductivity relationships during consolidation, time-dependent loading, unload/reload effects, and an externally applied hydraulic gradient acting across the soil layer. Constitutive relationships for the soil are defined using discrete data points and can take nearly any desired form. The contaminant transport algorithm of CST2 is two-dimensional and accounts for advection, longitudinal and transverse dispersion, first-order decay reactions, linear and nonlinear sorption isotherm, and equilibrium and non-equilibrium sorption. Contaminant transport is consistent with temporal and spatial variations of porosity and seepage velocity in the consolidating soil layer. The key to the CST2 model is the definition of two Lagrangian fields of elements that follow the motions of fluid and solid phases separately.

2.2.2 Contaminant transport under CRS consolidation

Both experimental and numerical investigations of consolidation-induced contaminant transport have been conducted for general loading conditions such as instantaneous surcharge loading, corresponding to either single load or incremental load conditions. On the other hand, to the author's knowledge, no work (analytical, numerical, or experimental) has ever been conducted for the case of consolidation-induced contaminant transport under constant rate of strain (CRS) loading condition. Such an investigation has potential laboratory and field applications such as mechanical dewatering of contaminated sludge using plate and frame filter press. A model that

accounts for this problem would be an important addition to the existing transport literature.

Based on the CS2 framework, using CST2 (Fox and Lee 2008) and CCRS1 (Pu et al. 2013) as a point of departure, a piecewise-linear numerical model, called CSTCRS1, was developed (Pu and Fox 2014). CSTCRS1 is the first model in the current literature for coupled CRS consolidation and contaminant transport. CSTCRS1 follows similar procedures with regard to geometry, constitutive relationships, initial void ratio distribution, settlement, advection, dispersion and sorption. The model development and numerical investigations of coupled large strain consolidation and contaminant transport under CRS loading conditions will be discussed in detail in Chapter 5.

2.2.3 Contaminant transport in landfill liner system

Bottom liner systems are required for modern sanitary landfills to isolate leachate and waste materials from the surrounding environment. These systems contain mineral barrier layers consisting of a compacted clay liner (CCL), a geosynthetic clay liner (GCL), or both. The focus of this paper is contaminant transport through CCL-based liner systems. For such systems, transport analysis is traditionally performed using advective-dispersive models with the assumption that the CCL remains rigid during the transport process. This assumption ignores consolidation of the CCL and associated transient advective flows and changes in CCL transport properties. In reality, the vertical stress on a CCL increases greatly with time due to ongoing waste placement operations. Such stresses are low, often approximately 20 kPa or less, shortly after construction and then reach high values, up to and sometimes exceeding 1000 kPa, at final closure.

Although most aspects of transport analysis for CCL-based liner systems can be handled within existing contaminant transport theory, the effect of CCL consolidation on transport has received relatively little attention (Rowe 2005).

The consolidation of a CCL in response to waste placement can be important from two standpoints. First, water effluent from the consolidation process can contribute to flows in an underlying leachate detection system (LDS). Although CCL consolidation water can be misinterpreted as leakage through the liner, differences in chemical composition from landfill leachate can be used, at least initially, to distinguish such flows (Bonaparte and Gross 1993, Moo-Young et al. 2004). Second, CCL consolidation can influence contaminant transport through the CCL. Field studies reported by Workman (1993) and Othman et al. (1997) indicate that contaminant breakthrough occurred much earlier than theoretical predictions based on diffusive transport. Some researchers have attributed this to transient advective flows associated with CCL consolidation (Othman et al. 1997, Rowe 1998). A related effect is the change of CCL transport properties that can occur as a result of decreasing void ratio. Most obviously, the thickness of the CCL decreases with time during consolidation. Hydraulic conductivity and transport properties, such as effective diffusion coefficient, also decrease. For example, Rowe (2005) reported that the annual average hydraulic conductivity of Keele Valley Landfill liner decreased by more than an order of magnitude during filling operations. Although not a CCL material, Lee et al. (2009) conducted an experimental study to investigate the effect of consolidation on transport properties for soft kaolinite clay and found that effective diffusion coefficient and hydrodynamic dispersion coefficient experienced

significant reductions during clay consolidation whereas sorption isotherm and longitudinal dispersivity were largely unchanged.

Several numerical modeling studies have also investigated consolidation-induced transport effects for CCLs. Peters and Smith (2002) conducted the first detailed investigation of coupled consolidation and contaminant transport using a large strain model based on material coordinates and found that, when consolidation was considered, contaminant breakthrough occurred substantially earlier than that predicted by rigid-media analysis for a composite geomembrane (GML)/CCL liner system. Numerical simulations conducted by Fox (2007a; 2007b) indicated that CCL consolidation can have an important influence on transport not only during the consolidation stage but also long after excess pore pressures have dissipated. Fox (2007b) concluded that consolidation has a lasting effect on contaminant migration because transient advective flows change the distribution of solute mass, which then becomes the initial condition for subsequent transport processes. Zhang et al. (2013) recently corroborated this basic conclusion for partially saturated CCLs using a finite deformation numerical model. On the other hand, Rowe and Nadarajah (1995) found that, for typical liner properties, the change in flow due to consolidation was within the typical range of uncertainty concerning the hydraulic conductivity, and that the effect on contaminant transport and hence impact on a receptor aquifer was not significant for the cases examined. Based on a review of existing research, Rowe (2005) concluded that the effects of CCL consolidation appear to be small for typical low-compressibility CCLs, and thus conventional advective-diffusive contaminant transport modeling is suitable for a wide range of practical applications. Lewis et al. (2009a) also found that consolidation had little effect on contaminant

breakthrough from a clay liner due to the assumed low compressibility of the clay. A more extensive parametric study conducted by Lewis et al. (2009b) indicated that contaminant breakthrough time strongly depends on CCL compressibility. This work was performed using a constant coefficient of consolidation and focused primarily on contaminant breakthrough time at the exclusion of other important considerations such as contaminant concentrations, mass outflows, and concentration profiles.

The foregoing review indicates a lack of consensus with regard to the effect of CCL consolidation on contaminant transport for CCL-based landfill liner systems. A rigorous and comprehensive analysis is needed to clarify how consolidation affects the contaminant transport through a landfill liner system.

Chapter 3

Enhanced CS2 Model for Large Strain Consolidation

3.1 Introduction

Fox and Berles (1997) presented a piecewise-linear numerical model, called CS2, for one-dimensional large strain consolidation of a single homogeneous saturated soil layer. Several important capabilities not included in the original CS2 model include time-dependent loading, an external hydraulic gradient, and unload/reload effects. Time-dependent loading is more appropriate than instantaneous loading for many practical problems, with both analytical and numerical solutions available for small strain conditions (Schiffman 1958; Schiffman and Stein 1970; Olson 1977; Conte and Troncone 2006; Hsu and Lu 2006). An external hydraulic gradient acting across a consolidating layer is also a common case and, while past research has investigated the effects of

hydraulic gradient on measured hydraulic conductivity (Pane et al. 1983; Fox 1996), little work has been conducted on the effects of an external hydraulic gradient on consolidation behavior itself. Likewise, consolidation models often cannot accommodate changing vertical stress conditions due to unloading and reloading. A large strain consolidation model that includes the foregoing capabilities would be useful from a practical standpoint.

This chapter presents the development and performance of several interesting enhancements to the CS2 numerical model. The consolidation algorithm is one-dimensional and, like the original version, accounts for vertical strain, soil self-weight, general constitutive relationships, relative velocity of fluid and solid phases, and changing hydraulic conductivity and compressibility during the consolidation process. The enhanced CS2 model also accommodates time-dependent loading, an external hydraulic gradient acting across the consolidating layer, and unload/reload effects. Development of these additional capabilities is first presented, and is followed by verification checks for time-dependent loading. Some interesting numeric examples are then presented to illustrate the effects of time-dependent loading, external hydraulic gradient, unload/reload, and stress path on the consolidation behavior of clay.

Using the enhanced CS2 model as a point of departure, a CS3 model is developed to simulate more realistic soil conditions. CS3 has all the capabilities of the enhanced CS2 model and, in addition, accounts for layered soil heterogeneity, time-dependent boundary head conditions, and variable profiles for preconsolidation stress and applied stress increment. This work is published by the Journal of Geotechnical and Geoenvironmental Engineering titled “CS3: Large Strain Consolidation Model for

Layered Soils" with authors, Patrick J. Fox, Hefu Pu, and James D. Berles (2014). The dissertation author is the second author of this paper. This work is presented in Appendix A.

3.2 Model Development

The enhanced CS2 model was developed using the original version as a point of departure and follows similar procedures with regard to geometry, constitutive relationships, fluid flow, and settlement. Detailed descriptions of these aspects are provided by Fox and Berles (1997). The following sections summarize the enhanced model with focus on its new capabilities.

3.2.1 Geometry

A saturated homogeneous compressible soil layer of initial height, H_o, is treated as an idealized two-phase material in which the solid particles and pore fluid are incompressible. The term "homogeneous" refers to the compressibility and hydraulic conductivity constitutive relationships of the layer and not the distribution of initial void ratio within the layer. The initial geometry, prior to the application of a vertical stress increment at time $t = 0$, is shown in Figure 3.1(a). Vertical coordinate, *z*, is defined as positive upward from a fixed datum at the bottom of the layer. Element coordinate, *j*, is also directed upward from the bottom boundary, which represents a deviation from the original CS2. The layer is subdivided into R_j elements, each having unit cross-sectional area, constant initial height, L_o, and a central node located at initial elevation, $z_{o,j}$.

Nodes translate vertically and remain at the center of their respective elements throughout the consolidation process. An initial effective overburden stress, q_o, acts at the top boundary. Top and bottom boundaries can be specified as drained or undrained, and if drained are assigned individual constant total head values, h_t and h_b, respectively, taken with respect to the datum. These head values can be dissimilar to allow for the application of an external hydraulic gradient across the layer. The distribution of initial void ratio, $e_{o,j}$, within the layer may calculated by CS2 or specified by the user.

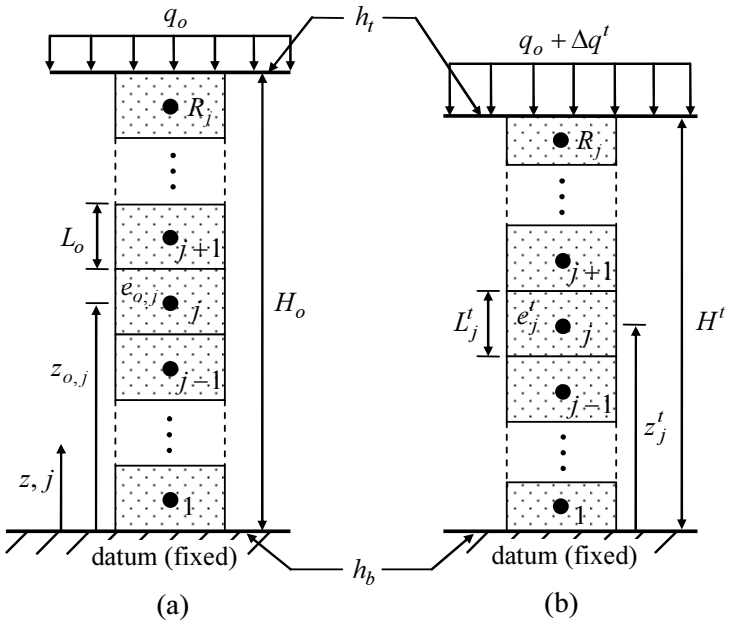

Figure 3.1 Geometry for CS2: (a) initial configuration; (b) configuration after application of vertical stress increment.

3.2.2 Constitutive Relationships

Constitutive relationships for the compressible layer, shown in Figure 3.2, are specified using discrete data points. The compressibility relationship (Figure 3.2(a)) is defined by $R_s \geq 2$ pairs of corresponding vertical effective stress, $\hat{\sigma}'$, and void ratio, $\hat{e}$, and allows for unload/reload. Depending on the choice of data points, this relationship may reflect normally consolidated or overconsolidated conditions. Throughout a simulation, a value of preconsolidation (i.e., maximum past) stress, $\sigma'^{t}_{p,j}$, and the corresponding void ratio, $e^{t}_{p,j}$, is maintained for each element. If the vertical effective stress decreases below $\sigma'^{t}_{p,j}$, unloading and reloading follow an identical path defined by $\sigma'^{t}_{p,j}$, $e^{t}_{p,j}$, and a constant recompression index $C_r = \Delta e / \Delta \log \sigma'$.

The hydraulic conductivity relationship (Figure 3.2(b)) is defined by $R_t \geq 2$ pairs of corresponding void ratio, $\bar{e}$, and vertical hydraulic conductivity, $\bar{k}$. CS2 uses the same hydraulic conductivity relationship for normally consolidated and overconsolidated conditions, which is consistent with the findings of Al-Tabbaa and Wood (1987), Nagaraj et al. (1994), and Fox (2007b).

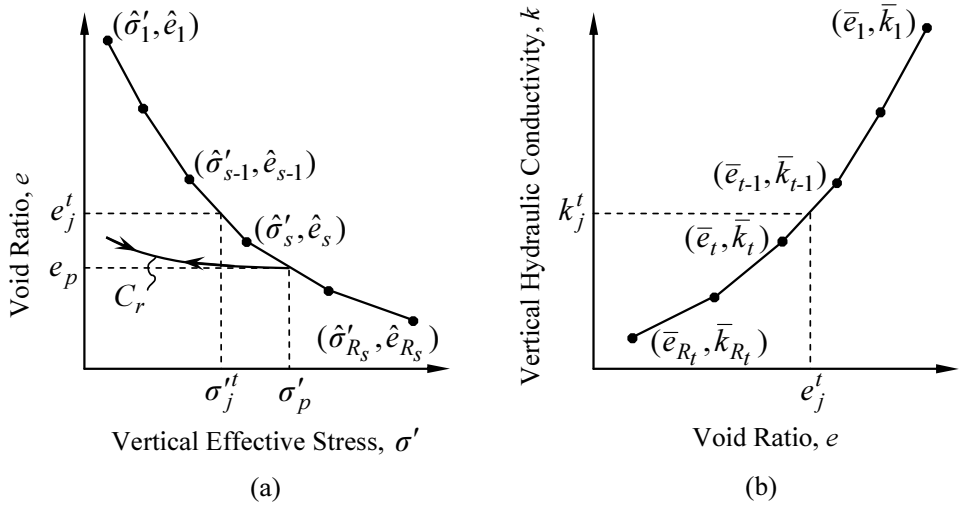

Figure 3.2 Soil constitutive relationships: (a) compressibility; (b) hydraulic conductivity.

Aside from unload/reload effects, a one-to-one correspondence is assumed for each constitutive relationship in Figure 3.2. Thus, CS2 does not account for the effects of strain rate, secondary compression, or aging on the compressibility or hydraulic conductivity of the soil. The constitutive relationships can, however, take essentially any desired form by choosing the appropriate number of points.

3.2.3 Initial Void Ratio Distribution

A distribution of initial void ratio is needed to begin a CS2 simulation. This distribution can be in equilibrium or nonequilibrium with initial stress conditions and soil material properties.

3.2.3.1 Equilibrium

An iteration procedure is used to calculate an initial void ratio distribution that is in equilibrium with q_o, the constitutive relationships and self-weight of the soil, and seepage forces due to an external hydraulic gradient acting across the layer (if $h_t \neq h_b$). In this case, initial excess pore pressures (i.e., the difference between total and steady state pore pressures) are zero. Starting at the top of the layer, the initial vertical effective stress at the node for element R_j, σ'_{o,R_j}, is estimated as q_o and the corresponding initial void ratio, e_{o,R_j}, is calculated from the compressibility relationship (Figure 3.2(a)). This void ratio is used to calculate the initial buoyant unit weight of the element, γ'_{o,R_j}, which yields a new value of vertical effective stress as

$$\sigma'_{o,R_j} = q_o + \frac{L_o}{2}\left(\gamma'_{o,R_j} - f_{o,R_j}\right) \tag{3.1}$$

where f_{o,R_j} is the initial seepage force per unit volume (positive upward) acting on element R_j. Seepage forces on all elements are taken as zero for the first pass. Using σ'_{o,R_j}, an updated value of e_{o,R_j} is calculated from the compressibility relationship and this process is repeated until the change in σ'_{o,R_j} between successive iterations is negligible. Once convergence is obtained for element R_j, the effective stress at the top of element $R_j - 1$ is also known $\left(= \sigma'_{o,R_j} + 0.5L_o(\gamma'_{o,R_j} - f_{o,R_j})\right)$. The iterative procedure is then repeated for element $R_j - 1$ and the remaining elements, which yields the equilibrium distribution of $\sigma'_{o,j}$ and $e_{o,j}$ for the case of no seepage across the layer.

If an external hydraulic gradient is present, the iteration procedure includes an additional loop to account for the effect of associated seepage forces. The initial vertical hydraulic conductivity of each element $k_{o,j}$ is calculated from $e_{o,j}$ and the hydraulic conductivity relationship (Figure 3.2(b)). The steady discharge velocity, v_o, through the layer (positive upward) is

$$v_o = \frac{h_b - h_t}{\sum_{j=1}^{R_j} \frac{L_o}{k_{o,j}}} \tag{3.2}$$

and the corresponding seepage forces are

$$f_{o,j} = \frac{v_o \gamma_w}{k_{o,j}} \qquad j = 1, 2, ..., R_j \tag{3.3}$$

where γ_w is the unit weight of water (constant). With updated values of $f_{o,j}$, the entire process is repeated until the change in $\sigma'_{o,j}$ for all elements between successive iterations is negligible.

3.2.3.2 Nonequilibrium

CS2 can also accommodate a user-specified distribution of initial void ratio. The most common example is a uniform e_o profile. User-specified initial void ratios will generally not be in equilibrium with initial conditions, which produces nonzero values of excess pore pressure within the layer at the start of loading.

3.2.4 Application of Surcharge Load

While the original CS2 only considered an instantaneous and constant surcharge load, the enhanced model can accommodate time-dependent loading. Beginning at $t = 0$, a time-dependent vertical effective stress, Δq^t, is applied to the layer and moves with the top boundary thereafter (Figure 3.1). The value of Δq^t is interpolated from a series of $\tilde{t}$ vs. $\Delta\tilde{q}$ data points that, similar to Figure 3.2, are entered by the user to define the time schedule of loading. Excess pore pressures generated within the layer cause fluid flow to all drainage boundaries. Soil deformation is one-dimensional and occurs in response to the net fluid outflow from each element. Void ratio is assumed to remain uniform within each element at all times. At time t, the height of the layer is H^t and the height and node elevation for the j^{th} element are L_j^t and z_j^t, respectively.

3.2.5 Stress, Pore Pressure, Fluid Flow, and Settlement

The enhanced CS2 model calculates stresses, pore pressure, fluid flow, and settlement using the same method as the original version. Fox and Berles (1997) presented detailed information on these aspects and only a brief review is provided here. The vertical total stress at node j is calculated from the overburden stress on the layer and the self-weight of overlying elements as

$$\sigma_j^t = q_o + \Delta q^t + \left(h_t - H^t\right)\gamma_w + \frac{L_j^t \gamma_j^t}{2} + \sum_{b=j+1}^{R_j} L_b^t \gamma_b^t \qquad j = 1, 2, ..., R_j \qquad (3.4)$$

where $\gamma_j^t \left(=\gamma_w(G_s+e_j^t)/(1+e_j^t)\right)$ is the saturated unit weight of element j, e_j^t is the corresponding void ratio, and G_s is the specific gravity of solids for the soil layer (constant).

Vertical effective stress, $\sigma_j'^t$, is calculated from e_j^t by interpolation between data points in Figure 3.2(a) if $e_j^t \le e_{p,j}^t$ or using the recompression curve if $e_j^t > e_{p,j}^t$. In this latter case,

$$\sigma_j'^t = \sigma_{p,j}'^t \exp\left(2.303\frac{e_{p,j}^t - e_j^t}{C_r}\right) \qquad j = 1, 2, ..., R_j \qquad (3.5)$$

Vertical hydraulic conductivity, k_j^t, is calculated from e_j^t by interpolation between data points in Figure 3.2(b). The pore pressure at node j is the difference between total and effective stresses,

$$u_j^t = \sigma_j^t - \sigma_j'^t \qquad j = 1, 2, ..., R_j \qquad (3.6)$$

Flow between contiguous elements accounts for the relative motion of fluid and solid phases. The relative discharge velocity (positive upward) between nodes j and $j+1$ is

$$v_{rf,j}^t = -k_{s,j}^t i_j^t \qquad j = 1, 2, ..., R_j - 1 \qquad (3.7)$$

where the hydraulic gradient between nodes j and $j+1$ is

$$i_j^t = \frac{h_{j+1}^t - h_j^t}{z_{j+1}^t - z_j^t} \qquad j = 1, 2, ..., R_j - 1 \qquad (3.8)$$

the total head at node j is

$$h_j^t = z_j^t + \frac{u_j^t}{\gamma_w} \qquad j = 1, 2, ..., R_j \qquad (3.9)$$

and the equivalent series hydraulic conductivity between nodes j and $j+1$ is

$$k_{s,j}^t = \frac{k_{j+1}^t k_j^t \left(L_{j+1}^t + L_j^t\right)}{L_{j+1}^t k_j^t + L_j^t k_{j+1}^t} \qquad j = 1, 2, ..., R_j - 1 \qquad (3.10)$$

Corresponding expressions are required at the top and bottom boundaries:

$$v_{rf,R_j}^t = -k_{R_j}^t \frac{h_t - h_{R_j}^t}{H^t - z_{R_j}^t} \qquad (3.11)$$

$$v_{rf,0}^t = -k_1^t \frac{h_1^t - h_b}{z_1^t} \qquad (3.12)$$

If the top boundary is undrained, $v_{rf,R_j}^t = 0$, and if the bottom boundary is undrained, $v_{rf,0}^t = 0$.

Once the relative discharge velocities are known, a new height is calculated for each element using the net fluid outflow over time increment Δt,

$$L_j^{t+\Delta t} = L_j^t - (v_{rf,j}^t - v_{rf,j-1}^t)\Delta t \qquad j = 1, 2, ..., R_j \qquad (3.13)$$

New values of void ratio, layer height, settlement, and average degree of consolidation are, respectively,

$$e_j^{t+\Delta t} = \frac{L_j^{t+\Delta t}(1+e_{o,j})}{L_o} - 1 \qquad j = 1, 2, ..., R_j \qquad (3.14)$$

$$H^{t+\Delta t} = \sum_{j=1}^{R_j} L_j^{t+\Delta t} \qquad (3.15)$$

$$S^{t+\Delta t} = H_o - H^{t+\Delta t} \qquad (3.16)$$

$$U_{avg}^{t+\Delta t} = \frac{S^{t+\Delta t}}{S_{ult}} \qquad (3.17)$$

where S_{ult} is the ultimate settlement corresponding to 100% consolidation. The final void ratio distribution, and hence S_{ult}, can be calculated at the beginning of a simulation if the final data point is the largest value in the Δq^t loading schedule. Otherwise, unloading will occur, S_{ult} will not be known a priori, and U_{avg} values are not calculated during the course of a simulation.

The above method ensures that the weight of solids contained within each element is invariant throughout the consolidation process (Fox and Berles 1997). Thus, solid particles do not cross from one element to the next and element interfaces, as well as the nodes, can be considered as embedded in the soil skeleton. As such, the method follows the motion of the solid phase and consideration of relative discharge velocity between contiguous elements is sufficient to ensure mass balance. Fox and Berles (1997) and Fox

(2000) showed that numerical solutions obtained using this method are equivalent to analytical and numerical solutions obtained using material coordinates (Gibson et al. 1967, Schiffman et al. 1984) and the moving boundary approach of Lee and Sills (1979).

3.2.6 Time Increment

CS2 uses explicit time integration with a variable time increment, Δt. At each time step, the time increment is taken as the minimum of three values, two of which are given by

$$\Delta t = \min\left\{ \frac{\alpha \gamma_w a_{v,j}^t (L_j^t)^2}{k_j^t (1+e_j^t)}, \left| \frac{0.01 L_o (e_{o,j} - e_{f,j})}{(1+e_{o,j})(v_{rf,j}^t - v_{rf,j-1}^t)} \right| \right\} \tag{3.18}$$

where α = 0.4, $a_{v,j}^t$ is the coefficient of compressibility calculated at e_j^t from Figure 3.2(a), and $e_{f,j}$ is the final void ratio for element j. Values of $e_{f,j}$ are calculated from the final vertical effective stress increment assuming no unload/reload and may be approximate if unload/reload occurs. The terms in Equation 3.18 are needed for numerical stability of the consolidation algorithm and accurate time integration of discharge velocity near drainage boundaries during the early stages of a simulation (Fox and Berles 1997). CS2 also decreases Δt as needed to properly follow the loading schedule Δq^t for the layer, which forms a third constraint. Using these criteria, CS2 performs a search over all elements to find the smallest value of Δt, which is then used to advance the solution forward in time for all elements.

3.3 Model Performance

The accuracy of the CS2 method has been verified extensively using analytical solutions, numerical solutions, and experimental data (Fox and Berles 1997; Fox 2000; Fox et al. 2003; Lee and Fox 2005; Berilgen et al. 2006; Kwon et al. 2007; Fox 2007b; Lee and Fox 2009; Meric et al. 2010). New capabilities of the model are demonstrated in the following sections using several numeric examples. Material properties are taken from measured values for kaolinite clay (LL = 47.6, PI = 21.8, G_s = 2.61) provided by Lee and Fox (2009), with some small modifications as needed for illustrative purposes. Constitutive relationships for compressibility and hydraulic conductivity are

$$e = 1.60 - 0.65 \log\left(\frac{\sigma'(\text{kPa})}{20}\right) \tag{3.19}$$

$$e = 8.16 + 0.765 \log(k(\text{m/s})) \tag{3.20}$$

3.3.1 Time-Dependent Loading

3.3.1.1 Small Strain

The first example considers time-dependent loading and small strains such that the results can be compared with the analytical solution of Olson (1977). A double-drained layer has an initial height of 5 m and is in equilibrium under an effective overburden stress of 20 kPa. The total head at both boundaries is 5 m, soil self-weight is neglected (G_s = 1), and the initial void ratio is 1.6 over the entire depth of the layer. The coefficient of compressibility and the hydraulic conductivity are both constant, having values of 0.005/kPa and 2.66 × 10^{-9} m/s, respectively, and the corresponding coefficient

of consolidation, c_v, is 1.41 × 10^{-7} m^2/s. The schedule of applied vertical effective stress at the top of the layer is shown in Figure 3.3, where T is the dimensionless Terzaghi time factor,

$$T = \frac{t\, c_v}{H_{dr}^2} \tag{3.21}$$

and H_{dr} is the longest drainage path (= $0.5H_o$). The maximum applied stress is 0.0004 kPa, which yields a final vertical strain of 7.7 × 10^{-7}.

Table 3.1 compares U_{avg} values obtained using the Olson (1977) analytical solution and four CS2 simulations with R_j increasing from 20 to 200. Each numerical solution is in good to excellent agreement with the exact value and the accuracy improves with increasing numerical resolution (i.e., increasing R_j). For R_j = 200, the error decreases from 0.03% at T= 0.1 to 0.001% at T= 3. The maximum error for R_j = 20 is 3%, which indicates that CS2 has good accuracy even at low numerical resolution.

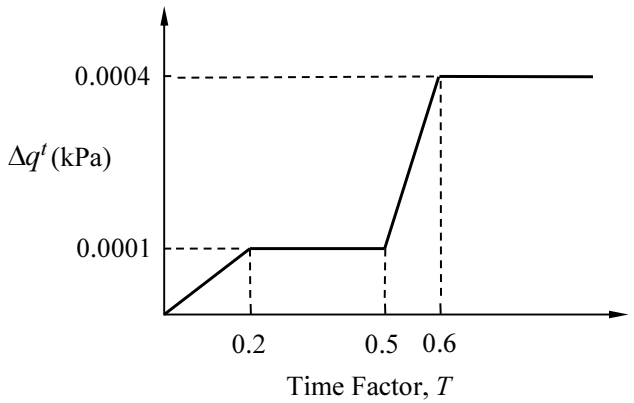

Figure 3.3 Loading schedule for small strain time-dependent loading simulations.

Table 3.1 Comparison of solutions for time-dependent loading (small strain).

Time Factor T	Average degree of consolidation, U_{avg} (%)				
	Olson (1977) analytical solution	CS2 $R_j = 20$	CS2 $R_j = 50$	CS2 $R_j = 100$	CS2 $R_j = 200$
0.1	2.974	2.873	2.957	2.970	2.973
0.2	8.409	8.267	8.386	8.403	8.407
0.3	12.448	12.379	12.437	12.446	12.448
0.4	15.230	15.182	15.222	15.228	15.229
0.5	17.370	17.338	17.365	17.369	17.370
0.6	36.880	36.413	36.780	36.855	36.874
0.7	52.954	52.791	52.912	52.943	52.951
0.8	63.440	63.338	63.411	63.432	63.437
1.0	77.699	77.668	77.686	77.696	77.698
1.2	86.386	86.386	86.381	86.384	86.385
2.0	98.109	98.120	98.110	98.109	98.109
3.0	99.839	99.842	99.840	99.840	99.840

3.3.1.2 Large Strain

A second example is provided to illustrate the effect of large strains for time-dependent loading conditions. The parameters are unchanged except that the loading schedule is the simple ramp shown in Figure 3.4. Different magnitudes of maximum applied stress, Δq_{max}, were specified to achieve final strains ranging from 0.01% to 30%. Ramp loading is completed at $T = 0.2$, which corresponds to 103 d in each case. Although large strains would normally introduce significant changes in compressibility and hydraulic conductivity, material properties were held constant to highlight the large

strain effect. Plots of settlement and U_{avg} vs. time are presented in Figure 3.5. The curves show similar behavior and indicate that consolidation is slightly faster at higher strain levels. Large strains decrease the drainage path length and expedite the rate of consolidation, which is similar to the findings of Gibson et al. (1981) and Fox and Berles (1997) for instantaneous loading.

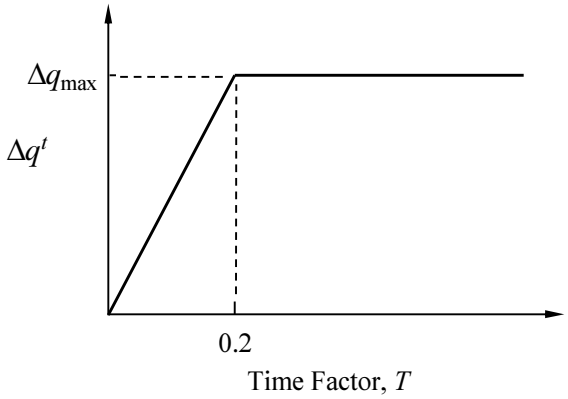

Figure 3.4 Loading schedule for large strain time-dependent loading simulations.

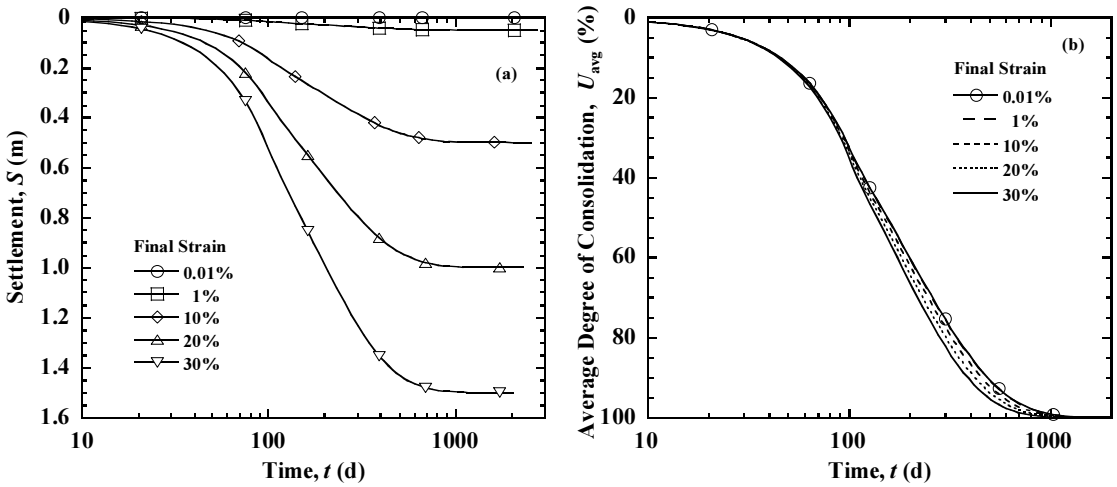

Figure 3.5 Time-dependent loading simulations for variable final strain: (a) settlement; (b) U_{avg}.

3.3.2 External Hydraulic Gradient

The effect of an external hydraulic gradient on consolidation behavior was investigated for a double-drained layer with H_o = 5 m, q_o = 20 kPa, Δq = 100 kPa (instantaneous loading), G_s = 2.61, and compressibility and hydraulic conductivity relationships defined by Eqs. (19) and (20). CS2 simulations were conducted for five cases (R_j = 200):

- Case 1: h_t = 5 m, h_b = 5 m
- Case 2: h_t = 5 m, h_b = 2.5 m
- Case 3: h_t = 5 m, h_b = 0 m
- Case 4: h_t = 5 m, h_b = 5 m at t = 0

  h_t = 5 m, h_b = 2.5 m for t > 0
- Case 5: h_t = 5 m, h_b = 5 m at t = 0

  h_t = 5 m, h_b = 0 m for t > 0

The initial void ratio profile for Case 1 is in equilibrium with hydrostatic boundary head conditions. Initial void ratio profiles for Cases 2 and 3 are in equilibrium with external hydraulic gradients of 0.5 and 1.0, respectively, acting across the layer. Cases 4 and 5 have the same initial void ratio profile as Case 1 and then the external hydraulic gradient and surcharge load are applied simultaneously at t = 0.

Plots of settlement and U_{avg} are presented in Figure 3.6 and initial and final void ratio profiles are presented in Figure 3.7 for each case. Case 1 has a total settlement of

0.785 m, which corresponds to an average final strain of 16%. External hydraulic gradients for Cases 2 and 3 induce downward seepage forces on the clay layer, which might be expected to produce larger settlements. However, due to decreasing compressibility of the clay with increasing effective stress, higher external gradients yield less settlement because the effect of seepage on the initial void ratio distributions is greater than on the final void ratio distributions (Figure 3.7). When the external hydraulic gradient is applied simultaneously with the surcharge, higher gradients for Cases 4 and 5 produce larger changes in void ratio and larger settlements. Although the settlements are differentiated according to external gradient conditions, U_{avg} values are almost identical because the final strains are not so dissimilar. By contrast, greater differences in final strain for the simulations in Figure 3.5 produce more segregation of the U_{avg} curves.

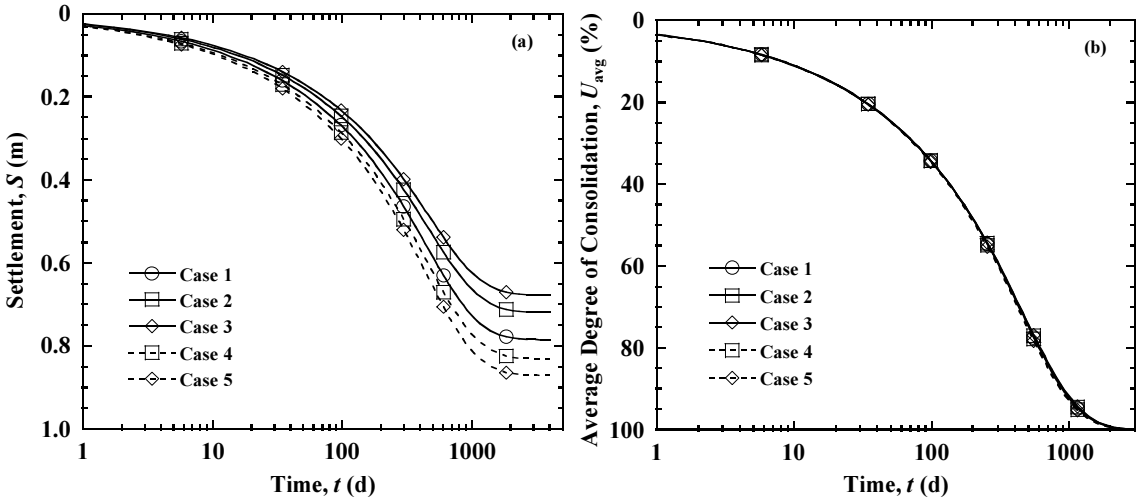

Figure 3.6 External hydraulic gradient simulations: (a) settlement; (b) U_{avg}.

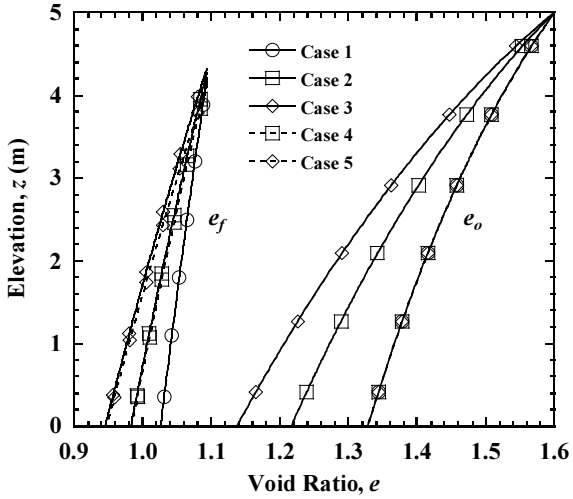

Figure 3.7 Initial and final void ratio profiles for external hydraulic gradient simulations.

Profiles of excess pore pressure, u_{ex}, for Cases 1, 3, and 5 are shown in Figure 3.8 for t = 0 (just after surcharge loading), t = 1 month, and t = 1 year. Cases 1 and 3 have uniform initial excess pore pressure, while Case 5 shows a linear profile due to the simultaneous application of external hydraulic gradient and surcharge. Thereafter, excess pore pressure profiles for Case 1 and Case 3 are similar during consolidation, whereas Case 5 consistently yields higher values over the depth of the layer. This example illustrates that an external hydraulic gradient can have an important effect on final settlement, void ratio distribution and excess pore pressures but may not have a significant effect on the rate of consolidation.

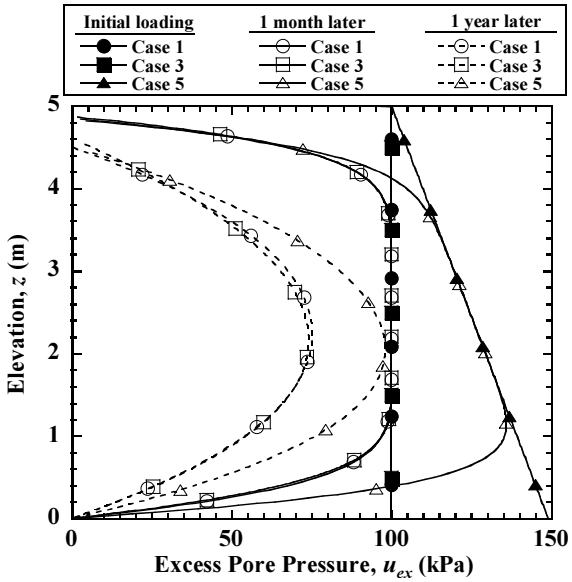

Figure 3.8 Excess pore pressure profiles for external hydraulic gradient simulations.

3.3.3 Unload/Reload

The effects of unload/reload during consolidation were investigated for a double-drained layer with $H_o = h_t = h_b = 5$ m and $q_o = 20$ kPa. Constitutive relationships are described by Eqs. (19) and (20) and a recompression index $C_r = 0.025$. At $t = 0$, an instantaneous surcharge load $\Delta q = 100$ kPa is applied to the layer, removed when $U_{avg} = 50\%$, and then reapplied 100 days later. Thus, the sequence of vertical total stress is 20–120–20–120 kPa. CS2 simulations ($R_j = 209$) were conducted for $G_s = 1$ and $G_s = 2.61$ to investigate the effect of soil self-weight. Simulations were also conducted without unload/reload for comparison.

Settlement curves are presented in Figure 3.9 and initial and final void ratio profiles are presented in Figure 3.10. Simulations without unload/reload indicate that

total settlement is larger when soil self-weight is neglected, which is due to the greater change in void ratio during consolidation. When unload/reload occurs, surcharge removal produces a total swelling of 14 mm and 12 mm for G_s = 1 and G_s = 2.61, respectively, over the 100 day unloading period. After reloading, Figure 3.9 shows that the rate of consolidation increases such that, in this case, the time at the end of consolidation is essentially unchanged by the unload/reload process. Final settlement is the same for each G_s value as expected.

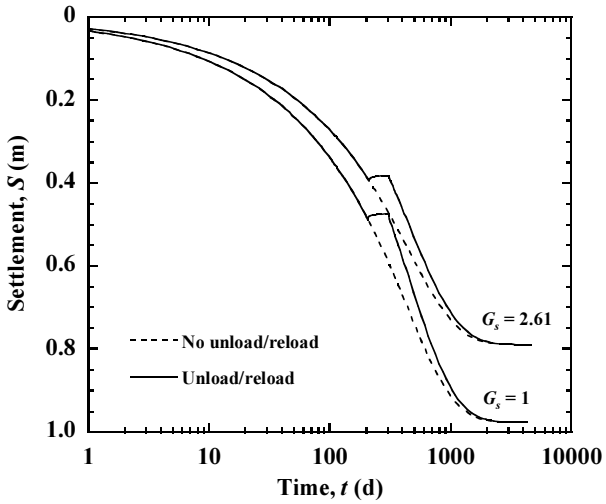

Figure 3.9 Settlement curves for unload/reload simulations.

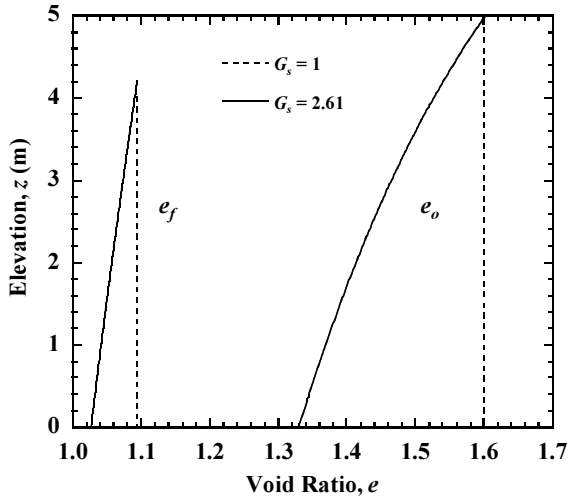

Figure 3.10 Initial and final void ratio profiles for unload/reload simulations.

Profiles of excess pore pressure are shown in Figure 3.11 for G_s = 2.61 and several times during the unload/reload process: t = 0 (just after initial loading), t = 1 d, t = 1 min before unloading, t = 1 min after unloading, t = 1 d after unloading, t = 1 min before reloading (i.e., 100 d after unloading), t = 1 d after reloading, and U_{avg} = 90%. Initial loading produces a uniform initial excess pore pressure of 100 kPa which then decreases to the indicated profile 1 min before unloading. Surcharge removal shifts the profile by -100 kPa, resulting in negative u_{ex} values throughout the clay layer, and the layer begins to swell in response (Figure 3.9). One day after unloading, the u_{ex} profile takes an interesting shape as pore pressures change rapidly near the drainage boundaries. One hundred days after unloading, excess pore pressures are only slightly negative. Reloading then essentially replicates the initial u_{ex} profile, although the subsequent dissipation is more rapid than for initial loading due to the overconsolidated condition, and lower compressibility, of the clay.

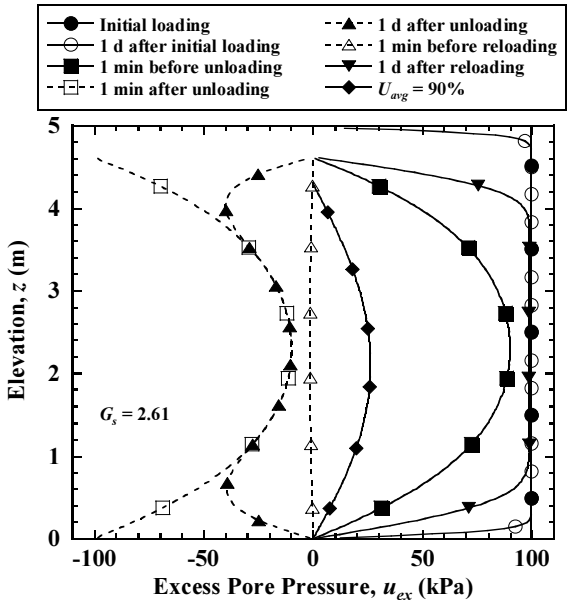

Figure 3.11 Excess pore pressure profiles for unload/reload simulations.

Due to spatial and temporal variations of effective stress, soil elements take different paths on the compressibility plot during unload/reload. To illustrate, the effective stress paths for nine soil elements, labeled as A through I in Figure 3.12, are presented in Figure 3.13 for the complete load/unload/reload process. Figure 3.13(a) shows paths without the influence of soil self-weight. In this case, paths taken by symmetrically located elements (e.g., C and G) are identical. The preconsolidation stress and the minimum effective stress reached during unloading vary with element position. When self-weight is included (Figure 3.13(b)), stress paths for symmetrically located elements are different. Figure 3.13 indicates that elements closer to drainage boundaries have a higher preconsolidation stress than those in the interior of the layer when surcharge is removed during consolidation. Figure 3.13 also indicates the general importance of soil self-weight for consolidation analysis.

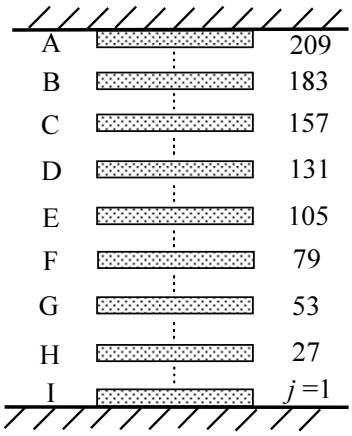

Figure 3.12 Monitored soil elements for unload/reload simulations.

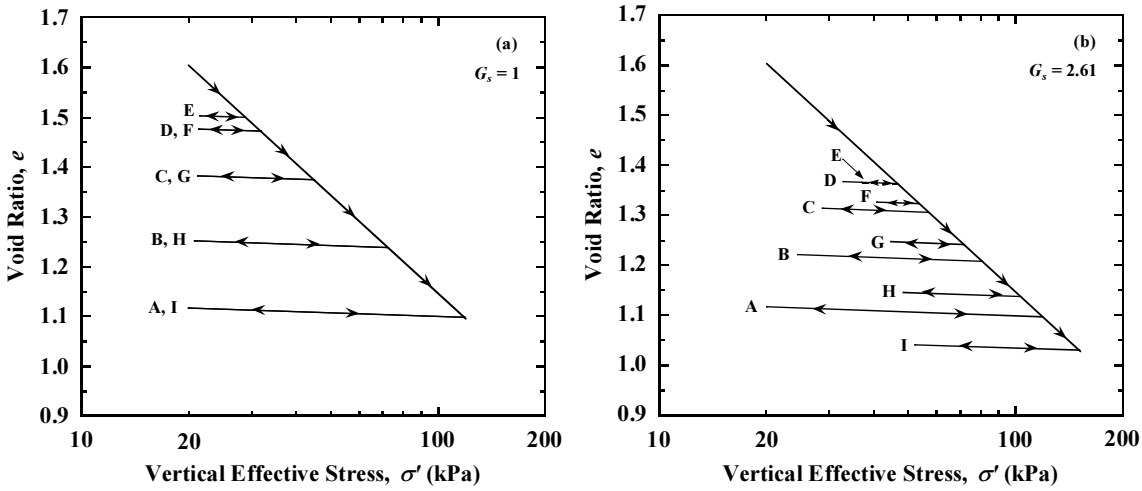

Figure 3.13 Stress paths for unload/reload simulations: (a) $G_s = 1$; (b) $G_s = 2.61$.

3.3.4 Stress Path

Inspired by trends of Figure 3.13, a final set of simulations was conducted to investigate the effect of stress path during consolidation. A double-drained layer has $H_o = h_t = h_b = 5$ m, $q_o = 20$ kPa, $\Delta q = 100$ kPa, $G_s = 1$, and $k = 1.382 \times 10^{-9}$ m/s.

Simulations were performed for R_j = 200 and two effective stress paths taken between points A and C, as shown in Figure 3.14. Path $\overline{AC}$ corresponds to a normally consolidated clay with a constant compression index C_c = 0.366 and path $\overline{ABC}$ corresponds to an overconsolidated clay with C_r = 0.025 and C_c = 0.65. Point coordinates for these paths are σ'_A = 20 kPa, e_A = 1.383, σ'_B = 45.11 kPa, e_B = 1.374, σ'_C = 120 kPa, and e_C = 1.098.

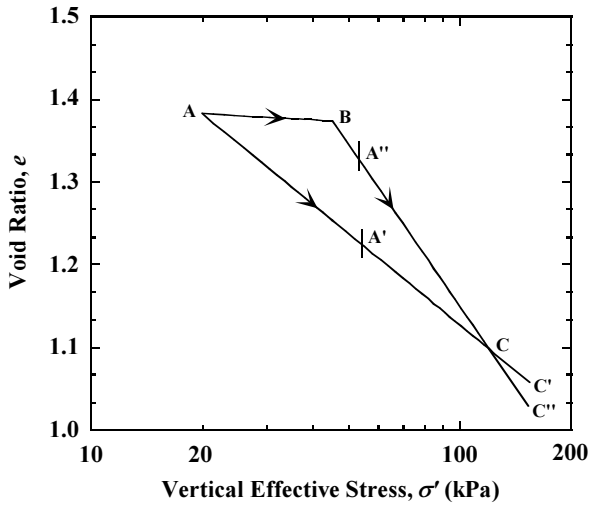

Figure 3.14 Effective stress paths for stress path simulations.

Settlement curves are presented in Figure 3.15 and initial and final void ratio profiles are presented in Figure 3.16. Without self-weight, the magnitude of final settlement is the same because both paths start and end with the same uniform void ratio profiles. Consolidation for path $\overline{AC}$, however, occurs more rapidly than for $\overline{ABC}$ because the void ratio for $\overline{AC}$ is lower than for $\overline{ABC}$ at any given effective stress

(Figure 3.14). This is consistent with the findings of Olson and Ladd (1979), who also studied the effect of nonlinear compressibility relationships.

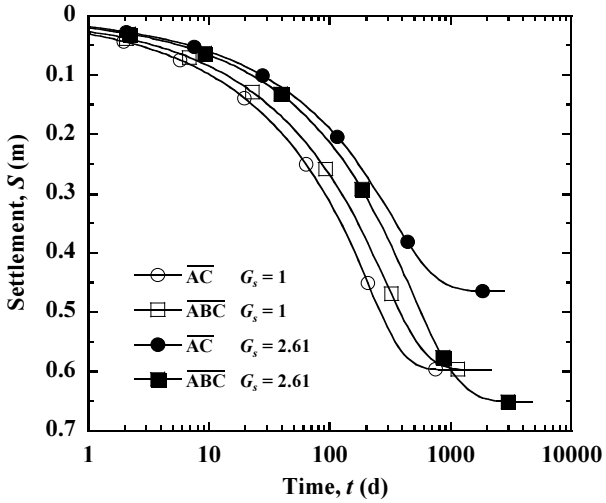

Figure 3.15 Settlement curves for stress path simulations.

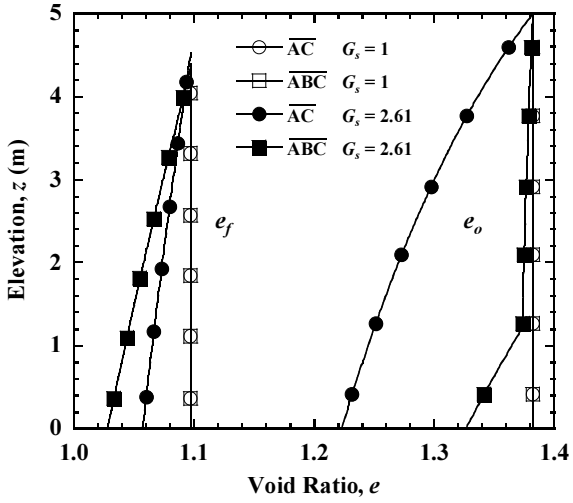

Figure 3.16 Initial and final void ratio profiles for stress path simulations.

Two additional simulations were conducted for more realistic conditions in which soil self-weight (G_s = 2.61) and changing hydraulic conductivity (Equation 3.20) were

taken into account. These results are also shown in Figures. 3.14 – 3.16. With self-weight included, initial void ratio decreases with depth and the range is indicated as $\overline{\mathrm{AA}'}$ for path $\overline{\mathrm{AC}}$ and $\overline{\mathrm{AA}''}$ for path $\overline{\mathrm{ABC}}$ in Figure 3.14. Similarly, the range of final void ratio is $\overline{\mathrm{CC}'}$ for path $\overline{\mathrm{AC}}$ and $\overline{\mathrm{CC}''}$ for path $\overline{\mathrm{ABC}}$. Interestingly, the preconsolidation stress (pt. B) is also manifest as a break in slope on the e_o profile for $\overline{\mathrm{ABC}}$. Final settlement for $\overline{\mathrm{ABC}}$ is substantially larger than for $\overline{\mathrm{AC}}$ due to the greater change in void ratio that occurs during consolidation. Compared to corresponding curves for G_s = 1 and constant k, consolidation for both paths is delayed due to decreasing hydraulic conductivity with increasing settlement. This final example illustrates the importance of compressibility and hydraulic conductivity constitutive relationships and self-weight of the soil in particular on the rate of consolidation and final settlement. Failure to correctly account for these effects can lead to significant errors in a consolidation analysis.

3.4 Acknowledgements

Chapter 3 of this dissertation is based on material published by the International Journal of Geomechanics titled “Enhanced CS2 Model for Large Strain Consolidation” with authors, Patrick J. Fox and Hefu Pu (2012). The dissertation author is the second author of this paper.

Chapter 4

Model for Large Strain Consolidation under Constant Rate of Strain

4.1 Introduction

As reviewed in Chapter 2, the simplifying assumptions with regard to soil constitutive relationships made in the existing literatures (e.g., Smith and Wahls 1969; Wissa et al. 1971; Lee 1981; Znidarcic et al. 1986) yield mathematical advantage but generally fall short of real soil behavior, especially when large strains occur. Thus a large strain CRS consolidation model that can account for more general constitutive relationships as well as changing compressibility and hydraulic conductivity during consolidation would represent a significant advance in the area of CRS consolidation. For the purpose of making such an advance, a new model is developed and presented below.

This chapter presents a piecewise-linear numerical model for one-dimensional large strain consolidation under constant rate of strain loading conditions called CCRS1 (Consolidation for Constant Rate of Strain 1). The algorithm accounts for vertical strain, general constitutive relationships, relative velocity of fluid and solid phases, changing hydraulic conductivity and compressibility during consolidation, and an externally applied hydraulic gradient. Soil self-weight is also included for completeness, although this effect is insignificant for typical laboratory specimens. Development of CCRS1 is first presented, and is followed by verification checks with available analytical and numerical solutions. Numeric examples are then used to investigate the effect of soil compressibility and hydraulic conductivity relationships on CRS consolidation response. The usefulness of small strain theory as an approximation for large strain conditions with changing coefficient of consolidation is also examined.

Using the CCRS1 numerical model, current ASTM D4186 equations are evaluated and the errors for nonlinear data analysis equations are identified. Modified nonlinear (MNL) theory method is proposed for improved CRS consolidation test interpretation. This work is published by the Journal of Geotechnical and Geoenvironmental Engineering titled “Evaluation of Data Analysis Methods for the CRS Consolidation Test” with authors, Patrick J. Fox, Hefu Pu, and John T. Christian (2014). The dissertation author is the second author of this paper, but this work is not included in the dissertation.

4.2 Model Development

The CCRS1 model was developed using CS2 (Fox and Berles 1997; Fox and Pu 2012) as a point of departure and follows similar procedures with regard to geometry, constitutive relationships, fluid flow, and settlement. The numerical algorithm is presented in the following sections and illustrated using the flow chart shown in Figure 4.1.

4.2.1 Geometry

A saturated homogeneous compressible soil specimen of initial height, H_o, is treated as an idealized two-phase material in which the solid particles and pore fluid are incompressible. The term "homogeneous" refers to the compressibility and hydraulic conductivity constitutive relationships of the soil and not the distribution of initial void ratio within the specimen. Initial geometry, prior to the start of loading at time $t = 0$, is shown in Figure 4.2(a). Vertical coordinate, z, and element coordinate, j, are defined as positive upward from a fixed datum at the bottom boundary. A column of R_j elements is defined within the specimen, each having unit cross-sectional area, constant initial height, L_o, and a central node located at initial elevation, $z_{o,j}$. Nodes translate vertically and remain at the center of their respective elements throughout the consolidation process. An initial vertical effective stress, q_o, acts at the top boundary. Top and bottom boundaries can be specified as drained or undrained and, if drained, are assigned individual constant total head values, h_t and h_b, respectively, taken with

respect to the datum. These head values can be unequal to allow for an external hydraulic gradient across the specimen.

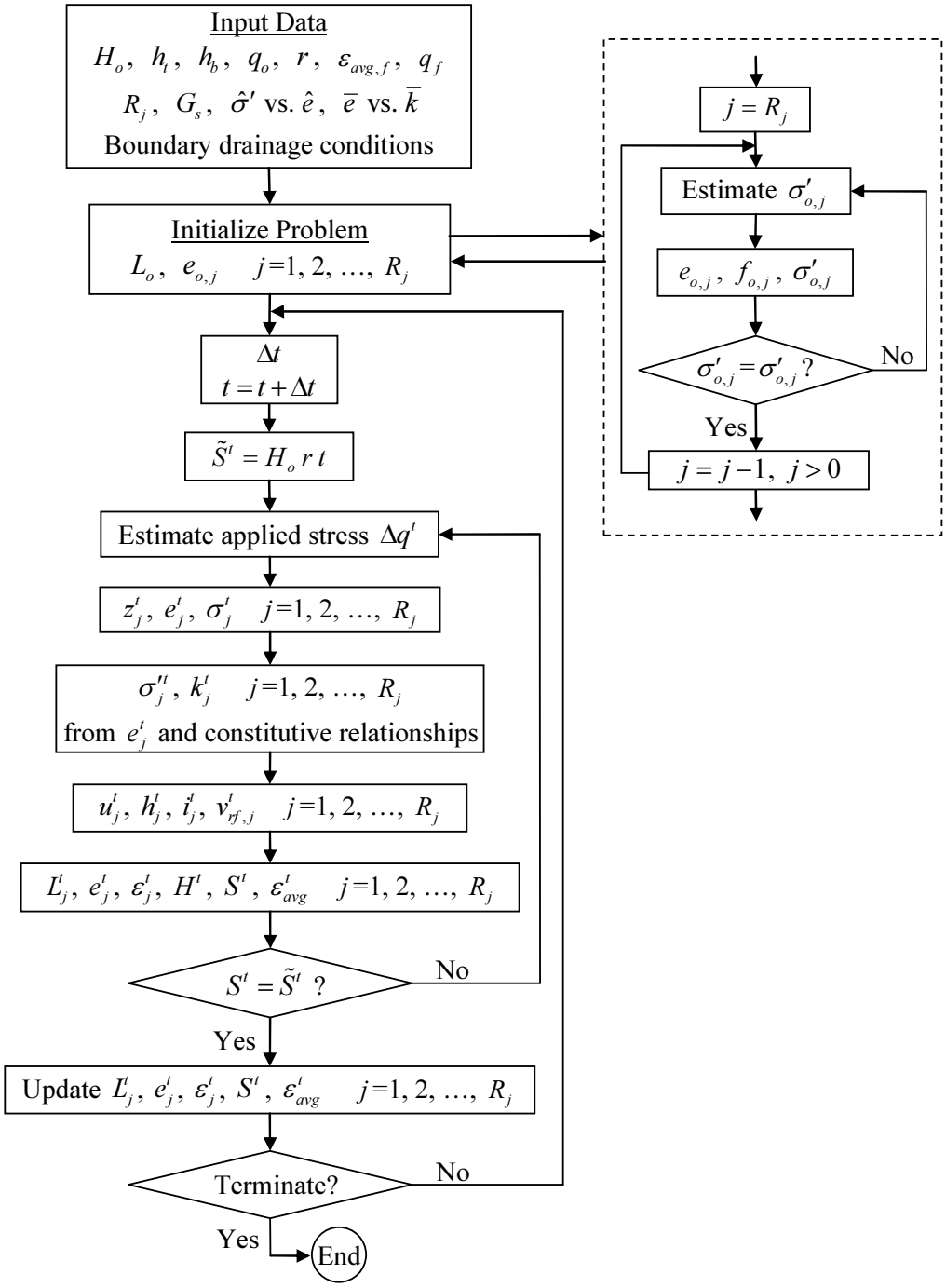

Figure 4.1 Flow chart for CCRS1.

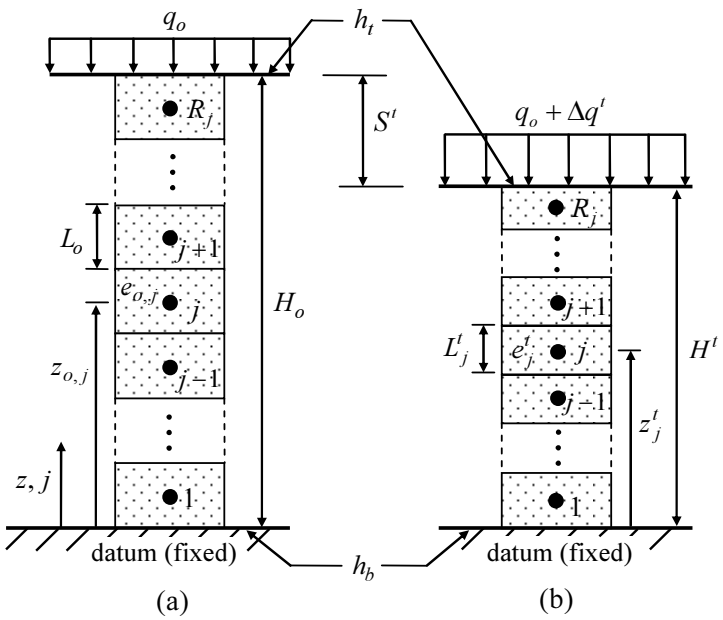

Figure 4.2 Geometry for CCRS1: (a) initial configuration; (b) configuration during loading.

4.2.2 Constitutive Relationships

Soil constitutive relationships, shown in Figure 4.3, are specified using discrete data points. The compressibility relationship is defined by $R_s \geq 2$ pairs of corresponding vertical effective stress, $\hat{\sigma}'$, and void ratio, $\hat{e}$. Depending on the choice of data points, this relationship may reflect normally consolidated or overconsolidated conditions. The hydraulic conductivity relationship is defined by $R_t \geq 2$ pairs of corresponding void ratio, $\overline{e}$, and vertical hydraulic conductivity, $\overline{k}$. CCRS1 uses the same hydraulic conductivity relationship for normally consolidated and overconsolidated conditions, which is consistent with the findings of Al-Tabbaa and Wood (1987), Nagaraj et al. (1994), Fox (2007b), and Lee and Fox (2009).

A one-to-one correspondence is assumed for each constitutive relationship in Figure 4.3. Thus, CCRS1 does not account for the effects of strain rate or creep on the compressibility and hydraulic conductivity of the soil. The constitutive relationships can, however, take essentially any desired form by choosing the appropriate number of points. As the dependence of compressibility on applied strain rate is commonly observed for soils with strong interparticle bonding and structure, the current model is most appropriate for less structured soils, such as reconstituted clays (Sheahan and Watters 1997).

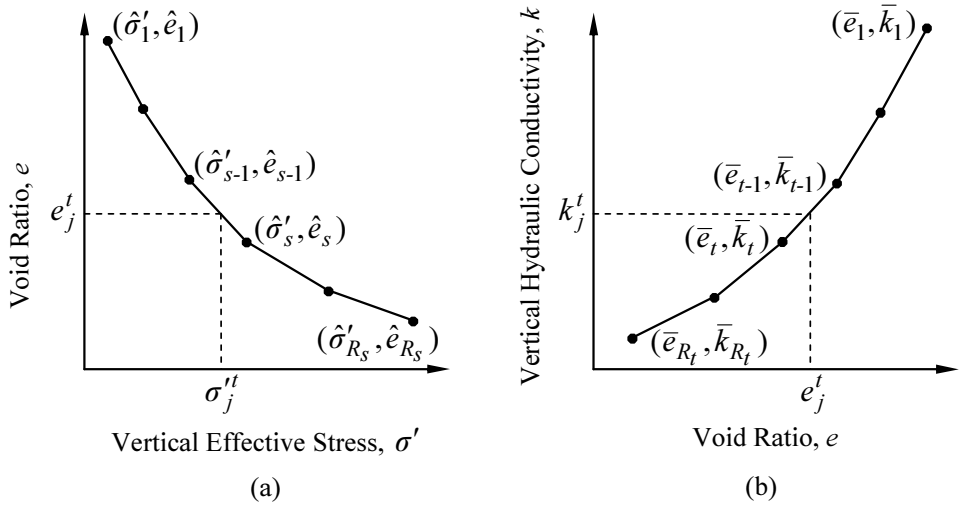

Figure 4.3 Soil constitutive relationships: (a) compressibility; (b) hydraulic conductivity.

4.2.3 Initial Void Ratio Distribution

A distribution of initial void ratio is needed to begin a CCRS1 simulation. This distribution can be in equilibrium or nonequilibrium with initial stress conditions and soil material properties.

4.2.3.1 Equilibrium

Iteration is used to calculate an initial void ratio distribution that is in equilibrium with q_o, the constitutive relationships and self-weight of the soil, and seepage forces due to an external hydraulic gradient acting across the specimen (if $h_t \neq h_b$). In this case, initial excess pore pressures (i.e., the difference between total and steady state pore pressures) are zero. Starting at the top of the specimen, the initial vertical effective stress at the node for element R_j, σ'_{o,R_j}, is estimated as q_o and the corresponding initial void ratio, e_{o,R_j}, is calculated from the compressibility relationship (Figure 4.3(a)). This void ratio is used to calculate the initial buoyant unit weight of the element, γ'_{o,R_j}, which yields a new value of vertical effective stress as

$$\sigma'_{o,R_j} = q_o + \frac{L_o}{2}\left(\gamma'_{o,R_j} - f_{o,R_j}\right) \tag{4.1}$$

where f_{o,R_j} is the initial seepage force per unit volume (positive upward) acting on element R_j. Seepage forces on all elements are taken as zero for the first pass. Using σ'_{o,R_j}, an updated value of e_{o,R_j} is calculated from the compressibility relationship and this process is repeated until the change in σ'_{o,R_j} between successive iterations is

negligible. Once convergence is obtained for element R_j, the effective stress at the top of element $R_j - 1$ is also known $\left(= \sigma'_{o,R_j} + 0.5 L_o (\gamma'_{o,R_j} - f_{o,R_j})\right)$. The iterative procedure is then repeated for element $R_j - 1$ and the remaining elements, which yields the equilibrium distribution of $\sigma'_{o,j}$ and $e_{o,j}$ for the case of no seepage across the specimen.

If an external hydraulic gradient is present, the iteration procedure includes an additional loop to account for the effect of associated seepage forces. The initial vertical hydraulic conductivity of each element $k_{o,j}$ is calculated from $e_{o,j}$ and the hydraulic conductivity relationship (Figure 4.3(b)). The steady discharge velocity, v_o, through the specimen (positive upward) is

$$v_o = \frac{h_b - h_t}{\sum_{j=1}^{R_j} \frac{L_o}{k_{o,j}}} \tag{4.2}$$

and the corresponding seepage forces are

$$f_{o,j} = \frac{v_o \gamma_w}{k_{o,j}} \qquad j = 1, 2, ..., R_j \tag{4.3}$$

where γ_w is the unit weight of water (constant). With updated values of $f_{o,j}$, the entire process is repeated until the change in $\sigma'_{o,j}$ for all elements between successive iterations is negligible.

4.2.3.2 Nonequilibrium

CCRS1 can also accommodate a user-specified distribution of initial void ratio. The most common example is a uniform e_o profile. User-specified initial void ratios will

generally not be in equilibrium with initial conditions and soil material properties, which produces nonzero values of excess pore pressure within the specimen at the start of loading.

4.2.4 Application of Stress

The piecewise-linear method used to develop CS2 is a stress-controlled approach in which an applied surcharge stress is specified and the resulting settlement is calculated through time. In CCRS1, a constant average rate of strain, r, is specified and the necessary value of applied stress is calculated to yield the required settlement (i.e., displacement at the top boundary) at each time step.

Beginning at t = 0, a time-varying value of vertical effective stress change, Δq^t, is applied to the specimen and moves with the top boundary thereafter (Figure 4.2(b)). At any time t, the height of the specimen is H^t and the height and node elevation for the j^{th} element are L_j^t and z_j^t, respectively. Iteration is used to adjust the value of Δq^t at each time step until the difference between the computed settlement, $S^t = H_o - H^t$, and the required settlement, $\tilde{S}^t = H_o r t$, is negligible.

4.2.5 Stress, Pore Pressure, Fluid Flow, and Settlement

CCRS1 calculates stresses, pore pressure, fluid flow, and settlement using the same method as CS2. Fox and Berles (1997) presented detailed information on these aspects. The vertical total stress at node j is calculated from the vertical stress at the top boundary and the self-weight of overlying elements as

$$\sigma_j^t = q_o + \Delta q^t + \left(h_t - H^t\right)\gamma_w + \frac{L_j^t \gamma_j^t}{2} + \sum_{b=j+1}^{R_j} L_b^t \gamma_b^t \qquad j = 1, 2, ..., R_j \qquad (4.4)$$

where $\gamma_j^t \left(= \gamma_w (G_s + e_j^t)/(1 + e_j^t)\right)$ is the saturated unit weight of element j, e_j^t is the corresponding void ratio, and G_s is the specific gravity of solids (constant). Soil self-weight can be neglected by choosing $G_s = 1$.

Vertical effective stress, $\sigma_j'^t$, is calculated from e_j^t by interpolation between data points in Figure 4.3(a). Vertical hydraulic conductivity, k_j^t, is calculated from e_j^t by interpolation between data points in Figure 4.3(b). The pore pressure at node j is the difference between total and effective stresses,

$$u_j^t = \sigma_j^t - \sigma_j'^t \qquad j = 1, 2, ..., R_j \qquad (4.5)$$

Excess pore pressures generated within the specimen cause fluid flow to all drainage boundaries. Flow between contiguous elements accounts for the relative motion of fluid and solid phases. The relative fluid discharge velocity (positive upward) between nodes j and $j+1$ is

$$v_{rf,j}^t = -k_{s,j}^t \, i_j^t \qquad j = 1, 2, ..., R_j - 1 \qquad (4.6)$$

where the hydraulic gradient between nodes j and $j+1$ is

$$i_j^t = \frac{h_{j+1}^t - h_j^t}{z_{j+1}^t - z_j^t} \qquad j = 1, 2, ..., R_j - 1 \qquad (4.7)$$

the total head at node j is

$$h_j^t = z_j^t + \frac{u_j^t}{\gamma_w} \qquad j = 1, 2, ..., R_j \qquad (4.8)$$

and the equivalent series hydraulic conductivity between nodes j and $j+1$ is

$$k_{s,j}^t = \frac{k_{j+1}^t k_j^t \left(L_{j+1}^t + L_j^t\right)}{L_{j+1}^t k_j^t + L_j^t k_{j+1}^t} \qquad j = 1, 2, ..., R_j - 1 \qquad (4.9)$$

Similar corresponding expressions are required at the top and bottom boundaries:

$$v_{rf,R_j}^t = -k_{R_j}^t \frac{h_t - h_{R_j}^t}{H^t - z_{R_j}^t} \qquad (4.10)$$

$$v_{rf,0}^t = -k_1^t \frac{h_1^t - h_b}{z_1^t} \qquad (4.11)$$

If the top boundary is undrained, $v_{rf,R_j}^t = 0$, and if the bottom boundary is undrained, $v_{rf,0}^t = 0$.

Soil deformation is one-dimensional and occurs in response to the net fluid outflow from each element over time increment, Δt. New element heights are calculated as

$$L_j^{t+\Delta t} = L_j^t - (v_{rf,j}^t - v_{rf,j-1}^t)\Delta t \qquad j = 1, 2, ..., R_j \qquad (4.12)$$

and new values of void ratio, vertical strain, specimen height, settlement, and average vertical strain are, respectively,

$$e_j^{t+\Delta t} = \frac{L_j^{t+\Delta t}(1+e_{o,j})}{L_o} - 1 \qquad j = 1, 2, ..., R_j \qquad (4.13)$$

$$\varepsilon_j^{t+\Delta t} = 1 - \frac{L_j^{t+\Delta t}}{L_o} \qquad j = 1, 2, ..., R_j \qquad (4.14)$$

$$H^{t+\Delta t} = \sum_{j=1}^{R_j} L_j^{t+\Delta t} \qquad (4.15)$$

$$S^{t+\Delta t} = H_o - H^{t+\Delta t} \qquad (4.16)$$

$$\varepsilon_{avg}^{t+\Delta t} = \frac{S^{t+\Delta t}}{H_o} \qquad (4.17)$$

where the void ratio and vertical strain are assumed to be uniform within each element at any time.

The above method ensures that the weight of solids contained within each element is invariant throughout the consolidation process (Fox and Berles 1997). Thus, solid particles do not cross from one element to the next and element interfaces, as well as the nodes, can be considered as embedded in the soil skeleton. As such, the method follows the motion of the solid phase and consideration of relative discharge velocity between contiguous elements is sufficient to ensure mass balance. Fox and Berles (1997) and Fox (2000) showed that numerical solutions obtained using this method are equivalent to analytical and numerical solutions obtained using material coordinates (Gibson et al. 1967; Schiffman et al. 1984) and the moving boundary approach of Lee and Sills (1979).

4.2.6 Time Increment

CCRS1 uses explicit time integration with a variable time increment. At each time step, the time increment is taken as the minimum of two values:

$$\Delta t = \min\left\{ \frac{\alpha \gamma_w a_{v,j}^t (L_j^t)^2}{k_j^t (1+e_j^t)}, \ \left| \frac{0.001 L_j^t}{(v_{rf,j}^t - v_{rf,j-1}^t)} \right| \right\} \tag{4.18}$$

where α = 0.4, $a_{v,j}^t = -(\hat{e}_s^t - \hat{e}_{s-1}^t)/(\hat{\sigma}_s'^t - \hat{\sigma}_{s-1}'^t)$ is the coefficient of compressibility calculated at e_j^t from Figure 4.3(a). The terms in Equation 4.18 are needed for numerical stability of the consolidation algorithm and accurate time integration of discharge velocity near drainage boundaries during the early stages of a simulation (Fox and Berles 1997). Using these criteria, CCRS1 performs a search over all elements to find the smallest value of Δt, which is then used to advance the solution forward in time for all elements. A simulation is terminated when a specified value of final average strain, $\varepsilon_{avg,f}$, or final effective stress at the top boundary, q_f, is reached.

4.3 Model Verification

The performance of CCRS1 is investigated using four numeric examples. Material properties are taken from measured values for kaolinite clay provided by Lee and Fox (2009), with some modifications as needed. The kaolinite has a specific gravity of solids = 2.61, liquid limit = 47.6, and plasticity index = 21.8, and is classified

according to the Unified Soil Classification System as CL, Lean Clay. Constitutive relationships for compressibility and hydraulic conductivity are

$$e = 2.0 - 0.65 \log\left(\frac{\sigma' \text{ (kPa)}}{5} \right) \tag{4.19}$$

$$e = 8.16 + 0.765 \log\left(k(\text{m/s}) \right) \tag{4.20}$$

4.3.1 Small Strains

4.3.1.1 Linear Theory

Example 4.1 considers small strains and constant values for a_v and coefficient of consolidation, c_v $\left(= k(1+e)/a_v \gamma_w\right)$, such that results can be compared with the linear theory of Wissa et al. (1971). A top-drained clay specimen has an initial height H_o = 50 mm and is in equilibrium under an effective vertical stress q_o = 5 kPa. The total head at the top boundary h_t = 50 mm, soil self-weight is neglected (G_s = 1), initial void ratio e_o = 2.0 (uniform), and a_v = 0.05/kPa. Simulations were performed using constant strain rate r = 1.0×10^{-4} %/h and terminated at $\varepsilon_{avg,f}$ = 1.5×10^{-5}.

Table 4.1 compares the change of vertical effective stress at the top boundary Δq as a function of Terzaghi time factor T $(= t c_v / H_o^2)$ for small strain linear theory and four CCRS1 simulations with R_j increasing from 20 to 200. Numerical values are in good to excellent agreement with the analytical solution and the accuracy improves with increasing numerical resolution (i.e., increasing R_j). For R_j = 20, the error decreases

from 2.9% at T = 0.01 to 0.025% at T = 1.2, which indicates that CCRS1 has good accuracy even for low resolution. For R_j = 200, the agreement is exact for the number of digits provided. Table 4.2 presents profiles of local vertical strain ε versus normalized elevation, Z ($= z/H^t$) for four values of T , as obtained from another CCRS1 simulation conducted with R_j = 210. Local strains increase nonlinearly with both elevation and time and are in excellent agreement with corresponding analytical solutions obtained using small strain linear theory.

Table 4.1 Comparison of vertical effective stress change at top of specimen for Example 4.1.

Time Factor T	Vertical effective stress change, $\Delta q \times 10^{-4}$ (kPa)				
	Wissa et al. (1971)	CCRS1 R_j = 20	CCRS1 R_j = 50	CCRS1 R_j = 100	CCRS1 R_j = 200
0.01	0.866	0.891	0.867	0.867	0.866
0.05	1.937	1.948	1.939	1.938	1.937
0.1	2.740	2.747	2.740	2.740	2.740
0.2	3.879	3.884	3.880	3.879	3.879
0.3	4.782	4.786	4.783	4.782	4.782
0.4	5.601	5.604	5.601	5.601	5.601
0.5	6.387	6.391	6.388	6.387	6.387
0.6	7.162	7.165	7.162	7.162	7.162
0.8	8.701	8.704	8.702	8.701	8.701
1.0	10.237	10.240	10.239	10.239	10.237
1.2	11.773	11.776	11.775	11.773	11.773

Table 4.2 Comparison of local strain profiles for Example 4.1.

Normalized Elevation Z	Local vertical strain, $\varepsilon \times 10^{-5}$							
	$T = 0.1$		$T = 0.5$		$T = 1$		$T = 1.2$	
	A	B	A	B	A	B	A	B
0.95	0.395	0.395	1.002	1.002	1.644	1.644	1.900	1.900
0.85	0.290	0.290	0.887	0.887	1.529	1.529	1.785	1.785
0.75	0.206	0.206	0.785	0.785	1.426	1.426	1.682	1.682
0.65	0.142	0.142	0.696	0.696	1.337	1.337	1.593	1.593
0.55	0.094	0.094	0.620	0.620	1.260	1.260	1.516	1.516
0.45	0.061	0.061	0.556	0.556	1.196	1.196	1.452	1.452
0.35	0.038	0.038	0.506	0.506	1.145	1.145	1.401	1.401
0.25	0.023	0.023	0.468	0.468	1.106	1.106	1.362	1.362
0.15	0.014	0.014	0.443	0.443	1.081	1.081	1.337	1.337
0.05	0.011	0.011	0.430	0.430	1.068	1.068	1.324	1.324

A = Wissa et al. (1971)

B = CCRS1 ($R_j = 210$)

4.3.1.2 Nonlinear Theory

Soil compressibility for Wissa et al. (1971) small strain nonlinear theory is defined by a constant value of compression index, C_c. Using this theory, Evangelista and Viggiani (1973) provided equations for vertical effective stress change and excess pore pressure distribution. Example 4.2 considers the same conditions as Example 4.1 except that soil compressibility is defined by Equation 4.19 with $C_c = 0.65$.

Values of vertical effective stress change at the top boundary, as obtained from nonlinear theory and four CCRS1 simulations, are presented in Table 4.3. Good to excellent agreement is observed and the accuracy of CCRS1 improves with increasing resolution. Four profiles of excess pore pressure, u_{ex}, presented in Table 4.4, are also in

excellent agreement with analytical solutions, as are corresponding values of local strain (not shown) for the nonlinear case.

Table 4.3 Comparison of vertical effective stress change at top of specimen for Example 4.2.

Time Factor T	Vertical effective stress change, $\Delta q \times 10^{-4}$ (kPa)				
	Evangelista and Viggiani (1973)	CCRS1 $R_j = 20$	CCRS1 $R_j = 50$	CCRS1 $R_j = 100$	CCRS1 $R_j = 200$
0.01	0.866	0.890	0.867	0.867	0.866
0.05	1.937	1.948	1.939	1.938	1.937
0.1	2.740	2.747	2.740	2.740	2.740
0.2	3.879	3.884	3.880	3.879	3.879
0.3	4.782	4.787	4.783	4.783	4.782
0.4	5.601	5.604	5.601	5.601	5.601
0.5	6.388	6.391	6.388	6.388	6.388
0.6	7.163	7.166	7.163	7.163	7.163
0.8	8.702	8.705	8.702	8.702	8.702
1.0	10.238	10.241	10.239	10.239	10.238
1.2	11.774	11.777	11.776	11.775	11.774

Table 4.4 Comparison of excess pore pressure profiles for Example 4.2.

Normalized Elevation Z	Excess pore pressure, $u_{ex} \times 10^{-4}$ (kPa)							
	$T = 0.05$		$T = 0.2$		$T = 0.7$		$T = 1.2$	
	A	B	A	B	A	B	A	B
0.95	0.360	0.360	0.372	0.372	0.374	0.375	0.374	0.375
0.85	0.938	0.938	1.042	1.042	1.065	1.066	1.066	1.067
0.75	1.345	1.344	1.616	1.616	1.679	1.680	1.680	1.681
0.65	1.609	1.609	2.099	2.099	2.216	2.217	2.217	2.218
0.55	1.768	1.768	2.495	2.495	2.677	2.678	2.678	2.679
0.45	1.857	1.857	2.812	2.812	3.060	3.061	3.062	3.063
0.35	1.902	1.902	3.054	3.054	3.367	3.368	3.369	3.370
0.25	1.923	1.923	3.230	3.230	3.597	3.598	3.600	3.601
0.15	1.932	1.932	3.344	3.344	3.750	3.751	3.753	3.754
0.05	1.935	1.935	3.400	3.400	3.827	3.828	3.830	3.831

A = Evangelista and Viggiani (1973)
B = CCRS1 ($R_j = 210$)

4.3.2 Large Strains

4.3.2.1 Lee (1981)

Example 4.3 involves large strains with constant c_v such that CCRS1 results can be compared with the analytical solution of Lee (1981). Initial conditions are the same as for Example 4.2. To maintain constant c_v ($= 4.81 \times 10^{-8}$ m^2/s) during consolidation, k_j^t was adjusted at each time step according to

$$k_j^t = k_o \frac{a_{v,j}^t (1 + e_o)}{a_{vo} (1 + e_j^t)} \qquad j = 1, 2, ..., R_j \tag{4.21}$$

where $k_o = 8.87 \times 10^{-9}$ m/s, $e_o = 2.0$, and a_{vo} (= 0.056/kPa) is the initial tangent value to the compressibility curve at e_o. Simulations were performed for $R_j = 200$ and two

values of applied strain rate, r = 6.827×10^{-2} %/h and 6.827%/h, which correspond to normalized strain rates, $\beta = rH_o^2/c_v$ = 0.01 and 1, respectively.

Table 4.5 and Table 4.6 compare local strain profiles for ε_{avg} = 5% to 30%. Analytical solutions were calculated using the finite difference method with 201 grid points and an average vertical strain increment of 0.0001% for each time step. Interpolation was used to obtain CCRS1 values at the specified elevations. CCRS1 values are again in excellent agreement with analytical solutions for both slow and fast strain rates. Table 4.5 and Table 4.6 also indicate that local strain profiles are strongly dependent on the applied strain rate and become more nonlinear as the rate increases. With increasing strain rate, the rate of water outflow from the specimen increases, which requires larger hydraulic gradients and thus larger gradients for excess pore pressure, effective stress, and local strain.

Table 4.5 Comparison of local strain profiles for Example 4.3 with $\beta = 0.01$.

Normalized Elevation Z	Local vertical strain, $\varepsilon\times10^{-1}$							
	ε_{avg} = 5%		ε_{avg} = 10%		ε_{avg} = 20%		ε_{avg} = 30%	
	A	B	A	B	A	B	A	B
0.9	0.521	0.521	1.019	1.019	2.015	2.015	3.012	3.012
0.8	0.514	0.514	1.012	1.012	2.010	2.010	3.008	3.008
0.7	0.507	0.507	1.006	1.006	2.005	2.005	3.004	3.004
0.6	0.501	0.501	1.001	1.001	2.001	2.001	3.001	3.001
0.5	0.496	0.496	0.997	0.997	1.997	1.997	2.998	2.998
0.4	0.492	0.492	0.993	0.993	1.994	1.994	2.996	2.996
0.3	0.489	0.489	0.990	0.990	1.992	1.992	2.994	2.994
0.2	0.487	0.487	0.988	0.988	1.991	1.991	2.993	2.993
0.1	0.485	0.485	0.987	0.987	1.990	1.990	2.992	2.992

A = Lee (1981)
B = CCRS1

Table 4.6 Comparison of local strain profiles for Example 4.3 with $\beta = 1$.

Normalized Elevation Z	Local vertical strain, $\varepsilon \times 10^{-1}$							
	ε_{avg} = 5%		ε_{avg} = 10%		ε_{avg} = 20%		ε_{avg} = 30%	
	A	B	A	B	A	B	A	B
0.9	1.493	1.493	2.293	2.292	3.321	3.320	4.091	4.091
0.8	0.948	0.947	1.742	1.741	2.850	2.849	3.718	3.718
0.7	0.556	0.556	1.273	1.272	2.410	2.409	3.364	3.364
0.6	0.302	0.301	0.895	0.894	2.012	2.011	3.037	3.037
0.5	0.152	0.151	0.606	0.605	1.664	1.663	2.744	2.744
0.4	0.071	0.070	0.397	0.397	1.373	1.372	2.493	2.493
0.3	0.030	0.030	0.254	0.254	1.144	1.143	2.290	2.290
0.2	0.012	0.012	0.164	0.163	0.979	0.978	2.141	2.141
0.1	0.0050	0.0050	0.114	0.114	0.880	0.879	2.050	2.050

A = Lee (1981)
B = CCRS1

4.3.2.2 CS2

The accuracy of the CS2 method has been verified extensively using analytical solutions, numerical solutions, and experimental data (Fox and Berles 1997; Fox 2000; Fox et al. 2003; Lee and Fox 2005; Berilgen et al. 2006; Kwon et al. 2007; Fox 2007; Lee and Fox 2009; Meric et al. 2010; Fox and Pu 2012). In Example 4.4, the enhanced CS2 model with the capability for time-dependent loading (Fox and Pu 2012) is used to verify CCRS1. A CCRS1 simulation was conducted for a top-drained clay specimen with H_o = h_t = 50 mm, G_s = 1, e_o = 2.0 (uniform), q_o = 5 kPa, R_j = 200, and r = 1.80%/h. Constitutive relationships are defined by Equations 4.19 and 4.20, and thus c_v varies during consolidation. The simulation was terminated at $\varepsilon_{avg,f}$ = 50.4% (t = 28 h). Calculated values for Δq versus t from CCRS1 were then used as the input loading

schedule for CS2. Local strain profiles obtained using CS2 and CCRS1 are shown in Table 4.7 and are identical. Corresponding profiles of excess pore pressure (not shown) are also identical. Exact correspondence between CS2 and CCRS1 results is not unexpected as both codes are based on the same core algorithm but does verify that CCRS1 can correctly simulate large strain conditions with general constitutive relationships and changing material properties during consolidation.

Table 4.7 Comparison of local strain profiles for Example 4.4.

Element j	Local vertical strain, $\varepsilon \times 10^{-1}$							
	t = 1 h		t = 10 h		t = 20 h		t = 28 h	
	A	B	A	B	A	B	A	B
200	0.723	0.723	2.315	2.315	3.904	3.904	5.228	5.228
180	0.525	0.525	2.181	2.181	3.822	3.822	5.177	5.177
160	0.361	0.361	2.054	2.054	3.746	3.746	5.129	5.129
140	0.235	0.235	1.937	1.937	3.677	3.677	5.087	5.087
120	0.144	0.144	1.831	1.831	3.616	3.616	5.049	5.049
100	0.084	0.084	1.738	1.738	3.562	3.562	5.016	5.016
80	0.046	0.046	1.660	1.660	3.518	3.518	4.989	4.989
60	0.024	0.024	1.598	1.598	3.483	3.483	4.968	4.968
40	0.012	0.012	1.552	1.552	3.457	3.457	4.953	4.953
20	0.0061	0.0061	1.525	1.525	3.442	3.442	4.944	4.944
1	0.0045	0.0045	1.516	1.516	3.437	3.437	4.941	4.941

A = CS2
B = CCRS1

4.4 Effect of Constitutive Relationships

CCRS1 has the capability to accommodate more general constitutive relationships than previous CRS consolidation models. A series of simulations was performed to investigate the effect of soil compressibility and hydraulic conductivity on CRS

consolidation response for conditions that include large strains and varying coefficient of consolidation. A top-drained clay specimen has H_o = h_t = 50 mm, G_s = 1, e_o = 2.0 (uniform), q_o = 5 kPa, and hydraulic conductivity defined by Equation 4.20. CCRS1 simulations were performed using R_j = 200, r = 1%/h, $\varepsilon_{avg,f}$ = 30%, and three compressibility relationships taken between point A and point C in Figure 4.4. Case 1 corresponds to linear compressibility with a_v = 0.00774/kPa. Case 2 is a normally consolidated clay with nonlinear compressibility defined by Equation 4.19. Case 3 is an overconsolidated clay with a_v = 0.001/kPa in the overconsolidated range, a_v = 0.012/kPa in the normally consolidated range, and a preconsolidation stress of approximately 50 kPa. These compressibility relationships are defined by σ'_A = 5.0 kPa, e_A= 2.0, σ'_B= 49.97 kPa, e_B= 1.955, σ'_C= 121.2 kPa, and e_C= 1.1.

An output compressibility relationship, expressed as average void ratio, e_{avg}, versus average vertical effective stress, σ'_{avg}, given by each CCRS1 simulation is also shown in Figure 4.4. Values of e_{avg} were calculated from specimen settlement and values of σ'_{avg} were calculated as the simple arithmetic average over all 200 elements at the same time (i.e., $\frac{1}{R_j}\sum_{j=1}^{R_j}\sigma'^{t}_{j}$). The e_{avg} versus σ'_{avg} relationship for r = 1%/h is nearly identical with the true compressibility relationship (e vs. σ') in each case. Interestingly, other simulations (not shown) have indicated that, for higher strain rates, these relationships diverge even when soil compressibility is rate-independent. These

investigations are the subject of ongoing research and are beyond the scope of the current study.

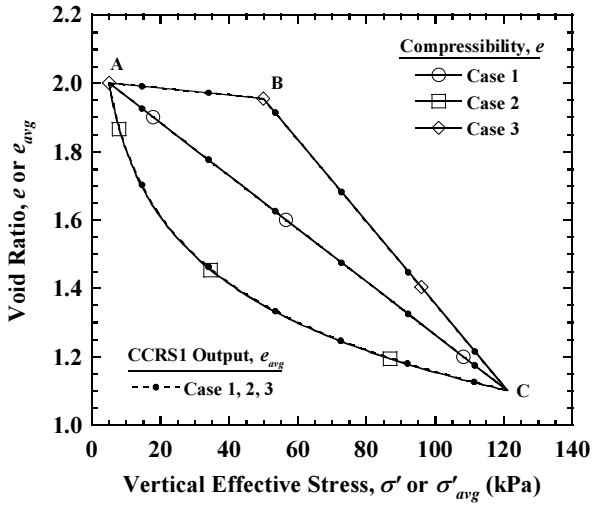

Figure 4.4 Three compressibility relationships for CCRS1 simulations.

Values of Δq are shown as a function of ε_{avg} for each compressibility relationship in Figure 4.5. Analytical solutions for Case 1 and Case 2 were obtained using the linear and nonlinear theories of Wissa et al. (1971) and, for Case 2, the equations of Evangelista and Viggiani (1973). These solutions were calculated using values of c_v corresponding to initial conditions (e_o = 2), which are equal to 3.50×10^{-7} m^2/s and 4.80×10^{-8} m^2/s for Case 1 and Case 2, respectively. Linear theory produces an initial transient response (ε_{avg} < 1%) and a subsequent steady state response in which Δq increases linearly with increasing ε_{avg} due to constant values for both a_v and c_v. Nonlinear theory also gives an initial transient response; however, decreasing soil compressibility produces a nonlinear increase in Δq. Numerical solutions obtained using

CCRS1 for Case 1 and Case 2 are very close to the analytical values at early times and then show progressively larger deviations, which is due primarily to changing c_v with increasing vertical strain. For Case 1, a_v is constant and k decreases with increasing vertical strain, which causes c_v to decrease and produces higher values of Δq than the analytical solution. For Case 2, a_v decreases faster than k, which causes c_v to increase and produces lower values of Δq than the analytical solution. The effect of vertical strain is to shorten the drainage path length, which would reduce Δq; however, at least for Case 2 this effect is not controlling. For Case 3, CCRS1 indicates that the bilinear compressibility curve produces a sharp break in the Δq vs. ε_{avg} relationship at Δq = 45 kPa. Recalling that q_o = 5 kPa, this Δq value corresponds closely with the true preconsolidation stress of 50 kPa. The simulations in Figure 4.5 suggest that both compressibility and hydraulic conductivity relationships can have an important effect on the applied vertical stress for a CRS test and that analytical solutions obtained using small strain theory can be in significant error for large strain conditions with varying c_v.

Corresponding excess pore pressures at the base of the specimen, $u_{ex,b}$, are presented in Figure 4.6. After the initial transient phase, analytical values are constant for linear theory and increase for nonlinear theory due to decreasing soil compressibility. CCRS1 values are in close agreement with the analytical solutions at early times and then, interestingly, follow nearly the same nonlinear trend regardless of compressibility relationship. This is likely a reflection of the similar hydraulic conductivity profiles for each average strain level. A detail plot for the early time data, also presented in Figure

4.6, indicates that initial values of $u_{ex,b}$ increase with decreasing soil compressibility. This plot also shows a sharp decrease in $u_{ex,b}$ for Case 3 at approximately ε_{avg} = 1.5%, which corresponds to the preconsolidation strain in Figure 4.4. The simulations presented in Figure 4.6 indicate that excess pore pressures obtained using small strain theory may be completely invalid at large strains.

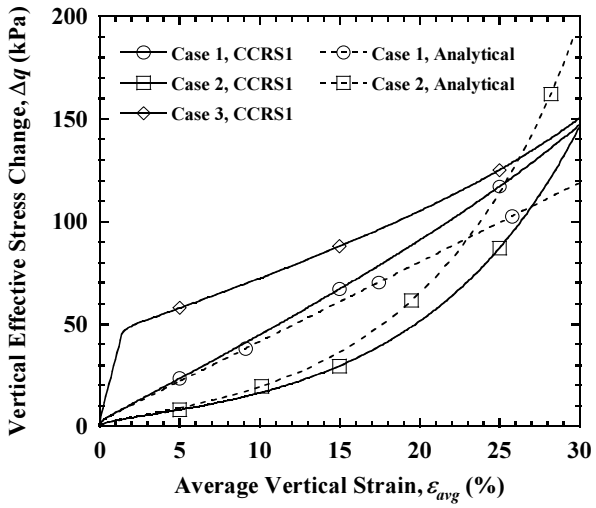

Figure 4.5 Changes of vertical effective stress at top boundary for three compressibility relationships.

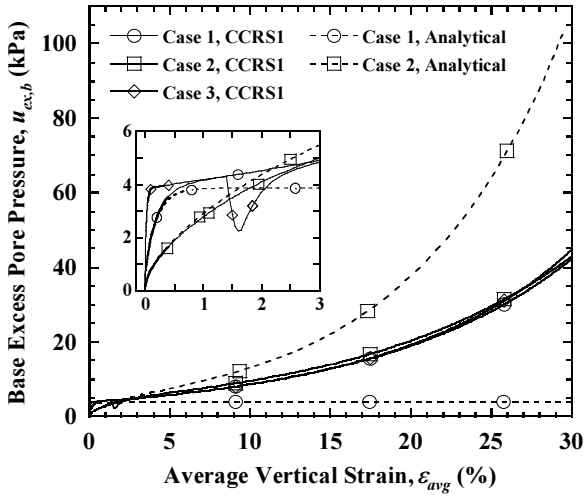

Figure 4.6 Excess pore pressures at base of specimen for three compressibility relationships.

Lastly, Figure 4.7 presents local strain profiles for ε_{avg} = 1%, 15%, and 30%. Analytical and CCRS1 values are in close agreement for ε_{avg} = 1% and then diverge at higher average strain levels in response to changing values of c_v. The different trends can be interpreted by considering the normalize strain rate, β. For Case 1, c_v decreases (i.e., β increases) with increasing vertical strain, which produces a CCRS1 local strain profile that is less uniform than the analytical solution. The opposite occurs for Case 2 and the CCRS1 strain profile is more uniform than the analytical solution. These trends are consistent with the findings of Lee (1981) and Example 4.3 in which smaller β yields more uniform local strains. During consolidation, β increases from 0.0198 to 0.426 for Case 1, decreases from 0.145 to 0.04 for Case 2, and increases from 0.0026 to 0.66 for Case 3. As a result, the CCRS1 strain profile for Case 2 is the most nonlinear profile for ε_{avg} = 1% and the least nonlinear for ε_{avg} = 30%. On the other hand, Case 3

shows the least nonlinear strain profile for ε_{avg} = 1% and the most nonlinear profile for ε_{avg} = 30%. These simulations indicate that soil constitutive relationships can have an important effect on the local strain profile and again demonstrate that analytical solutions from small strain theory can be in significant error for conditions involving large strains and changing c_v.

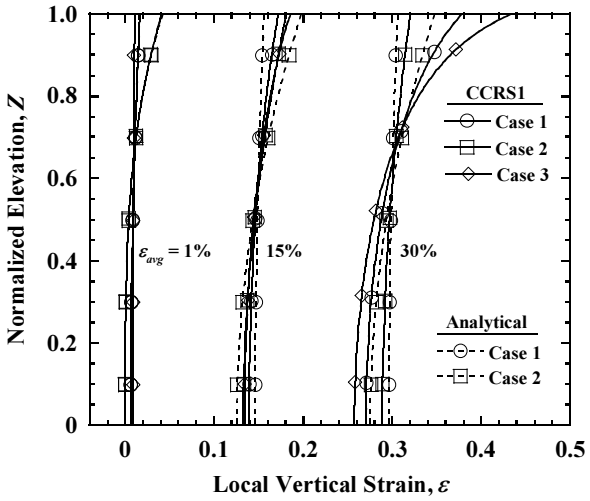

Figure 4.7 Local strain profiles for three compressibility relationships.

4.5 Acknowledgements

Chapter 4 of this dissertation is based on material published by the International Journal for Numerical and Analytical Methods in Geomechanics titled “Model for Large Strain Consolidation under Constant Rate of Strain” with authors, Hefu Pu, Patrick J. Fox, and Yong Liu (2013). The dissertation author is the first author of this paper.

Chapter 5

Coupled Solute Transport and Constant Rate of Strain Consolidation

5.1 Introduction

Using the Enhanced CS2 (see Chapter 3) and CCRS1 (see Chapter 4), a model, called CSTCRS1 (Consolidation and Solute Transport for Constant Rate of Strain 1), is developed for coupled one-dimensional large strain consolidation and solute transport under constant rate of strain (CRS) loading conditions. This chapter presents the model development and the associated numerical investigations. CSTCRS1 is based on a dual-Lagrangian framework that tracks separately the motions of fluid and solid phases. The consolidation algorithm accounts for vertical strain, general constitutive relationships, relative velocity of fluid and solid phases, changing compressibility and hydraulic conductivity during consolidation, and an external hydraulic gradient. Soil

compressibility is rate-independent and, as such, CSTCRS1 is most appropriate for less structured soils. The solute transport algorithm accounts for advection, dispersion, linear and nonlinear sorption isotherm, and equilibrium and nonequilibrium sorption. The development of CSTCRS1 is first described, followed by verification checks. Numerical simulations are then presented to illustrate the effects of initial concentration distribution, transport conditions, applied strain rate, initial specimen height, and drainage and concentration boundary conditions on consolidation-induced solute transport for CRS loading conditions.

5.2 Model Development

CSTCRS1 was developed by combining CST2 (Fox and Lee 2008) and CCRS1 (Pu et al. 2013) and follows similar procedures with regard to geometry, constitutive relationships, initial void ratio distribution, settlement, advection, dispersion and sorption. The general methodology is described by Fox and Berles (1997), Fox and Pu (2012), Fox (2007a,b), Fox and Lee (2008), and Pu et al. (2013). The following sections briefly summarize the CSTCRS1 model with focus on its new capabilities.

5.2.1 Geometry

A homogeneous saturated soil specimen of initial height H_o is treated as an idealized two-phase material in which the solid particles and pore fluid are incompressible. The term “homogeneous” refers to the compressibility and hydraulic conductivity constitutive relationships and not the distribution of initial void ratio within

the specimen. Although soil consolidation and solute transport may generally occur in three dimensions, the following development is restricted to one-dimensional conditions. The initial geometry of the soil specimen, prior to the application of a vertical stress increment at time $t = 0$, is shown in Figure 5.1. The solid phase is represented as a column of R_j elements. Vertical coordinate z and solid element coordinate j are defined as positive upward (against gravity) from a fixed datum at the base of the specimen. Each j^{th} solid element has initial height L_{so}, unit cross-sectional area, a central node located at initial elevation $z_{so,j}$, and initial void ratio $e_{o,j}$. The distribution of void ratio is assumed to be uniform within each solid element and varies vertically among solid elements depending on the initial vertical effective stress at the top of the specimen q_o, the compressibility and self-weight of the soil, and any vertical seepage forces due to an external hydraulic gradient acting across the column (Fox 2007a).

The pore fluid is also represented as a column of elements, with R_{mo} fluid elements initially in the column. Fluid elements are defined by vertical element coordinate m. Each m^{th} fluid element has initial height L_{fo}, unit cross-sectional area, and a central node located at initial elevation $z_{fo,m}$. For cases without sorption/desorption, the initial positions of fluid and solid elements are coincident (i.e., $R_{mo} = R_j$ and $L_{fo} = L_{so}$). This is the configuration shown in Figure 5.1(a). For cases involving sorption/desorption, higher numerical resolution is needed for the fluid phase (i.e., $R_{mo} > R_j$ and $L_{fo} < L_{so}$) and the fluid in each solid element is divided into an odd integer number (typically three) of smaller fluid elements. Each m^{th} fluid element has initial

fluid (i.e., dissolved) concentration $c_{o,m}$ [mass solute/volume fluid] and initial dissolved solute mass $C_{fo} = c_{o,m} V_{fo,m}$, where $V_{fo,m} = L_{fo} e_{o,j} / (1 + e_{o,j})$ is initial volume of fluid in the element and $e_{o,j}$ is the initial void ratio of the solid element at the same elevation. The initial sorbed concentration for each solid element $s_{o,j}$ [mass solute/mass solid] is assumed to be in equilibrium with the local fluid concentration.

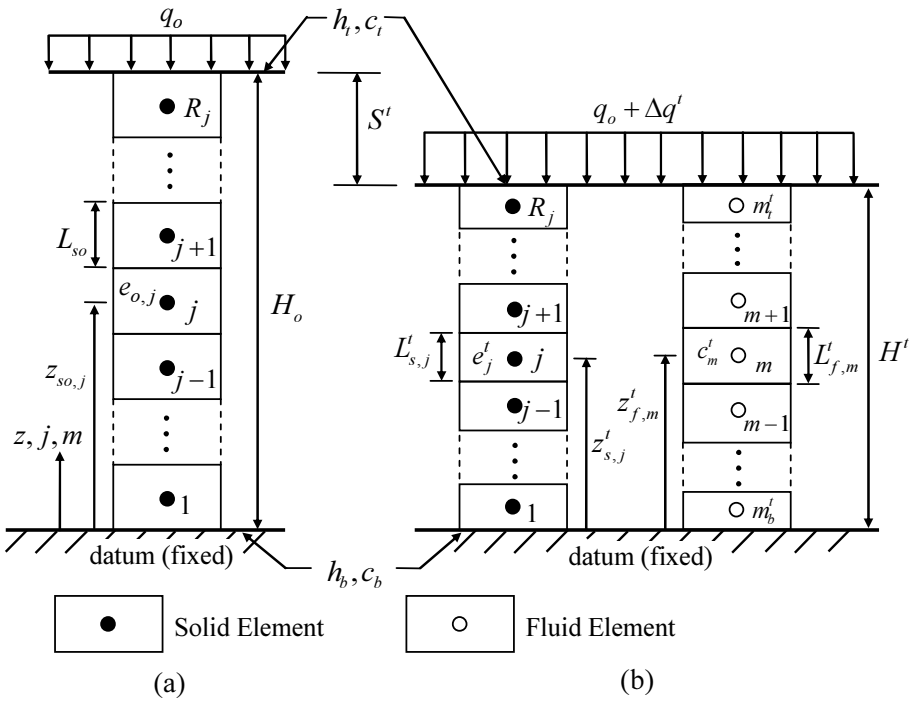

Figure 5.1 Geometry for CSTCRS1: (a) initial configuration; (b) configuration during loading.

5.2.2 Boundary Conditions

Top and bottom boundaries of the compressible specimen can be specified as drained or undrained and, if drained, are assigned individual constant total hydraulic head values, h_t and h_b, taken with respect to the datum (Figure 5.1). Transport conditions for the top and bottom boundaries can be specified as prescribed concentration (Type I), prescribed concentration gradient (Type II), or prescribed solute mass flux (Type III) (Fox 2007a,b). Figure 5.1 shows Type I conditions in which the top and bottom boundaries are maintained at constant concentrations c_t and c_b. CSTCRS1 can also accommodate a reservoir boundary which represents an accumulating well-mixed aqueous reservoir formed above the specimen from fluid outflow at the top boundary (Fox and Lee 2008).

5.2.3 Application of Stress

At each time step, CSTCRS1 calculates the applied stress needed to yield the required settlement (i.e., displacement at the top boundary) corresponding to a constant value of applied average strain rate r. Beginning at $t=0$, a time-varying value of vertical effective stress change Δq^t is applied to the specimen and moves with the top boundary thereafter. Iteration is used to adjust the value of Δq^t at each time step until the difference between the computed settlement, $S^t = H_o - H^t$, where H^t = height of specimen at time t, and the required settlement, $\tilde{S}^t = H_o r t$, is negligible. Excess pore pressures created as a result of stress changes cause fluid flow from the interior of the

specimen to all drainage boundaries. Soil deformation occurs in response to the net fluid outflow from each solid element. Solute transport occurs by advection and dispersion in the fluid phase and sorption onto moving solid elements. Figure 5.1(b) shows the configuration of the system at some later time t. Fluid and solid elements are laterally separated for clarity but, similar to Figure 5.1(a), occupy the same physical space. Fluid elements become vertically disconnected from their original solid elements and move in response to the local seepage velocity field. At time t, the height and void ratio of the j^{th} solid element are $L_{s,j}^{t}$ and e_{j}^{t}, and the height of the m^{th} fluid element is $L_{f,m}^{t}$. Solid and fluid elements have node elevations $z_{s,j}^{t}$ and $z_{f,m}^{t}$, respectively, which are updated at each time step. Nodes translate vertically and remain at the center of their respective elements throughout the consolidation process. Fluid elements have concentration c_{m}^{t} and dissolved solute mass $C_{f,m}^{t}$. The volume of fluid in each fluid element $V_{f,m}$ is always equal to the original fluid volume $V_{fo,m}$ unless the element is adjacent to a drainage boundary. Thus, for problems involving consolidation, as opposed to swelling, the height of fluid elements will increase as the porosity of the associated soil elements decreases. Fluid elements move through, and possibly out of, the consolidating layer in response to excess pore pressures and any external hydraulic gradient (if $h_t \neq h_b$). Thus, unlike the number of solid elements, which is always constant, the number of fluid elements may decrease/increase during the consolidation/swelling process. Fluid elements adjacent to the top and bottom boundaries are designated as m_t^t and m_b^t, respectively. Based on the computed distribution of void ratio and fluid flows across drainage boundaries,

CSTCRS1 uses the same Lagrangian method as CST1 to track the advection of fluid elements within the column (Fox 2007a).

5.2.4 Solute Transport

The dual-Lagrangian framework of CSTCRS1 automatically accounts for advection transport in the fluid phase and sorption transport on the solid phase. Effective diffusion coefficient D^* is dependent on solid element porosity as (Fox and Lee 2008)

$$D_j^{*t} = D_o (n_j^t)^M \tag{5.1}$$

where n_j^t = porosity of the j^{th} solid element; M = constant; and D_o = free solution diffusion coefficient. The longitudinal dispersion mass flow rate $J_{z,m}^t$ between fluid element nodes m and $m+1$ is

$$J_{z,m}^t = -D_{Ls,m}^t i_{cz,m}^t \tag{5.2}$$

where the vertical solute concentration gradient $i_{cz,m}^t$ is

$$i_{cz,m}^t = \frac{c_{m+1}^t - c_m^t}{z_{f,m+1}^t - z_{f,m}^t} \tag{5.3}$$

and the equivalent series hydrodynamic dispersion coefficient between nodes m and $m+1$ is

$$D_{Ls,m}^t = \frac{z_{f,m+1}^t - z_{f,m}^t}{\sum_{j=1}^{R_j} \frac{N_{L,j,m}^t}{n_j^t}} \tag{5.4}$$

where $N^t_{L,j,m}$ is determined by values of elevation, longitudinal dispersivity α_L, porosity, effective diffusion coefficient, and relative discharge velocity for the associated solid and fluid elements. Details for the calculation of $N^t_{L,j,m}$ are provided by Fox (2007a).

5.2.5 Mass Balance and Sorption/Desorption

CSTCRS1 accounts for sorption/desorption by permitting solute mass transfer between fluid and solid elements. The general case corresponds to the following nonlinear nonequilibrium (i.e., kinetic) sorption model (Travis and Etnier 1981)

$$\frac{\partial s}{\partial t} = \lambda(K_p c^F - s) \tag{5.5}$$

where s = sorbed concentration; λ = sorption rate constant; and K_p and F = constants describing a nonlinear Freundlich isotherm. The rate of solute mass transfer is controlled by the imbalance of concentrations with respect to equilibrium, which is defined as $s = K_p c^F$. Mass transfer occurs between fluid and solid elements when the solid element node lies within the fluid element. To ensure good accuracy for simulations with sorption, a larger number of fluid elements than solid elements is typically specified (e.g., $R_{mo} = 3R_j$) such that only one fluid element exchanges solute mass with one solid element during any given time step.

The updated solute mass $C^{t+\Delta t}_{f,m}$ in each fluid element at time $t+\Delta t$ is calculated from inter-element mass flow rates and sorption/desorption mass transfer as

$$C^{t+\Delta t}_{f,m} = C^t_{f,m} + (J^t_{z,m-1} - J^t_{z,m})\Delta t - \Delta s^t \rho^{t+\Delta t}_{d,j} L^{t+\Delta t}_{s,j} \tag{5.6}$$

where $\Delta s^t = \lambda(K_{p,j}(c_m^t)^F - s_j^t)\Delta t$; s_j^t = sorbed concentration for solid element j; $\rho_{d,j}^{t+\Delta t}$ = $\rho_w G_s / (1+e_j^{t+\Delta t})$ = updated dry density; ρ_w = density of water (constant); and G_s = specific gravity of solids (constant). For Equation 5.6, the node of solid element j is assumed to be within the boundaries of fluid element m (i.e., $z_{s,j}^{t+\Delta t} > z_{fb,m}^{t+\Delta t}$ and $z_{s,j}^{t+\Delta t} \le z_{ft,m}^{t+\Delta t}$). Like CST1, CSTCRS1 uses explicit time integration with a variable time increment Δt based on several conditions related to numerical stability and accuracy (Fox 2007a). Once the value of $C_{f,m}^{t+\Delta t}$ is known, the updated fluid element concentration is

$$c_m^{t+\Delta t} = \frac{C_{f,m}^{t+\Delta t}}{V_{f,m}^{t+\Delta t}} \tag{5.7}$$

and the updated sorbed concentration is

$$s_j^{t+\Delta t} = s_j^t + \Delta s^t \tag{5.8}$$

Conceptually, equilibrium sorption can be achieved using the above kinetic model with $\lambda \to \infty$. However, large values of λ require a very small time increment to avoid spurious oscillations in concentration (Zhou and Selim 2001). To increase computational efficiency, CSTCRS1 uses the method from CST1 to directly calculate equilibrium sorption for nonlinear isotherms (Fox 2007a). The updated solute mass in the m^{th} fluid element is

$$C_{f,m}^{t+\Delta t} = C_{f,m}^t + (J_{z,m-1}^t - J_{z,m}^t)\Delta t \tag{5.9}$$

and the sorbed mass for solid element j is

$$C_{s,m}^{t+\Delta t} = s_j^t \rho_{d,j}^{t+\Delta t} L_{s,j}^{t+\Delta t} \tag{5.10}$$

The total solute mass $C_m^{t+\Delta t}$ associated with fluid element m is then equal to

$$C_m^{t+\Delta t} = C_{f,m}^{t+\Delta t} + C_{s,m}^{t+\Delta t} \tag{5.11}$$

This total mass is partitioned between fluid element m and solid element j according to $s = K_p c^F$. The updated fluid element concentration $c_m^{t+\Delta t}$ is calculated from

$$C_m^{t+\Delta t} = c_m^{t+\Delta t} V_{f,m}^{t+\Delta t} + K_{p,j} (c_m^{t+\Delta t})^F \rho_{d,j}^{t+\Delta t} L_{s,j}^{t+\Delta t} \tag{5.12}$$

and the updated equilibrium sorbed concentration is

$$s_j^{t+\Delta t} = K_{p,j} (c_m^{t+\Delta t})^F \tag{5.13}$$

If F = 1, the foregoing method reduces to a linear equilibrium model where

$$s_j^{t+\Delta t} = K_{d,j} c_m^{t+\Delta t} \tag{5.14}$$

and $K_{d,j}$ = distribution coefficient for solid element j. As with CST1, first-order decay reactions can also be taken into account with CSTCRS1, however these would generally not be important over the relatively short duration of a CRS test procedure.

5.3 Model Verification

As CSTCRS1 is the first model for coupled CRS consolidation and solute transport, no solutions are available to verify its accuracy. However, a complete verification check was performed using CST2, which includes the capability for time-dependent loading (Fox and Lee 2008). The accuracy of CST2, and its precursor CST1, has been verified extensively using analytical solutions, numerical solutions, and experimental data (Fox 2007a; Fox 2007b; Fox and Lee 2008; Lee and Fox 2009). For

model verification purposes, we consider a specimen of clay soil with initial height H_o = 50 mm. The specimen contains an uncontaminated upper layer and a contaminated lower layer, both with an initial thickness of 25 mm. The contaminated layer contains an unspecified solute with an initial uniform fluid concentration c_o = 100 mg/L and a corresponding equilibrium sorbed concentration for the solid phase. The initial vertical effective stress at the top boundary is q_o = 5 kPa. Material properties for both layers were taken from measurements for kaolinite clay (Lee and Fox 2009). The specific gravity of solids G_s = 2.61, liquid limit LL = 47.6, plasticity index PI = 21.8, and the Unified Soil Classification is CL, Lean Clay. Constitutive relationships for compressibility and hydraulic conductivity are

$$e = e_o - C_c \log\left(\frac{\sigma'}{\sigma'_o}\right) \tag{5.15}$$

$$e = 8.16 + 0.765 \log\left(k(\text{m/s})\right) \tag{5.16}$$

where e_o = 2.0; C_c = compression index = 0.65; σ' = vertical effective stress; σ'_o = 5 kPa; and k = vertical hydraulic conductivity. The initial void ratio distribution is nearly uniform and ranges from 2.0 at the top of the specimen to 1.99 at the bottom (variation due to self-weight). The top boundary is drained with constant total head h_t = 50 mm and zero concentration gradient, whereas the bottom boundary is zero flux for both pore fluid and solute mass. The effective diffusion coefficient is defined by Equation 5.1 with D_o = 1.96×10^{-9} m^2/s and M = 1.82, mechanical dispersion is defined by α_L = 20 mm, and nonlinear equilibrium sorption is defined by K_p = 19.6 mL/g and F = 0.608.

Simulations were performed with R_j = 200 solid elements, R_{mo} = 600 initial fluid elements, an applied average strain rate r = 1%/h, and a termination criterion of 40% final average strain. Calculated values for Δq versus t from CSTCRS1 were then used as the specified loading schedule for CST2, which reproduced a constant average strain rate of 1%/h in the CST2 simulation.

Table 5.1 Local strain and fluid concentration profiles for verification example.

Normalized Elevation Z	ε_{avg} = 1%		ε_{avg} = 10%		ε_{avg} = 20%		ε_{avg} = 40%	
	A	B	A	B	A	B	A	B
0.9	2.946	0.000	12.716	0.000	22.114	0.000	41.196	4.055
0.8	1.984	0.000	11.770	0.000	21.381	1.075	40.783	10.361
0.7	1.271	0.000	10.918	0.868	20.721	9.093	40.412	19.783
0.6	0.773	0.000	10.166	15.839	20.139	24.795	40.085	31.644
0.5	0.445	46.583	9.518	45.672	19.636	45.413	39.802	45.008
0.4	0.243	99.968	8.979	75.043	19.216	66.141	39.565	58.733
0.3	0.126	100.000	8.551	92.654	18.880	82.778	39.373	71.636
0.2	0.063	100.000	8.237	98.870	18.630	93.378	39.228	82.747
0.1	0.033	100.000	8.039	99.932	18.466	98.312	39.130	90.963

A = local strain (%) calculated using CST2 and CSTCRS1
B = fluid concentration (mg/L) calculated using CST2 and CSTCRS1

Profiles of local strain ε and fluid concentration versus normalized elevation Z (= z/H) for average strain ε_{avg} = 1%, 10%, 20%, and 40% are shown in Table 5.1. Results obtained from CST2 and CSTCRS1 are identical to 5 significant figures. Corresponding profiles of excess pore pressure and sorbed concentration, not shown for brevity, are also identical. Additional verification checks were conducted for examples involving different soil constitutive relationships, applied strain rates, linear and

nonlinear equilibrium sorption, and linear and nonlinear nonequilibrium sorption. In each case, CTSCRS1 solutions were identical with those obtained using CST2. The foregoing verification exercises indicate that CSTCRS1 is valid for simulation of coupled large strain consolidation and solute transport under CRS loading conditions.

5.4 Simulation Results

5.4.1 Initial Uniform Contamination

5.4.1.1 Effect of Transport Boundary Condition

We first consider a soil specimen with initial uniform contamination of an unspecified solute. The specimen has H_o = 50 mm, G_s = 2.61, q_o = 5 kPa, constitutive relationships defined by Equations 5.15 and 5.16, single upward drainage with h_t = 50 mm, and c_o = 100 mg/L. CSTCRS1 simulations were conducted for CRS consolidation with r = 1%/h and five transport conditions: (1) advection only (A), (2) advection + diffusion (ADf), (3) advection + dispersion (AD), (4) advection + dispersion + equilibrium sorption (ADS), and (5) advection + dispersion + kinetic sorption (ADkS). Transport parameters are provided in Table 5.2. Sorption was characterized using a linear equilibrium isotherm, which yielded an initial uniform sorbed concentration s_o = 300 mg/kg for the ADS and ADkS simulations. The solid phase was represented using R_j = 200 elements and the fluid phase was represented using $R_{mo} = R_j$ for simulations without sorption and $R_{mo} = 3R_j$ for simulations with sorption. Although transport parameters were constant (Table 5.2), spatial and temporal changes in porosity and

seepage velocity produced variations of hydrodynamic dispersion coefficient D_L ($=D^* + \alpha_L v_s$), retardation factor R_f ($=1+\rho_d K_d / n$), and Peclet number P ($=v_s H / D_L$) within the specimen during consolidation. The bottom boundary was zero flux with regard to solute mass and the top boundary was modeled using three concentration conditions: (1) zero concentration, (2) zero concentration gradient, and (3) reservoir.

Table 5.2 Transport parameters for uniform initial contamination simulations.

Transport condition	Effective diffusion coefficient D^* (m^2/s)	Longitudinal dispersivity α_L (m)	Distribution coefficient K_d (mL/g)	Sorption rate constant λ (1/s)
A (advection only)	0	0	0	-
ADf (advection + diffusion)	9.37×10^{-10}	0	0	-
AD (advection + dispersion)	9.37×10^{-10}	0.02	0	-
ADS (advection + dispersion + equilibrium sorption)	9.37×10^{-10}	0.02	3	-
ADkS (advection + dispersion + kinetic sorption)	9.37×10^{-10}	0.02	3	1×10^{-5}

Plots of settlement S and cumulative solute mass outflow M_e per unit area for several transport and boundary conditions are shown in Figure 5.2(a). Settlement increases linearly for all cases to a final value of 20 mm at t = 40 h, which corresponds to a final average strain of 40%. For the A simulations, M_e also increases linearly regardless of top boundary concentration condition because fluid outflow is proportional to settlement, fluid concentration is constant, and all other transport mechanisms are

disabled. Interestingly, Figure 5.2(a) shows the same linear M_e relationship for ADf, AD, ADS, and ADkS when the top boundary is defined as zero concentration gradient or reservoir. No concentration gradients are created for these boundary conditions and thus additional transport mechanisms (diffusion, mechanical dispersion, and sorption) do not occur. However, these transport mechanisms become important when zero concentration is specified for the top boundary and concentration gradients are created. In this case, M_e for ADf is greater than for A due to additional upward diffusion transport. Mechanical dispersion ($\alpha_L > 0$) further increases solute mass outflow for the AD case. The ADS simulation gives the largest mass outflow because of the larger initial solute mass (dissolved + sorbed) within the specimen. By comparison, mass outflow is smaller for ADkS due to the additional time required for kinetic desorption. Although the values are greater, mass outflows for ADS and ADkS are less than the others on a percentage basis. At t = 40 h, the percentage of initial solute mass that has left the specimen is 60% for A, 65% for ADf, 83% for AD, 35% for ADS, and 30% for ADkS. Final fluid concentration c_f profiles are shown in Figure 5.2(b). Concentrations remain unchanged ($_c$ = 100 mg/L) for the zero concentration gradient and reservoir boundary conditions and display nonlinear profiles for the zero concentration boundary condition. Final sorbed concentration profiles, shown in Figure 5.2(c), indicate similar trends with the ADkS displaying less desorption at each elevation than ADS and, interestingly, a non-zero $_s$ value at the top boundary.

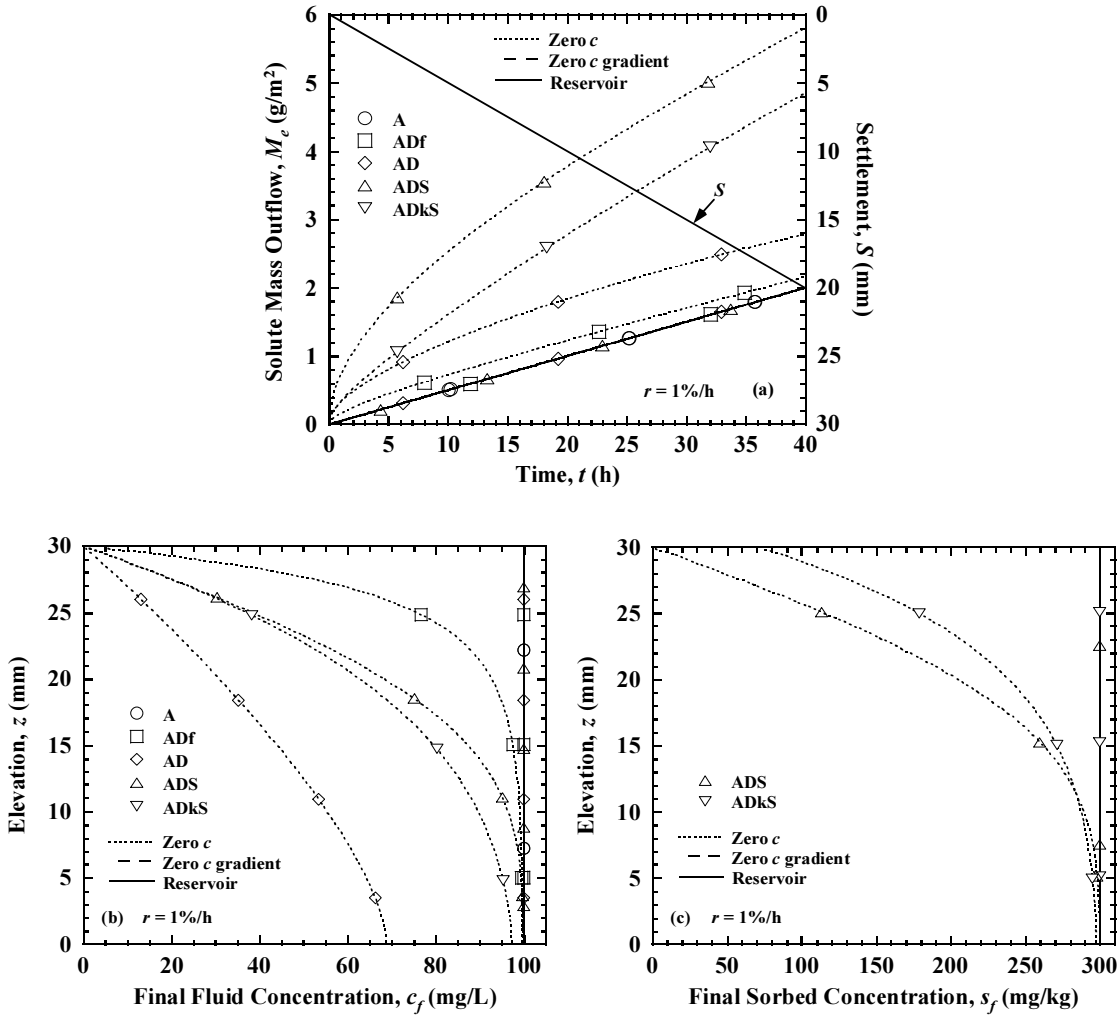

Figure 5.2 Simulation results for initial uniform contamination: (a) settlement and solute mass outflows; (b) final fluid concentration profiles; (c) final sorbed concentration profiles.

5.4.1.2 Effect of Strain Rate

AD and ADS simulations were performed for r = 0.2, 1, and 5%/h to investigate the effect of applied strain rate on consolidation and solute transport. Normalized profiles of local strain, shown in Figure 5.3(a) for ε_{avg} = 5%, 20% and 40%, are strongly affected by strain rate and become more nonuniform as strain rate increases. Figure

5.3(b) shows corresponding normalized profiles of seepage velocity. Higher strain rates produce larger fluid outflow rates from the top boundary and larger seepage velocities, and hence larger values of hydrodynamic dispersion, within the specimen.

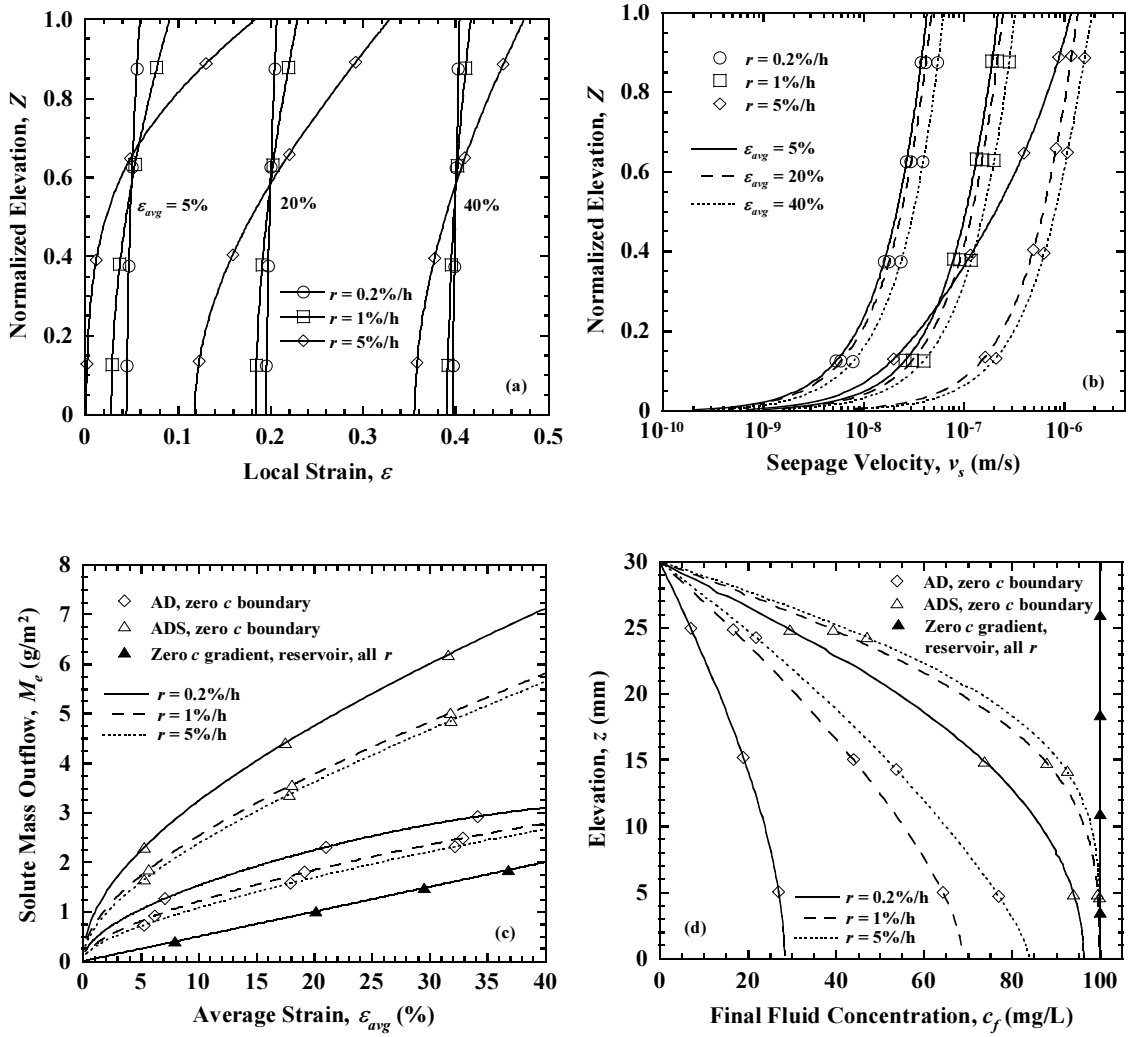

Figure 5.3 Simulation results for initial uniform contamination and three applied strain rates: (a) local strain profiles; (b) seepage velocity profiles; (c) solute mass outflows; (d) final fluid concentration profiles.

Figure 5.3(c) presents solute mass outflows for different strain rates and boundary conditions. When the top boundary is specified as zero concentration gradient or

reservoir, concentration gradients are not created within the specimen and M_e increases linearly with average strain for all cases. Applied strain rate and transport conditions become important when the top boundary is specified as zero concentration. Higher strain rates yield smaller M_e for both AD and ADS, which suggests that reduced time for dispersion has a greater effect than larger values of hydrodynamic dispersion coefficient for these simulations. Final fluid concentration profiles, shown in Figure 5.3(d), are uniform for zero concentration gradient and reservoir boundary conditions, and display gradients that vary with strain rate for the zero concentration boundary condition. Focusing on the latter case, the AD simulation for r = 0.2%/h has the lowest concentrations and lowest concentration gradients due to the greater time available for dispersion. Figure 5.3(d) also shows that strain rate has a more important effect on the final concentration profile for AD transport condition due to the lack of retardation when sorption is included.

To further investigate the effect of applied strain rate on solute mass outflow for initial uniform contamination, additional simulations were performed for strain rates ranging from 0.1%/h to 10%/h. As before, solute mass outflow is proportional to settlement regardless of strain rate or transport condition for zero concentration gradient or reservoir boundaries. However, when zero concentration is maintained at the top boundary, concentration gradients are created and applied strain rate has an effect. These results are shown in Figure 5.4 for M_{ef} / M_o versus r, where M_{ef} is the final solute mass outflow and M_o is the initial total solute mass in the specimen. The final average strain is 40% for each simulation and thus, total consolidation time decreases from 400 h at r =

0.1%/h to 4 h at r = 10%/h. For the A condition, strain rate has no effect on solute mass outflow. When diffusion transport is included (ADf), values of M_{ef} / M_o are significantly greater at low strain rates and then, as strain rate increases and consolidation time is reduced, decrease to merge with the advection value. ADf and AD simulations yield nearly the same values of M_{ef} / M_o at low strain rates because seepage velocities and corresponding contributions from mechanical dispersion ($\alpha_L v_s$) are small. However, unlike diffusion, effects of dispersion do not vanish at high strain rates for the AD condition because larger seepage velocities increase hydrodynamic dispersion and, although consolidation time is short, still produce significant upward dispersion transport. When equilibrium sorption is included, the ADS simulations yield smaller M_{ef} / M_o at all strain rates due to the larger M_o value. For the ADkS condition, values of M_{ef} / M_o are almost the same as for ADS at low strain rates and then, as r increases, diverge to yield smaller values due to delayed desorption effects.

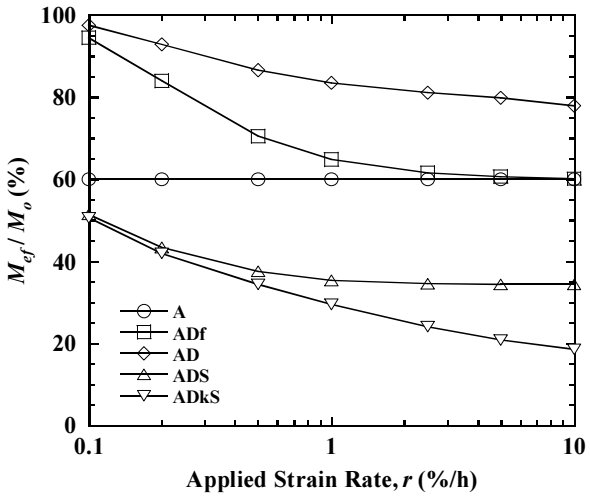

Figure 5.4 Effect of applied strain rate on final solute mass outflow for initial uniform contamination and zero concentration boundary.

5.4.2 Initial Lower Half Contamination

5.4.2.1 Effect of Transport Boundary Condition

A second series of simulations was performed for the same conditions except that the soil specimen is initially contaminated in the lower half (z = 0 to 25 mm, c_o = 100 mg/L, s_o = 300 mg/kg) and uncontaminated in the upper half (z = 25 to 50 mm, c_o = s_o = 0). Figure 5.5(a) presents effluent concentrations c_e for CRS tests with r = 1%/h and A, AD, and ADS transport conditions. First considering the zero concentration gradient boundary condition, c_e is initially zero for the advection only case and then makes a step increase to c_o when the solute front reaches the top boundary (t = 33.3 h). The AD simulation includes dispersion and produces earlier solute breakthrough and a gradual increase of c_e to the end of the test. By comparison, breakthrough time is longer and effluent concentrations are lower for ADS due to sorption in the initially uncontaminated layer. For the reservoir boundary condition, each simulation indicates lower effluent concentrations, which occurs as a result of dilution with initially uncontaminated flow into the reservoir.

Corresponding solute mass outflows are shown in Figure 5.5(b). With other transport mechanisms disabled, M_e for advection only is the same for all top boundary concentration conditions. For the AD and ADS simulations, mass outflows are consistently largest for zero concentration, intermediate for reservoir, and smallest for zero concentration gradient boundary conditions. Final fluid concentration profiles in Figure 5.5(c) show uniform $c_f = c_o$ profiles for advection only and concentration

gradients for the other cases. Comparison of Figure 5.5(b) and Figure 5.5(c) indicates that final M_e values increase with higher average concentration gradient across the specimen and larger M_e values produce lower average final concentrations. Final profiles also show smooth transitions between initially contaminated and uncontaminated layers. The AD condition produces more uniform profiles than ADS because sorption slows redistribution of solute mass inside the specimen. Sorption also mutes the effect of top boundary concentration condition and produces final concentration profiles that are essentially coincident for the bottom part of the specimen.

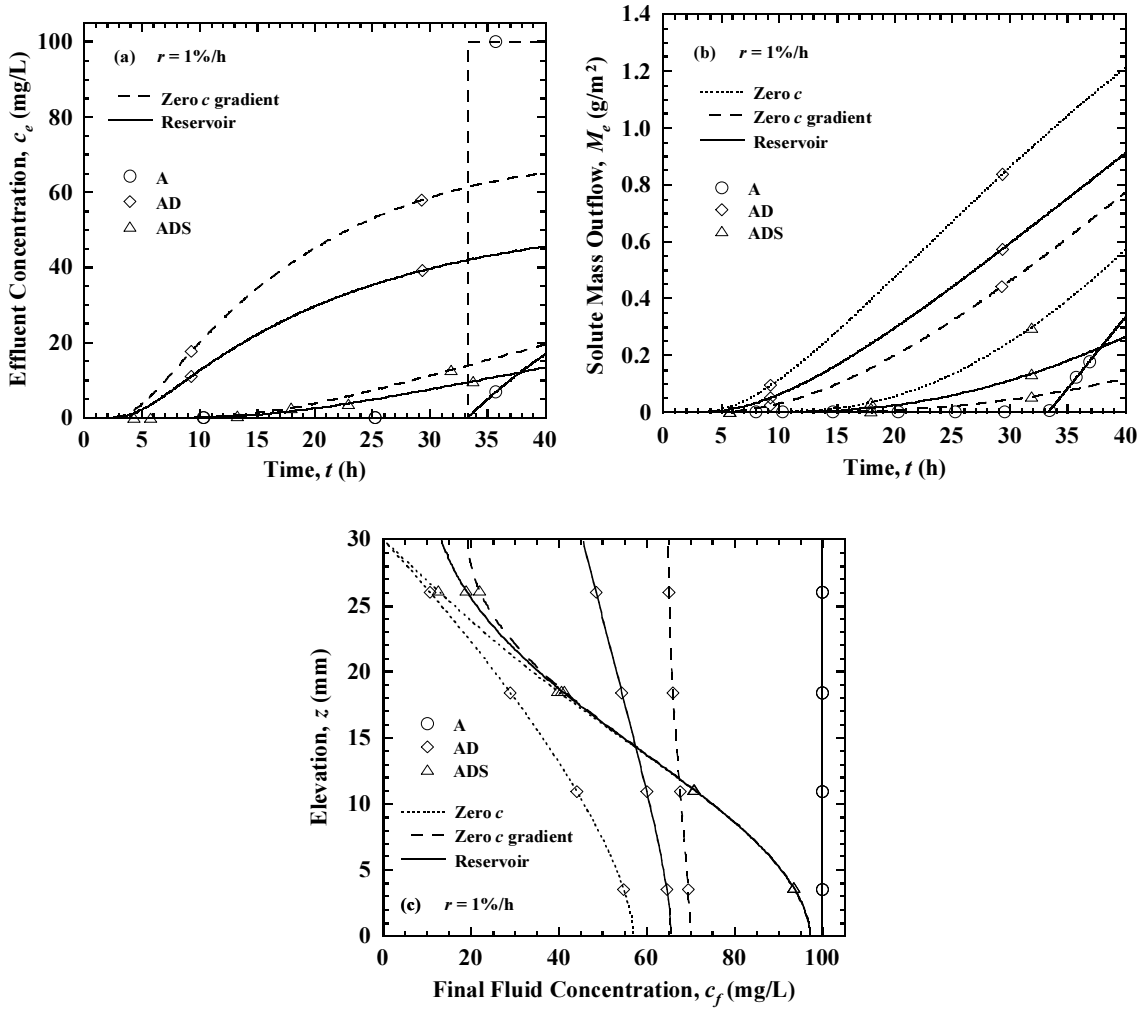

Figure 5.5 Simulations results for initial lower half contamination: (a) effluent concentrations; (b) solute mass outflows; (c) final fluid concentration profiles.

5.4.2.2 Effect of Strain Rate

AD and ADS simulations were performed for initial lower half contamination, a zero concentration gradient boundary, and three applied strain rates. The zero concentration gradient condition represents a case in which the effluent is drained away from the boundary upon exiting. Effluent concentrations, shown in Figure 5.6(a), are generally lower for higher strain rates due to less time available for upward dispersion

transport. The interesting exception is the reverse trend for AD at high r values, where larger seepage velocities produce greater dispersion and higher c_e despite the shorter test duration. The curves also indicate that higher strain rates cause solute breakthrough at a higher average strain. Final fluid concentration profiles in Figure 5.6(b) show larger gradients at higher strain rates due to less time available for solute redistribution by dispersion. The final concentration profile for AD with r = 0.2%/h is almost uniform, which is consistent with the nearly flat slope of the c_e curve at the end of consolidation in Figure 5.6(a). The ADS simulations again display larger concentration gradients due to sorption.

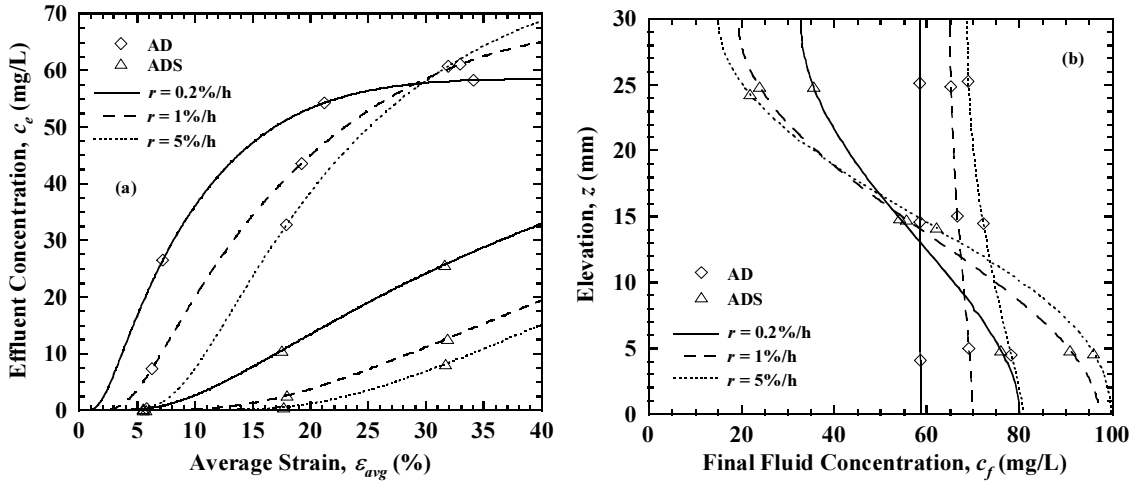

Figure 5.6 Simulation results for initial lower half contamination with zero concentration gradient boundary and three applied strain rates: (a) effluent concentrations; (b) final fluid concentration profiles.

Figure 5.7 presents a corresponding plot of M_{ef} / M_o versus r for five transport conditions. Results for the A, ADf, AD, and ADS simulations display similar trends to

those in Figure 5.4. However, the ADkS condition yields larger M_{ef} / M_o values than ADS at higher strain rates. Relative to equilibrium conditions, kinetic sorption becomes increasingly delayed at higher strain rates and this produces faster transport through the uncontaminated layer for the ADkS case. A corresponding plot (not shown) for a reservoir boundary condition shows trends very similar to Figure 5.7.

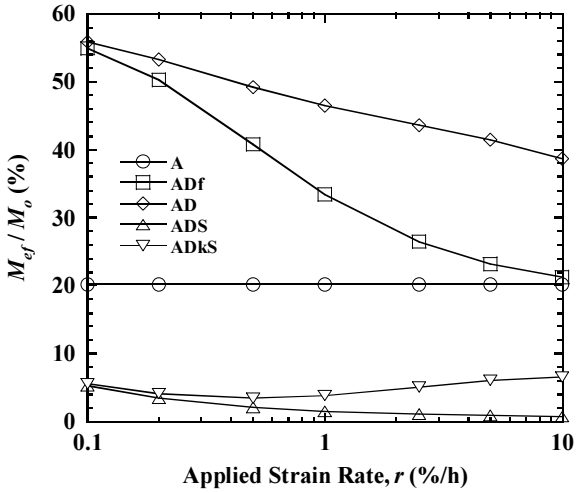

Figure 5.7 Effect of applied strain rate on final solute mass outflow for initial lower half contamination and zero concentration gradient boundary.

5.4.2.3 Effect of Initial Specimen Height

Figure 5.8 demonstrates the effect of initial height for specimens with lower half contamination. Simulations were performed for r = 1%/h, zero concentration gradient boundary, two transport conditions, and two initial specimen heights. The H_o (= 50 mm) simulations are the same as those previously shown in Figure 5.5 and the $2H_o$ (= 100 mm) simulations are identical except that the contaminated and uncontaminated layers are each initially twice as thick. Interestingly, Figure 5.8(a) indicates that larger

specimen height yields longer breakthrough and generally lower effluent concentrations even though both H_o and $2H_o$ specimens are consolidated to the same average strain at any given time.

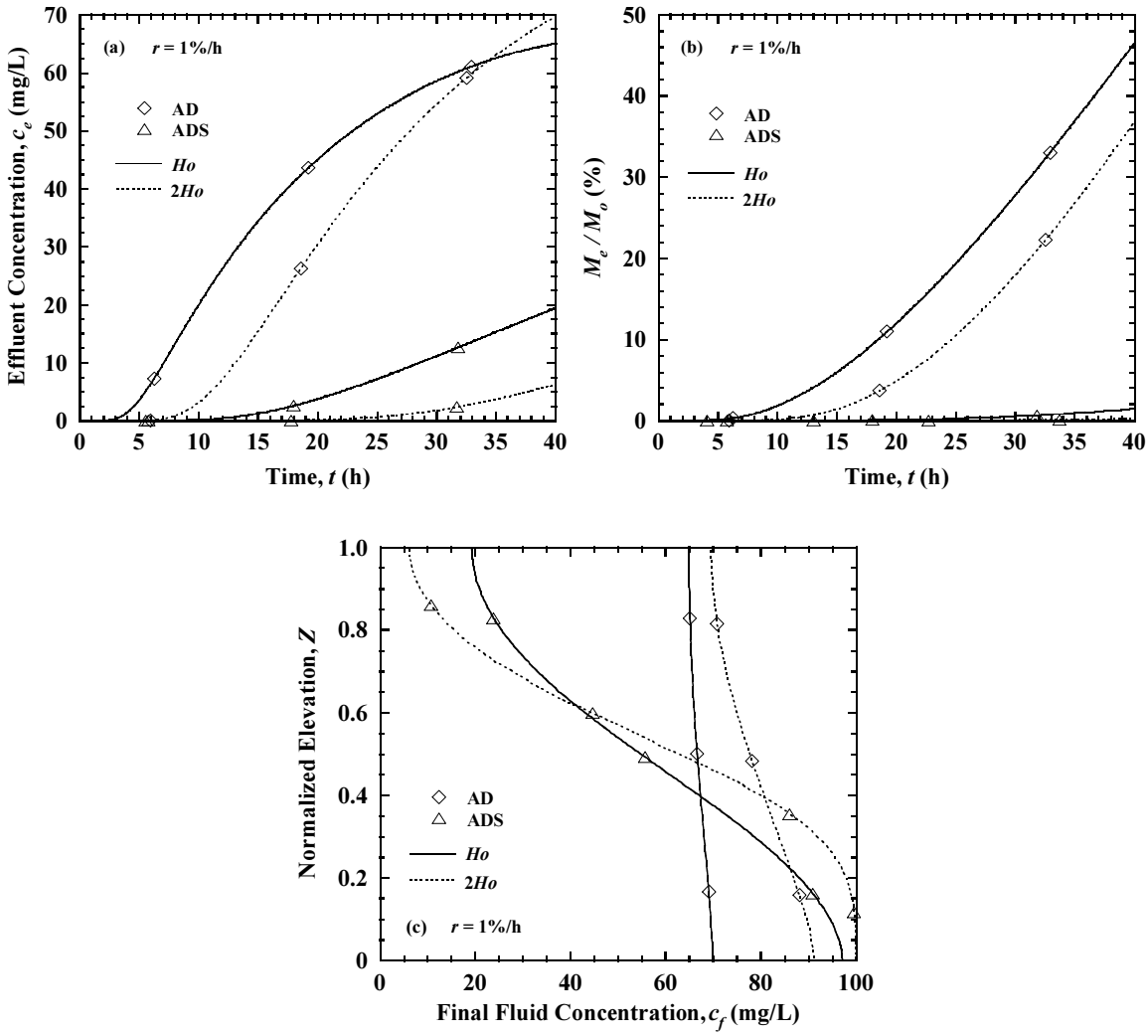

Figure 5.8 Simulation results for initial lower half contamination with zero concentration gradient boundary and two specimen heights: (a) effluent concentrations; (b) solute mass outflows; (c) final normalized fluid concentration profiles.

The corresponding plot for M_e / M_o in Figure 5.8(b) shows specimen height has an effect on solute mass outflow as well. For the AD case, 46% of the initial solute mass is transported out of the H_o specimen, whereas 37% is transported out of the $2H_o$ specimen. For ADS, final solute mass outflows are 1.5% and 0.28% for H_o and $2H_o$, respectively. Final normalized concentration profiles in Figure 5.8(c) show similar trends for the H_o and $2H_o$ specimens, with the ADS simulations again displaying larger gradients.

5.4.2.4 Effect of Boundary Drainage Condition

Several additional simulations were conducted to investigate the effect of boundary drainage conditions for initial lower half contamination with r = 1%/h. Single-drained (SD) simulations are the same as those in Figure 5.5 and double-drained (DD) simulations correspond to an identical specimen with drainage permitted at both boundaries ($h_b = h_t$ = 50 mm). Zero concentration gradients were maintained at all drainage boundaries. Settlements for SD and DD conditions are equal to those in Figure 5.2(a); however, internal seepage velocities and boundary fluid outflows vary greatly with drainage condition. Effluent concentrations, presented in Figure 5.9(a), show large differences for SD and DD simulations. The SD case shows solute breakthrough at the top boundary and a gradual increase in c_e thereafter. For the DD case, transport behavior is different for each drainage boundary. At the bottom boundary, c_e is initially equal to c_o and then decreases with time for both transport conditions. This decrease is much less for ADS than AD due to the reserve of sorbed mass in the contaminated layer.

At the top boundary, breakthrough occurs similar to the SD case; however, effluent concentrations are lower because of concurrent loss of solute at the bottom boundary.

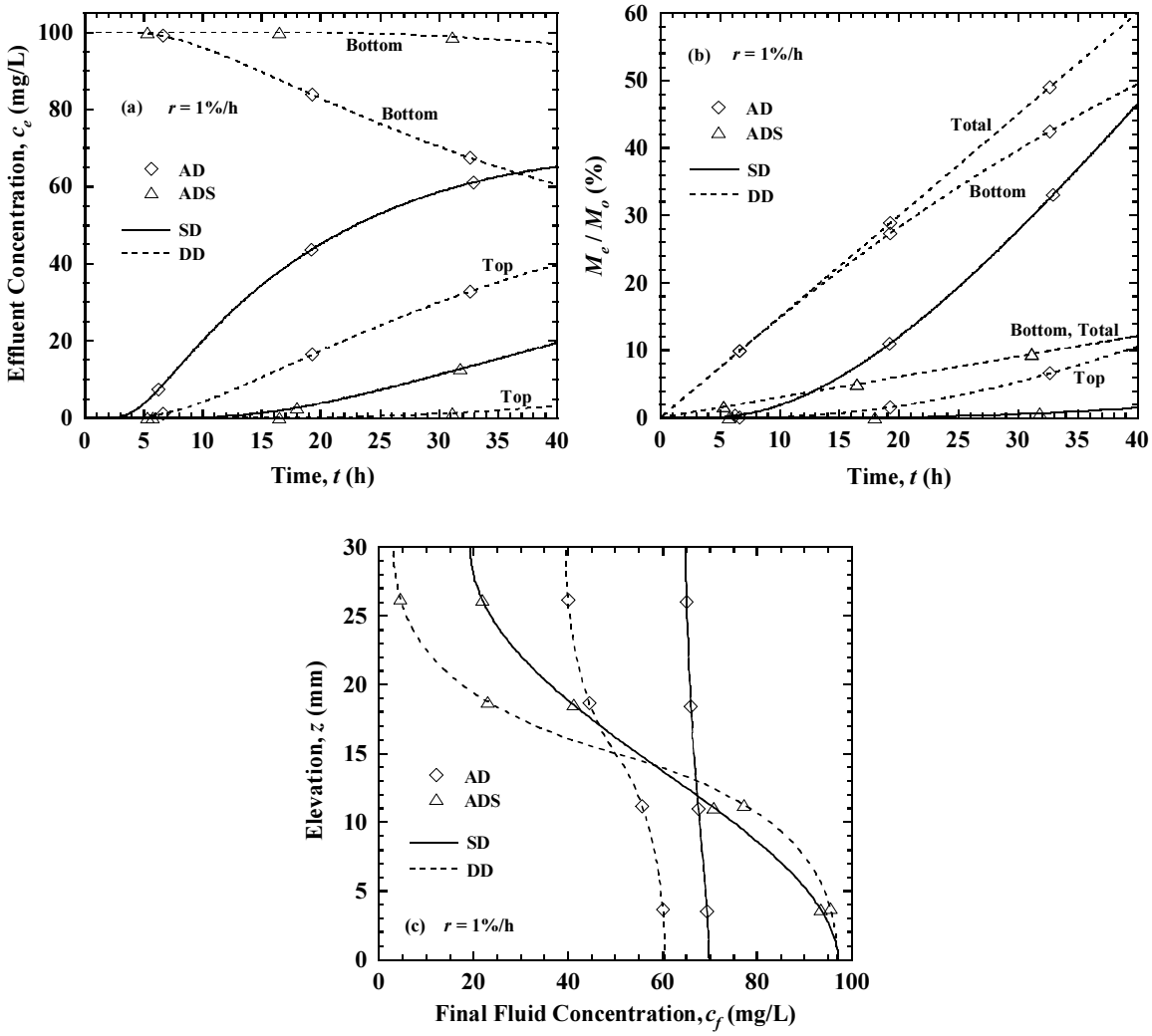

Figure 5.9 Simulations for initial lower half contamination with single- and double-drained conditions and zero concentration gradient boundaries: (a) effluent concentrations; (b) solute mass outflows; (c) final fluid concentration profiles.

Solute mass outflows are shown in Figure 5.9(b) and consistent with the c_e curves. The close proximity of the contaminated layer to the bottom boundary produces

higher outflows for the DD case. At the end of consolidation, total mass outflow for the AD condition is 60% for DD and 46% for SD. Corresponding values for ADS are 12% for DD and less than 2% for SD. Interestingly, final fluid concentration profiles in Figure 5.9(c) show higher gradients for the DD case for both AD and ADS transport conditions.

5.4.3 Initial Upper Half Contamination

5.4.3.1 Effect of Transport Condition

The last series of simulations was performed for a soil specimen initially contaminated in the upper half (z = 25 to 50 mm, c_o = 100 mg/L, s_o = 300 mg/kg) and uncontaminated in the lower half (z = 0 to 25 mm, c_o = s_o = 0). Transport parameters and boundary conditions are the same as Section 5.4.1. Figure 5.10 presents c_e values for CRS tests with r = 1%/h and three transport conditions. For advection only, c_e is initially equal to c_o and then makes a step decrease to zero at t = 33.3 h as the final solute leaves the specimen. The AD curve shows a significant decrease in c_e soon after the start of loading as dispersion moves solute downward, against the direction of advection, and into the uncontaminated layer. Effluent concentrations decrease more slowly for ADS because sorption delays this downward transport process. Figure 5.11 compares solute mass outflows for initial upper half and initial lower half contamination specimens and three transport conditions with r = 1%/h and a zero concentration gradient boundary. For each condition, the upper half specimen produces much larger mass outflows due to the shorter distance to the top drainage boundary.

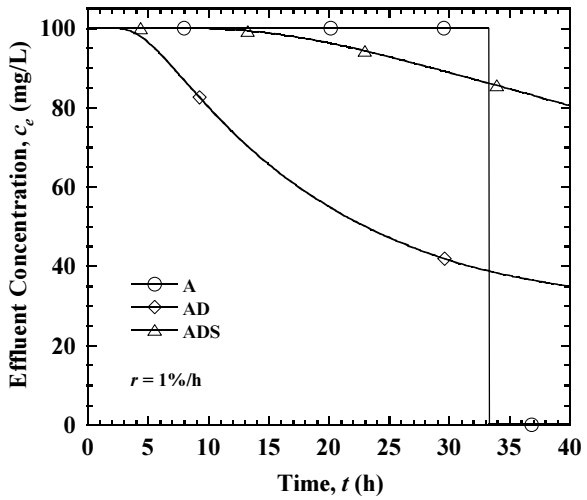

Figure 5.10 Effluent concentrations for initial upper half contamination with a zero concentration gradient boundary.

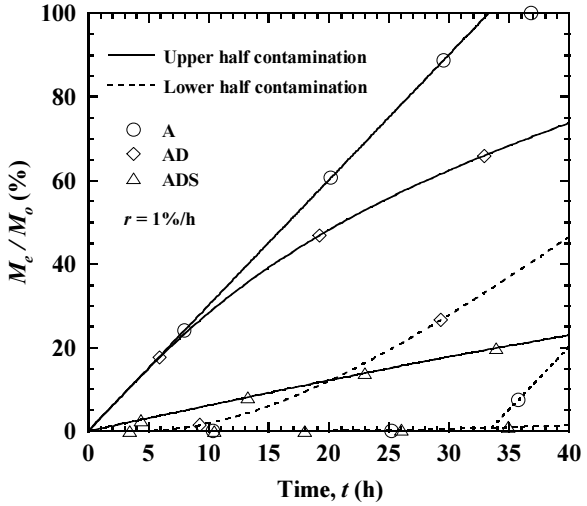

Figure 5.11 Solute mass outflows for specimens with initial upper half contamination and initial lower half contamination with a zero concentration gradient boundary.

5.4.3.2 Effect of Strain Rate

AD and ADS simulations were performed for initial upper half contamination, zero concentration gradient boundary, and three applied strain rates. Effluent concentrations, shown in Figure 5.12(a), are generally larger for higher strain rates d ue to less time available for downward dispersion transport and, similar to Figure 5.6(a), show a reverse trend for AD at high r values. Final fluid concentration profiles in Figure 5.12(b) again indicate smooth transitions between initially uncontaminated and contaminated layers and larger gradients for higher strain rates. Figure 5.13 presents a corresponding plot of M_{ef} / M_o versus r for five transport conditions. Several reverse trends are observed when compared to Figure 5.7. Solute mass is transported completely out of the specimen regardless of strain rate for advection only. For ADf, values of M_{ef} / M_o are significantly smaller at low strain rates and then increase to merge with the advection value at high r. At low r, mechanical dispersion is insignificant and ADf and AD yield nearly equal M_{ef} / M_o. Similar to Figure 5.7, the effects of dispersion do not vanish at high strain rates. When sorption is included, ADS and ADkS yield substantially smaller values of M_{ef} / M_o. For low r, kinetic effects are unimportant and M_{ef} / M_o is essentially the same, whereas at higher r ADkS produces slightly smaller values due to delayed desorption in the contaminated layer.

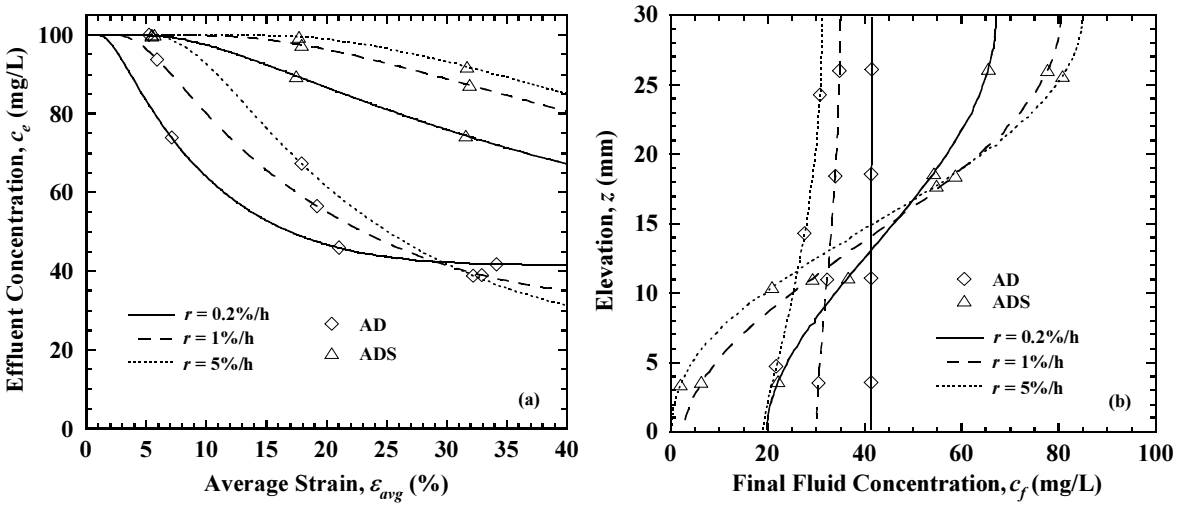

Figure 5.12 Strain rate effect for initial upper half contamination with zero concentration gradient boundary: (a) effluent concentrations; (b) final fluid concentration profiles.

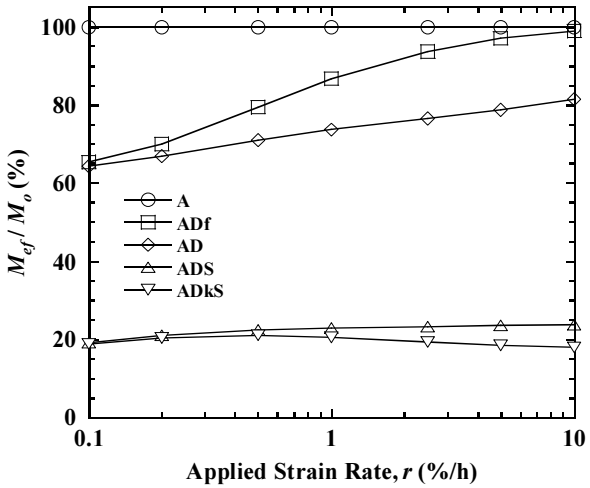

Figure 5.13 Effect of applied strain rate on final solute mass outflow for initial upper half contamination and zero concentration gradient boundary.

5.5 Acknowledgements

Chapter 5 of this dissertation is based on material published by the Journal of Geotechnical and Geoenvironmental Engineering titled “Consolidation-Induced Solute Transport for Constant Rate of Strain. I: Model Development and Simulation Results” with authors, Hefu Pu, and Patrick J. Fox (2014). The dissertation author is the first author of this paper.

Chapter 6

Comparison of Consolidation-Induced Solute Transport for Incremental Loading and Constant Rate of Strain Conditions

6.1 Introduction

Incremental loading (IL) and constant rate of strain (CRS) tests are widely used to measure the consolidation properties of fine-grained soils. When such soils are contaminated, consolidation causes transport, redistribution, and outflow of the contaminants. Consolidation-induced transport processes are similar to those for steady flow through rigid porous media and include advection, dispersion, and sorption. The

difference is that consolidation involves transient advective flows that are governed by the distribution of excess pore pressures. These flows produce volumetric strains that in turn, cause changes in soil porosity, compressibility, and hydraulic conductivity. To date, experimental and numerical research has been conducted to investigate consolidation-induced transport for IL conditions (Peters and Smith 2002; Fox 2007a,b; Lee and Fox 2009) and only very recently numerical research has been conducted for CRS conditions (Pu and Fox 2014); however, no studies have been conducted to compare consolidation-induced transport for IL and CRS. Such a study would be a useful addition to the literature and provide a better understanding of each process.

Fox and Berles (1997) published the numerical model CS2, including the original source code, for one-dimensional large strain consolidation of a homogeneous saturated soil layer with instantaneous surcharge loading. An enhanced version of CS2 was presented by Fox and Pu (2012) and includes time-dependent loading, unload/reload effects, and an external hydraulic gradient. Using the CS2 method, Fox (2007a) developed the model CST1 to simulate consolidation-induced solute transport for IL conditions. Fox and Lee (2008) upgraded CST1 to CST2, which also accounts for nonlinear sorption, nonequilibrium (kinetic) sorption, and a void ratio-dependent effective diffusion coefficient. Again using the CS2 method, Pu et al. (2013) developed CCRS1 to simulate large strain consolidation for CRS loading. Pu and Fox (2014) then combined CST2 and CCRS1 to produce CSTCRS1, the first model to simulate consolidation-induced solute transport for CRS. With the availability of CST2 and CSTCRS1, a comparative study of consolidation-induced solute transport for IL and CRS conditions is now possible. This chapter presents such an investigation and includes

numerical simulations to illustrate the effects of transport conditions, concentration boundary conditions, initial concentration distribution, initial layer height, multiple loading increments, and applied strain rate on consolidation-induced solute transport.

6.2 Numerical Models

CST2 (Fox and Lee 2008) and CSTCRS1 (Pu and Fox 2014) are numerical models that simulate coupled large-strain consolidation and solute transport for IL and CRS conditions, respectively. For each model, the consolidation algorithm is one-dimensional and accounts for vertical strain, soil self-weight, general constitutive relations, relative velocity of fluid and solid phases, changing hydraulic conductivity and compressibility during consolidation, time-dependent loading, unload/reload effects, and an external hydraulic gradient. Soil constitutive relationships are defined using discrete points and can take nearly any desired form. Soil compressibility is rate-independent and, as such, CST2 and CSTCRS1 are most appropriate for less structured soils. The solute transport algorithm accounts for advection, dispersion, equilibrium and nonequilibrium sorption, linear and nonlinear sorption isotherm, and void ratio-dependent effective diffusion coefficient. Solute transport is consistent with temporal and spatial variations of porosity and seepage velocity in the consolidating layer. The key to the transport model is the definition of two Lagrangian fields of elements that separately follow the motions of fluid and solid phases (Figure 6.1). This reduces numerical dispersion and simplifies transport calculations to that of dispersion mass flow between contiguous fluid elements (Fox 2007a). Transport conditions for the top and bottom

boundaries can be specified as prescribed concentration (Type I), prescribed concentration gradient (Type II), or prescribed solute mass flux (Type III). Figure 6.1 shows Type I conditions where the top and bottom boundaries are maintained at constant concentrations c_t and c_b. CST2 and CSTCRS1 can also accommodate a reservoir boundary, which represents an accumulating well-mixed aqueous reservoir formed by fluid outflow at the top boundary. Details regarding the development of CST2 and CSTCRS1 are provided by Fox (2007a,b), Fox and Lee (2008), and Pu and Fox (2014).

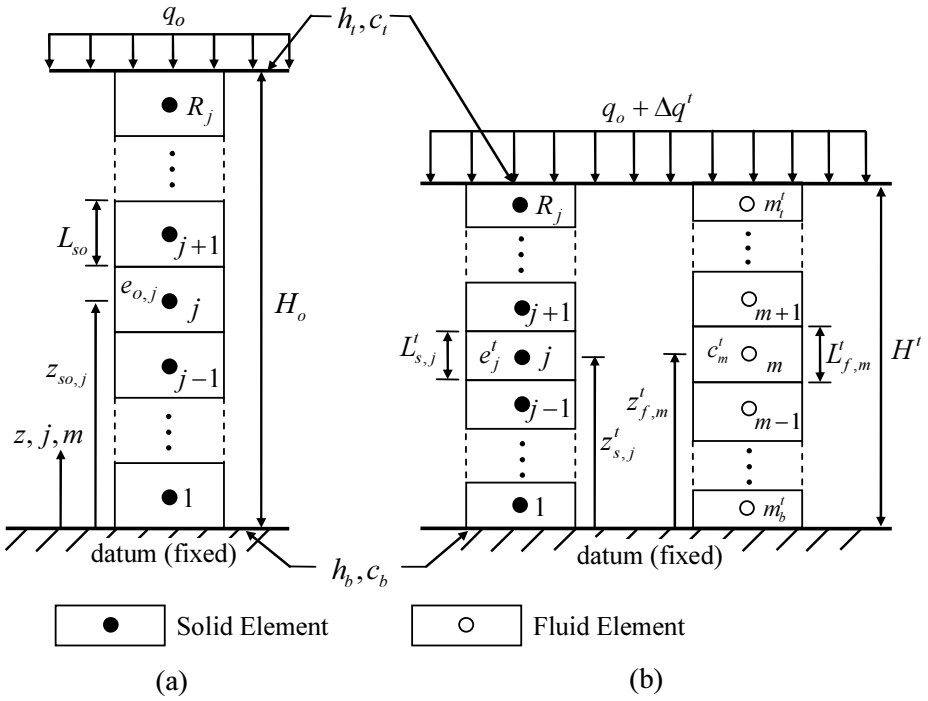

Figure 6.1 Geometry for CST2 and CSTCRS1: (a) initial configuration; (b) configuration during loading (see Fox and Lee 2008 for details).

6.3 Numerical Simulations

Numerical simulations were conducted using CST2 and CSTCRS1 to investigate solute transport during consolidation of kaolinite clay for IL and CRS conditions, respectively. The kaolinite specimens have variable initial height and a variable initial layered contamination profile. Material properties were taken from measurements by Lee and Fox (2009). The specific gravity of solids G_s = 2.61, liquid limit LL = 47.6, plasticity index PI = 21.8, and the Unified Soil Classification is CL, Lean Clay. Constitutive relationships for compressibility and hydraulic conductivity are,

$$e = e_o - C_c \log\left(\frac{\sigma'}{\sigma'_o}\right) \tag{6.1}$$

$$e = 8.16 + 0.765 \log\left(k(\text{m/s})\right) \tag{6.2}$$

where e_o = 2.0, C_c = compression index = 0.65, σ' = vertical effective stress, σ'_o = 5 kPa, and k = vertical hydraulic conductivity. Simulations were conducted for four transport conditions: (1) advection + diffusion (ADf), (2) advection + dispersion (AD), (3) advection + dispersion + equilibrium sorption (ADS), and (4) advection + dispersion + kinetic sorption (ADkS). Transport parameters are provided in Table 6.1. Although transport parameters are constant for each simulation, spatial and temporal changes in porosity and seepage velocity produce variations of hydrodynamic dispersion, retardation factor, and Peclet number during consolidation. Sorption is characterized using a linear equilibrium isotherm and can be in equilibrium or nonequilibrium with the associated fluid solute concentration. Contaminated layers within the specimens contain an unspecified solute with initial fluid concentration c_o = 100 mg/L and initial sorbed

concentration s_o = 300 mg/kg for ADS and ADkS simulations. The solid phase is represented using 200 solid elements and the fluid phase is represented using 200 fluid elements for simulations without sorption and 600 fluid elements for simulations with sorption. The bottom boundary is zero flux for both pore fluid and solute mass. The top boundary is drained and is modeled using one of three concentration conditions: (1) zero concentration, (2) zero concentration gradient, and (3) reservoir. The IL simulations were conducted for single load (SL) or multiple load (ML) conditions. The CRS simulations were performed at constant average strain rate r. For most CRS simulations, the average strain rate was chosen to give then same final strain as the corresponding SL or ML test in the same total time.

Table 6.1 Transport parameters for numerical simulations.

Transport condition	Effective diffusion coefficient D^* (m^2/s)	Longitudinal dispersivity α_L (m)	Distribution coefficient K_d (mL/g)	Sorption rate constant λ (1/s)
ADf (advection + diffusion)	9.37×10^{-10}	0	0	-
AD (advection + dispersion)	9.37×10^{-10}	0.02	0	-
ADS (advection + dispersion + equilibrium sorption)	9.37×10^{-10}	0.02	3	-
ADkS (advection + dispersion + kinetic sorption)	9.37×10^{-10}	0.02	3	1×10^{-5}

6.4 Results

6.4.1 Effect of Loading and Transport Conditions

The first series of simulations illustrate the effect of loading and transport conditions. Kaolinite specimens have initial height H_o = 50 mm, initial vertical effective stress at the top boundary q_o = 5 kPa, and a reservoir top boundary condition. Each specimen consists of an uncontaminated upper layer and a contaminated lower layer, both with an initial thickness of 25 mm. The initial void ratio distribution is nearly uniform, ranging from 2.0 at the top of the specimen to 1.99 at the bottom (variation due to self-weight). The SL simulations consist of an instantaneous stress increment Δq = 100 kPa that is applied to the specimen at time t = 0 and held constant for 12.91 h, giving a final average degree of consolidation U_{avg} = 99% and final average vertical strain ε_{avg} = 28.2%. The CRS simulations were conducted using r = 2.184%/h to produce the same final average strain at t = 12.91 h.

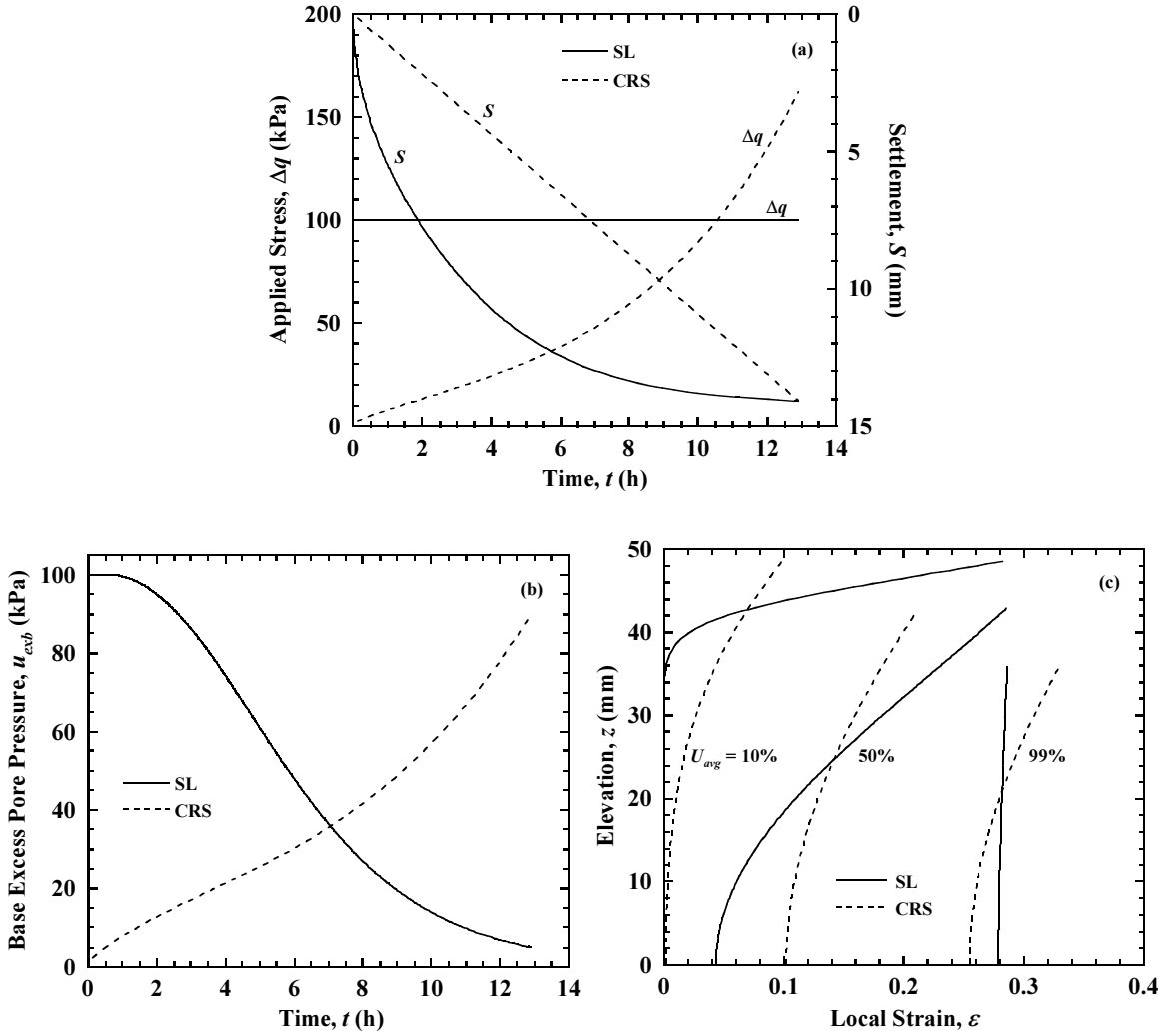

Figure 6.2 Simulation results for SL and CRS consolidation: (a) applied stress and settlement; (b) base excess pore pressure; (c) local strain.

Figure 6.2(a) shows settlement S and applied surcharge load Δq at the top boundary for the SL and CRS simulations. For SL, Δq is constant and S increases nonlinearly to a final value of 14.1 mm. For CRS, S increases linearly and Δq increases nonlinearly to a final value of 162.4 kPa. Settlement for SL is larger, and thus the total fluid outflow is also larger, than for CRS until the end of the simulations where

settlements are identical. Corresponding values of excess pore pressure at the base of the specimen u_{exb} are shown in Figure 6.2(b). For SL, u_{exb} is initially equal to the applied surcharge load (100 kPa) and then gradually decreases with time. For CRS, u_{exb} is initially zero and gradually increases with the applied stress. At t = 12.91 h, u_{exb} is 4.9 kPa and 89.4 kPa for SL and CRS, respectively. Figure 6.2(c) compares the local strain ε profiles for SL at U_{avg} = 10%, 50%, and 99%, and corresponding profiles for CRS taken at the same settlements. The ε profiles for SL and CRS are substantially different throughout the consolidation process. Figure 6.2 shows that SL and CRS conditions produce very different consolidation responses even though the total test duration and final average strain are the same for each.

Figure 6.3(a) presents cumulative solute mass outflow per unit area M_e for SL and CRS simulations with four transport conditions. First considering the SL relationships, ADf shows solute breakthrough at approximately t = 3 h with gradually increasing mass outflow to a value of 0.15 g/m^2 by the end of the simulation. The AD simulation includes mechanical dispersion and shows earlier breakthrough and substantially larger mass outflow. Seepage velocity v_s contributes to dispersion through the relationship,

$$D_L = D^* + \alpha_L v_s \tag{6.3}$$

where D_L = hydrodynamic dispersion coefficient, D^* = effective diffusion coefficient, and α_L = longitudinal (vertical) dispersivity. With upward drainage and concentration gradient, larger D_L produces faster solute transport to the top boundary for the AD case.

By comparison, breakthrough is longer and M_e is lower for ADS due to sorption in the initially uncontaminated layer. When kinetic sorption is specified (ADkS), mass outflow is initial coincident with the AD relationship but then is reduced in time as sorption takes effect. Interestingly, M_e decreases toward the end of the ADkS simulation as seepage velocities become small and solute mass is drawn back into the top layer from the overlying reservoir. The CRS relationships show similar trends but significantly different shapes due to differences in magnitude of seepage velocity over time. CRS yields later breakthrough than SL due to smaller effluent volume during the early stages of consolidation. However, CRS has higher effluent rates toward the end such that final M_e values are nearly the same as SL for each transport condition. Corresponding effluent concentrations, not shown for brevity, display similar trends to the M_e relationships in Figure 6.3(a).

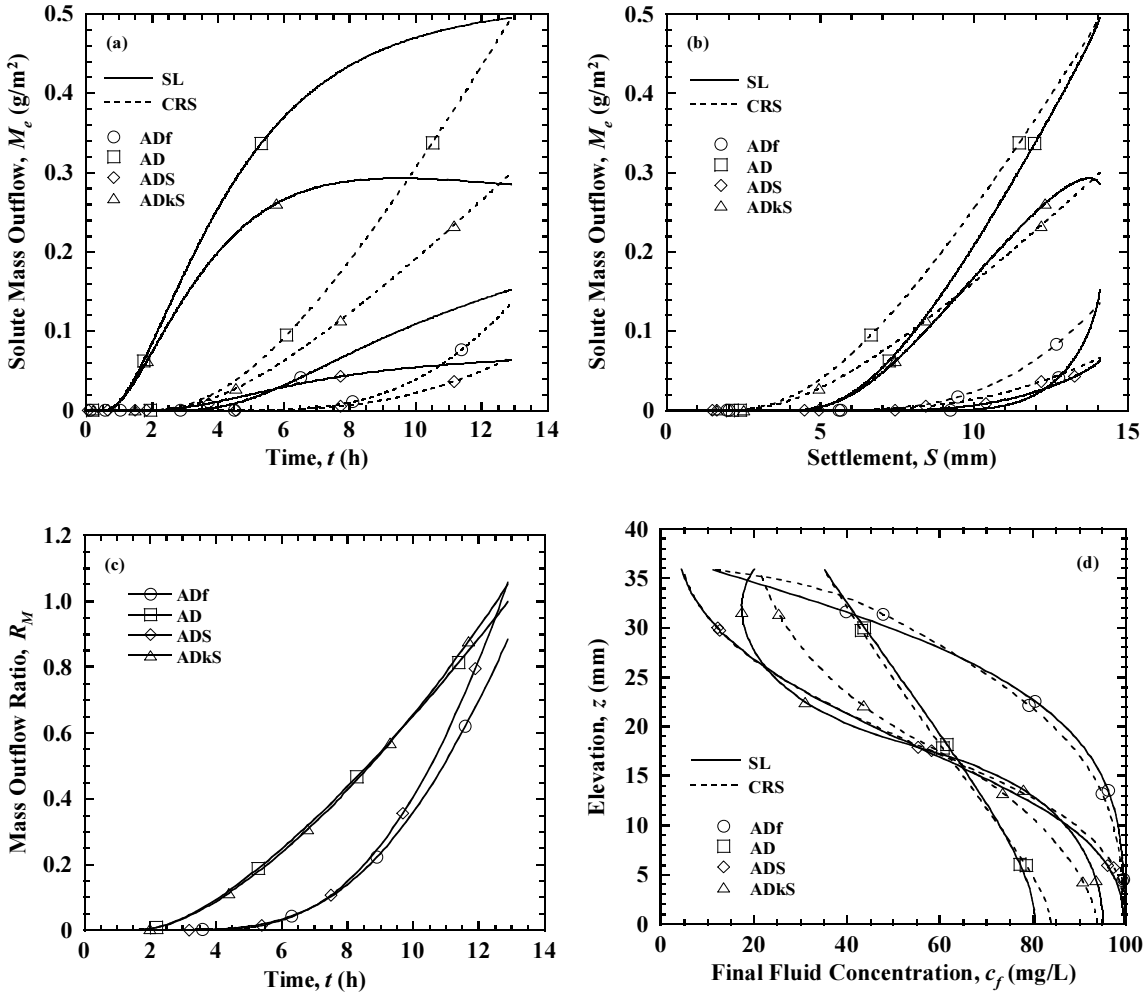

Figure 6.3 Simulation results for initial lower half contamination and reservoir boundary: (a) solute mass outflow versus time; (b) solute mass outflow versus settlement; (c) mass outflow ratio; (d) final fluid concentration.

When the same data is plotted versus settlement, as in Figure 6.3(b), the agreement for SL and CRS conditions is closer, with the AD and ADkS data grouping together and the ADf and ADS data grouping together as well. Interestingly, these data groupings are even closer in Figure 6.3(c), which shows mass outflow ratio R_M versus time where

$$R_M = \frac{M_e(\text{CRS})}{M_e(\text{SL})} \tag{6.4}$$

For each transport condition, R_M increases with time and reaches a value of approximately 1.0 by the end of the simulation. Final values of mass outflow ratio R_{Mf} are 0.89 for ADf, 1.00 for AD, 1.06 for ADS, and 1.05 for ADks. Final fluid concentration c_f profiles are shown in Figure 6.3(d). SL and CRS yield similar c_f profiles for ADf, AD, and ADS although the rate of settlement and profiles of excess pore pressure and local strain are significantly different during consolidation. Final concentration profiles for ADkS show greater differences between SL and CRS loading conditions with SL producing a higher concentration gradient within the specimen and, consistent with the ADkS relationship in Figure 6.3(a), a reverse trend near the top due to delayed sorption in the uncontaminated layer.

Additional simulations were conducted to investigate the effects of dispersivity α_L and sorption rate constant λ. Figure 6.4 shows R_{Mf} as a function of α_L for AD conditions. Starting at 0.89 for α_L = 0 (ADf), R_{Mf} increases with increasing α_L and indicates that M_{ef} values for SL and CRS are essentially equal for α_L > 10 mm. Figure 6.5 shows M_{ef} as a function of λ for ADkS conditions. M_{ef} decreases with increasing λ due to greater sorption in the uncontaminated layer and is nearly the same for IL and CRS conditions. Values approach the AD case for small λ and the ADS case for large λ.

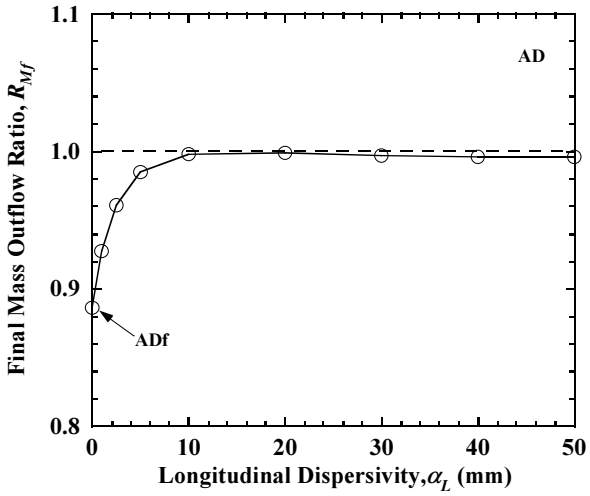

Figure 6.4 Effect of dispersivity on final mass outflow ratio for AD transport condition.

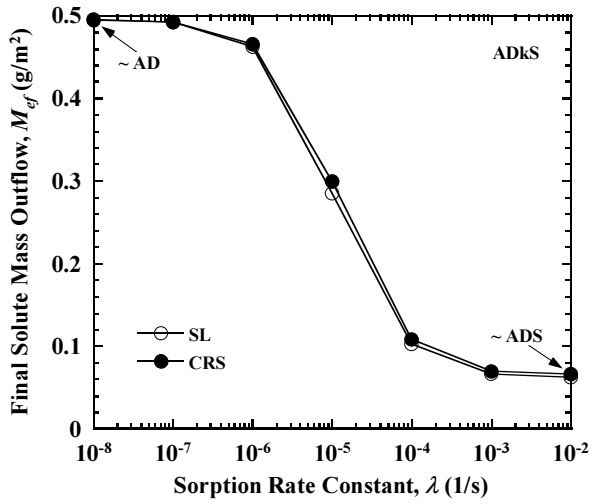

Figure 6.5 Effect of sorption rate constant on final solute mass outflow for ADkS transport condition.

6.4.2 Effect of Concentration Boundary Condition

AD and ADS simulations were performed for lower half contaminated specimens with reservoir, zero concentration, and zero concentration gradient conditions at the top boundary. Other parameters and conditions were unchanged from the previous simulations. M_e relationships and final concentration profiles are shown in Figure 6.6. Similar to Figure 6.3(a), mass outflows for SL are consistently larger than for CRS until the end of each simulation where the values are nearly equal. The highest outflows occur for the zero concentration boundary and the lowest outflows occur for the zero concentration gradient boundary. The ADS case produces longer breakthrough times and lower M_e values for all boundary conditions. The c_f profiles for AD are similar for SL and CRS, with the largest differences occurring for the zero concentration gradient condition. The zero concentration boundary condition produces the largest average concentration gradient, which is consistent with the highest mass outflow in Figure 6.6(a). Interestingly, c_f profiles for the ADS case (Figure 6.6(d)) are nearly identical for all three boundary conditions; although slight differences at the top are consistent with the trend of solute mass outflows in Figure 6.6(c). For AD, R_{Mf} values are 1.00 for reservoir, 0.98 for zero concentration, and 1.14 for zero concentration gradient condition. For ADS, the corresponding values are 1.06, 1.09, and 1.40, respectively.

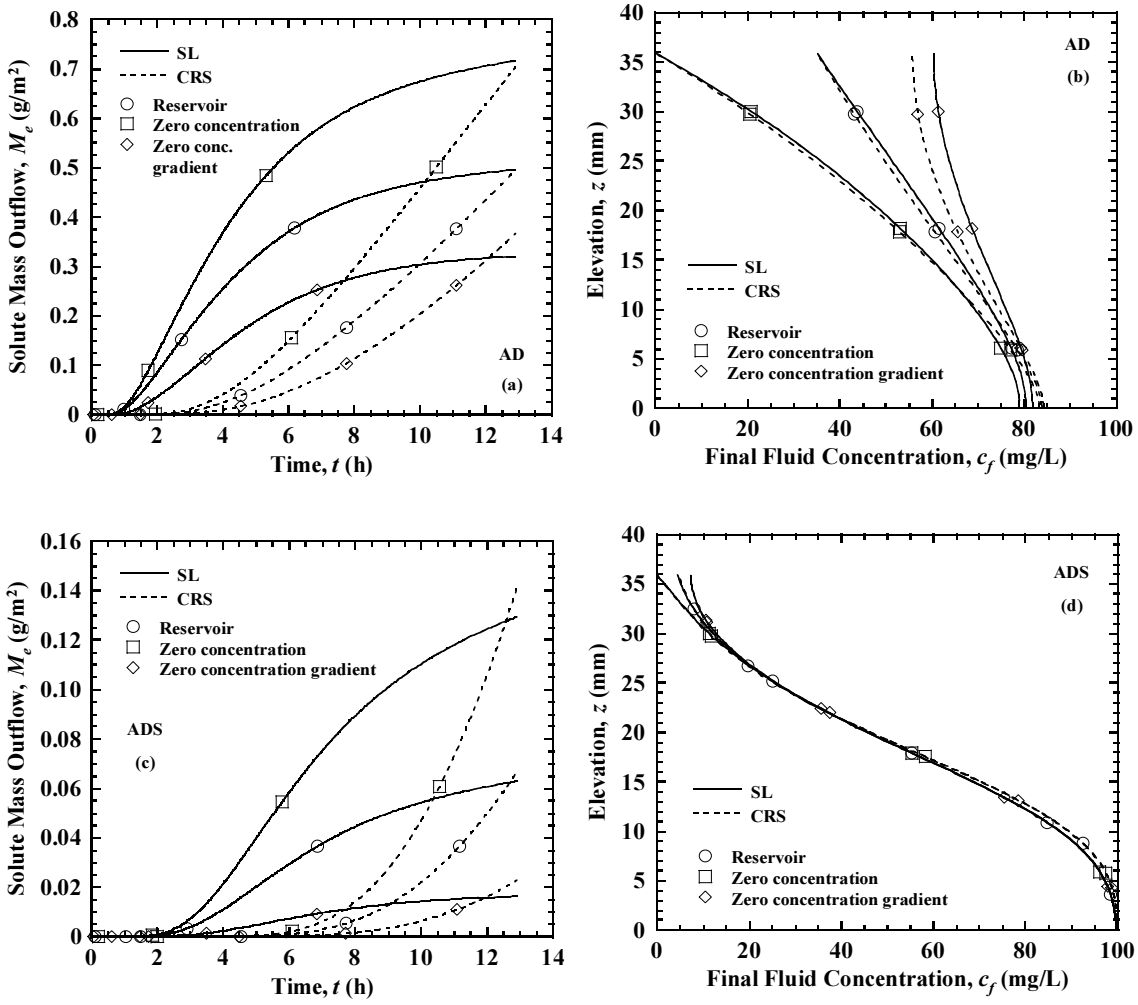

Figure 6.6 Effect of concentration boundary condition for initial lower half contamination: (a) solute mass outflow for AD; (b) final fluid concentration for AD; (c) solute mass outflow for ADS; (d) final fluid concentration for ADS.

6.4.3 Effect of Initial Concentration Distribution

Figure 6.7 presents results from simulations similar to those in Figure 6.3 but with the lower layer initially uncontaminated and the upper layer initially contaminated. Solute mass outflows, shown in Figure 6.7(a), are several times larger than for lower half contamination and breakthrough occurs immediately because the contaminated layer is

contiguous to the top boundary. Mass outflows are again consistently larger for SL than for CRS during consolidation until both relationships reach nearly the same final values. R_{Mf} is 1.01 for ADf, 1.00 for AD, 1.00 for ADS, and 0.98 for ADkS. Final concentration profiles, shown in Figure 6.7(b), are similar for SL and CRS, with the ADkS condition again displaying the greatest differences due to delayed sorption effects. AD shows the most nearly uniform c_f values due to high levels of dispersion that transport solute downward, against advection, and into the uncontaminated layer. Fluid concentrations are less uniform for ADS because sorption delays this downward transport process. Interestingly, ADf shows the least uniform profile, which indicates that diffusion alone is relatively ineffective for transporting solute against advection under these conditions.

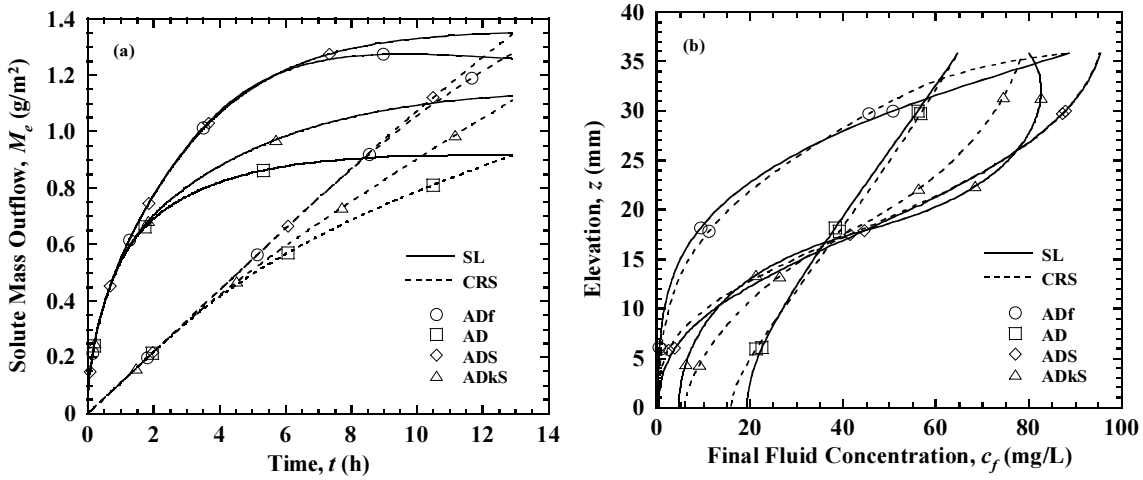

Figure 6.7 Simulation results for initial upper half contamination with reservoir boundary: (a) solute mass outflow; (b) final fluid concentration.

Figure 6.8 shows M_e relationships for the case of initial uniform contamination for the entire specimen. For a reservoir top boundary, transport parameters have no effect on solute mass outflow and M_e relationships are proportional to volumetric fluid outflow regardless of transport conditions. As such, at the end of the simulations, mass outflows for SL and CRS are exactly the same. Corresponding c_f profiles (not shown) indicate that concentrations remain unchanged (c_f = 100 mg/L) over the entire layer height for all simulations. The results in Figure 6.8 are also applicable for a zero concentration gradient boundary. However, differences in M_e and c_f profiles are observed for initial uniform contamination when the top boundary is zero concentration (Pu and Fox 2014).

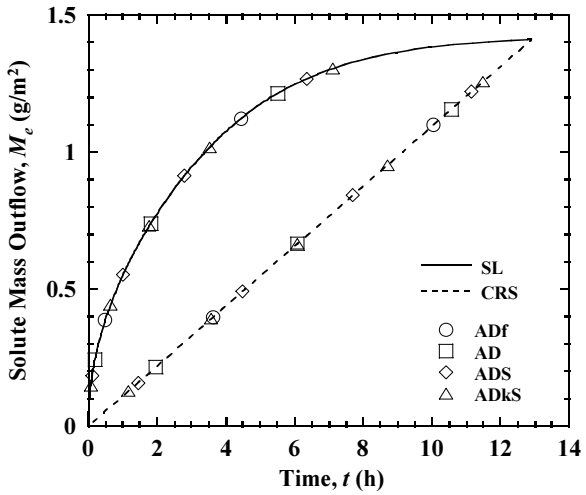

Figure 6.8 Solute mass outflow for initial uniform contamination with reservoir boundary.

6.4.4 Effect of Initial Specimen Height

Simulations were performed to investigate the effect of initial specimen height for initial lower half contamination, AD and ADS conditions, and a reservoir top boundary. The H_o (= 50 mm) simulations are the same as those in Figure 6.3 and the $2H_o$ (= 100 mm) simulations are identical except that the contaminated and uncontaminated layers are each initially twice as thick. The $2H_o$ SL specimen reached S = 28.04 mm at t = 51.73 h, which corresponds to U_{avg} = 99% and ε_{avg} = 28.04%. The slightly lower value of ε_{avg} as compared to the H_o case results from material self-weight and a slightly lower average initial void ratio. The CRS simulations were conducted using r = 0.54%/h to produce the same final ε_{avg} at t = 51.73 h. M_e relationships and final concentration profiles are shown in Figure 6.9. For AD conditions, the $2H_o$ specimen shows the same relative trends between SL and CRS as the H_o specimen and approximately 50% higher mass outflow. Mass outflow does not increase proportional to thickness for the $2H_o$ specimen because the longer transport distance reduces the average concentration gradient. However, for ADS, the $2H_o$ specimen produces less than one-half of the mass outflow for the H_o specimen. This indicates the strong effect of sorption in the uncontaminated layer. Final concentration profiles display close agreement between SL and CRS for both specimen heights and transport conditions. Exit concentration gradients are smaller for ADS, which is consistent with the lower solute mass outflows.

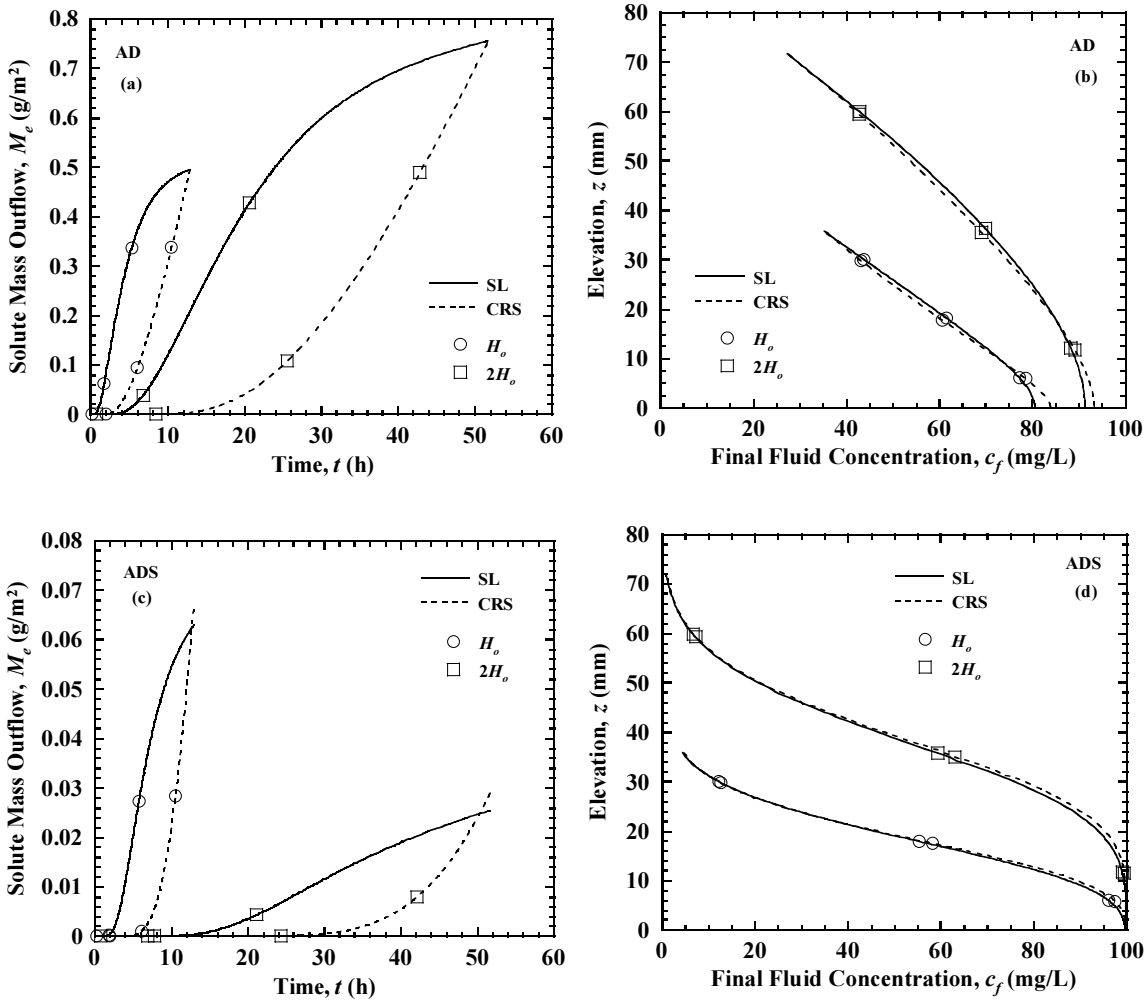

Figure 6.9 Effect of specimen height for initial lower half contamination and reservoir boundary: (a) solute mass outflow for AD; (b) final fluid concentration for AD; (c) solute mass outflow for ADS; (d) final fluid concentration for ADS.

6.4.5 Effect of Multiple Load Increments

A final set of simulations was performed for SL, ML, and CRS conditions with initial lower half contamination and a reservoir top boundary. The SL results are equal to those in Figure 6.3 (Δq = 100 kPa), except that the load increment duration was increased to 96 h. ML simulations were conducted using four load increments (Δq =

12.5 – 25 – 50 – 100 kPa), each with a duration of 24 h, to give a total applied stress of 100 kPa and a total time of 96 h. The SL and ML simulations produced equal values of final average strain (ε_{avg} = 28.5%) and CRS simulations were conducted using r = 0.30%/h to produce the same value at t = 96 h. Additional CRS simulations were conducted using higher strain rates $2r$ = 0.6%/h and $4r$ = 1.2%/h to produce ε_{avg} = 28.5% at 48 h and 24 h, respectively. Figure 6.10 presents plots of applied stress, settlement, and base excess pore pressure for each loading condition. Relationships for applied stress (Figure 6.10(a)) vary significantly from step loading for SL and ML to progressive increase for the CRS tests. The final value of applied stress increases with increasing strain rate for CRS. Settlement relationships (Figure 6.10(b)) show significant differences as well. Although final settlement is the same in each case, the initial rate of settlement is highest for SL and lowest for CRS with r = 0.30%/h. Base excess pore pressures are likewise significantly different and indicate a single large spike for SL, intermittent spikes for ML, and a gradual increase for CRS, depending on strain rate. Base excess pore pressures for ML show progressively higher peak values and indicate that consolidation was completed for each load increment. Advective flows are therefore intermittent and highly variable over the course of the SL and ML simulations.

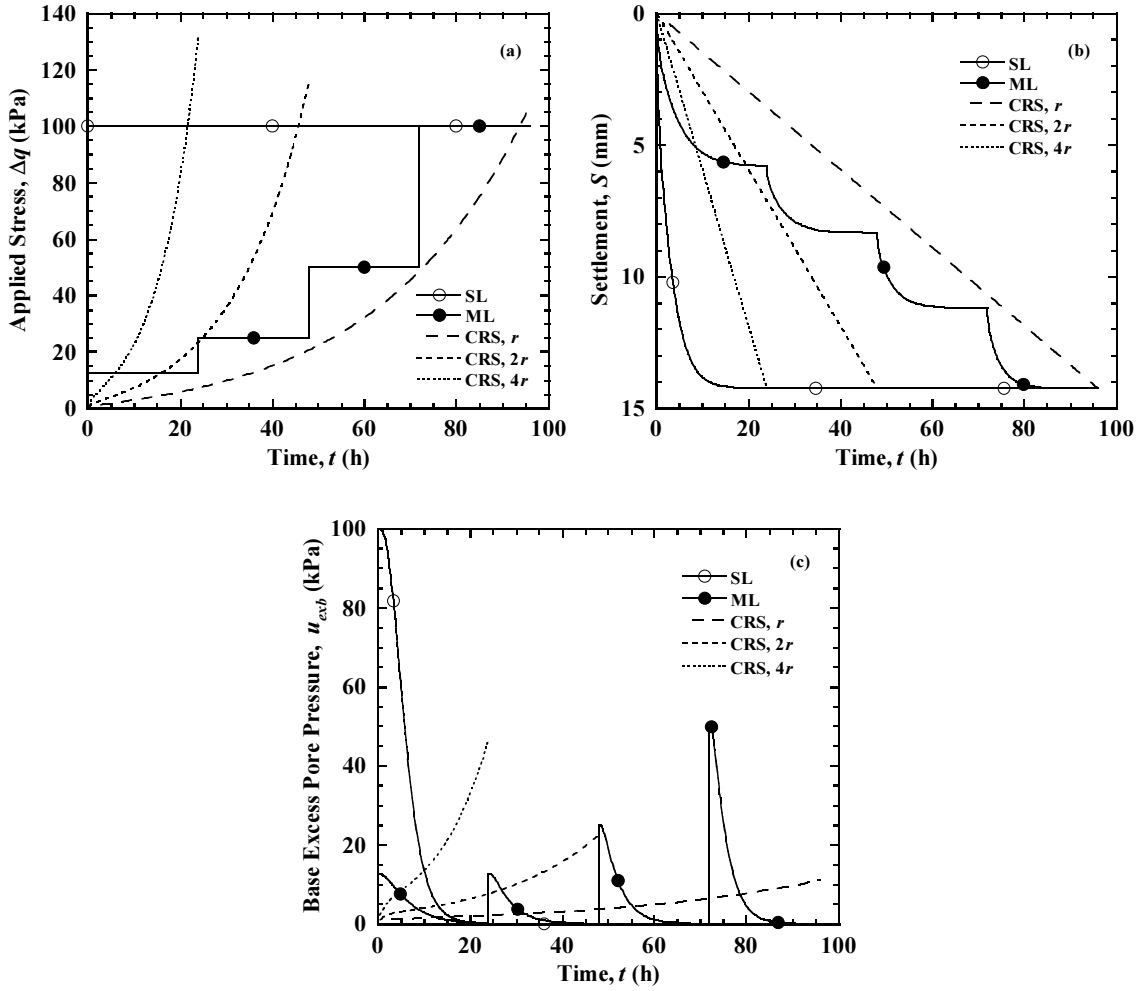

Figure 6.10 Simulation results for SL, ML, and CRS conditions with initial lower half contamination and reservoir boundary: (a) applied stress; (b) settlement; (c) base excess pore pressure.

Figure 6.11 compares solute mass outflows and final concentration profiles for AD, ADS, and ADkS transport conditions. First considering AD conditions (Figure 6.11(a)), the SL simulation indicates a sharp rise in M_e during the initial period of rapid advection, followed by a nearly constant (slightly decreasing) rate of outflow due to ongoing upward diffusion after the advection process has completed. The ML simulation shows the effect of intermittent advection, similar to the corresponding settlement in

Figure 6.10(b), and continuing diffusion outflow during periods of essentially zero advection. Mass outflow for the CRS simulation at strain rate r shows a gradual rise similar to Figure 6.3(a) and has almost the same final value as the SL and ML tests at t = 96 h. When the strain rate for CRS is increased to $2r$ and $4r$, mass outflow rises faster but to smaller final values because less time is available for dispersion transport. Fascinatingly, the final mass outflows for $2r$ and $4r$ fall almost exactly on the SL M_e relationship. This suggests that, for these conditions, solute mass outflow is largely governed by the total time and final average strain and is relatively independent of the specific loading condition used to consolidate the specimen. Corresponding relationships for ADS (Figure 6.11(b)) display smaller M_e values due to sorption but the same general trends. The ADkS relationships (Figure 6.12(a)) are particularly interesting. Similar to Figure 6.11(a), the SL simulation initially produces a sharp rise in mass outflow. This is followed by a significant decrease due to delayed sorption in the uncontaminated layer that draws solute back into the specimen from the overlying reservoir. Final solute mass outflows for SL, ML and CRS are again nearly equal at t = 96 h and the CRS outflows for $2r$ and $4r$ again fall close to the SL M_e relationship.

Corresponding final concentration profiles are shown in Figure 6.11(b), Figure 6.12(b), and Figure 6.13(b). For the AD condition, the SL, ML, and CRS r profiles are nearly identical. As the average strain rate is increased to $2r$ and $4r$, the CRS profiles show progressive deviations because of less time available for the solute redistribution by dispersion within the specimen. The profiles converge when equilibrium sorption is included (ADS) and are nearly identical when kinetic sorption is taken into account.

Again, interestingly, final concentration profiles for both sorption cases are nearly independent of the loading condition or average strain rate.

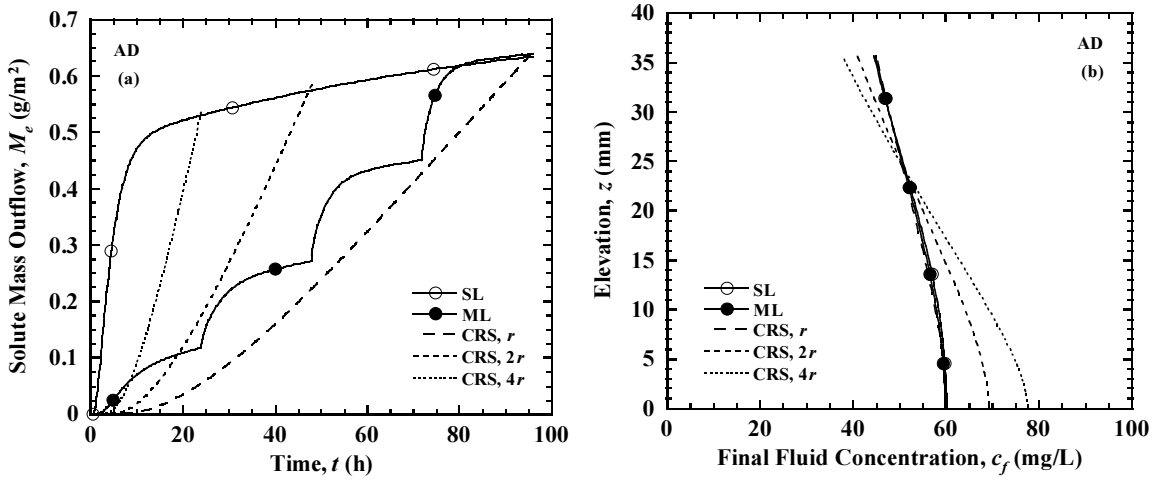

Figure 6.11 Simulation results for SL, ML, and CRS conditions with initial lower half contamination and reservoir boundary for AD: (a) solute mass outflow; (b) final fluid concentration.

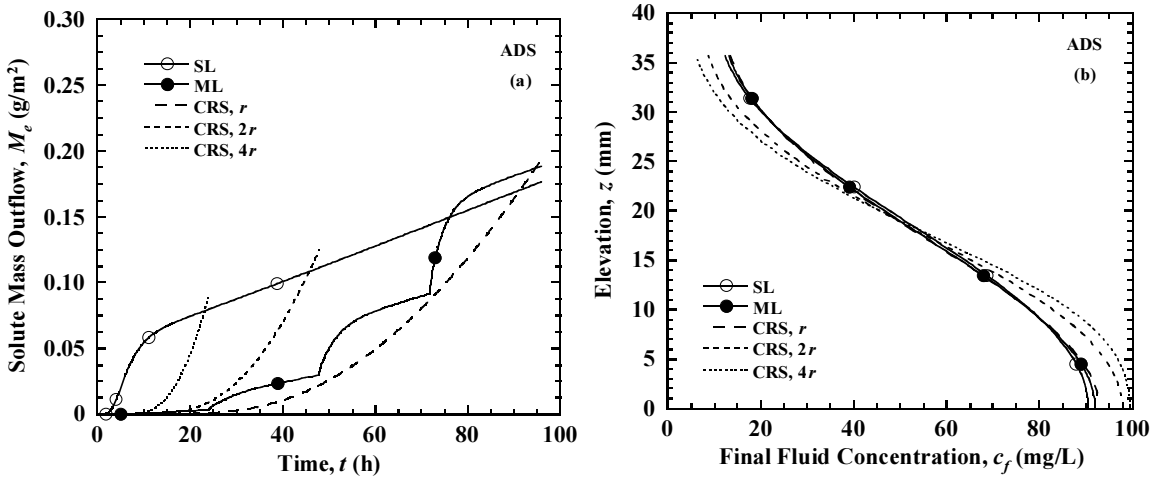

Figure 6.12 Simulation results for SL, ML, and CRS conditions with initial lower half contamination and reservoir boundary for ADS: (a) solute mass outflow; (b) final fluid concentration.

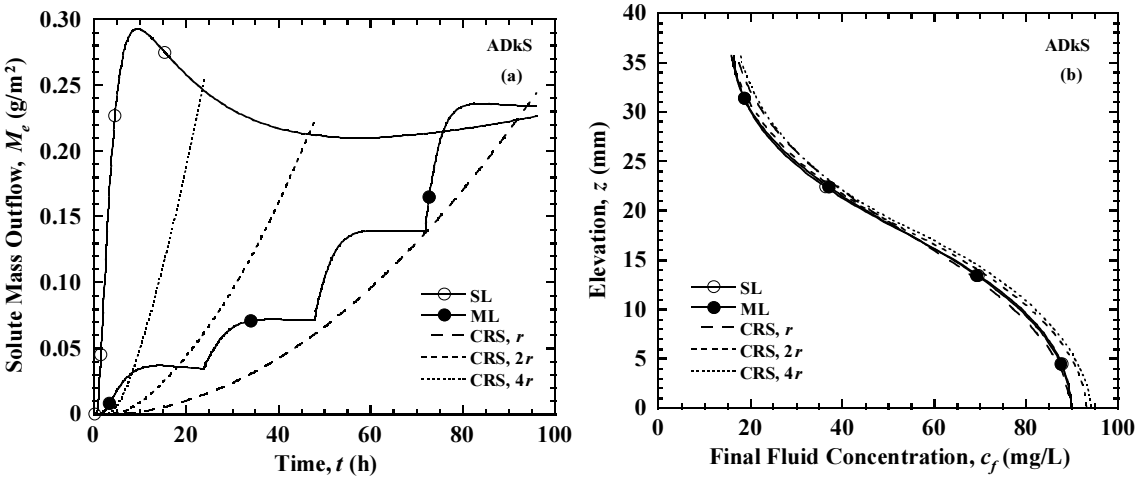

Figure 6.13 Simulation results for SL, ML, and CRS conditions with initial lower half contamination and reservoir boundary for ADkS: (a) solute mass outflow; (b) final fluid concentration.

6.5 Acknowledgements

Chapter 6 of this dissertation is based on material published by the Journal of Geotechnical and Geoenvironmental Engineering titled “Consolidation-Induced Solute Transport for Constant Rate of Strain. II: Comparison with Incremental Loading” with authors, Patrick J. Fox and Hefu Pu (2014). The dissertation author is the second author of this paper.

Chapter 7

Consolidation-Induced Contaminant Transport through Compacted Clay Liner Systems

7.1 Introduction

As noted in Chapter 2, there lacks a consensus with regard to the effect of compacted clay liner (CCL) consolidation on contaminant transport for CCL-based landfill liner systems. This chapter presents a comprehensive numerical investigation of the significance of this effect for single CCL and composite GML/CCL liners using realistic liner configurations, material properties, and loading schedules. Numerical simulations were conducted using the CST2 numerical model for coupled large strain consolidation-induced transport (Fox and Lee 2008). The CST2 model is first described, followed by a comparison of numerical simulation results for two CCL-based liner

systems and three analysis methods. A parametric study is presented to examine the influence of liner thickness, load magnitude, loading time, organic carbon fraction, and effective diffusion coefficient exponent on short-term and long-term transport through a CCL. Errors associated with traditional advective-diffusive analysis methods are discussed and a simplified advective-diffusive analysis method is proposed that can be used to partially compensate for the effect of CCL consolidation on resulting contaminant transport through a CCL-based liner system.

7.2 Numerical Model

CST2 is a numerical model for the simulation of coupled large strain consolidation and contaminant transport in saturated soil. Based on the CS2 method (Fox and Berles 1997), the consolidation algorithm for CST2 is one-dimensional and accounts for vertical strain, soil self-weight, general constitutive relationships, relative velocity of fluid and solid phases, changing hydraulic conductivity and compressibility during consolidation, time-dependent loading, unload/reload effects, and an external hydraulic gradient. Soil constitutive relationships are defined using discrete points and can take nearly any desired form. The contaminant transport algorithm accounts for advection, diffusion, mechanical dispersion, equilibrium and nonequilibrium sorption, linear and nonlinear sorption isotherm, and an effective diffusion coefficient that changes with soil porosity. Contaminant transport is consistent with temporal and spatial variations of porosity and seepage velocity in the consolidating soil. The key to the transport algorithm is the definition of two Lagrangian fields of elements that separately follow the

motions of fluid and solid phases. This reduces numerical dispersion and simplifies transport calculations to that of dispersion mass flow between contiguous fluid elements (Fox 2007a). Transport conditions for the top and bottom boundaries can be specified as prescribed concentration (Type I), prescribed concentration gradient (Type II), or prescribed solute mass flux (Type III). CST2 can also accommodate a reservoir boundary, which represents an accumulating well-mixed aqueous reservoir formed by fluid outflow at the top boundary.

7.3 Numerical Simulations

CST2 was used to evaluate the significance of consolidation-induced transport for two CCL-based landfill liner systems: a single CCL and a composite GML/CCL. The initial geometry for each is illustrated in Figure 7.1. The single CCL system consists, from top to bottom, of a leachate collection system (LCS), CCL, and subgrade layer. The initial height of the CCL is H_o. The subgrade can represent an underlying leachate detection layer or a natural soil subgrade. The top boundary of the CCL is drained and subjected to a constant leachate head of 0.3 m from the overlying LCS. The bottom boundary is also drained and subjected to constant atmospheric pressure from the underlying subgrade. Simulations for the single CCL can also approximate transport for a composite GML/CCL liner with a heavily damaged GML (i.e., many defects) or a GML with fewer defects but high transmissivity at the GML/CCL interface. The geometry for the composite GML/CCL system is identical to the single CCL with the addition of a 1.5 mm-thick intact high density polyethylene (HDPE) GML. The top

boundary of the CCL is undrained in this case. Leachate for both systems contains a volatile organic compound (VOC) that has constant concentration c_o and is sufficiently dilute so as to not alter properties of the CCL. Both CCLs are initially uncontaminated and have zero concentration at the base (constant). The bottom concentration condition ($c = 0$) allows for diffusion across the interface and results in the highest (i.e., most conservative) estimate of contaminant mass flux. For both systems, the VOC undergoes advective-diffusive transport through the CCL with sorption according to the organic carbon content of the clay. For the GML/CCL system, the VOC undergoes diffusion transport through the GML prior to reaching the CCL. Semipermeable membrane effects (e.g., solute restriction, chemico-osmosis) have been found to be negligible in engineered barriers comprised primarily of low activity clay minerals or absent of bentonite as a component (Kang and Shackelford 2010, Shackelford 2013) and are neglected for both systems.

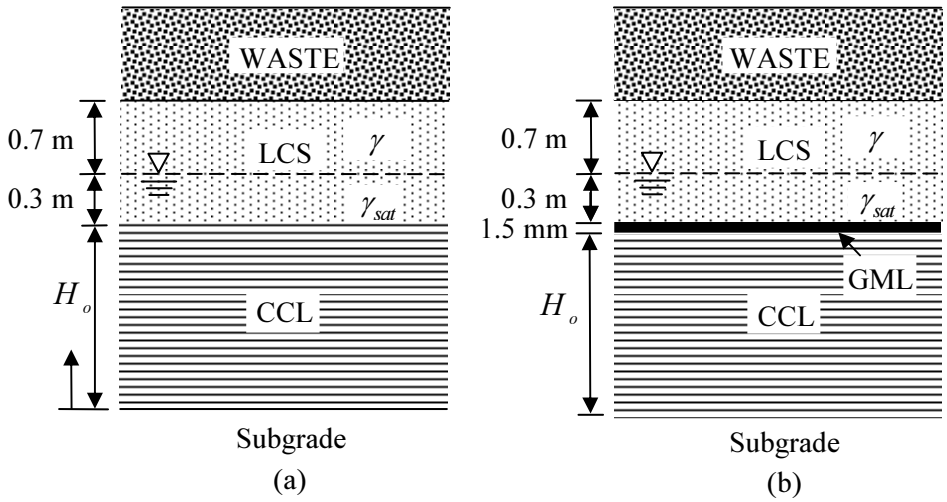

Figure 7.1 Initial geometry for liner systems: (a) single CCL; (b) composite GML/CCL.

VOC properties correspond to those for trichloroethylene (TCE). TCE transport parameters for the GML were taken from experimental investigations reported by Sangam and Rowe (2001), with diffusion coefficient D_{GML} = 4×10^{-13} m^2/s and partition coefficient K_{GML} = 85. TCE transport parameters for the CCL were taken from experimental investigations reported by Yaws (1995), Kim et al. (2001), Boving and Grathwohl (2001), Ullman and Aller (1982), Charbeneau (2000), and Mercer and Cohen (1990), and are provided in Table 7.1. Diffusion transport through the GML for the GML/CCL system was characterized using Fick's first law, which corresponds to a variable flux (Type III) boundary condition at the top of the CCL. Neglecting advective transport in the top half of the uppermost fluid element ($m = R_{mo}$), contaminant concentration at the top of the CCL is calculated as

$$c_t^t = \frac{D_{GML}K_{GML}(H^t - z_{f,R_{mo}}^t)c_o + n_{R_j}^t D^* H_{GML} c_{R_{mo}}^t}{D_{GML}K_{GML}(H^t - z_{f,R_{mo}}^t) + n_{R_j}^t D^* H_{GML}} \tag{7.1}$$

where H_{GML} = thickness of GML, H = CCL thickness, $z_{f,R_{mo}}$ = elevation of the top most fluid element, n_{R_j} = porosity of the top most solid element, $c_{R_{mo}}$ = contaminant concentration of the top most fluid element, and superscript t = time. The corresponding contaminant mass flux through GML is calculated as

$$J_{z,R_{mo}}^t = -D_{GML}K_{GML}\frac{c_o - c_t^t}{H_{GML}} \tag{7.2}$$

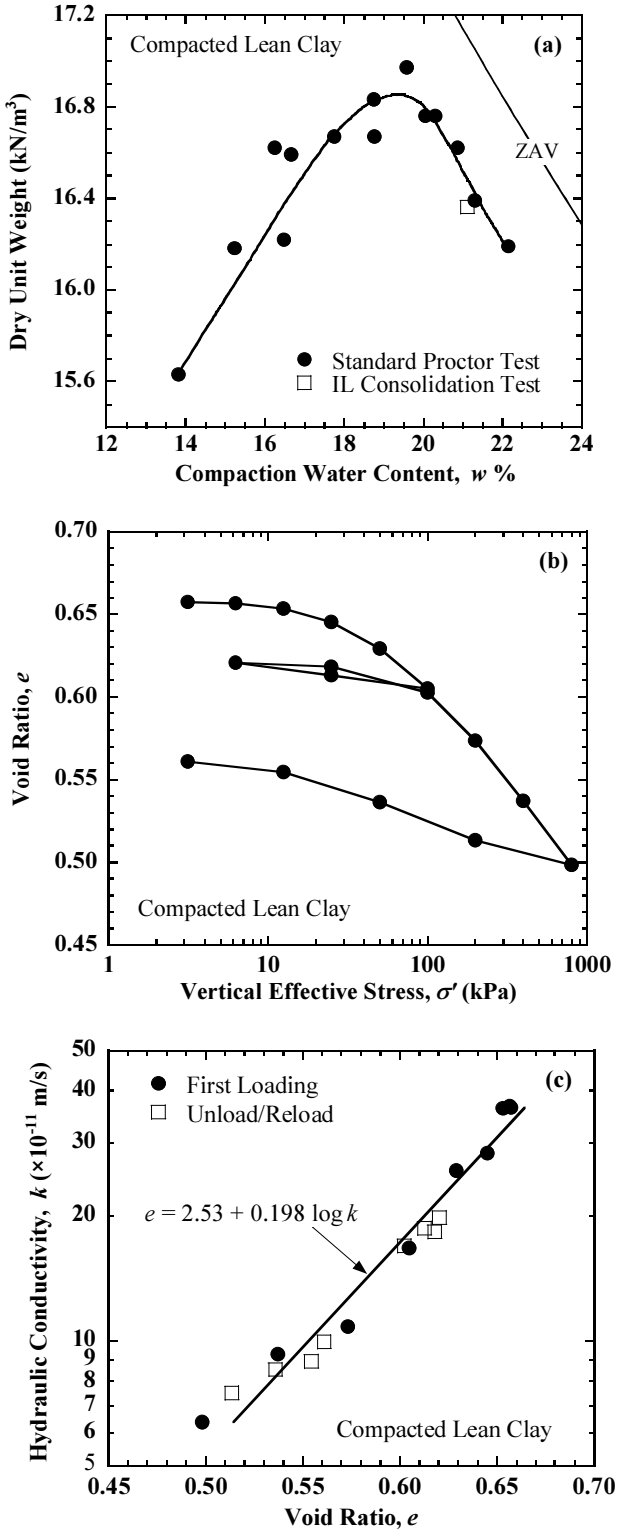

Figure 7.2 Material properties for CCL: (a) compaction; (b) compressibility; (c) hydraulic conductivity (Fox 2007b).

CCL properties were taken from tests conducted in 1998 on a lean clay (CL, G_s = 2.76, LL = 41, and PL = 20) used for CCL construction for a landfill operating in the Midwest U.S. (Fox 2007b). The standard Proctor compaction curve and compressibility and hydraulic conductivity constitutive relationships are shown in Figure 7.2. The constitutive relationships were obtained from an incremental-loading consolidation test performed on a specimen compacted at 2% wet of optimum. Hydraulic conductivity was measured after each load increment using a syringe flow pump. The constitutive relationships display trends similar to natural soils, including a nearly constant compression index and hydraulic conductivity that is primarily related to void ratio during unload/reload. The hydraulic conductivity relationship can be expressed as $e = 2.53 + 0.198 \log k$, where e = void ratio, and k = vertical hydraulic conductivity (m/s). CCL effective diffusion coefficient D^* varies with solid element porosity as $D^* = D_o n^M$ (Manheim 1970; Lerman 1978), where D_o = free solution diffusion coefficient, n = porosity, and M = effective diffusion coefficient exponent. Based on values reported by Yaws (1995), Boving and Grathwohl (2001), and Ullman and Aller (1982), D_o is 8.6×10^{-10} m^2/s and M = 1. TCE sorption is characterized using a linear equilibrium isotherm with distribution coefficient K_d expressed as $K_d = K_{oc} f_{oc}$ (Charbeneau 2000), where K_{oc} = organic carbon partition coefficient = 126 mL/g for TCE (Mercer and Cohen 1990), and f_{oc} = mass fraction of organic carbon within the CCL. TCE decay with time is ignored.

Initial stress conditions are calculated assuming each CCL is saturated and initially in hydraulic equilibrium (i.e., no flow), and therefore has uniform hydraulic head

h = 0, taken with respect to elevation z = 0, prior to waste placement. The LCS layer is 1 m thick (constant) with saturated unit weight γ_{sat} = 20.6 kN/m^3 for the lower 0.3 m and moist unit weight γ = 17.5 kN/m^3 for the upper 0.7 m. Under these conditions and neglecting the weight of the GML, the initial effective stress at the top of the CCL q_o = $0.7\gamma + 0.3\gamma'$ for the single CCL and $q_o = 0.7\gamma + 0.3\gamma_{sat} + H_o\gamma_w$ for the GML/CCL. Starting at time t = 0, vertical stress increases at a constant rate to a final value Δq over a total loading period t_q. The total elapsed time for each simulation was 40 years. Although transport parameters are constant for each numerical simulation, spatial and temporal changes in porosity and seepage velocity produce variations of hydrodynamic dispersion, retardation factor, and Peclet number during consolidation. Simulations were conducted using 120 solid phase elements, 120 fluid elements for simulations without sorption, and 360 fluid elements for simulations with sorption.

Table 7.1 TCE transport parameters for CCL.

Property	CCL with no organic carbon	CCL with organic carbon
Free solution diffusion coefficient, D_o (m^2/s)	8.6×10^{-10} [a]	8.6×10^{-10} [a]
D^* exponent for porosity, M	1[b]	1[b]
Longitudinal dispersivity, α_L (m)	0.02[c]	0.02[c]
Organic carbon content, f_{oc} (%)	0	0.5
Distribution coefficient, K_d (mL/g)	0	0.63[d]
Decay constant, λ_c (1/s)	0	0

[a]From Kim et al. 2001, original source: Yaws 1995
[b]Boving and Grathwohl 2001, Ullman and Aller 1982
[c]Kim et al. 2001
[d]Charbeneau 2000, Mercer and Cohen 1990

7.4 Simulation Results

7.4.1 Base Case

The base case corresponds to the first set of conditions considered. Numerical simulations were conducted for H_o = 1 m, f_{oc} = 0.5%, K_d = 0.63 mL/g, and M = 1. Corresponding results are also presented for a non-sorbing CCL (i.e., f_{oc} = 0, K_d = 0). The single CCL and GML/CCL systems have initial effective stress q_o = 15.49 kPa and 28.24 kPa, respectively, and are loaded at a constant rate of 100 kPa/yr for t_q = 10 years, giving a final applied stress Δq = 1000 kPa. This corresponds to a municipal solid waste

landfill with a final waste height of approximately 70 – 90 m and post-closure period of 30 years.

The applied stress Δq, settlement S, and boundary water outflows v for the single CCL and GML/CCL systems are presented in Figure 7.3. Applied stress increases linearly to a final value of 1000 kPa at 10 years and remains constant thereafter. Consolidation is completed at about t = 10.5 yr and the resulting final settlements are 97 mm and 94 mm for CCL and GML/CCL, respectively, corresponding to final average strains of 9.7% and 9.4%. The final settlement for CCL is larger than for GML/CCL because the single CCL has a lower value of q_o and downward seepage forces due to the external hydraulic gradient. Based on average void ratio, CCL k decreases approximately 84% over the same time period–from 2.96×10^{-10} m/s to 4.66×10^{-11} m/s for CCL and 2.80×10^{-10} m/s to 4.64×10^{-11} m/s for GML/CCL. Corresponding decreases in D^* are approximately 16%–from 3.37×10^{-10} m^2/s to 2.81×10^{-10} m^2/s for CCL and 3.35×10^{-10} m^2/s to 2.80×10^{-10} m^2/s GML/CCL. At the top boundary of the single CCL, outflow is initially positive and then turns negative (i.e., inflow) at t = 6.4 yr due to the external hydraulic gradient. Outflows at both bottom boundaries are relatively large at the start of loading and gradually decrease as the stiffness of the clay increases and then decrease rapidly at the cessation of loading (t = 10 yr). At t = 10.5 yr, dissipation of excess pore pressure is essentially completed and bottom boundary v reaches steady state values of 0.002 m/yr for CCL and zero for GML/CCL.

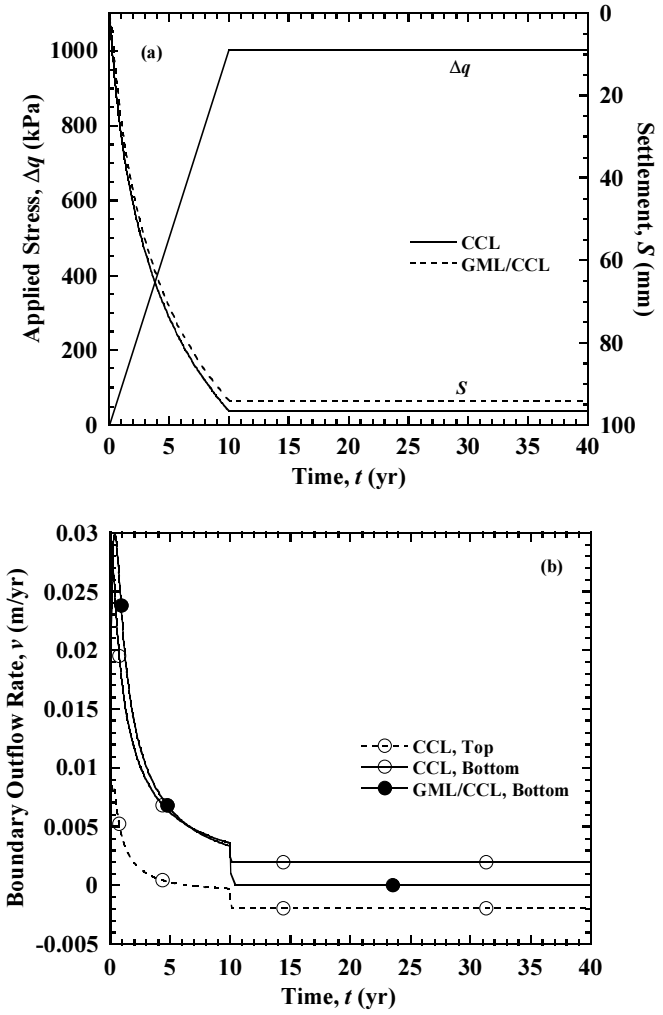

Figure 7.3 Consolidation response for liner systems: (a) applied stress and settlement; (b) boundary water outflow rates.

Simulation results for VOC transport through the single CCL liner system with base case conditions over the 40-yr simulation period are presented in Figure 7.4. Contaminant mass flux F at the base of the CCL is shown in Figure 7.4(a), normalized mass flux F/F_{ss} in Figure 7.4(b), and cumulative mass outflow M_e in Figure 7.4(c), where F_{ss} is steady-state mass flux. Values of F_{ss} were calculated using the analytical solution of Rabideau and Khandelwal (1998). Results for consolidation-induced

transport, obtained using CST2, are denoted as C. In addition to these data, Figure 7.4 also presents two additional data sets. The NC-I results were obtained for simulations with no CCL consolidation (Δq = 0) and for which transport occurred over the 40-yr period with constant initial conditions for the liner system (i.e., constant initial CCL thickness and initial profiles of void ratio, hydraulic conductivity, and effective diffusion coefficient). Similarly, the NC-F results were obtained for simulations with no CCL consolidation (Δq = 0) and for which transport occurred over the 40-yr period with constant final conditions for the liner system after consolidation has completed (i.e., constant final CCL thickness and final profiles of void ratio, hydraulic conductivity, and effective diffusion coefficient). Simulation results for C, NC-I, and NC-F simulations were obtained using CST2 and the input parameters provided in Table 7.2, where h_t = total head at top boundary, h_b = total head at bottom boundary, e_o = initial void ratio, and k_o = initial hydraulic conductivity. For the single CCL, VOC transport for NC-I and NC-F occurs by advection-dispersion-sorption with constant steady-state advection under the external hydraulic gradient, whereas transport for C corresponds to the full consolidation-induced transport analysis.

Table 7.2 Input parameters for three simulation cases.

	Single CCL			Composite GML/CCL		
	C	NC-I[a]	NC-F[b]	C	NC-I[a]	NC-F[b]
H_o (m)	1	1	0.903	1	1	0.906
h_t (m)	1.3	1.3	1.203	0	0	0
h_b (m)	0	0	0	0	0	0
q_o (kPa)	15.49	15.49	1015.49	28.24	28.24	1027.31
Δq (kPa)	1000	0	0	1000	0	0
Average e_o	0.643	0.643	0.484	0.639	0.639	0.484
Average k_o ($\times 10^{-10}$ m/s)	2.96	2.96	0.466	2.80	2.80	0.464
Average D^* ($\times 10^{-10}$ m^2/s)	3.37	3.37	2.81	3.35	3.35	2.80

[a]Conditions of NC-I are same as initial conditions of C simulation.
[b]Conditions of NC-F are same as final conditions of C simulation.

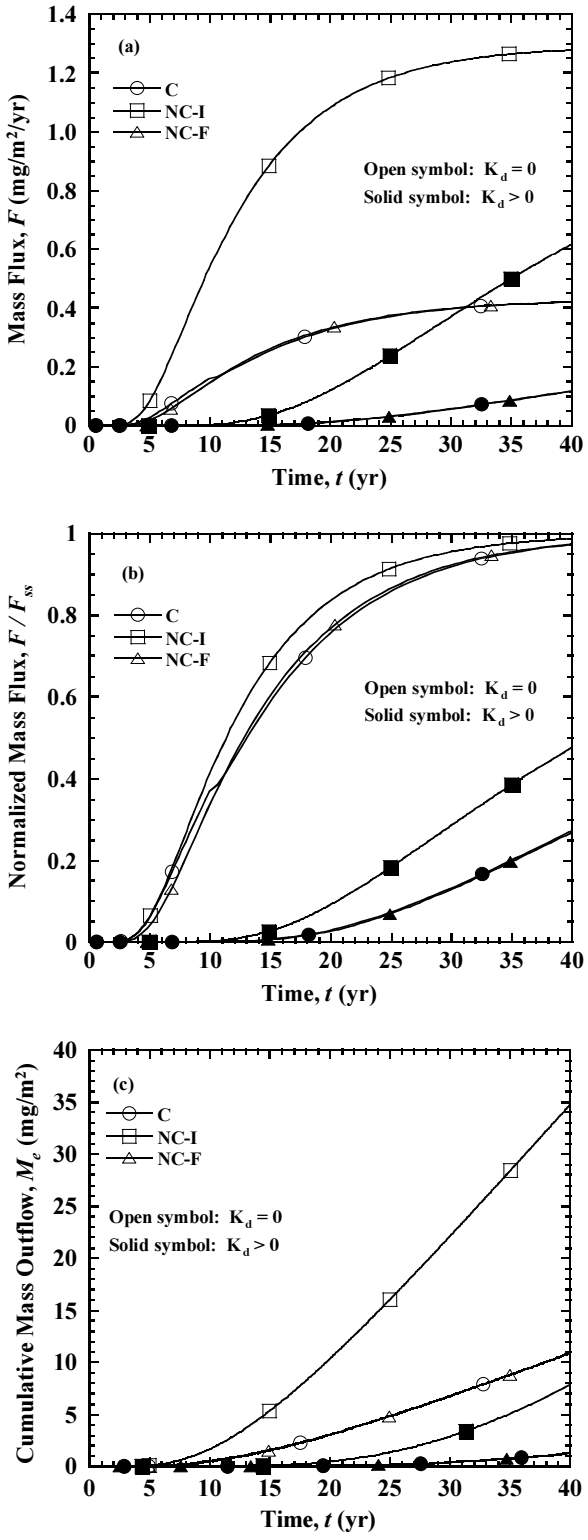

Figure 7.4 Simulation results at base of single CCL: (a) contaminant mass flux; (b) normalized contaminant mass flux; (c) cumulative contaminant mass outflow.

For a CCL without sorption (K_d = 0), the consolidation (C) results in Figure 7.4(a) indicate VOC breakthrough occurs in approximately 3 years. Thereafter, mass flux increases to approximately 0.4 mg/m^2/yr and then starts to level off as steady state conditions are approached near the end of the simulation period. The corresponding NC-F simulation produces slightly lower F in the early stages and slightly higher F in the later stages, but overall essentially the same results as for the coupled consolidation case. At steady-state, NC-F and C simulations produce exactly the same F value. On the other hand, the NC-I simulation predicts earlier breakthrough and substantially higher flux throughout the simulation period. The reason why F for NC-F is lower than that for C soon after end of consolidation is that F for C is only slightly above that for NC-F during consolidation stage and thus the rapid drop of F curve at cessation of loading (t = 10 yr) is able to bring the curve lower than NC-F. Depending on conditions, there are some other cases (e.g., H_o = 0.5 m with loading time = 10 yr, and H_o = 1 m with loading time = 15 yr) where F for C is much higher than that for NC-F during consolidation stage and thus the rapid drop at cessation of loading is not able to bring the curve lower than that for NC-F. For a CCL with sorption (K_d > 0), the C results indicate VOC breakthrough occurs in approximately 12 years, which presents a significant delay because of the retardation effect of sorption. At the end of the simulation period, mass flux is approximately 0.1 mg/m^2/yr, which is much smaller than the steady-state value. The corresponding NC-F simulation produces essentially the same flux as for the coupled consolidation case, whereas the corresponding NC-I simulation predicts earlier breakthrough and substantially higher flux throughout the simulation period. F/F_{ss}

curves in Figure 7.4(b) indicate that all the three simulation cases (C, NC-I , and NC-F) for non-sorbing CCL essentially approach steady state at t = 40 yr, but the corresponding curves for sorbing CCL are far less than steady state due to the retardation of sorption effect. M_e curves in Figure 7.4(c) indicate similar trends as the corresponding F curves in Figure 7.4(a), with C and NC-F showing essentially the same M_e values and NC-I showing much larger M_e values throughout the simulation period.

Simulation results for VOC transport through the composite GML/CCL liner systems with base case conditions over the 40-yr simulation period are presented in Figure 7.5. Contaminant mass flux at the base of the composite GML/CCL is shown in Figure 7.5(a), normalized mass flux in Figure 7.5(b), and cumulative mass outflow in Figure 7.5(c). Values of F_{ss} were calculated using the analytical solution of Foose et al. (2002). Similar to Figure 7.4, Figure 7.5 also presents NC-I and NC-F data sets to illustrate the effects of consolidation. Simulation results for C, NC-I, and NC-F simulations were obtained using CST2 and the input parameters provided in Table 7.2. For the composite GML/CCL, VOC transport for NC-I and NC-F occurs by diffusion-sorption with no advection (different from single CCL where advection occurs), whereas transport for C corresponds to the full consolidation-induced transport analysis.

For a non-sorbing CCL, the C results in Figure 7.5(a) indicate VOC breakthrough occurs in approximately 3 years. Thereafter, mass flux increases to approximately 0.3 mg/m^2/yr and then starts to level off as steady state conditions are approached near the end of the simulation period. From t = 10 yr to 10.5 yr, there is a rapid decrease of flux, because applied load reached the maximum value and stopped increasing and as a result

seepage velocity started to decrease (see Figure 7.3), which subsequently decreased the transport attributed to advection. The corresponding NC-F simulation produces lower F throughout the simulation period, but essentially the same results as for the coupled consolidation case at the end of simulation. On the other hand, the NC-I simulation predicts slightly later breakthrough and lower flux in the early stages but higher flux sooner after the end of consolidation stage. For sorbing CCL, the C results indicate VOC breakthrough occurs in approximately 12 years, which presents a significant delay because of the retardation effect of sorption. At the end of the simulation, flux is approximately 0.09 mg/m^2/yr, which is much smaller than the steady-state value. The corresponding NC-F simulation produces slightly lower flux than the C simulation throughout the simulation period, whereas the corresponding NC-I simulation predicts earlier breakthrough and substantially higher flux. F/F_{ss} curves in Figure 7.5(b) indicate that C simulation for non-sorbing CCL produces higher F/F_{ss} than NC-I and NC-F throughout the simulation period. For sorbing CCL, however, F/F_{ss} for C is lower than that for NC-I but higher than for NC-F. M_e curves in Figure 7.5(c) indicate similar trends as the corresponding F curves in Figure 7.5(a).

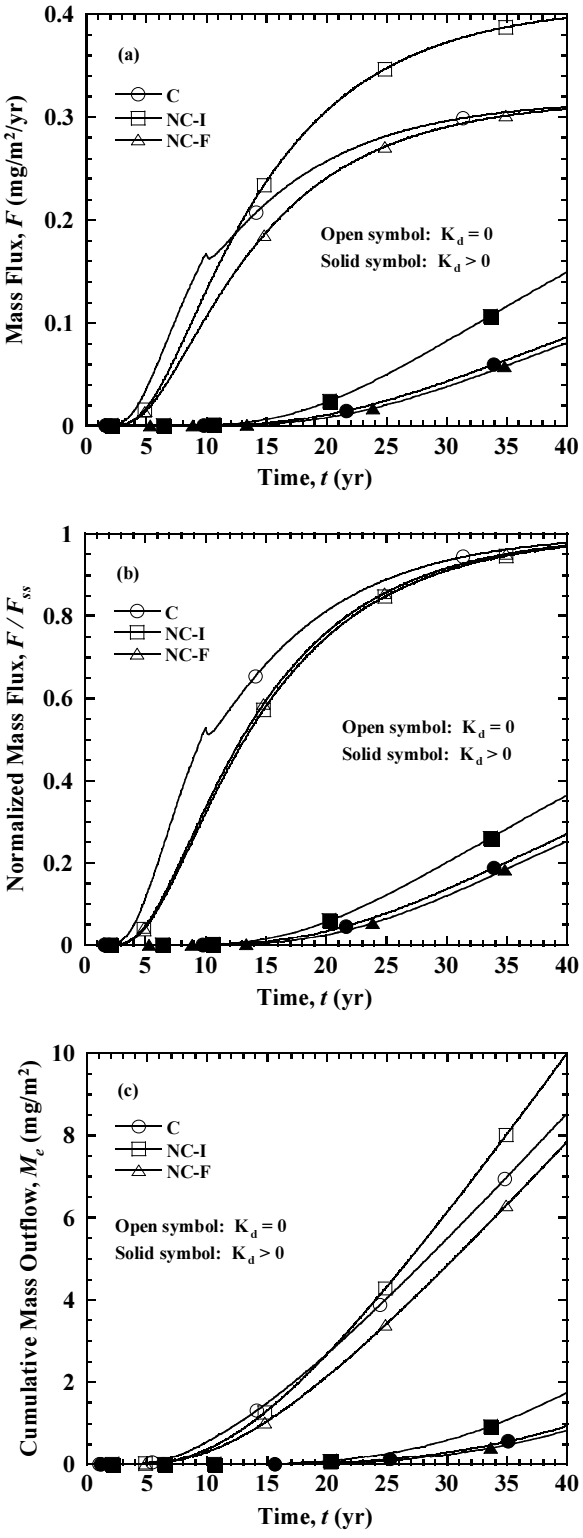

Figure 7.5 Simulation results at base of composite GML/CCL: (a) contaminant mass flux; (b) normalized contaminant mass flux; (c) cumulative contaminant mass outflow.

The effect of CCL consolidation on contaminant transport is indicated more clearly in Figure 7.6, which shows the ratio of consolidation results to no-consolidation results. Specifically, the ratio of C results to NC-I results is denoted as R_I, while the ratio of C results to NC-F results is denoted as R_F. Figure 7.6(b) indicates that R_I of cumulative mass outflow for non-sorbing CCL is approximately 0.33 throughout consolidation and post-consolidation stages, indicating that NC-I simulations overestimate M_e by about three times as compared with C simulation. Consolidation is more important for sorbing CCL, where R_I changes from 0.05 at t = 5.6 yr to 0.16 at t = 40 yr, indicating that NC-I simulation overestimates M_e by as much as 20 times at t = 5.6 yr and 6 times at t = 40 yr. The reason why NC-I yielded larger M_e than C does is that consolidation process changed CCL properties, giving six-fold decrease in k, six-fold decrease in v_s, and 16% decrease in D^*. These factors result in smaller transport rate but are not considered by NC-I simulation. Now looking at R_F curves, R_F for both non-sorbing and sorbing CCL is larger than 1 during the consolidation stage (because n, v_s, and D^* for NC-F are smaller than those for C in consolidation stage), indicating that NC-F simulation underestimates M_e in the early stages. At the end of simulations (i.e., t = 40 yr), interestingly, R_F for both non-sorbing and sorbing CCL is equal to 1 (because H, n, v_s, and D^* for NC-F are exactly the same as those for C at the end). This indicates that NC-F simulation can provide good estimate of the long-term cumulative mass outflow, despite its large deviation in the early stages. Figure 7.6(a) shows the corresponding R_I and R_F of mass flux for single CCL simulations and indicates similar trends and values.

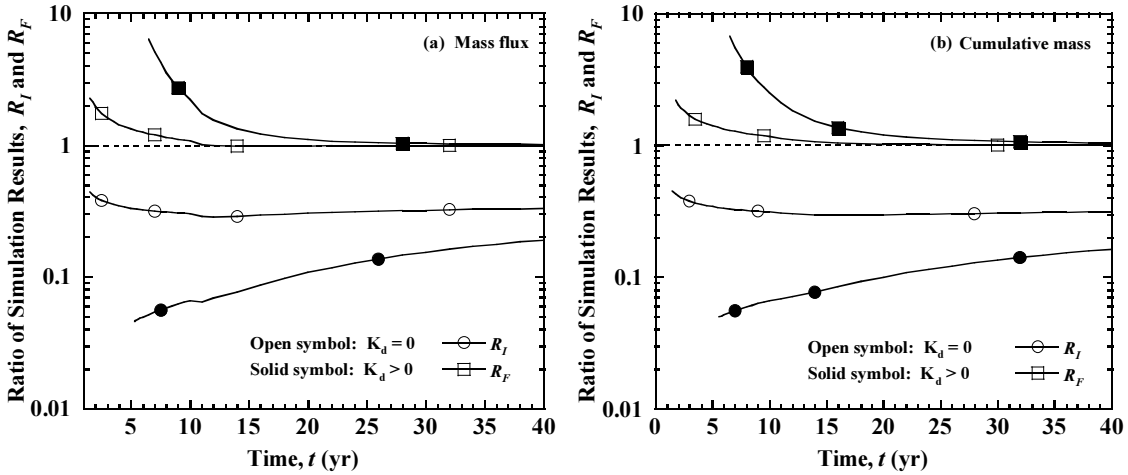

Figure 7.6 Ratio of simulation results at base of CCL: (a) contaminant mass flux; (b) cumulative contaminant mass outflow.

Figure 7.7(b) shows R_I and R_F of cumulative mass outflow for composite GML/CCL liner systems. R_I for non-sorbing CCL is much larger than 1 during consolidation stage (because consolidation yields downward advection which increases the downward transport and this effect outweighs the decrease in transport parameters such as D^* for C simulation), but smaller than 1 soon after consolidation process ended (because consolidation process changed liner properties and yielded 16% decrease in D^* for C). This indicates that, for composite GML/CCL simulations with non-sorbing CCL, NC-I simulation underestimates the short-term M_e but overestimates the long-term M_e, which is different from single CCL simulations where NC-I overestimates both short-term and short-term M_e. For sorbing CCL, however, R_I is always smaller than 1 (because transport is delayed by sorption and consolidation reduces D^* before contaminant reaches the liner bottom) and stays approximately 0.5 throughout the

simulations, indicating that NC-I simulation overestimates M_e by about 2 times. Now looking at R_F curves, R_F is larger than 1 during consolidation stage for both non-sorbing and sorbing CCL (consolidation-induced downward advection increases the transport process), indicating that NC-F simulation underestimates the mass flux in the early stages. At the end of simulation (t = 40 yr), interestingly, R_F for both non-sorbing and sorbing CCL is essentially equal to 1 (= 1.09 for non-sorbing and 1.13 for sorbing CCL), because the parameters associate with transport such as H, n, and D^* for NC-F are the same as those for C at the end of simulations. R_F curves indicate that NC-F simulation can provide good estimate of long-term M_e, despite its large deviation in the early stages. Figure 7.7(a) shows R_I and R_F of mass flux for composite GML/CCL simulations and indicates similar trends and values as the corresponding curves for M_e. Note that R_I and R_F of mass flux will constantly show similar trends and values as the corresponding curves for cumulative mass outflow throughout this chapter. To save space, only the figures for cumulative mass outflow will be shown from now on.

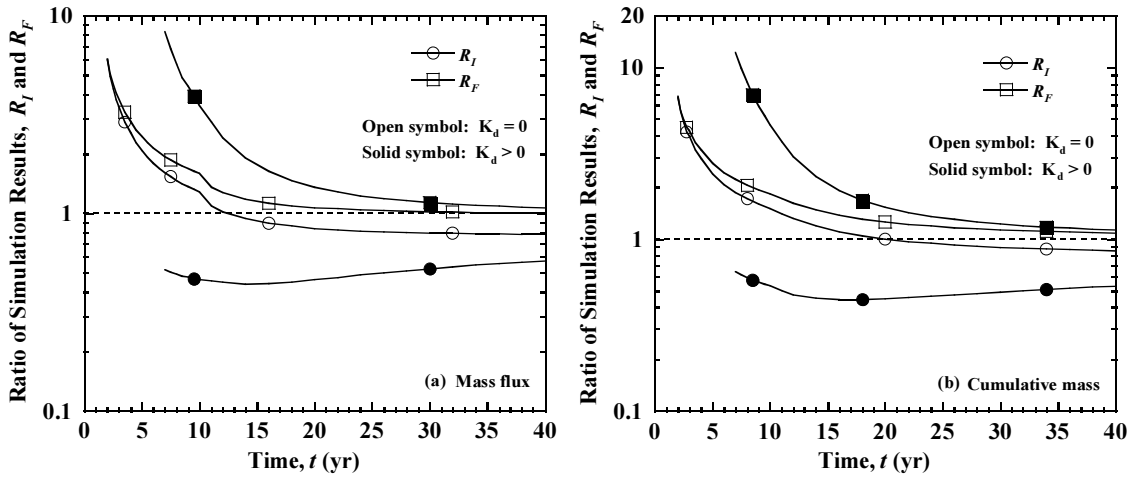

Figure 7.7 Ratio of simulation results at base of composite GML/CCL: (a) contaminant mass flux; (b) cumulative contaminant mass outflow.

To compare the performance of single CCL and composite GML/CCL liner systems, Figure 7.8 shows the mass flux for single CCL and composite GML/CCL with NC-I and C simulations. Figure 7.8(a) shows F curves for non-sorbing CCL and indicates that composite GML/CCL liner yields much smaller F values than single CCL liner. For NC-I simulations, F values at t = 40 yr are 1.28 mg/m^2/yr for CCL and 0.40 mg/m^2/yr for GML/CCL (31% of that for CCL). The corresponding values for C simulations are 0.42 mg/m^2/yr and 0.31 mg/m^2/yr, respectively. The reasons why GML/CCL yields smaller mass flux than CCL are that (1) GML decreases contaminant transport by providing an extra barrier, and (2) GML inhibits the water flow and, thus, transport attributed to advection is significantly decreased. Figure 7.8(b) shows the F curves for sorbing CCL and indicates the same conclusion that GML/CCL yields smaller mass flux. For NC-I simulations with sorbing CCL, F for GML/CCL is 24% of that for CCL at t = 40 yr. For C simulations with sorbing CCL, the corresponding value is 72%.

The corresponding cumulative contaminant mass outflow curves for CCL and GML/CCL are not shown for brevity, but they indicate the same conclusion that composite GML/CCL liner yields much smaller M_e values than single CCL liner.

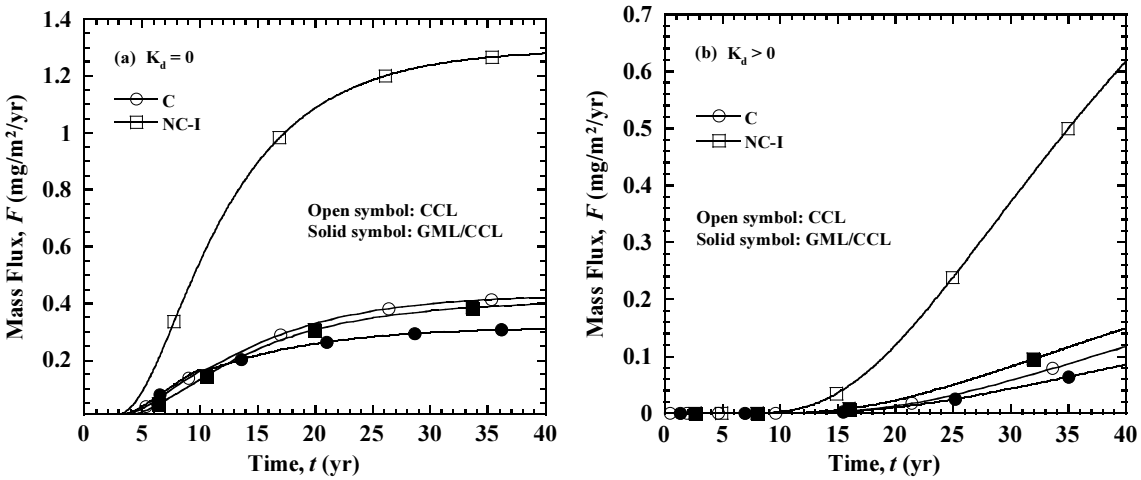

Figure 7.8 Comparison of contaminant mass flux at base of CCL and GML/CCL: (a) non-sorbing CCL; (b) sorbing CCL.

Figure 7.9(a) shows the relative pore-water concentration c/c_o versus normalized elevation Z for single CCL simulations with non-sorbing CCL at t = 5 yr, 10 yr, 25 yr, and 40 yr, where c_o = initial pore-water concentration in the leachate = 100 mg/L, Z = z/H^t, z = elevation of fluid element, and H^t = CCL thickness at time t. The profiles are consistent with the mass flux and cumulative mass outflow curves shown in Figure 7.4. At all times, the profiles for C are above those for NC-I. This is because (1) for t = 5 and 10 yr consolidation process yielded upward fluid flow at the upper portion of the liner which slow the downward transport, and (2) for t = 25 and 40 yr consolidation process compressed the liner and decreased the values of transport parameters (e.g., n, v_s, and

D^*) and thus decreased the subsequent transport. As shown in Figure 7.4(a), mass flux for non-sorbing CCL essentially reaches steady state at t = 40 yr. The concentration profiles at t = 40 yr, however, are not straight line, as would be expected for diffusive transport. Instead, they display a shape that skews toward the bottom, because steady seepage exists since the end of consolidation (t = 10.5 yr) and, as such, the steady state is not a diffusive transport. Figure 7.9(b) shows the corresponding concentration profiles for sorbing CCL at t = 5, 10, 25, and 40 yr and displays similar trends as those for non-sorbing CCL except that the profiles for sorbing CCL are delayed by sorption effect. The profiles for relative solid-phase concentration s/s_o (where $s_o = K_d c_o$ = 63 mg/L) for sorbing CCL are not shown for brevity but are exactly the same as the corresponding c/c_o profiles shown in Figure 7.9(b), because linear equilibrium sorption is assumed for the simulations.

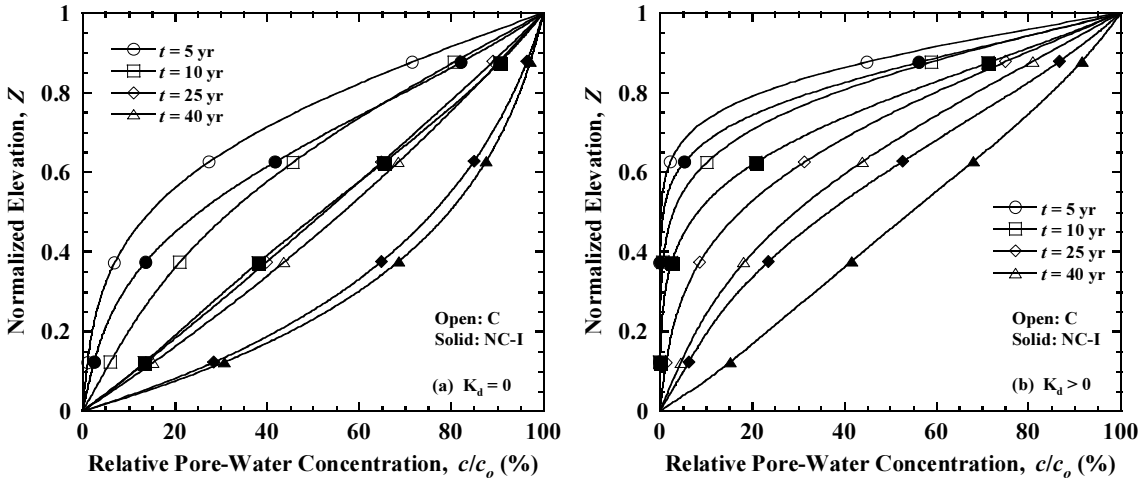

Figure 7.9 Pore-water concentration profiles for single CCL:
(a) non-sorbing CCL; (b) sorbing CCL.

Figure 7.10(a) shows c/c_o profiles for composite GML/CCL simulations with non-sorbing CCL at t = 5, 10, 25, and 40 yr. The profiles are consistent with the mass flux and cumulative mass outflow curves shown in Figure 7.5. The profiles for C are below those for NC-I, which is the opposite of the trends for single CCL. This is because, for composite GML/CCL, consolidation process induced downward seepage across the entire liner which increases the downward contaminant transport, whereas for single CCL, consolidation process induced upward seepage in the upper portion of the liner. At t = 40 yr, the profiles are essentially straight line, indicating steady-state diffusive transport is approached. Figure 7.10(b) shows the corresponding concentration profiles for composite GML/CCL liner system with sorbing CCL. Contrary to those shown in Figure 7.10(a), Figure 7.10(b) indicates that profiles for C are above those for NC-I, because transport is delayed by sorption effect and consolidation-induced advection is outweighed by consolidation-induced reduction in transport parameters (e.g., D^* and n). Again, s/s_o profiles for composite GML/CCL simulations (not shown) are exactly the same as the corresponding c/c_o profiles in Figure 7.10(b) because linear equilibrium sorption is assumed.

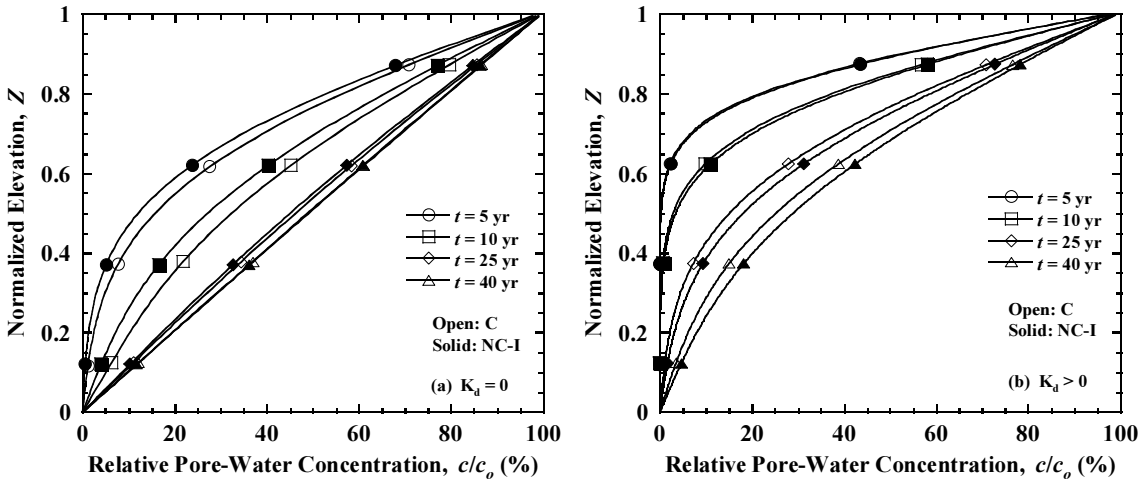

Figure 7.10 Pore-water concentration profiles for composite GML/CCL: (a) non-sorbing CCL; (b) sorbing CCL.

7.4.2 Effect of Initial Liner Thickness

To investigate the effect of initial liner thickness H_o, simulations were performed with H_o = 0.5, 0.75, 1.0, 1.25, 1.5 m for single CCL and composite GML/CCL liner systems. All other input parameters remain the same as those for the base case except that H_o, h_t, and q_o for NC-F simulations are changed accordingly so that the initial conditions for NC-F correspond to the end conditions for C. Figure 7.11(a) shows R_I of M_e vs. time for single CCL simulations with different H_o. For both non-sorbing and sorbing CCL, especially for the latter, R_I values decrease significantly with increasing H_o in both early and late stages. For sorbing CCL at t = 40 yr, R_I value decreases from 0.37 for H_o = 0.5 m to 0.055 for H_o = 1.5 m, indicating that NC-I overestimates M_e by 2.7 times for H_o = 0.5 m and by 18.2 times for H_o = 1.5 m. The

effect of H_o on R_I values is most important in the early stages. For sorbing CCL at t = 14 yr, for instance, R_I is approximately 0.01 for H_o = 1.5 m, indicating that NC-I overestimates M_e by about 100 times (i.e., 2 orders of magnitude). R_I curves for mass flux are not shown, but they indicate similar trends and values as the corresponding curves for M_e.

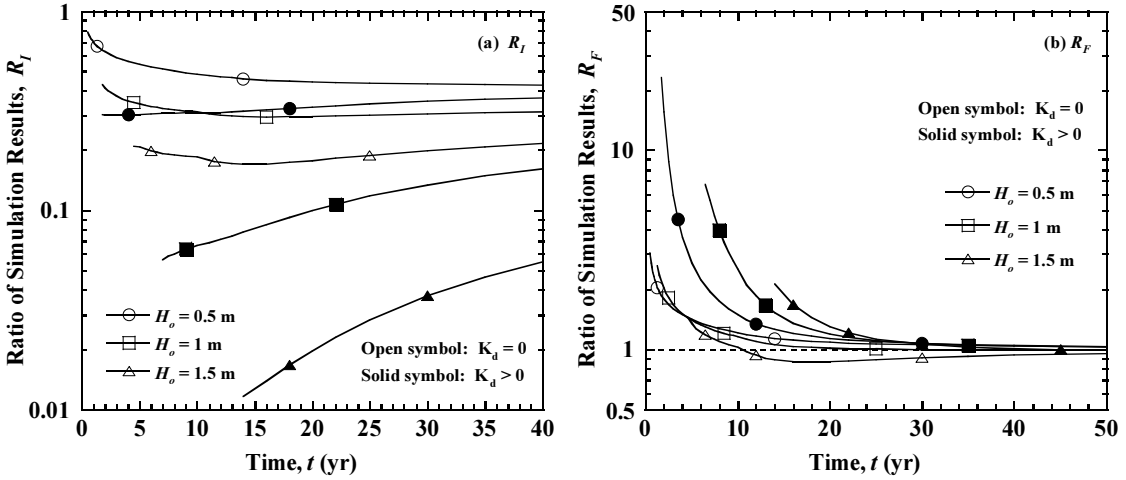

Figure 7.11 Ratio of cumulative mass outflow at base of single CCL with different H_o: (a) R_I vs. time; (b) R_F vs. time.

Figure 7.11(b) shows R_F of M_e for single CCL simulations with different H_o. For non-sorbing CCL, R_F values do not vary significantly with H_o. For sorbing CCL, on the other hand, H_o has important effect on R_F values in the early stages but has negligible effect in the late stages. For both non-sorbing and sorbing CCL, R_F values at t = 40 yr are essentially equal to 1 for all the H_o values considered. This indicates that

NC-F can provide good estimate of long-term M_e but can yield large deviations for short-term M_e. R_F curves for mass flux are not shown for brevity, but indicate similar trends and values as the corresponding curves for M_e.

Figure 7.12(a) shows R_I of M_e for composite GML/CCL liner simulations with different H_o. For non-sorbing CCL, H_o has important effect on R_I values in the early stages, but this effect becomes unimportant toward the end of the simulation period. At *t* = 5 yr, R_I value for non-sorbing CCL increases from 1.14 for H_o = 0.5 m to 9.22 for H_o = 1.5 m, indicating that NC-I underestimates M_e by 1.14 times for H_o = 0.5 m and by 9.22 times for H_o = 1.5 m. At *t* = 40 yr, R_I values for non-sorbing CCL are approximately 0.9 for all the H_o considered, indicating NC-I slightly overestimates long-term M_e. For sorbing CCL, on the other hand, H_o maintains important effect on R_I throughout the simulation period. At *t* = 40 yr, R_I value for sorbing CCL decreases from 0.72 for H_o = 0.5 m to 0.34 for H_o = 1.5 m, indicating that NC-I overestimates long-term M_e by 1.4 times for H_o = 0.5 m and by 2.9 times for H_o = 1.5 m. R_I curves for mass flux are not shown, but they indicate similar trends and values as the corresponding curves for M_e.

Figure 7.12(b) shows R_F of M_e for composite GML/CCL liner simulations with different H_o. For both non-sorbing and sorbing CCL, H_o has important effect on R_F values in the early stages with R_F increasing as the value of H_o, but this effect becomes

unimportant toward the end of the simulation period. At t = 40 yr, R_F value for H_o = 1.5 m is 1.05 for non-sorbing CCL and 1.20 for sorbing CCL, indicating that NC-F can provide good estimate of long-term M_e for all the H_o considered. R_F curves for mass flux (not shown) indicate similar trends and values as the corresponding curves for M_e.

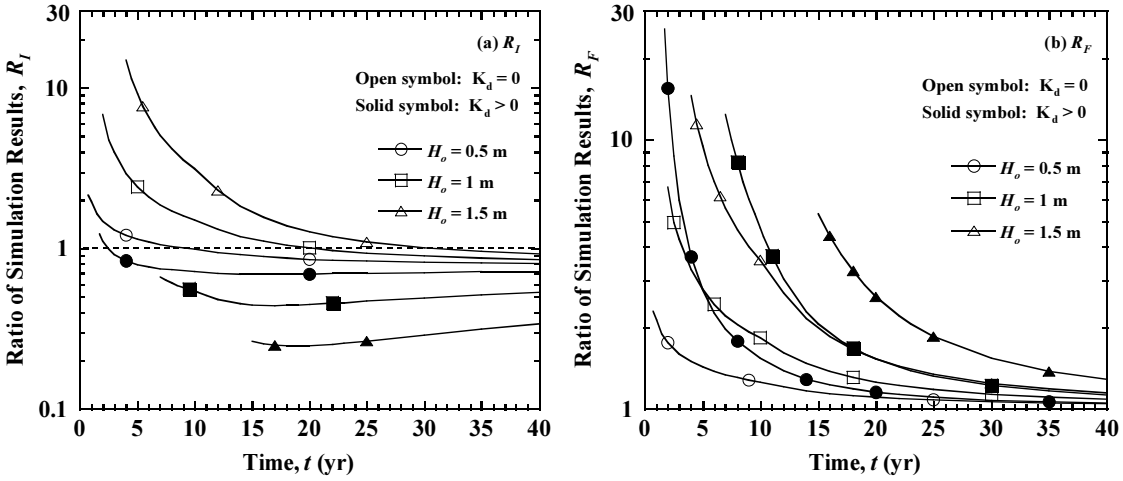

Figure 7.12 Ratio of cumulative mass outflow at base of composite GML/CCL with different H_o: (a) R_I vs. time; (b) R_F vs. time.

7.4.3 Effect of Load Magnitude

To investigate the effect of load magnitude Δq (i.e., waste height), simulations were performed with Δq = 250, 500, and 1000 kPa for CCL and GML/CCL simulations. All other input parameters remain the same as those for the base case except that H_o, h_t, and q_o for NC-F simulations are changed accordingly so that the initial conditions for NC-F correspond to the end conditions for C. Figure 7.13(a) shows R_I of M_e vs. time

for single CCL simulations with different Δq. R_I values decrease significantly with increasing load magnitude especially for sorbing CCL. Even for small load magnitude, consolidation still has important impact on transport. For sorbing CCL with Δq = 250 kPa, R_I at t = 40 yr is 0.34, indicating that NC-I overestimates long-term M_e by 3 times, even though the load magnitude is not large. Figure 7.13(b) shows R_F of M_e for single CCL with different Δq. Interestingly, the R_F curves group together for all the Δq considered and Δq has only slight effect on R_F during consolidation stage and has negligible effect after consolidation stage. At t = 40 yr, R_F for both non-sorbing and sorbing CCL is essentially 1 for all the Δq considered, indicating that NC-F provides good estimate of long-term M_e no matter what Δq. R_I and R_F curves for mass flux (not shown) indicate similar trends and values as the corresponding curves for M_e.

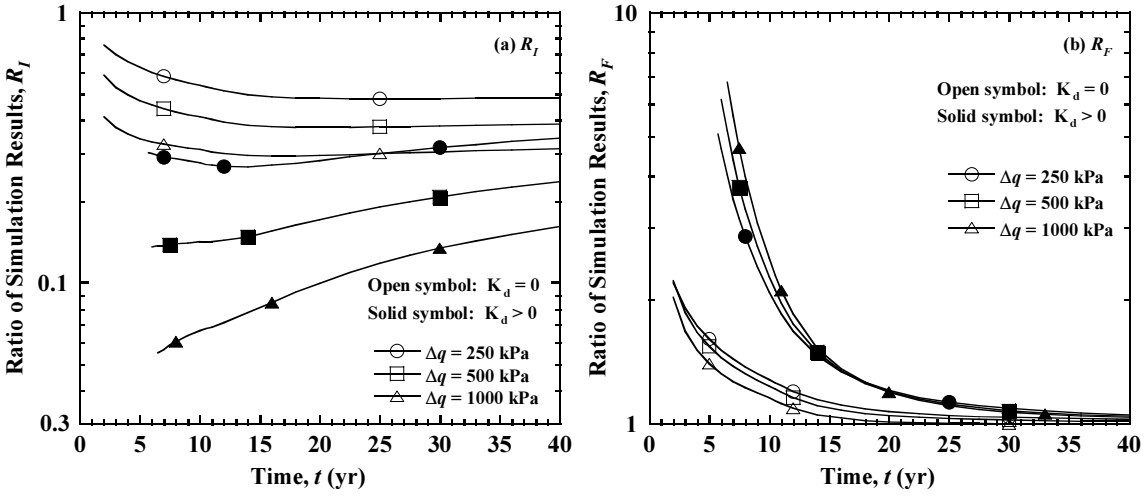

Figure 7.13 Ratio of cumulative mass outflow at base of single CCL with different Δq: (a) R_I vs. time; (b) R_F vs. time.

Figure 7.14(a) shows R_I of M_e for composite GML/CCL liner simulations with different Δq. Δq has some effect on R_I values but in general the effect is not significant, especially for non-sorbing CCL. Even for small Δq, consolidation still has important impact on the contaminant transport. For Δq = 250 kPa, R_I at t = 40 yr is 0.94 for non-sorbing CCL and 0.76 for sorbing CCL, indicating that NC-I overestimates long-term M_e by 1.1 times and 1.3 times respectively. Figure 7.14(b) shows R_F of M_e for composite GML/CCL with different Δq. Δq has important effect on R_F during consolidation stage but has negligible effect toward the end of the simulation period. At t = 40 yr, R_F ranges from 1.05 to 1.13 for all the Δq considered, indicating that NC-F provides good estimate of long-term M_e no matter what Δq. R_I and R_F curves for mass flux (not shown) indicate similar trends and values as the corresponding curves for M_e.

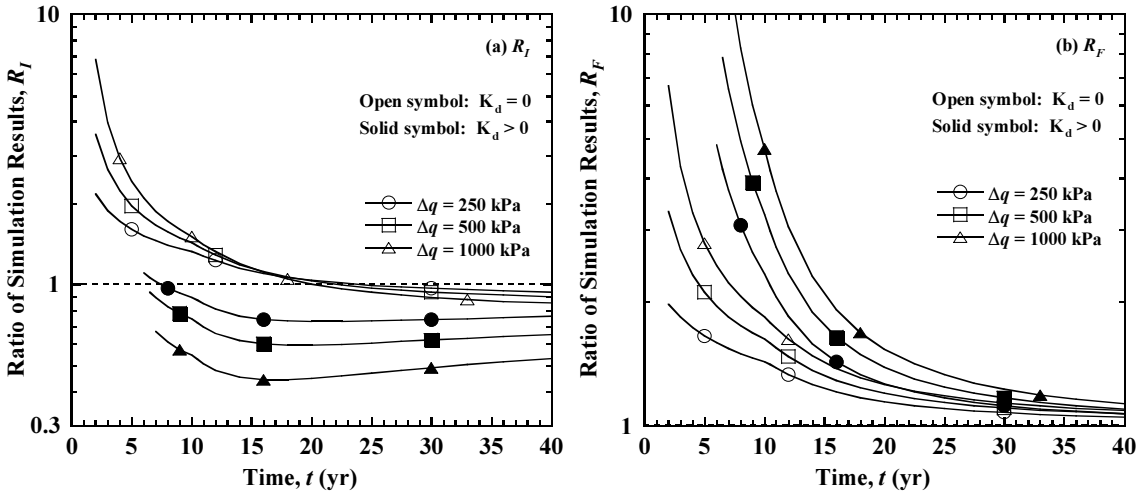

Figure 7.14 Ratio of cumulative mass outflow at base of composite GML/CCL with different Δq: (a) R_I vs. time; (b) R_F vs. time.

7.4.4 Effect of Loading Time

To investigate the effect of loading time t_q, simulations were performed with t_q = 0, 10, and 20 yr for single CCL and GML/CCL composite liner systems, where t_q = 0 represents to instantaneous loading. For C simulations, all other input parameters remain the same as those for the base case. For NC-I and NC-F simulations, no additional simulations are needed. Figure 7.15(a) shows R_I of M_e as a function of time for single CCL simulations with different t_q. In general, t_q has important effect on R_I in the early stages, especially for sorbing CCL, but has negligible effect toward the end of simulations. This is because t_q primarily affects the rate of consolidation but does not affect the final magnitude of consolidation. For sorbing CCL, R_I value at t = 10 yr increases from 0.03 for t_q = 0 yr to 0.14 for t_q = 20 yr, indicating that NC-I overestimates M_e by 33 times for t_q = 0 yr and by 7 times for t_q = 20 yr. R_I value increases as t_q increases because C simulation with larger t_q has slower loading rate and thus it takes longer time for consolidation process to change the associated transport parameters and thus R_I for larger t_q is closer to 1. At t = 40 yr, R_I is approximately 0.33 for non-sorbing CCL and 0.17 for sorbing CCL for all the t_q considered. Figure 7.15(b) shows R_F of M_e for single CCL with different t_q. Similar to the R_I curves shown in Figure 7.15(a), t_q has important effect on R_F in the early stages, especially for sorbing CCL, but has negligible effect toward the end of simulations. For sorbing CCL, R_F value at t = 10 yr increases from 1.18 for t_q = 0 yr to 5.4 for t_q = 20 yr, indicating that NC-F

underestimates M_e by 1.18 times for t_q = 0 yr and by 5.4 times for t_q = 20 yr. At t = 40 yr, R_F ranges from 1 to 1.09 for non-sorbing CCL and ranges from 1.02 to 1.19 for sorbing CCL for all the t_q considered, indicating that NC-F simulations provide reasonable estimate of long-term M_e for all the t_q considered. R_I and R_F curves for mass flux (not shown) indicate similar trends and values as the corresponding curves for M_e.

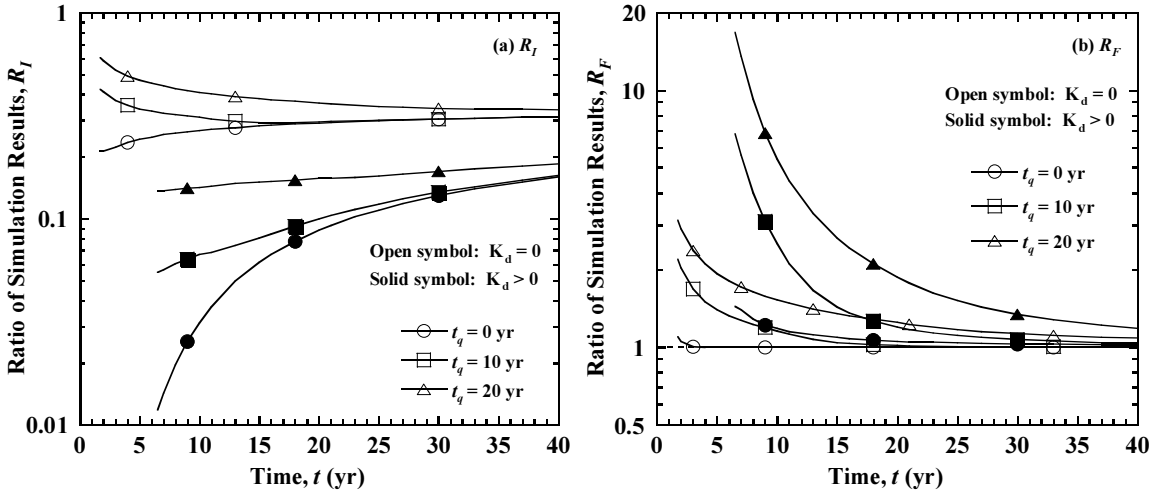

Figure 7.15 Ratio of cumulative mass outflow at base of single CCL with different t_q: (a) R_I vs. time; (b) R_F vs. time.

Figure 7.16(a) shows R_I of M_e for composite GML/CCL liner simulations with different t_q. t_q has important effect on R_I in the early stages but has negligible effect toward the end of simulations. For sorbing CCL, R_I value at t = 10 yr increases from 0.12 for t_q = 0 yr to 0.75 for t_q = 20 yr, indicating that NC-I overestimates M_e by 8.3

times for t_q = 0 yr and by 1.3 times for t_q = 20 yr. At t = 40 yr, R_I ranges from 0.79 to 0.91 for non-sorbing CCL and ranges from 0.47 to 0.6 for sorbing CCL for all the t_q considered, which represents only a slight change.

Figure 7.16(b) shows R_F of M_e for composite GML/CCL liner simulations with different t_q. t_q has important effect on R_F in the early stages but has negligible effect toward the end of simulations. At t = 40 yr, R_F ranges from 1 to 1.16 for non-sorbing CCL and ranges from 1 to 1.27 for sorbing CCL, indicating that, NC-F simulations provide reasonable estimate of long-term M_e for all the t_q considered, despite its large deviations for short-term values. R_I and R_F curves for mass flux (not shown) indicate similar trends and values as the corresponding curves for M_e.

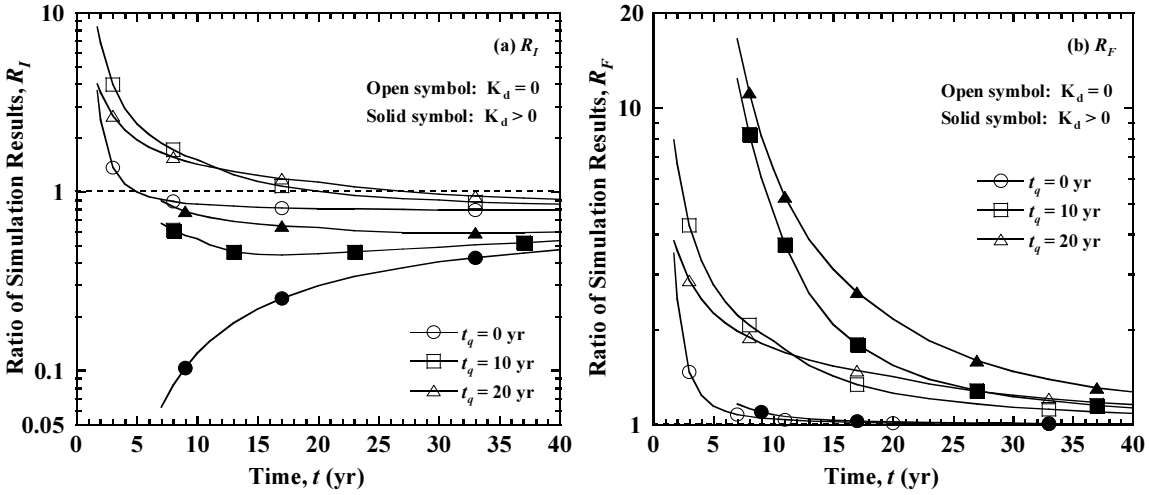

Figure 7.16 Ratio of cumulative mass outflow at base of composite GML/CCL with different t_q: (a) R_I vs. time; (b) R_F vs. time.

7.4.5 Effect of Organic Carbon Fraction

To investigate the effect of organic carbon fraction f_{oc} in the CCL, simulations were performed with f_{oc} = 0%, 1%, 2%, and 3% for single CCL and composite GML/CCL liner systems. All other input parameters remain the same as those for the base case. Figure 7.17 shows R_I and R_F of M_e as a function of time for single CCL with different f_{oc}. f_{oc} has very significant effect on R_I values throughout the simulations and has relatively smaller effect on R_F. At t = 40 yr, R_I value decreases from 0.31 for f_{oc} = 0% to 0.014 for f_{oc} = 3%, indicating that NC-I overestimates long-term M_e by 3.2 times for f_{oc} = 0% and by 71.4 times for f_{oc} = 3%, representing a significant change. R_F value at t = 40 yr, on the other hand, increases from 1 for f_{oc} = 0 to 1.53 for f_{oc} = 3%, indicating that NC-F simulations yield excellent estimate of long-term M_e for small f_{oc} but produce some deviation for large f_{oc}. Given the large errors yielded by NC-I simulations, NC-F produces satisfactory estimate of long-term M_e. R_I and R_F curves for mass flux (not shown) indicate similar trends and values as the corresponding curves for M_e.

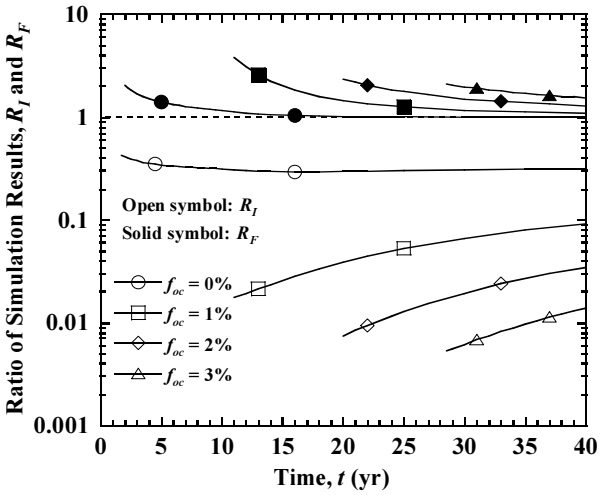

Figure 7.17 Ratio of cumulative mass outflow at base of single CCL with different f_{oc}: R_I and R_F vs. time.

Figure 7.18 shows R_I and R_F of M_e for composite GML/CCL liner simulations with different f_{oc}. f_{oc} has very significant effect on R_I values throughout the simulations but has relatively smaller effect on R_F. At t = 40 yr, R_I value decreases from 0.85 for f_{oc} = 0% to 0.064 for f_{oc} = 3%, indicating that NC-I overestimates long-term M_e by 1.2 times for f_{oc} = 0% and by 15.6 times for f_{oc} = 3%, representing a significant change. R_F values at t = 40 yr, on the other hand, increases from 1.09 for f_{oc} = 0% to 1.48 for f_{oc} = 3%, indicating that NC-F simulations yield satisfactory estimate of long-term M_e for all the f_{oc} considered. R_I and R_F curves for mass flux (not shown) indicate similar trends and values as the corresponding curves for M_e.

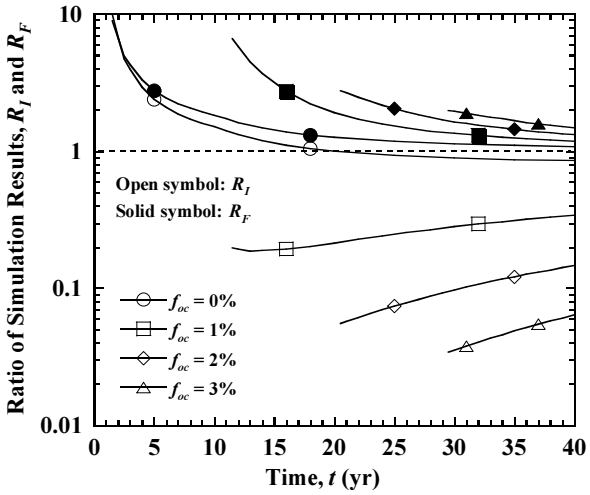

Figure 7.18 Ratio of cumulative mass outflow at base of composite GML/CCL with different f_{oc}: R_I and R_F vs. time.

7.4.6 Effect of Effective Diffusion Coefficient Exponent

To investigate the effect of effective diffusion coefficient exponent M, simulations were performed with M = 0, 1, and 2 for single CCL and composite GML/CCL liner systems, where M = 0 represents constant effective diffusion coefficient. All other input parameters remain the same as those for the base case. At the beginning of C simulations (also for NC-I) for single CCL, D^* = 8.6×10^{-10}, 3.37×10^{-10}, and 1.32×10^{-10} m^2/s for M = 0, 1, and 2, respectively. At the end of C simulations (also for NC-F), the corresponding D^* values = 8.6×10^{-10}, 2.81×10^{-10}, and 9.16×10^{-11} m^2/s.

Figure 7.19(a) shows R_I of M_e as a function of time for single CCL simulations with different M. M has very significant effect on R_I values for both non-sorbing and sorbing CCL, especially for the latter, throughout the simulations. For non-sorbing CCL,

R_I value at t = 40 yr decreases from 0.62 for M = 0 to 0.082 for M = 2, indicating that NC-I overestimates M_e by 1.6 times for M = 0 and by 12.2 times for M = 2. For sorbing CCL, the corresponding R_I value decreases from 0.58 to 0.004, indicating that NC-I overestimates M_e by 1.7 times for M = 0 and by 250 times for M = 2, which represents a very significant change. Figure 7.19(b) shows R_F of M_e for single CCL with different M. Considering that the corresponding R_I values change by more than 2 orders of magnitude for M changing from 0 to 2, M has relatively small effect on R_F values especially at the end of the simulation period. For non-sorbing CCL, R_F value at t = 40 yr decreases from 1 for M = 0 to 0.96 for M = 2, indicating that NC-F provides excellent estimate of long-term M_e for all the M considered. For sorbing CCL, the corresponding R_F value increases from 1 to 1.17, indicating that NC-F provides excellent estimate of long-term M_e for M = 0 and slightly underestimates M_e for M = 2. Considering the error of orders of magnitude yielded by NC-I simulations, NC-F simulations provide reasonable long-term M_e value for all the M values considered. One thing noticed is that R_F value for non-sorbing CCL with M = 0 is much smaller than 1 at the very beginning of simulations while that for other cases is much larger than 1. This is probably because NC-F simulation has a smaller liner thickness (i.e., shorter transport distance) than C simulation at the beginning. Although this is also true for the simulations with M = 1 and 2, NC-F starts with smaller D^* and n than C, which seems to outweigh the effect of shorter transport distance. R_I and R_F curves for mass flux (not shown) indicate similar trends and values as the corresponding curves for M_e.

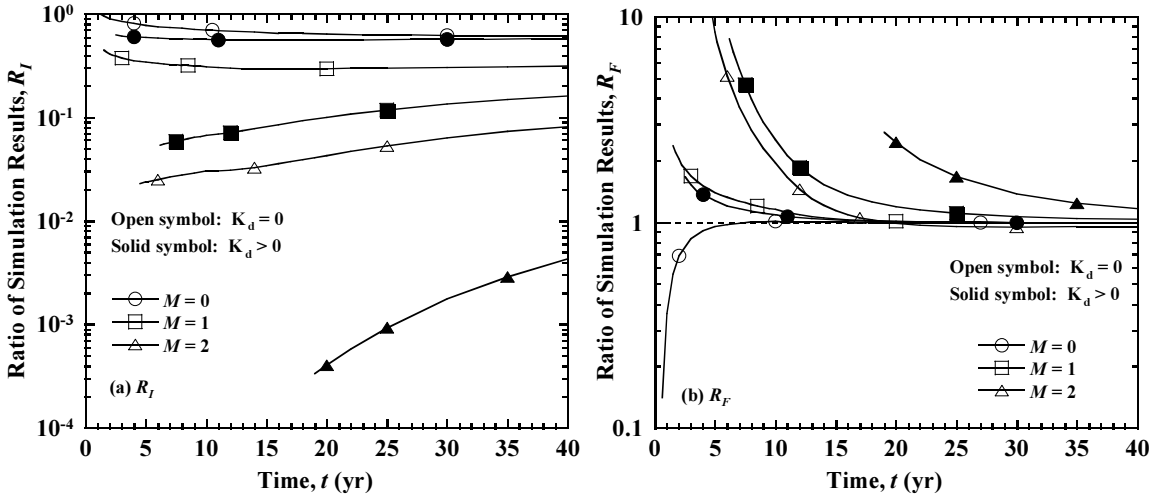

Figure 7.19 Ratio of cumulative mass outflow at base of single CCL with different M: (a) R_I vs. time; (b) R_I vs. time.

Figure 7.20(a) shows R_I of M_e as a function of time for composite GML/CCL with different M. M has very significant effect on R_I values for both non-sorbing and sorbing CCL, especially for the latter, throughout the simulations. At t = 40 yr, R_I value for sorbing CCL decreases from 0.94 for M = 0 to 0.078 for M = 2, indicating that NC-I overestimates long-term M_e by only 1.06 times for M = 0 and by as much as 12.8 times for M = 2, which presents a significant change. Figure 7.20(b) shows R_F of M_e for composite GML/CCL liner with different M. M has significant effect on R_F in the early stages but has small effect toward the end of simulations. For non-sorbing CCL, R_F value at t = 40 yr increases from 1.03 for M = 0 to 1.26 for M = 2, indicating that NC-F provides excellent estimate of M_e for M = 0 and slightly underestimates M_e for M = 2. For sorbing CCL, the corresponding R_F value increases from 1.03 to 1.68. This

indicates that, despite its large deviation in the early stages, NC-F simulations provide reasonable long-term M_e for all the M values considered. R_I and R_F curves for mass flux (not shown) indicate similar trends and values as the corresponding curves for M_e.

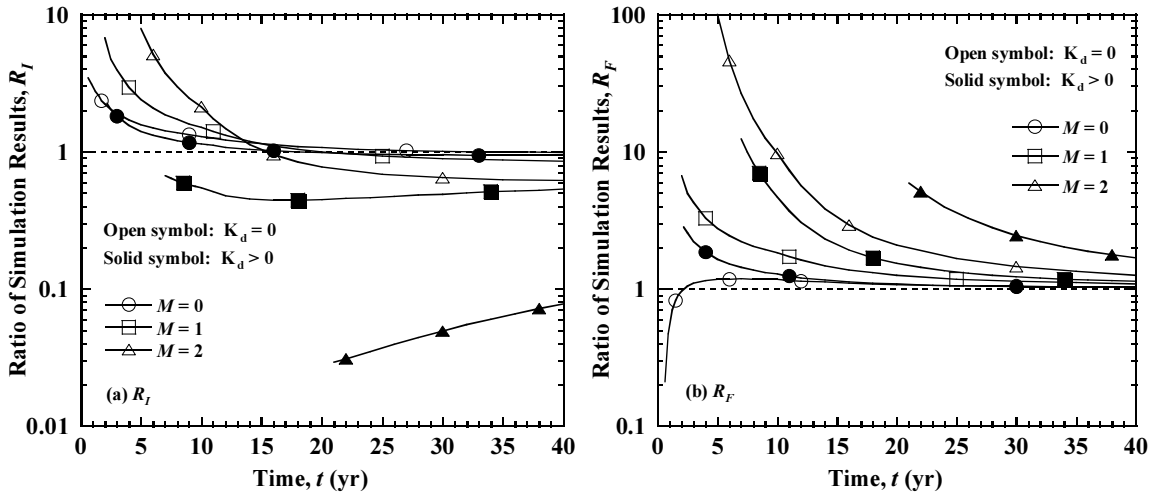

Figure 7.20 Ratio of cumulative mass outflow at base of composite GML/CCL with different M: (a) R_I vs. time; (b) R_I vs. time.

7.5 Acknowledgements

Chapter 7 of this dissertation is based on material from a manuscript under preparation for publication, tentatively titled "Assessment of Consolidation-Induced Contaminant Transport for Geoenvironmental Applications: Compacted Clay Liner Systems," with a preliminary author list of Hefu Pu, Patrick J. Fox, and Charles D. Shackelford (2014). The dissertation author is the first author of this paper.

Chapter 8

Conclusions and Recommendations

The following conclusions are reached as a result of: 1) the development of the enhanced CS2 numerical model and subsequent investigations of the importance of time-dependent loading, external hydraulic conductivity, unload/reload effect, and stress path for one-dimensional large strain consolidation, 2) the development of the CCRS1 numerical model and subsequent investigations of the effect of soil constitutive relationships on constant rate of strain (CRS) consolidation responses, 3) the development of the CSTCRS1 numerical model and subsequent investigations of the effects of initial concentration distribution, transport conditions, applied strain rate, initial specimen height, and drainage and concentration boundary conditions on consolidation-induced solute transport for CRS loading conditions, 4) a comparative study of consolidation-induced solute transport for incremental loading and constant rate of strain loading conditions, and 5) the investigations of consolidation-induced contaminant transport through compacted clay liner (CCL)-based landfill bottom liner systems.

8.1 Enhanced CS2 Model for Large Strain Consolidation under General Loading

1. The enhanced CS2 model represents the next level of sophistication beyond the original version. The algorithm accounts for large strains, soil self-weight, general constitutive relationships, relative velocity of fluid and solid phases, changing compressibility and hydraulic conductivity during consolidation, time-dependent loading, unload/reload effects, and an externally applied hydraulic gradient acting across the layer.
2. Verification checks were performed for consolidation under time-dependent loading and excellent agreement was achieved with the Olson (1977) analytical solution for small strains. Additional simulations indicated that, for constant material properties, large strains accelerate the rate of consolidation under time-dependent loading.
3. An external hydraulic gradient acting across a consolidating layer can have an important effect on final settlement, void ratio distribution and excess pore pressures but may not have a strong effect on the rate of consolidation.
4. Unload/reload during consolidation can produce complex behavior. Soil elements take different paths on the compressibility plot and excess pore pressures can vary dramatically with changes in applied stress. Elements in close proximity to drainage boundaries will have a higher preconsolidation stress than those in the interior of the layer when unloading occurs before the completion of consolidation.

5. Compressibility and hydraulic conductivity constitutive relationships and self-weight of the soil in particular can have an important effect on the rate of consolidation and final settlement. Failure to correctly account for these aspects can lead to significant errors in a consolidation analysis.

8.2 CCRS1 Model for Large Strain Consolidation under Constant Rate of Strain Loading

1. CCRS1 is a piecewise-linear numerical model for consolidation under constant rate of strain (CRS). The algorithm accounts for vertical strain, general constitutive relationships, relative velocity of fluid and solid phases, changing compressibility and hydraulic conductivity during consolidation, and an externally applied hydraulic gradient. Soil self-weight is included, although this effect is insignificant for typical laboratory specimens. Compressibility is rate-independent and thus the current model is most appropriate for less structured soils, such as reconstituted clays.
2. Verification checks of CCRS1 simulations show excellent agreement with analytical and numerical solutions for several examples involving different constitutive relationships and final strain conditions.
3. Compressibility and hydraulic conductivity relationships can have an important effect on CRS consolidation response, including the applied vertical stress, base excess pore pressure, and local strain profile. Results also indicate that analytical

solutions obtained using small strain theory can be in significant error for large strain conditions with changing coefficient of consolidation.

8.3 CSTCRS1 Model for Coupled Solute Transport and CRS Consolidation

1. CSTCRS1 is based on a dual-Lagrangian framework that separately tracks the motions of fluid and solid phases. The consolidation algorithm accounts for vertical strain, general constitutive relationships, relative velocity of fluid and solid phases, changing compressibility and hydraulic conductivity during consolidation, and an external hydraulic gradient. Soil compressibility is rate-independent and, as such, CSTCRS1 is most appropriate for less structured soils. The solute transport algorithm accounts for advection, dispersion, linear and nonlinear sorption isotherm, and equilibrium and nonequilibrium sorption.
2. Verification checks of CSTCRS1 show excellent agreement with a validated numerical model in which CRS conditions were replicated using a time-dependent loading capability.
3. Numerical simulations were conducted to investigate the importance of initial concentration distribution, transport conditions, applied strain rate, initial specimen height, and drainage and concentration boundary conditions on CRS consolidation-induced solute transport. Results indicate that all of these factors

can significantly affect transport behavior, including effluent concentrations, solute mass outflows, and final concentration profiles.

4. For the conditions considered, solute mass outflow was generally found to increase with shorter initial specimen height, double drained boundary conditions, lower applied strain rate, advection/dispersion transport without sorption, and the specification of a zero concentration boundary condition.

8.4 Comparison of Consolidation-Induced Solute Transport for IL and CRS Loading

1. Incremental loading (IL) and CRS conditions produce significantly different responses during the course of a consolidation test, including applied stress, rate of settlement, excess pore pressure, and local strain.
2. For a given set of conditions, final solute mass outflows and final concentration profiles for IL and CRS tests were consistently in close agreement provided that the total test duration and final average strain were the same. Such agreement occurred for varying initial specimen height, initial concentration distribution, incremental loading procedure, transport condition, and top boundary concentration condition. Thus, final solute mass outflows were largely governed by total time and average strain and were relatively independent of the specific loading condition.

3. For a consistent set of conditions, solute mass outflows were not in close agreement during the course of IL and CRS tests, even if the total test duration and final average strain were the same. Prior to the end of the tests, solute mass outflows were consistently higher for IL conditions due to higher fluid outflow at the drainage boundary.

8.5 Consolidation-Induced Contaminant Transport through Landfill Liner Systems

1. Consolidation has an important effect on contaminant transport through compacted clay liner-based landfill liner systems, not only during the course of consolidation but also long after consolidation has ended. Consolidation has a lasting effect on contaminant transport because the consolidation process changes liner properties including liner thickness, porosity, hydraulic conductivity, seepage velocity, and effective diffusion coefficient, which subsequently changes the coupled transport process. Although consolidation is usually finished within short period of time (as compared to contaminant transport time), its influence on contaminant transport is long lasting and will not vanish with time.
2. Single CCL and composite GML/CCL liner systems are compared. It is shown that the composite GML/CCL liner has better contaminant containment performance than a single CCL liner. This is because GML inhibits the water flow and, thus, significantly decreases the transport attributed to advection.

3. Three analysis methods (denoted as C, NC-I, and NC-F) are compared to evaluate the effects of consolidation on contaminant transport. Method C simulation is the coupled consolidation-transport analysis and thus represents the most accurate results. Methods NC-I and NC-F simulations fail to consider the effect of consolidation on the transport process and, as a result, yield erroneous transport results including contaminant mass flux, cumulative contaminant mass outflow, and profiles of pore-water concentration and solid-phase concentration of contaminants. Even though average strain of the clay liner caused by consolidation is only a few percent, the NC-I simulation may, depending on conditions, overestimate or underestimate transport results by orders of magnitude throughout the simulation, especially during the consolidation stage. The NC-F simulation may overestimate or underestimate transport results by orders of magnitude in the early stages, but generally yield reasonable estimates of long-term transport results.
4. To obtain approximate estimations of long-term transport results or steady-state results, NC-F simulation is recommended over NC-I simulation, because NC-F can partially compensate for the effect of consolidation. To obtain accurate transport results for both consolidation stage and post-consolidation stage, however, it is recommended to perform a coupled consolidation-transport analysis (i.e., C simulation).
5. Liner thickness has important effect on consolidation-induced transport. The errors of NC-I and NC-F simulations increase with increasing liner thickness, especially during consolidation stage.

6. Load magnitude (i.e., waste height) has important effect on consolidation-induced transport. The errors of NC-I and NC-F simulations generally increase with increasing load magnitude.
7. Loading time (i.e., rate of waste placement) has important effect on consolidation-induced transport in the early stages, but has negligible effect in the late stages. Depending on conditions, the errors of NC-I and NC-F simulations in the early stages may increase or decrease with increasing loading time.
8. Organic carbon fraction of CCL has tremendous effect on consolidation-induced transport. The errors of NC-I and NC-F simulations increase dramatically with increasing organic carbon fraction. For CCL containing high organic carbon content, simulation without considering consolidation can lead to errors of orders of magnitude.
9. Effective diffusion coefficient exponent M has tremendous effect on consolidation-induced transport. The errors of NC-I and NC-F simulations increase dramatically with increasing M. For the conditions with $M > 1$, simulation without considering consolidation can lead to errors of orders of magnitude.

8.6 Recommendations for Future Research

The following topics are recommended for future research:

1. The current CCRS1 model is strain rate-independent and thus only appropriate for less structured soils. An upgraded version of CCRS1 model that accounts for strain rate-dependent constitutive relationship should be developed. Such a model will be advantageous for analyzing CRS consolidation tests of structured soils that exhibit strain rate dependence.
2. The coupled CRS consolidation and contaminant transport has been used investigated in this dissertation using CSTCRS1 numerical model. However, no experimental studies have been conducted to validate this model and the associated investigations. Such studies are needed.
3. The CST2 model is used to investigate the consolidation-induced contaminant transport through two compacted clay liner (CCL)-based landfill bottom liner systems: single CCL and composite Geomembrane/CCL. Geosynthethic clay liner (GCL) has been widely used as a component of liner system but is not investigated in this dissertation. Semipermeable membrane effects (e.g., solute restriction, chemico-osmosis) are found to be significant in GCL containing bentonite (Malusis and Shackelford 2002). CST2 should be adapted to account for the semipermeable membrane effects and investigate liner systems that include GCL.

Appendix A

CS3: Large Strain Consolidation Model for Layered Soils

A.1 Introduction

Fox and Berles (1997) presented a piecewise-linear numerical model, called CS2, for one-dimensional large strain consolidation of a single homogeneous saturated soil layer. CS2 accounts for vertical strain, general constitutive relationships, soil self-weight, relative velocity of fluid and solid phases, and changing material properties during consolidation. An enhanced version of CS2, with the ability to accommodate time-dependent loading, unload/reload, and an external hydraulic gradient, was presented by Fox and Pu (2012). In the CS2 method, all variables pertaining to geometry, material properties, fluid flow, and effective stress are updated at each time step with respect to a fixed coordinate system. Mass conservation is strictly enforced using a Lagrangian approach that follows the motion of the solid phase throughout the consolidation process.

Soil constitutive relationships are specified using discrete data points and do not require mathematical approximations or derivative functions. These features give CS2 high accuracy and considerable versatility to accommodate additional effects with excellent results. Using the CS2 method, subsequent large strain consolidation models have been developed to investigate accreting layers (Fox 2000), vertical and radial flows (Fox et al. 2003), compressible pore fluid (Fox and Qiu 2004), high-gravity conditions in a geotechnical centrifuge (Fox et al. 2005; Lee and Fox 2005), coupled solute transport (Fox 2007a, 2007b; Fox and Lee 2008; Lee and Fox 2009; Pu and Fox 2014), wave propagation (Qiu and Fox 2008), and consolidation under constant rate of strain (Pu et al. 2013; Fox et al. 2014). These studies have extensively verified the accuracy of the CS2 method using analytical solutions, numerical solutions, and experimental data, including solutions obtained using material coordinates (Gibson et al. 1967) and the moving boundary approach of Lee and Sills (1979). CS2 and related models have also been widely used by other researchers for new applications and to validate numerical analyses (Aydilek et al. 2000; Berilgen et al. 2000; Kokusho and Kojima 2002; Berilgen 2004; Bicer 2005; Berilgen et al. 2006; Kwon et al. 2007; Lewis 2009; Meric et al. 2010; Bharat and Sharma 2011; Lee and Park 2013). Most recently, the CS2 method has been adapted to model electro-osmotic consolidation (Zhou et al. 2013), and coupled contaminant transport (Meric et al. 2013) with impressive results.

An important capability not included in the above models is layered soil heterogeneity (i.e., multiple layers), which often occurs in practical applications. Previous research on consolidation of layered soils has been primarily conducted within the context of small (i.e., infinitesimal) strain theory. Assuming small strains, linear soil

compressibility, and a constant coefficient of consolidation, Schiffman and Stein (1970) developed an analytical solution for one-dimensional consolidation of layered soils with general boundary conditions, initial conditions, and loading history. Lee et al. (1992) improved on this work and presented a more explicit form of the solution. Other researchers have also made valuable contributions on consolidation modeling for layered soils under small strain conditions, including methods to account for depth-dependent loading (Zhu and Yin 1999a), partially drained boundaries (Xie et al. 1999), nonlinear soil compressibility (Xie et al. 2002), vertical and radial flows (Tang and Onitsuka 2001; Nogami and Li 2002, 2003; Wang and Jiao 2004; Walker et al. 2009) and various solution techniques such as finite differences (Hazzard et al. 2008; Kim and Mission 2011), differential quadrature (Chen et al. 2005), matrix transfer (Nogami and Li 2002, 2003), and the spectral method (Walker et al. 2009). Perrone (1998) developed the elasto-visco-plastic finite element model CONSOL97, which can simulate consolidation of layered soils with time-dependent compressibility (i.e., creep) effects. This model uses an incremental small strain approach with a coefficient of consolidation that varies with effective stress. Zhu and Yin (1999b) likewise developed a small strain, elasto-visco-plastic model for layered clay soils using the finite element method. Mesri and Choi (1985) developed the finite difference model ILLICON using finite strain theory, which accounts for time-dependent loading, depth-dependent applied stress, changing material properties, and secondary compression.

Piecewise-linear consolidation models are generally considered to have excellent versatility with regard to initial conditions, boundary conditions, and material heterogeneity (Townsend and McVay 1990). This chapter presents a piecewise-linear

model for one-dimensional large strain consolidation of layered soils called CS3 (Consolidation Settlement 3). CS3 has all the capabilities of the original CS2 code (Fox and Berles 1997) and, in addition, accounts for layered heterogeneity, unload/reload effects, time-dependent loading and boundary head conditions, an external hydraulic gradient, and variable profiles for preconsolidation stress and applied stress increment. Constitutive relationships are defined in terms of conventional parameters, as opposed to individual data points in CS2, and allow for direct input of laboratory and field data to facilitate modeling for practical applications. The development of CS3 is first described and is followed by verification checks. Several numeric examples are provided to illustrate the effects of large strain, multiple layers, preconsolidation stress profile, and stress increment profile on soil consolidation behavior. Finally, settlement estimates obtained using CS3 are compared with field measurements for the Gloucester test fill.

A.2 Model Description

CS3 was developed using CS2 as a point of departure and follows similar procedures with regard to geometry, effective stress, fluid flow, and settlement (Berles 1995; Fox and Berles 1997; Fox and Pu 2012). The Lagrangian framework of CS2 is well suited for multi-layer analysis because layer interfaces are automatically tracked and mass balance is satisfied by consideration of interlayer fluid flows. The following sections summarize the CS3 model with focus on its new capabilities.

A.2.1 Geometry

A saturated compressible soil stratum has initial height H_{To} and contains R_i horizontal layers. The initial geometry, prior to application of load at time t = 0, is shown in Figure A.1. The stratum is sufficiently wide that all quantities vary only in the vertical direction and consolidation can be treated as one-dimensional. Vertical coordinate z and layer coordinate i are defined as positive upward from a fixed datum at the base of the stratum. Each layer i has initial height $H_{o,i}$, material properties given by a soil "sample" at initial elevation $z_{os,i}$, and $R_{j,i}$ vertical elements. The total number of elements for the stratum is $R_T \left(= \sum_{i=1}^{R_i} R_{j,i} \right)$. Layer elevation coordinate z_i and layer element coordinate j are defined as positive upward from the base of each layer. Each element j of layer i has unit cross-sectional area (plan view), initial height $L_{o,i}$, specific gravity of solids $G_{s,i}$, a central node at initial elevation $z_{o,i,j}$, and initial void ratio $e_{o,i,j}$. Nodes translate vertically and remain at the center of their respective elements throughout the consolidation process. Top and bottom boundaries for the stratum can be specified as drained or undrained, and if drained, are assigned individual total head values, h_{to} and h_{bo}, respectively, taken with respect to the datum. The stratum contains no internal drainage layers. Internal drainage layers can be treated by modeling separately each section of the stratum.

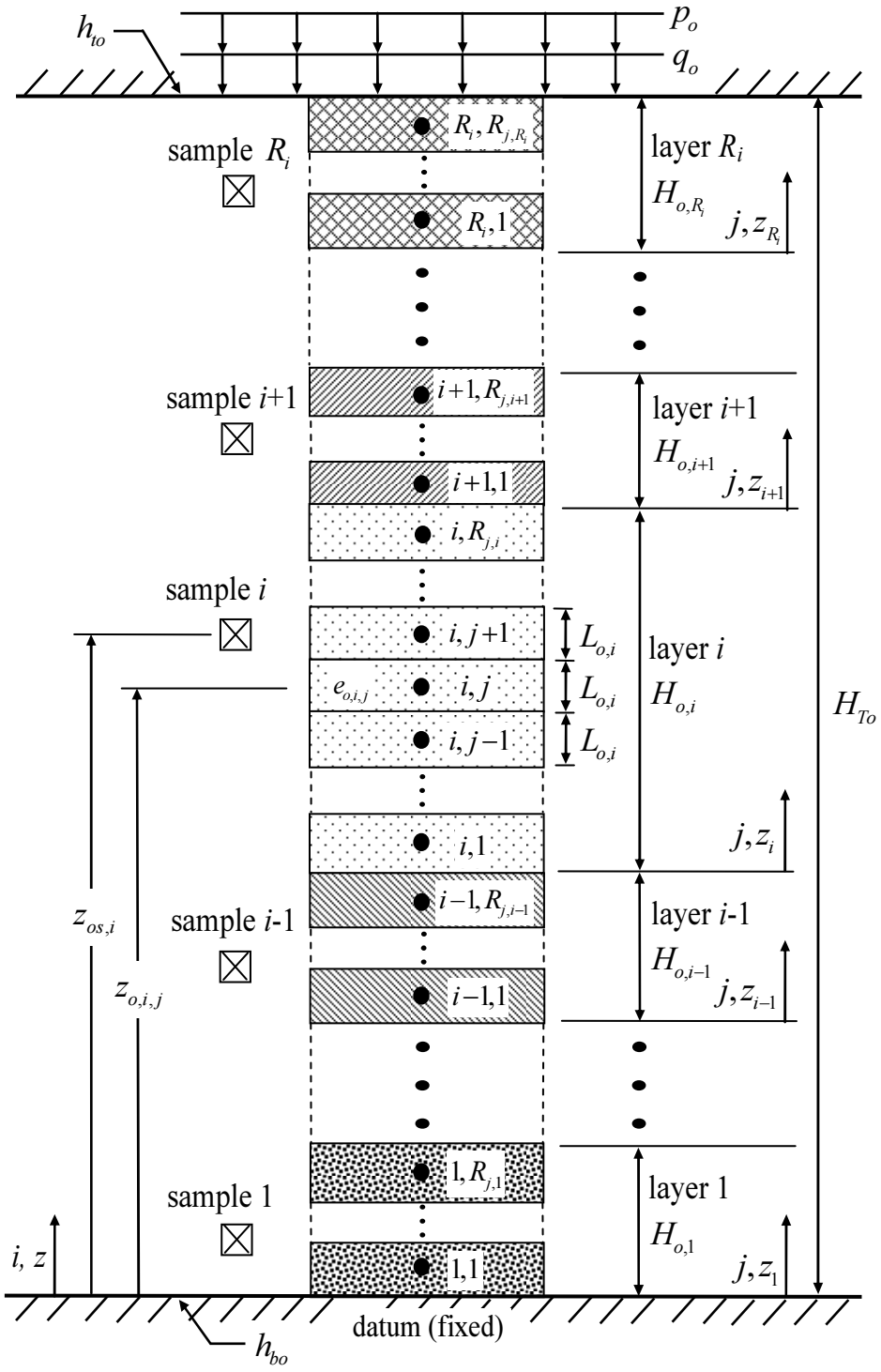

Figure A.1 Initial geometry for CS3.

A.2.2 Constitutive Relationships

Rather than defining constitutive relationships using discrete data points as in CS2, which can be burdensome for multiple soil layers, constitutive relationships are defined in CS3 using conventional log-linear parameters for each layer. The compressibility relationship is shown in Figure A.2(a). Each element is characterized as normally consolidated (NC) or overconsolidated (OC). If NC, the compressibility relationship is defined by $e_{o,i,j}$ and compression index $C_{c,i}$. If OC, the compressibility relationship is defined by $e_{o,i,j}$, preconsolidation stress $\sigma'_{p,i,j}$, recompression index $C_{r,i}$, and $C_{c,i}$. The preconsolidation stress for an element is defined as the maximum past vertical effective stress at the corresponding node. Throughout a CS3 simulation, values of preconsolidation stress $\sigma''^{t}_{p,i,j}$ and corresponding void ratio $e^{t}_{p,i,j}$ are maintained for each element. If the vertical effective stress decreases below $\sigma''^{t}_{p,i,j}$, unloading and reloading follow an identical path defined by $\sigma''^{t}_{p,i,j}$, $e^{t}_{p,i,j}$, and $C_{r,i}$.

Hydraulic conductivity for each element, is defined by a log-linear relationship between vertical hydraulic conductivity k and void ratio e, shown in Figure A.2(b), where $C'_{k,i} = \Delta \log k / \Delta e$ is the reciprocal of the parameter C_k defined by Tavenas et al. (1983). CS3 uses the same hydraulic conductivity relationship for NC and OC conditions, which is consistent with the findings of Al-Tabbaa and Wood (1987), Nagaraj et al. (1994), and Fox (2007b). Aside from unload/reload effects, a one-to-one correspondence is assumed for each constitutive relationship in Figure A.2. Thus, CS3

does not account for the effects of strain rate, secondary compression, or aging on the compressibility or hydraulic conductivity of the soil.

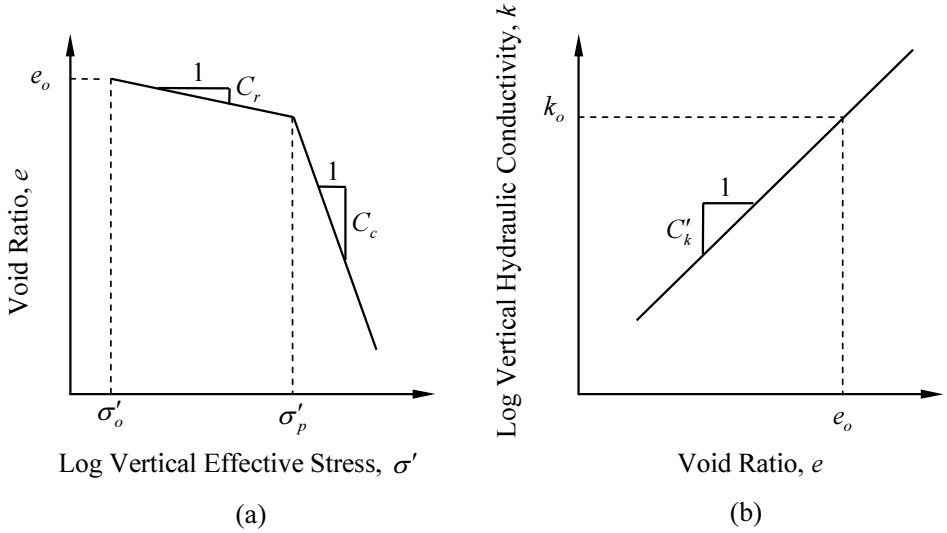

Figure A.2 Soil constitutive relationships: (a) compressibility; (b) hydraulic conductivity.

A.2.3 Soil Sample Points

Material properties for each soil layer are defined at a single elevation, or "sample" point, within the layer (Figure A.1). Sample points may correspond to actual in situ soil sampling locations or fictitious locations chosen by the user based on other considerations. The following properties are constant for the i^{th} soil layer and are taken from the corresponding i^{th} soil sample: $G_{s,i}$, $C_{r,i}$, $C_{c,i}$, and $C'_{k,i}$. The following properties are also taken at the location of the i^{th} soil sample but vary vertically within the layer: initial void ratio $e_{os,i}$, initial preconsolidation stress $\sigma'_{ps,i}$, and initial vertical hydraulic conductivity, $k_{os,i}$. Soil sample properties can be measured using laboratory

and field tests or estimated from empirical correlations (Azzouz et al. 1976; Kulhawy and Mayne 1990).

A.2.4 Preconsolidation Stress Profile

The profile of preconsolidation stress σ'_p for each layer is characterized using one of four methods: 1) constant preconsolidation stress σ'_p, 2) constant overconsolidation ratio OCR = σ'_p / σ'_o, 3) constant preconsolidation stress difference $\Delta\sigma' = \sigma'_p - \sigma'_o$, and 4) user-defined preconsolidation stress, where σ'_o is the initial vertical effective stress. Each method is illustrated in Figure A.3.

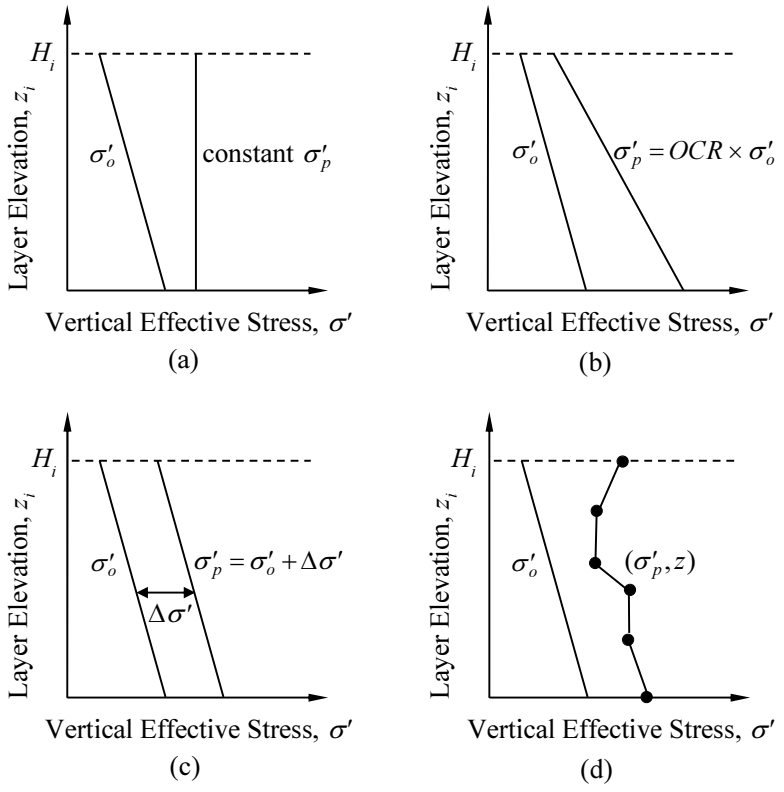

Figure A.3 Profiles for preconsolidation stress: (a) constant σ'_p; (b) constant OCR; (c) constant $\Delta\sigma'$; (d) user-defined.

A.2.5 Initial Applied Stress Distribution

CS3 calculates initial vertical total stress σ_o as the sum of soil self-weight and applied stresses at the top of the stratum. The initial applied effective stress at each node i, j consists of a depth-independent component q_o and a depth-dependent component $F_{i,j} p_o$, where p_o is the value at the top of the stratum and $F_{i,j}$ is a fraction between 0 and 1 used to account for stress distribution effects with depth. Although not strictly applicable to 1-D conditions, depth-dependent applied stress components are a useful approximation for many practical applications. Values of $F_{i,j}$ are specified for the entire stratum using one of three methods: 1) linear, 2) bilinear, and 3) user-defined. Each method is illustrated in Figure A.4, where F_t, F_m, and F_b indicate values at the top, middle, and bottom of the stratum, respectively.

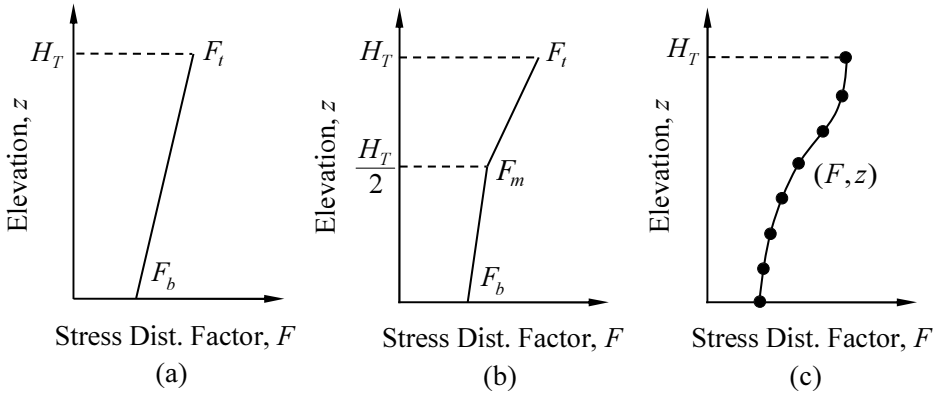

Figure A.4 Profiles for stress distribution factor: (a) linear; (b) bilinear; (c) user-defined.

A.2.6 Initial Void Ratio Distribution

A distribution of initial void ratio is needed to begin a CS3 simulation. This distribution can be in equilibrium or nonequilibrium with initial stress conditions and soil material properties. Once obtained, the initial void ratio distribution is used to calculate a value of initial hydraulic conductivity for each element.

A.2.6.1 Equilibrium

Iteration is used to calculate an initial void ratio distribution within each layer that is in equilibrium with initial stress conditions, soil self-weight and constitutive relationships, and seepage forces due to an external hydraulic gradient acting across the stratum (if $h_{to} \neq h_{bo}$). In this case, initial excess pore pressures (i.e., the difference between total and steady state pore pressures) are zero. For the first iteration loop, CS3 calculates the initial buoyant unit weight of each i^{th} soil sample as $\gamma'_{os,i} = \gamma_w (G_{s,i} - 1)/(1 + e_{os,i})$. Using these values and starting at the top of the stratum with known values of q_o, p_o and $F_{i,j}$, the initial vertical effective stress is calculated at each sample location $\sigma'_{os,i}$ and at the node for each element $\sigma'_{o,i,j}$. CS3 uses the initial condition of sample i ($\sigma'_{os,i}$, $e_{os,i}$), along with $C_{r,i}$, $C_{c,i}$, $\sigma'_{p,i,j}$ and $\sigma'_{o,i,j}$, to estimate the initial void ratio $e_{o,i,j}$ for all elements in each layer i. These estimates are then used to re-calculate the initial buoyant unit weight of each element $\gamma'_{o,i,j}$, which yields new values of $\sigma'_{os,i}$, $\sigma'_{o,i,j}$, and $e_{o,i,j}$. This process is repeated until changes in $\sigma'_{o,s,i}$ and $\sigma'_{o,i,j}$ become negligible for successive iterations. If an external hydraulic gradient is present,

the iteration procedure includes an additional loop to account for associated seepage forces (Fox and Pu 2012).

A.2.6.2 Nonequilibrium

CS3 can also accommodate a user-defined distribution of initial void ratio. The most common example is a uniform e_o profile. User-defined initial void ratios will generally not be in equilibrium with initial conditions and soil material properties, which produces nonzero values of excess pore pressure within the stratum at the start of loading.

A.2.7 Application of Surcharge Load

Surcharge load is applied to the stratum beginning at $t = 0$. The vertical effective stress at the top boundary is equal to $q' + p'$, where $q' = q_o + \Delta q'$ and $p' = p_o + \Delta p'$, and effective stress increments $\Delta q'$ and $\Delta p'$ can vary independently with time. The value of $\Delta q'$ is constant with depth, whereas the effect of $\Delta p'$ changes with depth according to the stress distribution factor $F_{i,j}$ (Figure A.4). Thus, the applied effective stress at node i, j is equal to $q' + F_{i,j} p'$ and values of $F_{i,j}$ are assumed to remain constant during consolidation. Boundary head values, h_t' and h_b', can also vary independently with time. In response to surcharge loading, excess pore pressures generated within the layer cause fluid flow to all drainage boundaries. Soil deformation is one-dimensional and occurs in response to the net fluid outflow from each element. Void ratio is assumed to remain uniform within each element throughout the consolidation process. At time t, the total

height of the stratum is H_T^t, height of the i^{th} layer is H_i^t, height of the j^{th} element is $L_{i,j}^t$, and elevation of any node i, j is $z_{i,j}^t$.

A.2.8 Stress, Pore Pressure, Fluid Flow and Settlement

The vertical total stress at node i, j is obtained from the applied stress conditions and self-weight of overlying elements as,

$$\sigma_{i,j}^t = q^t + F_{i,j} p^t + \left(h_t^t - H_T^t\right)\gamma_w + \frac{L_{i,j}^t \gamma_{i,j}^t}{2} + \sum_{b=j+1}^{R_{j,i}} L_{i,b}^t \gamma_{i,b}^t + \sum_{a=i+1}^{R_i} \sum_{b=1}^{R_{j,a}} L_{a,b}^t \gamma_{a,b}^t$$

$$i = 1, 2, ..., R_i \quad j = 1, 2, ..., R_{j,i} \qquad \text{(A.1)}$$

where $\gamma_{i,j}^t \left(= \gamma_w \frac{G_{s,i} + e_{i,j}^t}{1 + e_{i,j}^t}\right)$ is the saturated unit weight of element i, j, and $e_{i,j}^t$ is the corresponding void ratio. Vertical effective stress $\sigma_{i,j}^{\prime t}$ is calculated from $e_{i,j}^t$ and the compressibility relationship of the corresponding layer. Unload/reload effects are taken into account if $\sigma_{i,j}^{\prime t} < \sigma_{p,i,j}^{\prime t}$.

The pore pressure at node i, j is the difference between total and effective stresses,

$$u_{i,j}^t = \sigma_{i,j}^t - \sigma_{i,j}^{\prime t} \qquad i = 1, 2, ..., R_i \quad j = 1, 2, ..., R_{j,i} \qquad \text{(A.2)}$$

Pore pressures are used to calculate fluid flow between contiguous elements. The relative discharge velocity (positive upward) between nodes i, j and $i, j+1$ is

$$v_{rf,i,j}^{t} = -\left(\frac{k_{i,j+1}^{t} k_{i,j}^{t} \left(L_{i,j+1}^{t} + L_{i,j}^{t} \right)}{L_{i,j+1}^{t} k_{i,j}^{t} + L_{i,j}^{t} k_{i,j+1}^{t}} \right) \left(\frac{h_{i,j+1}^{t} - h_{i,j}^{t}}{z_{i,j+1}^{t} - z_{i,j}^{t}} \right)$$

$$i = 1, 2, ..., R_i \qquad j = 1, 2, ..., R_{j,i} - 1 \quad \text{(A.3)}$$

where $h_{i,j}^{t}$ $(= z_{i,j}^{t} + \frac{u_{i,j}^{t}}{\gamma_w})$ is the total hydraulic head at node i, j and $k_{i,j}^{t}$ is the vertical hydraulic conductivity of element i, j. Corresponding expressions are used at interfaces between contiguous layers (i.e., between node $i, R_{j,i}$ and node $i+1,1$), as well as at the top and bottom boundaries of the stratum.

Once the relative discharge velocities are known, a new height is calculated for each element from the net fluid outflow over time increment Δt,

$$L_{i,j}^{t+\Delta t} = L_{i,j}^{t} - (v_{rf,i,j}^{t} - v_{rf,i,j-1}^{t})\Delta t \qquad i = 1, 2, ..., R_i \qquad j = 1, 2, ..., R_{j,i} \quad \text{(A.4)}$$

where Δt is defined by Fox and Pu (2012). New values of void ratio, layer height, stratum height, settlement, and average degree of consolidation are then calculated as

$$e_{i,j}^{t+\Delta t} = \frac{L_{i,j}^{t+\Delta t}(1 + e_{o,i,j})}{L_{o,i}} - 1 \qquad i = 1, 2, ..., R_i \qquad j = 1, 2, ..., R_{j,i} \quad \text{(A.5)}$$

$$H_i^{t+\Delta t} = \sum_{j=1}^{R_{j,i}} L_{i,j}^{t+\Delta t} \qquad i = 1, 2, ..., R_i \quad \text{(A.6)}$$

$$H_T^{t+\Delta t} = \sum_{i=1}^{R_t} H_i^{t+\Delta t} \quad \text{(A.7)}$$

$$S^{t+\Delta t} = H_{To} - H_T^{t+\Delta t} \quad \text{(A.8)}$$

$$U_{avg}^{t+\Delta t} = \frac{S^{t+\Delta t}}{S_{ult}} \quad \text{(A.9)}$$

where S_{ult} is the ultimate settlement corresponding to 100% consolidation. The final void ratio distribution, and hence S_{ult}, can be calculated at the beginning of a simulation

if the final data point is the largest value in the surcharge loading schedule. Otherwise, unloading will occur, S_{ult} will not be known a priori, and U_{avg} values are not calculated during the course of a simulation.

The preceding method ensures that the weight of solids contained within each element is invariant throughout the consolidation process (Fox and Berles 1997). Solid particles do not cross from one element to the next and element nodes and interfaces, as well as layer interfaces, can be considered as embedded in the soil skeleton. As such, the method follows the motion of the solid phase and consideration of relative discharge velocity between contiguous elements is sufficient to ensure mass balance.

A.3 Model Performance

A.3.1 Verification

Example A.1 is used to compare the results of CS3 simulations to those obtained using small strain theory. A double-drained clay stratum has an initial total height of 11 m, contains three layers, and is in equilibrium under an initial effective overburden stress of 40 kPa. Layer properties are provided in Table A.1, where $a_{v,i}$ is the coefficient of compressibility ($=-\Delta e/\Delta\sigma'$) for layer i and soil sample locations are taken at the mid-height of each layer. A small modification to CS3 was necessary to accommodate constant values of a_v. Total heads at the top and bottom boundaries are 11 m (constant), soil self-weight is neglected ($G_s = 1$), and the initial void ratio is constant within each layer. At $t = 0$, a uniform ($p = 0$), instantaneous, and very small vertical effective stress

increment of Δq = 0.001 kPa is applied to the stratum, which yields a final average strain of 2.6×10^{-6}. The coefficient of compressibility, hydraulic conductivity, and coefficient of consolidation $c_{v,i}$ are constant for each layer during consolidation. Table A.2 compares values of U_{avg} obtained as a function of time from the analytical solution of Lee et al. (1992) and four CS3 simulations performed for $R_{j,i}$ = 50, 100, 200, and 300. Values are in good to excellent agreement and the accuracy of CS3 improves with increasing numerical resolution (i.e., increasing R_T). Table A.3 compares vertical profiles of excess pore pressure for elapsed times of 36, 650, and 2400 d, which approximately correspond to U_{avg} = 10%, 50%, and 90%, respectively. Values obtained from CS3 (R_T = 300) are essentially in exact agreement with the analytical solutions.

No analytical solutions exist for large strain consolidation of layered soils. However, CS2 produces results that are essentially identical to analytical solutions for large strain consolidation of a single layer (Fox and Berles 1997) and CS3 simulations exactly match those obtained from CS2 for R_i = 1. This agreement and the above agreement for small strains, which indicates that CS3 correctly handles boundary and layer interface conditions, strongly suggest that CS3 is valid for simulation of large strain consolidation of layered soils.

Table A.1 Soil layer properties for Examples A.1 and A.2.

Layer i	$H_{o,i}$ (m)	$z_{os,i}$ (m)	$e_{os,i}$	$a_{v,i}$ ($\times 10^{-3}$ /kPa)	$k_{os,i}$ ($\times 10^{-9}$ m/s)	$C'_{k,i}$
1	4	2	0.8	3	2	0
2	5	6.5	1.5	9	20	0
3	2	10	1.2	4	4	0

Table A.2 Average degree of consolidation for Example A.1.

Time, t (d)	Average degree of consolidation, U_{avg} (%)				
	Lee et al. (1992) theory	CS3 $R_{j,i} = 50$ $R_T = 150$	CS3 $R_{j,i} = 100$ $R_T = 300$	CS3 $R_{j,i} = 200$ $R_T = 600$	CS3 $R_{j,i} = 300$ $R_T = 900$
1	1.692	1.662	1.685	1.691	1.692
5	3.784	3.772	3.781	3.783	3.784
10	5.352	5.343	5.350	5.351	5.351
50	11.978	11.974	11.977	11.978	11.978
100	17.128	17.125	17.127	17.128	17.128
500	43.649	43.648	43.649	43.649	43.649
1000	64.510	64.509	64.510	64.510	64.510
5000	99.113	99.113	99.113	99.113	99.113

Table A.3 Excess pore pressure profiles for Example A.1.

Elevation z	Excess pore pressure, u_{ex} ($\times 10^{-4}$ kPa)					
	t = 36 d		t = 650 d		t = 2400 d	
	A	B	A	B	A	B
10.01	6.036	6.036	2.591	2.591	0.517	0.517
9.01	9.539	9.539	5.087	5.087	1.015	1.015
8.025	9.870	9.870	5.531	5.531	1.103	1.103
7.025	9.971	9.971	5.861	5.861	1.169	1.169
6.025	9.995	9.995	6.081	6.081	1.212	1.212
5.025	9.999	9.999	6.188	6.188	1.233	1.233
4.025	10.000	10.000	6.178	6.178	1.230	1.230
3.02	9.995	9.995	5.235	5.235	1.034	1.034
2.02	9.794	9.794	3.806	3.806	0.747	0.747
1.02	7.576	7.577	2.020	2.020	0.394	0.394

A = Lee et al. (1992)
B = CS3 ($R_{j,i}$ = 100; R_T = 300)

A.3.2 Parametric Study

A.3.2.1 Large Strain

Example A.2 illustrates the effect of large strain on rate of consolidation for the same soil stratum as described in Table A.1. Three simulations were conducted using CS3 ($R_{j,i}$ = 200) and the results are shown in Figure A.5. Values of U_{avg} for the first simulation correspond to small strain conditions with Δq = 0.001 kPa and constant soil properties as in Table A.1. For the second simulation, soil properties were unchanged but the stress increment was increased to Δq = 100 kPa to yield a final settlement of 2.83 m and a final vertical strain of 26%. Figure A.5 indicates that the rate of settlement for this

case increases slightly due to the progressively shorter drainage distance for pore water outflow from the stratum. The third simulation was identical to the second except that hydraulic conductivity was permitted to decrease with void ratio according to $C'_{k,i} = 2/e_{os,i}$, which reflects realistic conditions for many clay soils (Tavenas et al. 1983; Mesri et al. 1994). Allowing for variable hydraulic conductivity produces a four-fold increase in the time for U_{avg} = 95% as compared to the large strain case with constant k.

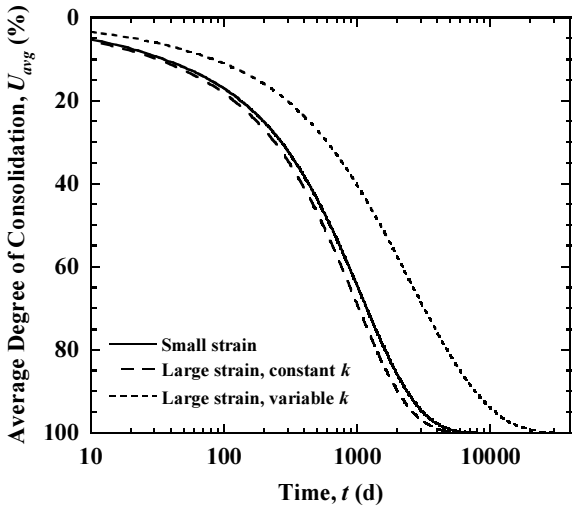

Figure A.5 Average degree of consolidation for Example A.2.

A.3.2.2 Multiple Layers

Example A.3 illustrates the effect of multiple layers on consolidation behavior. A double-drained stratum is defined by H_{To} = 9 m, G_s = 2.7, q_o = 20 kPa, $h_t = h_b$ = 9 m (constant), and the remaining values in Table A.4. The distribution of initial void ratio is in equilibrium with applied stress conditions and soil self-weight. An instantaneous and constant stress increment of Δq = 250 kPa is applied to the stratum and is uniform with

depth (p = 0). CS3 simulations were conducted for three cases (R_T = 300). Case 1 models the stratum as a single layer. Case 2 and Case 3 model the stratum using three layers with initial heights of 3 m and varying material properties. Case 3 considers a larger range of initial void ratio and compressibility and hydraulic conductivity properties than Case 2; however, average parameter values for both Case 2 and Case 3 are equal to values for Case 1. The preconsolidation stress is initially constant within each layer.

Table A.4 Soil layer properties for Example A.3.

Case	Layer i	$H_{o,i}$ (m)	$z_{os,i}$ (m)	$e_{os,i}$	$\sigma'_{ps,i}$ (kPa)	$C_{c,i}$	$C_{r,i}$	$k_{os,i}$ ($\times 10^{-9}$ m/s)	$C'_{k,i}$
1	1	9	4.5	2.5	100	1	0.1	2	0.8
2	1	3	1.5	2	125	1.25	0.125	1	1
	2	3	4.5	2.5	100	1	0.1	2	0.8
	3	3	7.5	3	75	0.75	0.075	3	0.6
3	1	3	1.5	1.5	150	1.5	0.15	0.5	1.1
	2	3	4.5	2.5	100	1	0.1	2	0.8
	3	3	7.5	3.5	50	0.5	0.05	3.5	0.5

Figure A.6 presents settlement and settlement ratio as a function of time for Example A.3, where settlement ratio is defined as settlement for Case 1 (single layer stratum) divided by settlement for Case 2 or Case 3 (multi-layer stratum). The use of compressibility properties with consistent average values produces final settlements that are nearly equal for all three cases. Prior to final settlement, maximum values of settlement ratio are 1.06 and 1.19 for Case 2 and Case 3, respectively. Consolidation for Cases 2 and 3 occurs more slowly than for Case 1, which results from the preponderant

effect of lower hydraulic conductivity in layer 1 for the multi-layer simulations. Figure A.7 compares profiles of excess pore pressure u_{ex} at t = 30, 300, and 1000 d. At t = 0, the initial excess pore pressure is uniform and equal to the applied surcharge (250 kPa) for each case. Pressures then dissipate in response to the distribution of material properties within the stratum. At t = 30 d, the Case 1 profile displays slight asymmetry due to the effect of soil self-weight and the transition from overconsolidated (OC) conditions near the center to normally consolidated (NC) conditions near the boundaries. Corresponding profiles for Case 2 and Case 3 show greater asymmetry due to greater soil heterogeneity. With increasing time, the effect of low hydraulic conductivity for layer 1 becomes more pronounced for the multi-layer simulations and causes the location of maximum excess pore pressure to skew toward the bottom of the stratum.

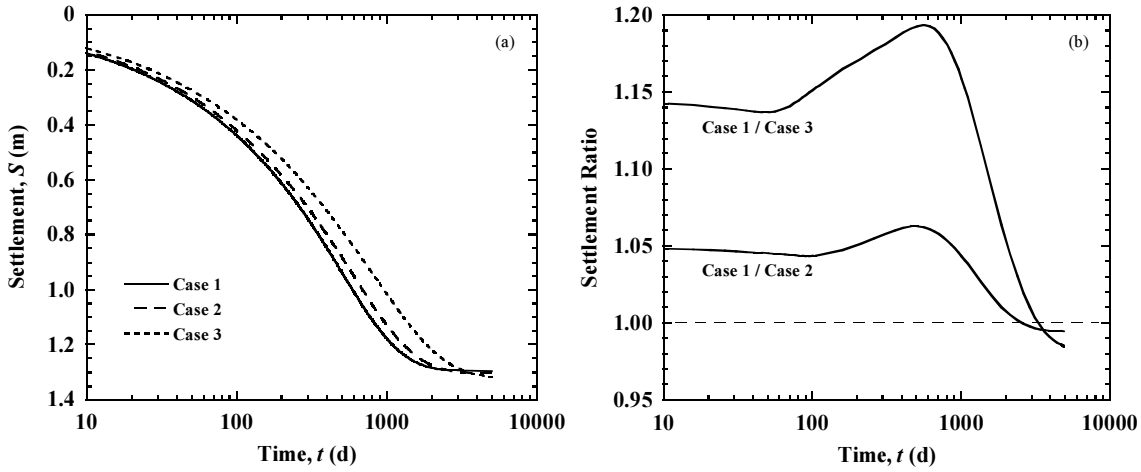

Figure A.6 Comparison of three cases for Example A.3: (a) settlement; (b) settlement ratio.

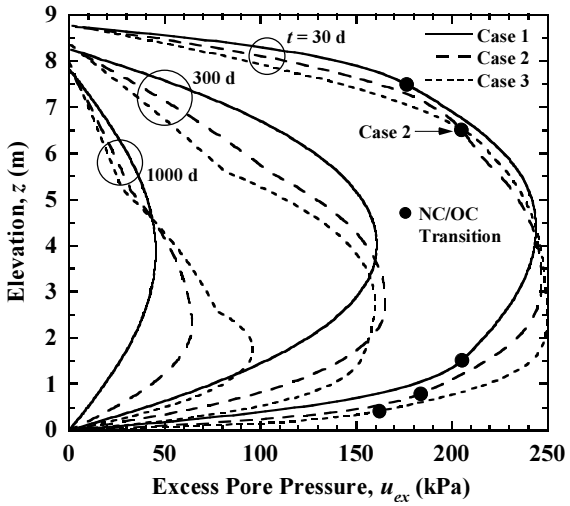

Figure A.7 Excess pore pressure profiles for Example A.3.

A.3.2.3 Preconsolidation Stress Profile

Example A.4 investigates the effect of preconsolidation stress profile. A single layer is defined by Case 1 in Example A.3 and three preconsolidation stress profiles shown in Figure A.8. The profiles pass through a common point at the mid-height of the layer and correspond to constant σ'_p = 100 kPa, constant OCR = 2.42, and constant $\Delta\sigma'$ = 58.6 kPa. Settlement curves are shown in Figure A.9 and indicate that, with the same average σ'_p, settlements are nearly identical. Other simulations (not shown) have however indicated larger deviations when the common point occurs either above or below the mid-height of the layer and the average σ'_p value is not the same. Profiles of excess pore pressure are shown in Figure A.10 for t = 30, 300, and 1000 d. Surcharge loading again produces a uniform initial excess pore pressure of 250 kPa. Thereafter, the curves display trends consistent with the initial distribution of $\sigma'_p - \sigma'_o$. Higher excess

pore pressures are observed at locations with lower initial values of $\sigma'_p - \sigma'_o$ because the soil transitions to NC earlier in the consolidation process. This transition produces a corresponding increase in compressibility and reduction in hydraulic conductivity, both of which slow the process of excess pore pressure dissipation.

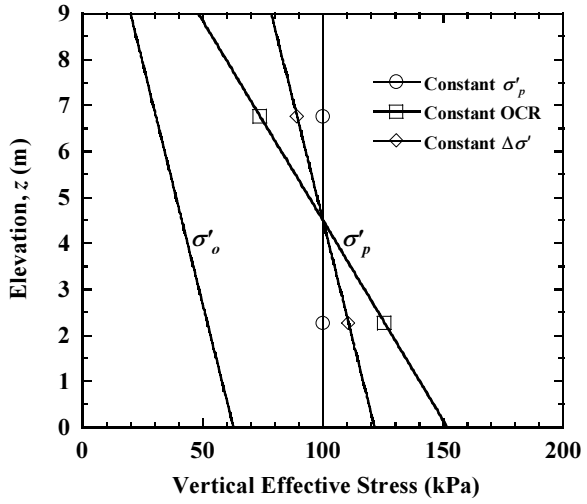

Figure A.8 Profiles of initial effective stress and preconsolidation stress for Example A.4.

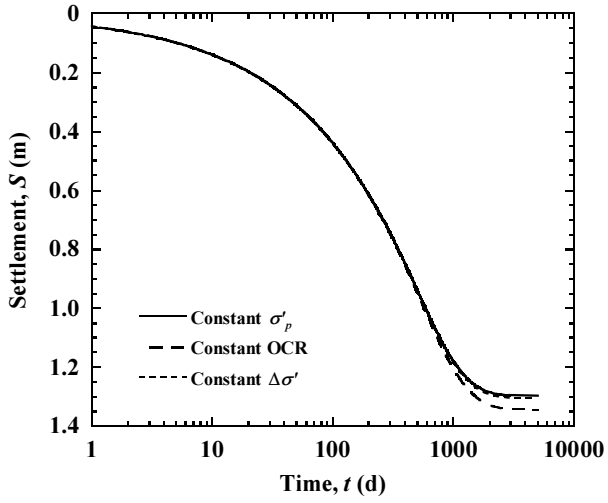

Figure A.9 Settlement curves for Example A.4.

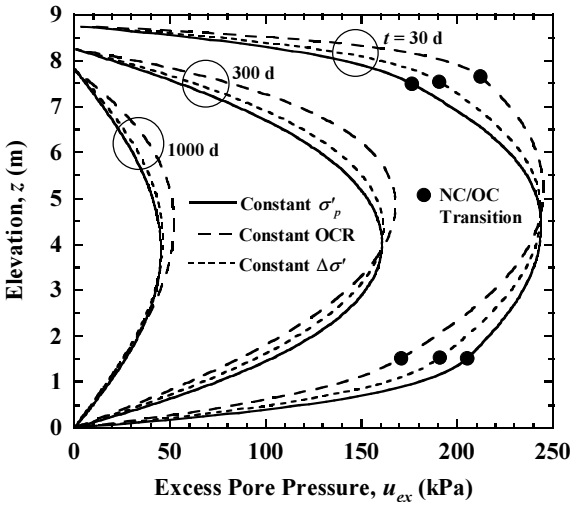

Figure A.10 Excess pore pressure profiles for Example A.4.

A.3.2.4 Stress Increment Profile

To investigate the effect of stress reduction with depth, Example A.5 again considers a single layer defined by Case 1 in Example A.3. The layer is subjected to a finite area loading. Using elastic theory, the loading yields the stress increment profile shown in Figure A.11 and includes vertical stress increments at the top $\Delta\sigma_t$, middle $\Delta\sigma_m$, and bottom $\Delta\sigma_b$ of 250 kPa, 118 kPa, and 55 kPa, respectively. Five other stress increment profiles are also shown: 1) uniform Δq = 250 kPa, 2) linear (Figure A.4a), 3) uniform approximation Δq_{avg} (= 152.2 kPa) to linear, 4) bilinear (Figure A.4b), and 5) uniform approximation Δq_{avg} (= 129.5 kPa) to bilinear. Uniform approximations to the linear and bilinear stress increment profiles were calculated as a weighted average using Simpson's rule,

$$\Delta q_{avg} = \frac{\Delta\sigma_t + 4\Delta\sigma_m + \Delta\sigma_b}{6} \tag{A.10}$$

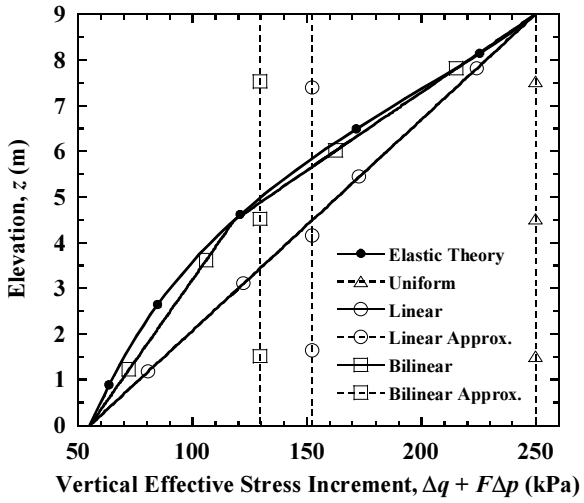

Figure A.11 Stress increment profiles for Example A.5.

CS3 simulations for settlement are shown in Figure A.12. The elastic theory profile was modeled using 43 data points (Figure A.4c) and yields a final settlement of 0.68 m. The uniform Δq = 250 kPa profile yields a final settlement of 1.3 m and indicates that failure to consider applied stress reduction with depth can produce significant error in calculated settlements. Settlements for the linear and bilinear profiles are also overestimated but are in much closer agreement to settlements calculated using the elastic theory profile (final settlement error = 20% for linear and 4% for bilinear). Interestingly, uniform loading using the Simpson's rule approximation produces very close estimates of settlement for the linear and bilinear profiles in this example. Likewise, it is also interesting that U_{avg} curves (not shown) are essentially identical for all six stress increment profiles. However, corresponding excess pore pressures for t = 30 d, shown in Figure A.13, indicate that although the settlement curves may be in close

agreement, excess pore pressures generated using Simpson's rule approximations, which do not capture the initial variation of excess pore pressure with depth, can be in substantial error.

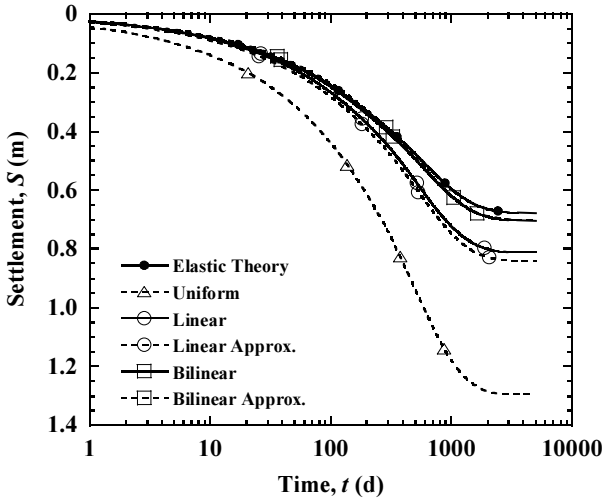

Figure A.12 Settlement curves for Example A.5.

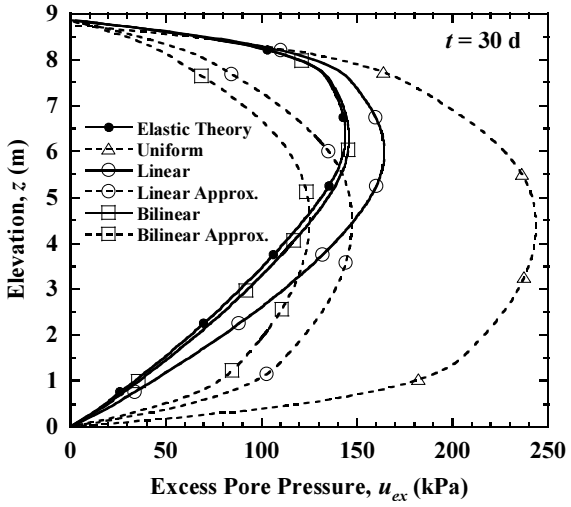

Figure A.13 Excess pore pressure profiles for Example A.5.

A.4 Case Study: Gloucester Test Fill

The Gloucester test fill was constructed in 1967 by the National Research Council of Canada at a location 21 km south of Ottawa, Canada. Information and data for the project were obtained primarily from Bozozuk (1972), Bozozuk and Leonards (1972), Lo et al. (1976), Leroueil et al. (1983), and Hinchberger and Rowe (1998). Subsurface conditions are described in Table A.5. The upper 1.8 m consisted of top soil and a thin desiccated crust. Below the crust were six layers of marine silty clays with sensitivity values ranging from approximately 10 to 100. The sensitive clays were underlain by a firm drained boundary at a depth of 20.2 m (Hinchberger and Rowe 1998). Subsurface profiles of initial water content, Atterberg limits, initial void ratio, initial vertical hydraulic conductivity, compression index, recompression index, and preconsolidation pressure are shown in Figures. A.14 – A.18. The groundwater table was located near the ground surface and experienced seasonal fluctuations (Bozozuk 1972; Leroueil et al. 1983).

In August 1967, a shallow excavation was made on the site to a depth of 1.2 m, which removed the top soil layer and part of the desiccated crust and produced a stress release of 24.2 kPa. One month later, the Gloucester fill was constructed inside the excavation. The fill had a height of 3.7 m, a top width of 9.1 m, a base width of 20.1 m, and a length equal to approximately twice the width. The applied stress at the base of the fill under the centerline was 67.7 kPa (Bozozuk and Leonards 1972). Settlement gages S1, S2, and S3 were installed under the centerline at depths of 0.30 m, 1.22 m, and 3.66 m, respectively, below the base of the fill. Total settlement measurements are presented

in Figure A.19 and, after almost 5000 d, indicate values of 0.33 m, 0.26 m, and 0.12 m at these depths.

Table A.5 Subsurface conditions for the Gloucester test fill.

Soil Profile [a]	Depth (m)	Layer i	$H_{o,i}$ (m)	$z_{os,i}$ (m)	Layer Average Values					
					$e_{o,i}$	$C_{c,i}$	$C_{r,i}$	$k_{o,i}$ [b]	$C'_{k,i}$ [c]	A_i
Black organic top soil; tan fine sand and silt	0 - 0.8	-	-	-	-	-	-	-	-	-
Desiccated gray-brown silty clay	0.8 - 1.8	7	0.61	18.68	2.04	1.32	0.096	6.25	0.20	1.47
Soft gray-brown silty clay; occasional decayed roots and small flat stones	1.8 - 2.7	6	0.91	17.92	1.97	1.65	0.076	1.25	0.27	1.47
Soft gray silty clay; some shells	2.7 - 5.3	5	2.59	16.17	1.93	1.70	0.075	1.25	0.43	1.76
Gray silty clay; some shells	5.3 - 7.0	4	1.68	14.03	1.59	0.89	0.075	1.25	0.35	0.81
Gray clay with black mottling; occasional small flat stones	7.0 - 13.9	3	6.86	9.76	2.41	3.06	0.079	1.0	0.38	3.10
Gray silty clay with black mottling; occasional shells and small stones	13.9 - 18.3	2	4.42	4.12	1.66	1.54	0.055	1.25	0.26	4.58
Gray varved clay and silt; heterogeneous deposit of gray clay, silt, fine sand and small stones	18.3 - 20.2	1	1.91	0.96	1.71	1.62	0.066	1.25	0.26	0.00

[a] Soil profile data from Bozozuk (1972)

[b] $k_{o,i}$ unit is $\times 10^{-9}$ m/s

[c] C'_k calculated from Table B-3 of Bozozuk (1972)

The compressible stratum for the Gloucester test fill was considered as the lower 7 layers in Table A.5 (i.e., from depth 0.8 m to 20.2 m). Four simulations were conducted using CS3 to calculate settlements (Table A.6). Total heads at the top and bottom of the stratum were based on a groundwater table at a constant depth of 1.8 m (base of crust), the initial void ratio profile was assumed to be in equilibrium with initial

conditions, and unloading/loading was applied in the correct time sequence. The Case 1 simulation considers the simplest conditions where the entire stratum is modeled as a single layer. The average value of e_o for the stratum was specified for one sample point at mid-height and CS3 used this value to calculate the remaining e_o profile, which was nearly linear with depth and deviated only slightly from the stratum average (Figure A.15). The k_o profile was calculated similarly, with the stratum average obtained from the k_o profile provided by Hinchberger and Rowe (1998) and the remaining k_o profile calculated from e_o values and C_k' (Figure A.16). Values of C_c, C_r, and C_k' were each constant and equal to the respective stratum averages (Table A.6, Figure A.17). Leroueil et al. (1983) established that the measured preconsolidation stress for Gloucester clays is strain-rate dependent, which is not taken into account by CS3. To partly compensate for this effect, the σ_p' profile of Hinchberger and Rowe (1998), in which measured oedometer values were corrected for strain rate effects (14% reduction), was used for each simulation. Figure A.18 presents this σ_p' profile along with the σ_o' profile calculated by CS3. A uniform stress increment of 48.4 kPa was applied to the compressible stratum for Case 1 and produced a corresponding uniform distribution of initial excess pore pressure of equal value. This uniform stress increment was calculated using Equation A.10 and stress increment values at the top, middle and bottom of the stratum as obtained from elastic theory.

Table A.6 Analysis methods for the Gloucester test fill.

	Case 1	Case 2	Case 3	Case 4
R_i	1	7	7	7
Applied Stress	Uniform (48.4 kPa)	Depth-dependent (elastic theory)	Depth-dependent (elastic theory)	Depth-dependent (elastic theory)
Immediate Settlement	Not included	Not included	Included	Included
Skempton-Bjerrum (1957) Correction	Not included	Not included	Included	Included
e_o	Depth-dependent, stratum average at mid-height (2.07)	Depth-dependent, layer averages at mid-heights (Table A.5)	Depth-dependent, layer averages at mid-heights (Table A.5)	Depth-dependent, layer averages at mid-heights (Table A.5)
σ'_p	Hinchberger and Rowe (1998)	Hinchberger and Rowe (1998)	Hinchberger and Rowe (1998)	Hinchberger and Rowe (1998)
C_c	Stratum average (2.09)	Layer average (Table A.5)	Layer average (Table A.5)	Layer average (Table A.5)
C_r	Stratum average (0.073)	Layer average (Table A.5)	Layer average (Table A.5)	Layer average (Table A.5)
k_o	Depth-dependent, stratum average at mid-height (1.17×10^{-9} m/s)	Depth-dependent, layer averages at mid-heights (Table A.5)	Depth-dependent, layer averages at mid-heights (Table A.5)	Depth-dependent, layer averages at mid-heights (Table A.5)
C'_k	Stratum average (2.7)	Stratum average (2.7)	Stratum average (2.7)	Layer average (Table A.5)

Case 2 includes several refinements to the Case 1 analysis. The stratum was modeled using 7 layers, the applied stress increment profile was calculated using elastic theory (i.e., depth-dependent), and average values of e_o, C_c, C_r, and k_o were specified for each layer individually (Table A.5). Sample points for e_o and k_o were specified at the mid-height of each layer (Figure A.15 and Figure A.16). Case 3 is identical to Case 2 except that the effects of lateral strain on pore pressure generation were taken in to account. Lateral strains may be important considering that the ratio of vertical to

horizontal displacements at the base of the fill midway between the shoulder and toe was approximately 4.4 (Bozozuk 1972). Immediate settlements were calculated using elastic theory with a Young's modulus of 19.2 MPa, Poisson's ratio of 0.4, and net applied stress increment of 43.5 kPa (Bozozuk and Leonards 1972). Consolidation settlements were calculated using CS3 and the Skempton-Bjerrum (1957) correction with layer-average pore pressure parameters A (Table A.5) provided by Bozozuk (1972) and changes in vertical and horizontal total stresses ($\Delta\sigma_1$ and $\Delta\sigma_3$) given by elastic theory. A small change to the CS3 code was needed to accommodate the Skempton-Bjerrum correction. Finally, Case 4 represents the most sophisticated analysis and is identical to Case 3 except that C_k' was defined using layer-average values (Table A.5).

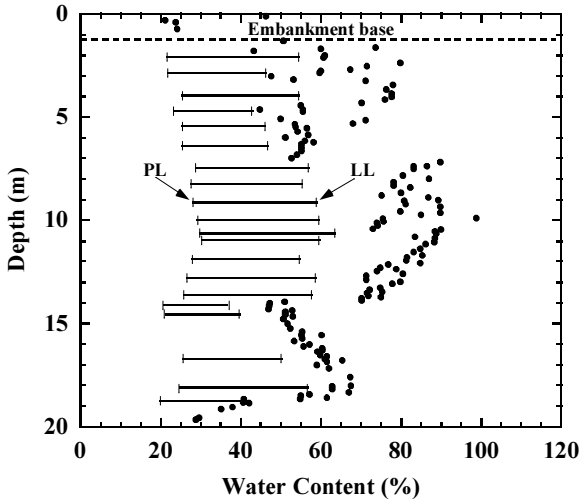

Figure A.14 Subsurface profiles of initial water content and Atterberg limits (data points scaled from Fig. 3 of Bozozuk 1972).

Measured heave for the excavation (gage S1) after unloading was 4 mm and calculated values obtained using CS3 are 13, 24, 19, and 18 mm for Cases 1-4,

respectively, which suggests that the C_r values based on laboratory tests (Bozozuk 1972) may be overestimated. The immediate settlement measured for gage S1 (26 mm) is in good agreement with the calculated value based on elastic theory (24 mm) for Cases 3 and 4. Field settlement measurements and corresponding settlement curves obtained using CS3 are shown for gages S1-S3 in Figure A.19. Interestingly, the CS3 curves for all four cases provide a reasonable first approximation to the measured data. This suggests that specific details for the various simulated cases are not critically important for this case study, which likely occurs because all simulations used the same Hinchberger and Rowe (1998) profile for preconsolidation stress. All simulated curves for the deepest gage (S3) underestimate the measured settlements, especially after 3000 d. For gages S1 and S2, measured settlements were underestimated by Case 1 and Case 3 and overestimated by Case 2. The Case 4 simulations, which were the most detailed, provided the closest estimate of measured settlements at S1 and S2. The CS3 curves also indicate that, for this case study, consideration of lateral strain effects reduces the calculated value of total settlement after about 400 d. Although the good agreement for the Case 4 simulation may be fortuitous, analysis of the Gloucester test fill demonstrates the capability of CS3 to provide estimates of consolidation settlement for complex conditions involving layered soils.

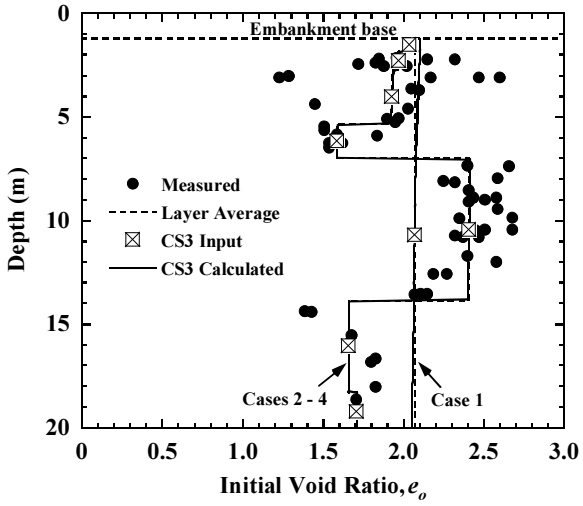

Figure A.15 Subsurface profile of initial void ratio (data points scaled from Fig. 23 of Bozozuk 1972).

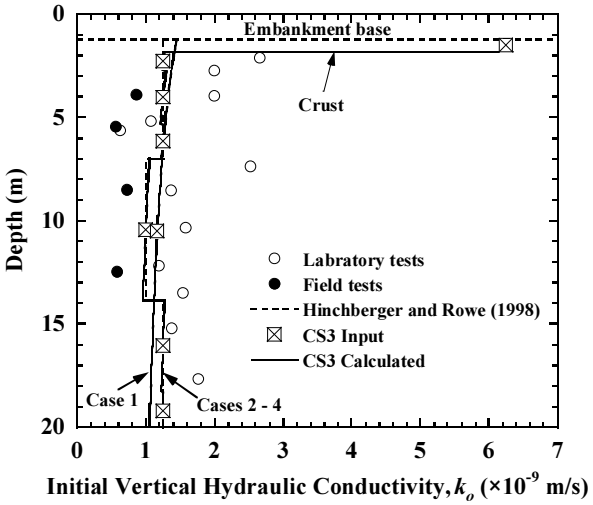

Figure A.16 Subsurface profile of initial vertical hydraulic conductivity (laboratory test data points from Table B-3 of Bozozuk 1972; field test data points scaled from Fig. 9 of Hinchberger and Rowe 1998).

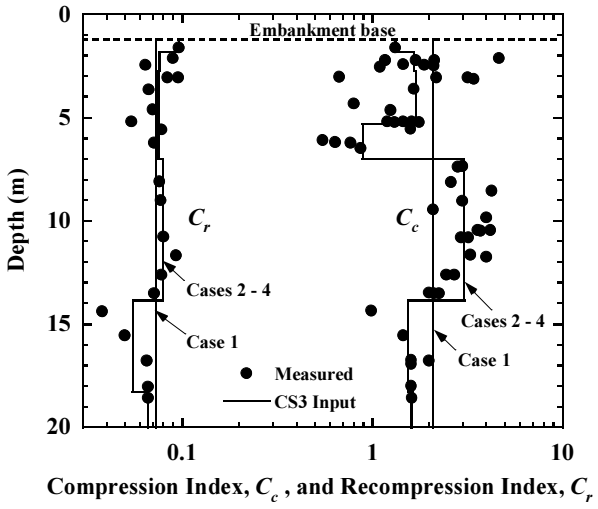

Figure A.17 Subsurface profiles of compression index and recompression index (C_c data points scaled from Fig. 23 of Bozozuk 1972; C_r data points calculated from Appendix B of Bozozuk 1972).

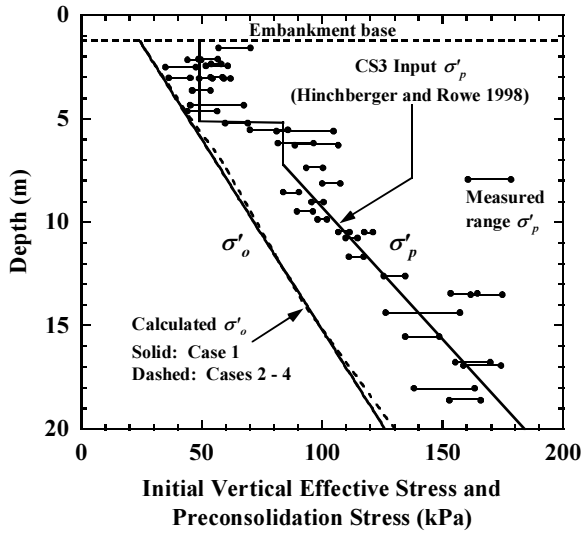

Figure A.18 Subsurface profiles of initial vertical effective stress and preconsolidation stress (data points scaled from Fig. 3 of Bozozuk 1972).

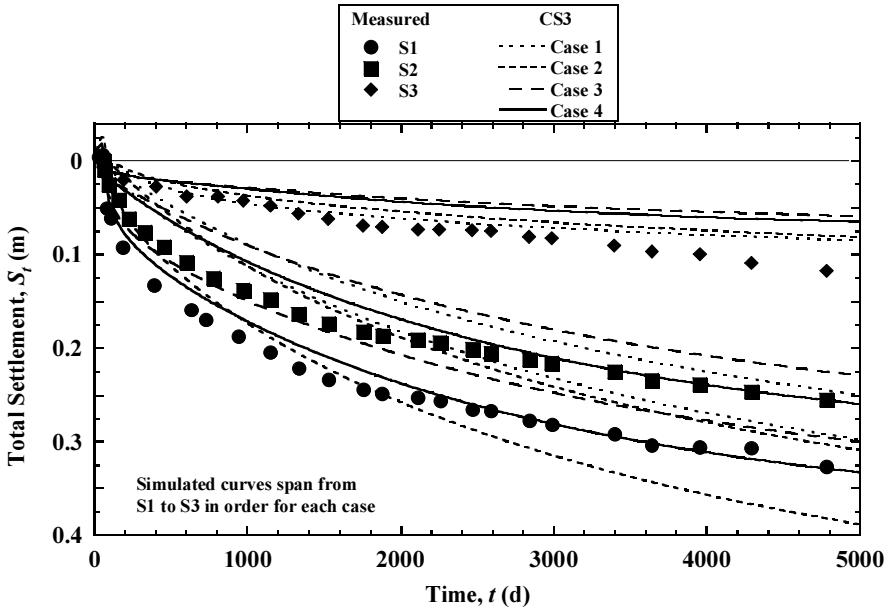

Figure A.19 Settlement curves for Gloucester test fill (data points for first 4 years scaled from Fig. D-1 of Bozozuk 1972; remaining data points scaled from Fig. 11 of Hinchberger and Rowe 1998).

A.5 Conclusions

The following conclusions are reached as a result of the development of CS3 and subsequent investigations of consolidation behavior using this model:

(1) CS3 is a numerical model for one-dimensional large strain consolidation of layered soils. The algorithm accounts for vertical strain, soil self-weight, changing material properties during consolidation, unload/reload, time-dependent loading and boundary conditions, an externally applied hydraulic gradient, and variable profiles for preconsolidation stress and applied stress increment. CS3 utilizes constitutive relationships defined in terms of conventional parameters, as opposed to individual

data points in CS2, and allows for direct input of laboratory and field data to facilitate modeling for practical applications.

(2) Verification checks of CS3 show excellent agreement with available analytical and numerical solutions.

(3) Layered soil heterogeneity can have important effects on calculated settlement and distribution of excess pore pressure. Characterization of a multi-layer system as a single layer with average properties may result in significant errors.

(4) Settlement estimates obtained using CS3 are in good agreement with field measurements for the Gloucester test fill and demonstrate the general capability of CS3 for analysis of complex conditions involving layered soils.

A.6 Acknowledgements

Appendix A of this dissertation is based on material published by the Journal of Geotechnical and Geoenvironmental Engineering titled “CS3: Large Strain Consolidation Model for Layered Soils” with authors, Patrick J. Fox, Hefu Pu, and James D. Berles (2014). The dissertation author is the second author of this paper.

References

ASTM D 4186-06. *Standard Test Method for One-Dimensional Consolidation Properties of Saturated Cohesive Soils Using Controlled-Strain Loading*, ASTM International, West Conshohocken, PA.

Alshawabkeh, A. N., Rahbar, N., and Sheahan, T. (2005). "A model for contaminant mass flux in capped sediment under consolidation." *Journal of Contaminant Hydrology*, 78(3), 147-165.

Al-Tabbaa, A., and Wood, D. M. (1987). "Some measurements of the permeability of kaolin." *Geotechnique*, 37(4), 499-503.

Armour, D. W., Jr., and Drnevich, V. P. (1986). "Improved techniques for the constant-rate-of-strain consolidation test." *Consolidation of Soils: Testing and Evaluation*, *ASTM STP 892*, R. N. Yong and F. C. Townsend, eds., ASTM International, West Conshohocken, Pennsylvania, 170-183.

Aydilek, A. H., Edil, T. B., and Fox, P. J. (2000). "Consolidation characteristics of wastewater sludge." *Geotechnics of High Water Content Materials*, Special Technical Publication 1374, T. B. Edil and P. J. Fox, eds., ASTM International, 309-323.

Azzouz, A. S., Krizek, R. J., and Corotis, R. B. (1976). "Regression analysis of soil compressibility." *Soils and Foundations*, 16(2), 19-29.

Bear, J. (1972). *Dynamics of fluids in porous media*, Dover, New York.

Berilgen, S. A. (2004). "Determination of consolidation behavior of halic dredged material by using a seepage induced consolidation testing system." *Journal of Engineering and Natural Sciences*, 3(3), 60-72.

Berilgen, M. M., Ozaydin, I. K., and Edil, T. B. (2000). "A case history: Dredging and disposal of Golden Horn sediments." *Geotechnics of High Water Content Materials*, Special Technical Publication 1374, T. B. Edil and P. J. Fox, eds., ASTM International, 324-336.

Berilgen, S. A., Berilgen, M. M., and Ozaydin, K. I. (2006). "Assessment of consolidation behavior of Golden Horn marine dredged material." *Marine Georesources and Geotechnology*, 24(1), 1-16.

Berles, J. D. (1995). *A Numerical Model for the Consolidation of Clay*. M.S.C.E. Thesis, School of Civil Engineering, Purdue University, West Lafayette, IN.

Bharat, T. V., and Sharma, J. (2011). "Prediction of compression and permeability characteristics of mine tailings using natural computation and large-strain consolidation framework." *Geo-Frontiers 2011, Geotechnical Special Publication No. 211*, J. Han and D. E. Alzamora, eds., ASCE, 3868-3877.

Bicer, P. (2005). "Geotechnical characteristics of soils having high water content." *Journal of Engineering and Natural Sciences*, 2, 51-63.

Bonaparte, R., and Gross, B. A. (1993). *LDCRS flow from double lined landfills and surface impoundments*, EPA/600/R-93/070. Springfield, VA: NTIS Publication PB93-179885.

Boving, T. B., and Grathwohl, P. (2001). "Tracer diffusion coefficients in sedimentary rocks: correlation to porosity and hydraulic conductivity." *Journal of Contaminant Hydrology*, 53(1-2), 85-100.

Bozozuk, M. (1972). *The Gloucester test fill*. Ph.D. Thesis, Purdue University, West Lafayette, IN.

Bozozuk, M., and Leonards, G. A. (1972). "The Gloucester test fill." *Proceedings of the ASCE Specialty Conference on Performance of Earth and Earth-Supported Structures*, Purdue University, West Lafayette, IN, 1(1), 299-317.

Charbeneau, R. J. (2000). *Groundwater Hydraulics and Pollutant Transport*. Prentice-Hall, Inc., Upper Saddle River, NJ.

Chen, R. P., Zhou, W. H., Wang, H. Z., and Chen, Y. M. (2005). "One-dimensional nonlinear consolidation of multi-layered soil by differential quadrature method." *Computers and Geotechnics*, 32(5), 358-369.

Crawford, C. B. (1988). "On the importance of rate of strain in the consolidation test." *Geotechnical Testing Journal*, 11(1), 60-62.

Conte, E., and Troncone, A. (2006). "One-dimensional consolidation under general time-dependent loading." *Canadian Geotechnical Journal*, 43(11), 1107–1116.

Duncan, J. M. (1993). "Limitations of conventional analysis of consolidation settlement." *Journal of Geotechnical Engineering*, 119(9), 1333-1359.

Evangelista, A., and Viggiani, C. (1973). "Discussion: Consolidation at constant rate of strain." *Journal of the Soil Mechanics and Foundations Division*, 99(SM1), 141-144.

Foose, G. J., Benson, C. H., and Edil, T. B. (2002). "Comparison of solute transport in three composite liners." *Journal of Geotechnical and Geoenvironmental Engineering*, 128(5), 391-403.

Fox, P. J. (1996). "Analysis of hydraulic gradient effects for laboratory hydraulic conductivity testing." *Geotechnical Testing Journal*, 19(2), 181-190.

Fox, P. J. (2000). "CS4: A large strain consolidation model for accreting soil layers." *Geotechnics of High Water Content Materials*, Special Technical Publication 1374, T. B. Edil and P. J. Fox, eds., ASTM International, 29-47.

Fox, P. J. (2007a). "Coupled large strain consolidation and solute transport. I: Model development." *Journal of Geotechnical and Geoenvironmental Engineering,* 133(1), 3-15.

Fox, P. J. (2007b). "Coupled large strain consolidation and solute transport. II: Model verification and simulation results." *Journal of Geotechnical and Geoenvironmental Engineering,* 133(1), 16-29.

Fox, P. J., and Berles, J. D. (1997). "CS2: A piecewise-linear model for large strain consolidation." *International Journal of Numerical and Analytical Methods in Geomechanics*, 21(7), 453-475.

Fox, P. J., Di Nicola, M., and Quigley, D. W. (2003). "Piecewise-linear model for large strain radial consolidation." *Journal of Geotechnical and Geoenvironmental Engineering*, 129(10), 940-950.

Fox, P. J., and Lee, J. (2008). "Model for consolidation-induced solute transport with nonlinear and nonequilibrium sorption." *International Journal of Geomechanics*, 8(3), 188-198.

Fox, P. J., and Pu, H. (2012). "Enhanced CS2 model for large strain consolidation." *International Journal of Geomechanics*, 12(5), 574-583.

Fox, P. J., and Qiu, T. (2004). "Model for large strain consolidation with compressible pore fluid." *International Journal of Numerical and Analytical Methods in Geomechanics*, 28(11), 1167-1188.

Fox, P. J., Lee, J., and Qiu, T. (2005). "Model for large strain consolidation by centrifuge." *International Journal of Geomechanics*, 5(4), 267-275.

Fox, P. J., and Shackelford, C. D. (2010). "State-of-the-Art: Consolidation-induced contaminant transport for high water content geo-materials." *GeoFlorida 2010: Advances in Analysis, Modeling and Design*, GSP No. 199, D. Fratta, A. J. Puppala, and B. Muhunthan, eds., ASCE, 129-138.

Fox, P. J., Pu, H.-F., and Christian, J. T. (2014). "Assessment of data analysis methods for the CRS consolidation test." *Journal of Geotechnical and Geoenvironmental Engineering*, 140(6), 04014020.

Freeze, R. A., and Cherry, J. A. (1979). *Groundwater*, Prentice-Hall, Englewood Cliffs, N.J.

Gibson, R. E., England, G. L., and Hussey, M. J. L. (1967). "The theory of one-dimensional consolidation of saturated clays, I. Finite non-linear consolidation of thin homogeneous layers." *Geotechnique*, 17(3), 261-273.

Gibson, R. E., Schiffman, R. L., and Cargill, K. W. (1981). "The theory of one-dimensional consolidation of saturated clays. II. Finite nonlinear consolidation of thick homogeneous layers." *Canadian Geotechnical Journal*, 18(2), 280-293.

Gorman, C. T., Hopkins, T. C., Deen, R. C., and Drnevich, V. P. (1978). "Constant-rate-of-strain and controlled-gradient consolidation testing," *Geotechnical Testing Journal*, 1(1), 3-15.

Hamilton, J. J., and Crawford, C. B. (1959). "Improved determination of preconsolidation pressure of a sensitive clay." *Papers on Soils*, Special Technical Publication No. 254, ASTM International, West Conshohocken, PA, 254-270.

Hazzard, J. F., Yacoub, T. E., and Curran, J. (2008). "Consolidation in multi-layered soils: A hybrid computation scheme." *GeoEdmonton '08: A Heritage of Innovation,* 61st Canadian Geotechnical Conference, Edmonton, 182-189.

Hinchberger, S. D., and Rowe, R. K. (1998). "Modelling the rate-sensitive characteristics of the Gloucester foundation soil." *Canadian Geotechnical Journal*, 35(5), 769-789.

Hsu, T. W., and Lu, S. C. (2006). "Behavior of one-dimensional consolidation under time-dependent loading." *Journal of Engineering Mechanics*, 132(4), 457-462.

Kang, J. -B., and Shackelford, C. D. (2010). "Membrane behavior of compacted clay liners." *Journal of Geotechnical and Geoenvironmental Engineering*, 136(10), 1368-1382.

Kim, H.-J., and Mission, J. L. (2011). "Numerical analysis of one-dimensional consolidation in layered clay using interface boundary relations in terms of infinitesimal strain." *International Journal of Geomechanics*, 11(1), 72-77.

Kim, J. Y., Edil, T. B., and Park, J. K. (2001). "Volatile organic compound (VOC) transport through compacted clay." *Journal of Geotechnical and Geoenvironmental Engineering*, 127(2), 126-134.

Kokusho, T., and Kojima, T. (2002). "Mechanism for postliquefaction water film generation in layered sand." *Journal of Geotechnical and Geoenvironmental Engineering,* 128(2), 129-137.

Kulhawy, F. H., and Mayne, P. W. (1990). *Manual on estimating soil properties for foundation design*. Report EPRI EL-6800, Electric Power Research Institute, Palo Alto

Kwon, Y., Kazama, M., and Uzuoka, R. (2007). "Geotechnical hybrid simulation system for one-dimensional consolidation analysis." *Soils and Foundations*, 47(6), 1133-1140.

Larsson, R., and Sälfors, G. (1986). "Automatic continuous consolidation testing in Sweden." *Consolidation of Soils: Testing and Evaluation*, STP 892, R. N. Yong and F. C. Townsend, eds., ASTM International, West Conshohocken, PA, 299-328.

Lee, K. (1981). "Consolidation with constant rate of deformation." *Geotechnique*, 31(2), 215-229.

Lee, J. (2007). *Experimental and numerical investigation of consolidation-induced solute transport*. Ph.D. Thesis, Ohio State University, Columbus, Ohio.

Lee, J., and Fox, P. J. (2005). "Efficiency of seepage consolidation for preparation of clay substrate for centrifuge testing." *Geotechnical Testing Journal*, 28(6), 577-585.

Lee, J., and Fox, P. J. (2009). "Investigation of consolidation-induced solute transport. II: Experimental and numerical results." *Journal of Geotechnical and Geoenvironmental Engineering,* 135(9), 1239-1253.

Lee, J., and Park, J. -W. (2013). "Numerical investigation for the isolation effect of in situ capping for heavy metals in contaminated sediments." *Korean Society of Civil Engineers, Journal of Civil Engineering,* 17(6), 1275-1283.

Lee, K., and Sills, G. C. (1979). "A moving boundary approach to large strain consolidation of a thin soil layer." *Proceedings*, *3rd International Conference on Numerical Methods in Geomechanics*, Aachen, Germany, 1, 163-173.

Lee, J., Fox, P. J., and Lenhart, J. J. (2009). "Investigation of consolidation-induced solute transport. I: Effect of consolidation on transport parameters." *Journal of Geotechnical and Geoenvironmental Engineering*, 135(9), 1228-1238.

Lee, K., Choa, V., Lee, S. H., and Quek, S. H. (1993). "Constant rate of strain consolidation of Singapore marine clay." *Geotechnique*, 43(3), 471-488.

Lee, P. K. K., Xie, K. H., and Cheung, Y. K. (1992). "A study on one-dimensional consolidation of layered systems." *International Journal of Numerical and Analytical Methods in Geomechanics*, 16(11), 815-831.

Lerman, A. (1978). "Chemical exchange across sediment-water interface." *Annual Review of Earth and Planetary Sciences*, 6, 281-303.

Leroueil, S., Tavenas, F., Samson, L., and Morin, P. (1983a). "Preconsolidation pressure of Champlain clays. Part II. Laboratory determination." *Canadian Geotechnical Journal*, 20(4), 803-816.

Leroueil, S., Samson, L., and Bozozuk, M. (1983b). "Laboratory and field determination of preconsolidation pressures at Gloucester." *Canadian Geotechnical Journal*, 20(3), 477-490.

Leroueil, S., Kabbaj, M., Tavenas, F., and Bouchard, R. (1985). "Stress-strain-strain rate relation for the compressibility of sensitive natural clays." *Geotechnique,* 35(2), 159-180.

Lewis, T. W. (2009). *Theoretical Effects of Consolidation on Solute Transport in Soil Barriers*. Ph.D. Thesis, University of Newcastle, NSW, Australia.

Lewis, T. W., Pivonka, P., and Smith, D. W. (2009a). "Theoretical investigation of the effects of consolidation on contaminant transport through clay barriers." *International Journal for Numerical and Analytical Methods in Geomechanics*, 33(1), 95-116.

Lewis, T. W., Pivonka, P., Fityus, S. G., and Smith, D. W. (2009b). "Parametric sensitivity analysis of coupled mechanical consolidation and contaminant transport through clay barriers." *Computers and Geotechnics*, 36, 31-40.

Lo, K. Y., Bozozuk, M., and Law, K. T. (1976). "Settlement analysis of the Gloucester test fill." *Canadian Geotechnical Journal*, 13(4), 339–354.

Loroy, J. J. C., Soga, K., Savvidou, C., and Britto, A. M. (1996). "Finite element analysis of consolidation and contaminant transport in porous media." Proceeding of 2nd International Congress on Environmental Geotechnics, M. Kamon, ed., Osaka, Japan, Vol. 1, 263–268.

Malusis, M. A., and Shackelford, C. D. (2002). "Chemico-osmotic efficiency of a geosynthetic clay liner." *Journal of Geotechnical and Geoenvironmental Engineering*, 128(2), 97-106.

Manheim, F. T. (1970). "The diffusion of ions in unconsolidated sediments." *Earth and Planetary Science Letters*, 9(4), 307-309.

Mercer, J. W., and Cohen, R. M. (1990). "A review of immiscible fluids in the subsurface: Properties, models, characterization and remediation." *Journal of Contaminant Hydrology*, 6(2), 107-163.

Meric, D., Sheahan, T. C., Alshawabkeh, A., and Shine, J. (2010). "A consolidation and contaminant transport device for assessing reactive mat effectiveness for subaqueous sediment remediation." *Geotechnical Testing Journal*, 33(6), 423-433.

Meric, D., Hellweger, F., Barbuto, S., Rahbar, N., Alshawabkeh, A. N., and Sheahan, T. C. (2013). "Model prediction of long-term reactive core mat efficacy for capping contaminated aquatic sediments." *Journal of Geotechnical and Geoenvironmental Engineering*, 139(4), 564–575.

Mesri, G., and Choi, Y. K. (1985). "Settlement analysis of embankments on soft clays." *Journal of Geotechnical Engineering*, 111(4), 441-464.

Mesri, G., Lo, D. O. K., and Feng, T.-W. (1994). "Settlement of embankments on soft clays." *Vertical and Horizontal Deformations of Foundations and Embankments, Geotechnical Special Publication No. 40*, Yeung, A. T., and Felio, G. Y., eds., ASCE, 1, 8-56.

Moo-Young, H., Johnson, B., Johnson, A., Carson, D., Lew, C., Liu, S., and Hancock, K. (2004). "Characterisation of infiltration rates from landfills: supporting groundwater modeling efforts." *Environmental Monitoring and Assessment* 96, 283-311.

Nagaraj, T. S., Pandian, N. S., and Narasimha Raju, P. S. R. (1994). "Stress-state-permeability relations for overconsolidated clays." *Geotechnique*, 44(2), 349-352.

Nogami, T., and Li, M. (2002). "Consolidation of system of clay and thin sand layers." *Soils and Foundations*, 42(4), 1-11.

Nogami, T., and Li, M. (2003). "Consolidation of clay with a system of vertical and horizontal drains." *Journal of Geotechnical and Geoenvironmental Engineering*, 129(9), 838–848.

Ogata, A. (1970). "Theory of dispersion in a granular medium." *Professional Paper 411-I*, U.S. Geological Survey.

Olson, R. E. (1977). "Consolidation under time dependent loading." *Journal of the Geotechnical Engineering Division*, 103(GT1), 55-60.

Olson, R. E., and Ladd, C. C. (1979). "One-dimensional consolidation problems." *Journal of the Geotechnical Engineering Division*, 105(GT1), 11-30.

Othman, M. A., Bonaparte, R., and Gross, B. A. (1997). "Preliminary results of composite liner field performance study." *Geotextiles and Geomembranes*, 15(4-6), 289-312.

Palermo, M., Maynord, S., Miller, J., and Reible, D. (1998). "Guidance for in-situ subaqueous capping of contaminated sediments." *EPA 905-B96-004*, Great Lakes National Program Office, Chicago, IL.

Pane, V., Croce, P., Znidarcic, D., Ko, H. Y., Olsen, H. W., and Schiffman, R. L. (1983). "Effects of consolidation on permeability measurements for soft clay." *Geotechnique*, 33(1), 67-72.

Perrone, V. J. (1998). *One dimensional computer analysis of simultaneous consolidation and creep of clay*. Ph.D. Thesis, Virginia Polytechnic Institute and State University.

Peters, G. P., and Smith, D. W. (1998). "One-dimensional contaminant transport through a consolidating soil: Application to contaminant transport through a geocomposite liner." *Proceeding of Biot Conference on Poromechanics*, J.-F. Thimus, Y. Abousleiman, A. H.-D. Cheng, O. Coussy, and E. Detournay, eds., Louvain, Belgium, 481-486.

Peters, G. P., and Smith, D. W. (2002). "Solute transport through a deforming porous medium." *International Journal of Numerical and Analytical Methods in Geomechanics*, 26(7), 683-717.

Potter, L. J., Savvidou, C., and Gibson, R. E. (1994). "Consolidation and pollutant transport associated with slurried mineral waste disposal." *Proceeding of 1st International Congress on Environmental Geotechnics*, W. D. Carrier, III, ed., Edmonton, Alta., Canada, 525-530.

Pu, H.-F., and Fox, P. J. (2014). "Consolidation-induced solute transport for constant rate of strain. I: Model development and numerical results." *Journal of Geotechnical and Geoenvironmental Engineering*, in press.

Pu, H. -F., Fox, P. J., and Liu, Y. (2013). "Model for large strain consolidation under constant rate of strain." *International Journal of Numerical and Analytical Methods in Geomechanics*, 37(11), 1574-1590.

Qiu, T., and Fox, P. J. (2008). "Numerical analysis of 1-D compression wave propagation in saturated poroelastic media." *International Journal for Numerical and Analytical Methods in Geomechanics*, 32(2), 161-187

Rabideau, A., and Khandelwal, A. (1998). "Boundary conditions for modeling transport in vertical barriers." *Journal of Environmental Engineering*, 124(11), 1135-1139.

Rowe, R. K. (1998). "Geosynthetics and the minimization of contaminant migration through barrier systems beneath solid waste." *Proceedings of the 6th International Conference on Geosynthetics*, Atlanta, March, Vol. 1, pp. 27-103, Industrial Fabrics Association International, St. Paul, MN.

Rowe, R. K. (2005). "Long-term performance of contaminant barrier systems." *Geotechnique*, 55(9), 631-678.

Rowe, R., and Nadarajah, P. (1995). "Transport modelling under transient flow conditions." *Proceedings of the 5th International Symposium on Numerical Models in Geomechanics*, Davos, Switzerland, 337-342.

Sample, K. M., and Shackelford, C. D. (2012). "Apparatus for constant rate-of-strain consolidation of slurry mixed soils." *Geotechnical Testing Journal*, 35(3), 409-419.

Sangam, H. P., and Rowe, R. K. (2001). "Migration of dilute aqueous organic pollutants through HDPE geomembranes." *Geotextiles and Geomembranes*, 19(6), 329-357.

Schiffman, R. L. (1958). "Consolidation of soil under time-dependent loading and varying permeability." *Proceedings, 37th Annual Meeting, Highway Research Board*, H. P. Orland, ed., Washington, DC, 37, 584-617.

Schiffman, R. L., and Stein, J. R. (1970). "One-dimensional consolidation of layered systems." *Journal of the Soil Mechanics and Foundations Division,* 96(SM4), 1499-1504.

Shackelford, C. D. (2013). "Membrane behavior in engineered bentonite-based containment barriers: State of the art." *Coupled Phenomena in Environmental Geotechnics*, M. Manassero, A. Dominijanni, S. Foti, and G. Musso, Eds., July 1-3, 2013, Torino, Italy, CRC Press/Balkema, Taylor & Francis Group, London, 45-60.

Sheahan, T. C. (2012). Personal communication. November 21.

Sheahan, T. C., and Watters, P. J. (1997). "Experimental verification of CRS consolidation theory." *Journal of Geotechnical and Geoenvironmental Engineering,* 123(5), 430-437.

Schiffman, R. L., Pane, V., and Gibson, R. E. (1984). "The theory of one-dimensional consolidation of saturated clays. IV. An overview of nonlinear finite strain sedimentation and consolidation." *Proceedings, Symposium on Sedimentation/ Consolidation Models: Prediction and Validation*, R. N. Yong and F. C. Townsend, eds., San Francisco, California, ASCE, 1-29.

Silvestri, V., Yong, R. N., Soulie, M., and Gabriel, F. (1986). "Controlled-strain, controlled-gradient, and standard consolidation testing of sensitive clays," *Consolidation of Soils: Testing and Evaluation*, STP 892, R. N. Yong and F. C. Townsend, eds., ASTM International, West Conshohocken, PA, 433-450.

Skempton, A. W., and Bjerrum, L. (1957). "A Contribution to the settlement analysis of foundations on clay." *Geotechnique*, 7(4), 168-178.

Smith, D. W. (1997). "One-dimensional contaminant transport through a deforming porous media: Theory and solution for a quasi-steady state problem." *Research Report No. 150.08.1997*, University of Newcastle, Callaghan, Australia.

Smith, R. E., and Wahls, H. E. (1969). "Consolidation under constant rate of strain." *Journal of the Soil Mechanics and Foundations Division*, 95(SM2), 519-539.

Tang, X. W., and Onitsuka, K. (2001). "Consolidation of double-layered ground with vertical drains." *International Journal of Numerical and Analytical Methods in Geomechanics*, 25(14), 1449-1465.

Tavenas, F., Jean, P., Leblond, P., and Leroueil, S. (1983). "The permeability of natural soft clays. Part II: Permeability characteristics." *Canadian Geotechnical Journal*, 20(4), 645-660.

Terzaghi, K. (1925). *Erdbaumechanik auf Bodenphysikalischer Grundlage*, Vienna, Deuticke.

Townsend, F. C., and McVay, M. C. (1990). "SOA: Large strain consolidation predictions." *Journal of Geotechnical Engineering*, 116(2), 222-243.

Travis, C. C., and Etnier, E. L. (1981). "A survey of sorption relationships for reactive solutes in soil." *Journal of Environmental Quality*, 10(1), 8–17.

Tavenas, F., Jean, P., Leblond, P., and Leroueil, S. (1983). "The permeability of natural soft clays. Part II: Permeability characteristics." *Canadian Geotechnical Journal*, 20(4), 645-660.

Ullman, W. J., and Aller, R. C. (1982). "Diffusion coefficients in nearshore marine sediments." *Limnology and Oceanography*, 27(3), 552-556.

U.S. Environmental Protection Agency (USEPA). (1998). *Guidance for In-Situ Subaqueous Capping of Contaminated Sediments*, Assessment and Remediation of Contaminated Sediments (ARCS) Program, EPA Report 905-B96-004, Great Lakes National Program Office, Chicago.

U.S. Environmental Protection Agency (USEPA). (2005). *Contaminated Sediment Remediation Guidance for Hazardous Waste Sites*. OSWER Directive 9355.0-85, USEPA, Office of Solid Waste and Emergency Response, Washington, D. C.

Vaid, Y. P., Robertson, P. K., and Campanella, R. G. (1979). "Strain rate behaviour of Saint-Jean-Vianney clay." *Canadian Geotechnical Journal*, 16(1), 34-42.

Van Impe, P. O., Mazzieri, F., Van Impe, W. F., and Constales, D. (2002). "A simulation model for consolidation and contaminant coupled flows in clay layers." *Proceeding of 4th International Congress on Environmental Geotechnics*, L. G. de Mello and M. Almeida, eds., Rio De Janeiro, Brazil, Vol. 1, 189-194.

Walker, R., Indraratna, B., and Sivakugan, N. (2009). "Vertical and radial consolidation analysis of multilayered soil using the spectral method." *Journal of Geotechnical and Geoenvironmental Engineering*, 135(5), 657-663.

Wang, X. S., and Jiao, J. J. (2004). "Analysis of soil consolidation by vertical drains with double porosity model." *International Journal for Numerical and Analytical Methods in Geomechanics*, 28(14), 1385–1400.

Wissa, A. E. Z., Christian, J. T., Davis, E. H., and Heiberg, S. (1971). "Consolidation at constant rate of strain." *Journal of the Soil Mechanics and Foundations Division*, 97(SM10), 1393-1413.

Workman, J. P. (1993). "Interpretation of leakage rates in double lined systems." Proceedings of the 7th GRI Conference: Geosynthetic Liner Systems, Philadelphia, 91-108.

Xie, K. H., Xie, X. Y., and Jiang, W. (2002). "A study on one-dimensional nonlinear consolidation of double-layered soil." *Computers and Geotechnics*, 29(2), 151-168.

Xie, K. H., Xie, X. Y., and Gao, X. (1999). "Theory of one dimensional consolidation of two-layered soil with partially drained boundaries." *Computers and Geotechnics*, 24(4), 265-278.

Yaws, C. L. (1995). *Handbook of transport property data*, Gulf Publishing, Houston.

Yong, R. N., Siu, S. K. H., and Sheeran, D. E. (1983). "On the stability and settling of suspended solids in settling ponds. Part I. Piece-wise linear consolidation analysis of sediment layer." *Canadian Geotechnical Journal*, 20(4), 817-826.

Zhang, H. J., Jeng, D. -S., Barry, D. A., Seymour, B. R., and Li, L. (2013). "Solute transport in nearly saturated porous media under landfill clay liners: A finite deformation approach." *Journal of Hydrology*, 479, 189-199.

Zhou, L., and Selim, H. M. (2001). "Solute transport in layered soils: Nonlinear and kinetic reactivity." *Soil Science Society of America Journal*, 65(4), 1056–1064.

Zhou, Y., Deng, A., and Wang, C. (2013). "Finite-difference model for one-dimensional electro-osmotic consolidation." *Computers and Geotechnics*, 54, 152-165.

Zhu, G., and Yin, J. H. (1999a). "Consolidation of double soil layers under depth-dependent ramp load." *Geotechnique*, 49(3), 415-421.

Znidarcic, D., Schiffman, R. L., Pane, V., Croce, P., Ko, H. Y., and Olsen, H. W. (1986). "The theory of one-dimensional consolidation of saturated clays: Part V, Constant rate of deformation testing and analysis." *Geotechnique,* 36(2), 227-237.